



*applied sciences*

Special Issue Reprint

---

# Remote Sensing Applications in Archaeology, Geography, and the Earth Sciences

---

Edited by  
Tung-Ching Su

[www.mdpi.com/journal/applsci](http://www.mdpi.com/journal/applsci)



# **Remote Sensing Applications in Archaeology, Geography, and the Earth Sciences**



# Remote Sensing Applications in Archaeology, Geography, and the Earth Sciences

Editor

**Tung-Ching Su**

MDPI • Basel • Beijing • Wuhan • Barcelona • Belgrade • Manchester • Tokyo • Cluj • Tianjin



*Editor*

Tung-Ching Su  
National Quemoy University  
Kinmen, Taiwan

*Editorial Office*

MDPI  
St. Alban-Anlage 66  
4052 Basel, Switzerland

This is a reprint of articles from the Special Issue published online in the open access journal *Applied Sciences* (ISSN 2076-3417) (available at: [https://www.mdpi.com/journal/applsci/special\\_issues/Archaeology\\_Geography\\_Earth](https://www.mdpi.com/journal/applsci/special_issues/Archaeology_Geography_Earth)).

For citation purposes, cite each article independently as indicated on the article page online and as indicated below:

LastName, A.A.; LastName, B.B.; LastName, C.C. Article Title. <i>Journal Name</i> <b>Year</b> , <i>Volume Number</i> , Page Range.
--

**ISBN 978-3-0365-8278-8 (Hbk)**

**ISBN 978-3-0365-8279-5 (PDF)**

© 2023 by the authors. Articles in this book are Open Access and distributed under the Creative Commons Attribution (CC BY) license, which allows users to download, copy and build upon published articles, as long as the author and publisher are properly credited, which ensures maximum dissemination and a wider impact of our publications.

The book as a whole is distributed by MDPI under the terms and conditions of the Creative Commons license CC BY-NC-ND.

# Contents

## **Tung-Ching Su**

Special Issue on Remote Sensing Applications in Archaeology, Geography, and the Earth Sciences

Reprinted from: *Applied Sciences* **2023**, *13*, 7631, doi:10.3390/app13137631 . . . . . 1

## **Michal Palčák, Pavol Kudela, Miriam Fandáková and Juraj Kordek**

Utilization of 3D Digital Technologies in the Documentation of Cultural Heritage: A Case Study of the Kunerad Mansion (Slovakia)

Reprinted from: *Applied Sciences* **2022**, *12*, 4376, doi:10.3390/app12094376 . . . . . 5

## **Carmen Marín-Buzón, Antonio Miguel Pérez-Romero, Manuel J. León-Bonillo, Rubén Martínez-Álvarez, Juan Carlos Mejías-García and Francisco Manzano-Agugliaro**

Photogrammetry (SfM) vs. Terrestrial Laser Scanning (TLS) for Archaeological Excavations: Mosaic of Cantillana (Spain) as a Case Study

Reprinted from: *Applied Sciences* **2021**, *11*, 11994, doi:10.3390/app112411994 . . . . . 29

## **Marilena Cozzolino, Antonio De Simone, Vincenzo Gentile, Paolo Mauriello and Amanda Piezzo**

GPR and Digital Survey for the Diagnosis and the 3D Representation of the Battle of Issus Mosaic from the House of the Faun, Pompeii (Naples, Italy)

Reprinted from: *Applied Sciences* **2022**, *12*, 6965, doi:10.3390/app12146965 . . . . . 45

## **Tung-Ching Su, Tsung-Chiang Wu, Ming-Hung Wun and Cheng-Wei Wang**

Style Recognition of Door God Paintings by Hypothesis Testing for Texture Features of Painting Patterns

Reprinted from: *Applied Sciences* **2022**, *12*, 2637, doi:10.3390/app12052637 . . . . . 65

## **Haoyang Jiao, Fayuan Li, Hong Wei and Wei Liu**

An Improved Shoulder Line Extraction Method Fusing Edge Detection and Regional Growing Algorithm

Reprinted from: *Applied Sciences* **2022**, *12*, 12662, doi:10.3390/app122412662 . . . . . 87

## **Yin-Chun Hung, Yu-Xiang Zhao and Wei-Chen Hung**

Development of an Underground Tunnels Detection Algorithm for Electrical Resistivity Tomography Based on Deep Learning

Reprinted from: *Applied Sciences* **2022**, *12*, 639, doi:10.3390/app12020639 . . . . . 105

## **Nabil Bachagha, Abdelrazek Elnashar, Moussa Tababi, Fatma Souei and Wenbin Xu**

The Use of Machine Learning and Satellite Imagery to Detect Roman Fortified Sites: The Case Study of Blad Talh (Tunisia Section)

Reprinted from: *Applied Sciences* **2023**, *13*, 2613, doi:10.3390/app13042613 . . . . . 123

## **Yan Li, Jinsong Chong and Zongze Li**

A Simulation Method of Two-Dimensional Sea-Surface Current Field for Trajectory Crossing Spaceborne SAR

Reprinted from: *Applied Sciences* **2022**, *12*, 5900, doi:10.3390/app12125900 . . . . . 141

## **Jiarui Shi, Qian Shen, Yue Yao, Fangfang Zhang, Junsheng Li and Libing Wang**

Field Radiometric Calibration of a Micro-Spectrometer Based on Remote Sensing of Plateau Inland Water Colors

Reprinted from: *Applied Sciences* **2023**, *13*, 2117, doi:10.3390/app13042117 . . . . . 153

**Peng Ye, Guowei Liu and Yi Huang**  
Geographic Scene Understanding of High-Spatial-Resolution Remote Sensing Images:  
Methodological Trends and Current Challenges  
Reprinted from: *Applied Sciences* **2022**, *12*, 6000, doi:10.3390/app12126000 . . . . . **167**

**Abeer Salman, Manahil Al-Tayib, Sulafa Hag-Elsafi, Faisal K. Zaidi and Nada Al-Duwarij**  
Spatiotemporal Assessment of Air Quality and Heat Island Effect Due to Industrial Activities  
and Urbanization in Southern Riyadh, Saudi Arabia  
Reprinted from: *Applied Sciences* **2021**, *11*, 2107, doi:10.3390/app11052107 . . . . . **195**

# Special Issue on Remote Sensing Applications in Archaeology, Geography, and the Earth Sciences

Tung-Ching Su

Department of Civil Engineering and Engineering Management, National Quemoy University, 1 Da Xue Rd., Kinmen 892, Taiwan; spcyj@nqu.edu.tw

## 1. Introduction

Remote sensing has played a pivotal role in advancing the fields of archaeology, geography, and earth sciences, offering new perspectives and unparalleled opportunities for research, analysis, and interpretation within these disciplines. With the continuous development and refinement of sensors, these sophisticated tools can now be deployed on various aerial platforms like satellites, aircrafts, and drones. This enables researchers to acquire invaluable observational data that enhances our understanding of both the Earth's natural and cultural landscapes. These data sources encompass a wide array of information, such as multispectral images, thermal data, LiDAR, radar data, and more. By harnessing these diverse types of observational data, researchers can delve into the study of environmental shifts, land use patterns, and archaeological sites with accuracy and efficiency. This Special Issue comprises 11 papers that center around the pioneering applications and advancements of remote sensing technology in areas such as monuments, traditional architectural art, and environmental monitoring. Moreover, it explores the integration of cutting-edge deep learning techniques to aid researchers in the detection and identification of archaeological remnants. The papers presented in this collection showcase the innovative utilization and extraction of insights from remote sensing data, contributing to the expansion of knowledge and the refinement of methodologies in these domains.

## 2. Remote Sensing Applications in Archaeology, Geography, and the Earth Sciences

This Special Issue presents a comprehensive exploration of the latest advancements in remote sensing detection technology, focusing on its applications in restoring and preserving cultural relics, detecting landscape features, and recognizing landforms. Moreover, it delves into the development of innovative algorithms specifically designed to tackle challenges related to landscape feature observation and the establishment of guidelines for the restoration and preservation of cultural relics. This Special Issue features four papers focused on restoring and preserving cultural relics. The papers in this domain emphasize the utilization of 3D file production techniques for the preservation and restoration of cultural relics, particularly emphasizing the safeguarding of cultural assets and buildings. The primary objective is to introduce the concept of "Digital Twin" to develop a detailed historical building information model (HBIM) [1]. The production of 3D files for cultural heritage preservation can be achieved through photogrammetry (structure from motion) or Terrestrial Laser Scanning (TLS) techniques. Marín-Buzón et al. [2] conducted a comparative analysis of the accuracy of archaeological excavation achieved by these two production techniques. In the field of painting art preservation, Cozzolino et al. [3] employed ground-penetrating radar (GPR) to assess the condition of paintings, serving as the foundation for 3D reconstruction of the internal mosaic structure of the artworks. Recognizing the importance of preserving the original painting style crafted by artists, Su et al. [4] conducted a study that involved extracting texture characteristics from "door god" paintings, a prominent form of Oriental architectural art. Their research aimed to delve into

**Citation:** Su, T.-C. Special Issue on Remote Sensing Applications in Archaeology, Geography, and the Earth Sciences. *Appl. Sci.* **2023**, *13*, 7631. <https://doi.org/10.3390/app13137631>

Received: 25 June 2023  
Accepted: 26 June 2023  
Published: 28 June 2023



**Copyright:** © 2023 by the author. Licensee MDPI, Basel, Switzerland. This article is an open access article distributed under the terms and conditions of the Creative Commons Attribution (CC BY) license (<https://creativecommons.org/licenses/by/4.0/>).



the genre of “door god” painting craftsmanship while striving to maintain the authenticity of the restoration process.

In regard to the detection of landscape features or the landform recognition, this Special Issue includes a total of five papers. Jiao et al. [5] proposed the utilization of shoulder lines to effectively capture the morphological characteristics of the Loess Plateau. However, the issue of maintaining continuous shoulder lines during the extraction process remains unresolved. To address this concern, they introduced a method that combines edge detection and regional growing algorithms, improving the extraction of shoulder lines. Furthermore, passive remote sensing systems are inadequate for effectively observing certain landscape features such as the distribution of underground military tunnels [6]. The application of deep learning techniques proves advantageous in enhancing the interpretability and resolution of 2-D Electrical Resistivity Tomography (ERT) data, enabling the clearer visualization of tunnel locations and paths. Bachagha et al. [7] effectively integrated the advanced technology of very-high-spatial-resolution satellite (PB1) and SAR data, showcasing the remarkable potential of satellite data and machine learning in uncovering hidden archaeological sites from an archaeological standpoint. In the realm of water remote sensing, Li et al. [8] presented a simulation method for generating a two-dimensional sea surface current field, aiming to overcome the challenge of limited trajectory crossings in spaceborne SAR data. Shi et al. [9] emphasized the significance of remote sensing reflectance as a crucial parameter in the remote sensing inversion of plateau inland water colors. They highlighted the necessity of conducting Field Radiometric Calibration of a Micro-Spectrometer to accurately measure the remote sensing reflectance in unmanned areas of plateau inland regions.

Among the included papers, the sole review explores the intricacies of geographic scene understanding in high-spatial-resolution remote sensing images, providing insightful analysis on methodological trends and addressing the present challenges in the field [10]. They indicated the prevailing challenges associated with the utilization of high-spatial-resolution remote sensing images in understanding geographic scenes. The main challenge stems from the use of high-spatial-resolution remote sensing data, which provides finer landscape details but simultaneously exacerbates the complexity of data processing for intelligent image interpretation.

### 3. Future Applications

Although this Special Issue includes 11 papers on the applications of remote sensing in archaeology, geography, and the earth sciences, there is still a future expectation for more investigations on the integration of multi-sensor remote sensing data (such as LiDAR, radar, and satellite imagery) with artificial intelligence and machine learning algorithms [11,12]. Besides assisting scientists in enhancing the efficiency of exploring landscape features in the mentioned applications, these approaches can also help them gain a better understanding and interpretation of the spatial distribution, interrelationships, and interactions between archaeological sites/landscape features and the geographical environment.

**Acknowledgments:** I would like to express my sincere appreciation to all the authors and the editorial team of this Special Issue for their exceptional contributions to the publication of *Applied Sciences*. Through your dedicated efforts and extensive expertise, this Special Issue has become an invaluable resource, offering valuable insights and information for research in the field of remote sensing applications in archaeology, geography, and the earth sciences. Finally, I would like to offer my special thanks to the section managing editor of this Special Issue from MDPI Branch Office, Beijing.

**Conflicts of Interest:** The authors declare no conflict of interest.

## References

1. Palčák, M.; Kudela, P.; Fandáková, M.; Kordek, J. Utilization of 3D Digital Technologies in the Documentation of Cultural Heritage: A Case Study of the Kunerad Mansion (Slovakia). *Appl. Sci.* **2022**, *12*, 4376. [[CrossRef](#)]
2. Marín-Buzón, C.; Pérez-Romero, A.M.; León-Bonillo, M.J.; Martínez-Álvarez, R.; Mejías-García, J.C.; Manzano-Agugliaro, F. Photogrammetry (SfM) vs. Terrestrial Laser Scanning (TLS) for Archaeological Excavations: Mosaic of Cantillana (Spain) as a Case Study. *Appl. Sci.* **2021**, *11*, 11994. [[CrossRef](#)]
3. Cozzolino, M.; De Simone, A.; Gentile, V.; Mauriello, P.; Piezzo, A. GPR and Digital Survey for the Diagnosis and the 3D Representation of the Battle of Issus Mosaic from the House of the Faun, Pompeii (Naples, Italy). *Appl. Sci.* **2022**, *12*, 6965. [[CrossRef](#)]
4. Su, T.-C.; Wu, T.-C.; Wun, M.-H.; Wang, C.-W. Style Recognition of Door God Paintings by Hypothesis Testing for Texture Features of Painting Patterns. *Appl. Sci.* **2022**, *12*, 2637. [[CrossRef](#)]
5. Jiao, H.; Li, F.; Wei, H.; Liu, W. An Improved Shoulder Line Extraction Method Fusing Edge Detection and Regional Growing Algorithm. *Appl. Sci.* **2022**, *12*, 12662. [[CrossRef](#)]
6. Hung, Y.-C.; Zhao, Y.-X.; Hung, W.-C. Development of an Underground Tunnels Detection Algorithm for Electrical Resistivity Tomography Based on Deep Learning. *Appl. Sci.* **2022**, *12*, 639. [[CrossRef](#)]
7. Bachagha, N.; Elnashar, A.; Tababi, M.; Souei, F.; Xu, W. The Use of Machine Learning and Satellite Imagery to Detect Roman Fortified Sites: The Case Study of Blad Talh (Tunisia Section). *Appl. Sci.* **2023**, *13*, 2613. [[CrossRef](#)]
8. Li, Y.; Chong, J.; Li, Z. A Simulation Method of Two-Dimensional Sea-Surface Current Field for Trajectory Crossing Spaceborne SAR. *Appl. Sci.* **2022**, *12*, 5900. [[CrossRef](#)]
9. Shi, J.; Shen, Q.; Yao, Y.; Zhang, F.; Li, J.; Wang, L. Field Radiometric Calibration of a Micro-Spectrometer Based on Remote Sensing of Plateau Inland Water Colors. *Appl. Sci.* **2023**, *13*, 2117. [[CrossRef](#)]
10. Ye, P.; Liu, G.; Huang, Y. Geographic Scene Understanding of High-Spatial-Resolution Remote Sensing Images: Methodological Trends and Current Challenges. *Appl. Sci.* **2022**, *12*, 6000. [[CrossRef](#)]
11. Masini, N.; Lasaponara, R. Satellite Remote Sensing in Archaeology: Past, Present and Future Perspectives. *J. Archaeol. Sci.* **2011**, *38*, 1995–2002.
12. Resler, A.; Yeshurun, R.; Natalio, F.; Giryas, R. A Deep-Learning Model for Predictive Archaeology and Archaeological Community Detection. *Humanit. Soc. Sci. Commun.* **2021**, *8*, 295. [[CrossRef](#)]

**Disclaimer/Publisher’s Note:** The statements, opinions and data contained in all publications are solely those of the individual author(s) and contributor(s) and not of MDPI and/or the editor(s). MDPI and/or the editor(s) disclaim responsibility for any injury to people or property resulting from any ideas, methods, instructions or products referred to in the content.



## Article

# Utilization of 3D Digital Technologies in the Documentation of Cultural Heritage: A Case Study of the Kunerad Mansion (Slovakia)

Michal Palčák \*, Pavol Kudela , Miriam Fandáková and Juraj Kordek

University Science Park UNIZA, University of Žilina, Univerzitná 8215/1, 010 26 Žilina, Slovakia; pavol.kudela@uniza.sk (P.K.); miriam.fandakova@uniza.sk (M.F.); juraj.kordek@uniza.sk (J.K.)  
\* Correspondence: michal.palcak@uniza.sk; Tel.: +421-41-513-75-23

**Abstract:** Preservation of cultural heritage plays an important role in society, significantly contributing to its sustainability, which is important for human development and quality of life. The issue of cultural heritage digitization has recently been the subject of increasing research and is part of the initiatives of the European Commission for the Promotion of Cultural Heritage. Therefore, it is necessary to define the stages of the digitization process, which is crucial for cultural heritage preservation. The aim of this article was to examine currently used technologies and their role in the digitization workflow, and to present a detailed historical building information model (HBIM) developed during the digitization project at the historic Kunerad Mansion. To meet these goals, we will describe the best practices for each discussed technology. Special attention is paid to data processing at the very end of the object modeling process. Additionally, particular findings alert the reader to the need to create object element databases in terms of effective point cloud modeling and present the advantages of the technologies examined over traditional ways of preserving cultural heritage. In addition to predicting procedures, cooperation at a multidisciplinary level is needed in a narrower context. On the whole, the article provides some useful suggestions for both practitioners and stakeholders.

**Keywords:** cultural heritage; laser scanning; UAV; photogrammetry; BIM; point cloud

**Citation:** Palčák, M.; Kudela, P.; Fandáková, M.; Kordek, J. Utilization of 3D Digital Technologies in the Documentation of Cultural Heritage: A Case Study of the Kunerad Mansion (Slovakia). *Appl. Sci.* **2022**, *12*, 4376. <https://doi.org/10.3390/app12094376>

Academic Editor: Tung-Ching Su

Received: 17 March 2022

Accepted: 25 April 2022

Published: 26 April 2022

**Publisher's Note:** MDPI stays neutral with regard to jurisdictional claims in published maps and institutional affiliations.



**Copyright:** © 2022 by the authors. Licensee MDPI, Basel, Switzerland. This article is an open access article distributed under the terms and conditions of the Creative Commons Attribution (CC BY) license (<https://creativecommons.org/licenses/by/4.0/>).

## 1. Introduction

The construction of new buildings includes modern methods that allow the creation of 3D digital models and complete drawing documentation in a form that covers all the necessary steps from idea to implementation. Tools used are mostly CAD (computer assisted design) [1] for civil engineers and BIM (building information modeling) [2] software, designed mostly for architects.

The situation is different in the case of old and historical buildings that are part of the cultural heritage of the given country. Many of them are damaged by weather, natural disasters, traffic impacts, air pollution, or destructive human activity. In many cases they require partial or complete reconstruction. Detailed printed documentation of the building is usually not available. During the reconstruction process, historical photographic documentation is used but, in such cases, it must be detailed enough. It is also possible to draw blueprints from detailed painted pictures. CAD and BIM [3] software cannot be used for the abovementioned purpose, but offers reverse engineering functions to support the reconstruction process. With the help of several modern technologies within the processes of reverse engineering, a very accurate 3D digital model can be created from an existing real object. At the end of the process, printed documentation can be generated from the created model. In such case it is possible to archive the current state of the cultural monument and, additionally, all steps of the reconstruction phase, where the model is updated according to completed work, new discoveries, or unintentional changes in the structure. The resulting

3D digital models can also be used for presentation and educational purposes and, in the case of an unexpected destruction of the building, they also provide a source of information for potential virtual models. They can be moved into virtual reality and enable virtual tours not only for small VR devices but also for large CAVE (computer assisted virtual environment) projection devices [4].

The SWA (School–Work Alternation) project [5], a training project focused on cultural heritage, deals with the acquisition of technical and methodological tools for knowledge access, preservation and enhancement of cultural heritage, with special regard to diagnostic tools and information and communication technologies. It also assesses the technical–professional and crosscutting skills that students have acquired or are expected to have.

The European Commission is active in the preservation of cultural heritage, not only in its physical but 3D digital forms. One of the digital platforms is the Europeana [6], which allows people to discover historic sites and hidden gems across Europe. It provides access to more than 51 million items (including images, text, sound, video and 3D materials) from the collections of more than 3700 libraries, archives, museums, galleries and audiovisual collections across the Europe [7].

Research in 3D scanning and reconstruction covers the problem of cultural heritage digitization. The authors of [8] present creation of a 3D model using photogrammetric and geodetic measurements, data transfer to AutoCAD and Adobe Photoshop and production of a final photorealistic digital model in 3D StudioMAX. However, they do not deal with the creation of printed construction documentation.

A case study of the Museum of King Jan III's Palace at Wilanów [9] describes the creation of a 3D model using terrestrial laser scanning (TLS) and photogrammetry. Since the building was in a good, fully functional state, it was not suitable for reconstruction activities (undertaken when no printed documentation is available and thus must be produced from an incomplete building).

A paper dealing with the digitization of the medieval castle of Haut-Andlau (Alsace, France) [10] compares geodetic, TLS and photogrammetry techniques, but provides no clear recommendation, since specific limitations were observed for each discussed method. The building consisted only of stone walls; there were no windows, doors or other decorated architectural style.

The Batawa project (Toronto, ON, Canada) [11] was very large project covering 600 hectares of an old manufacturing city with many buildings and the result provides a digital BIM archive of that area. Source data were drawings and paper copies of hand-drawn and computer-generated plans and documents with a black line, paper, digitized photographs (some from 1939) and digital and paper texts. Furthermore, TLS was used and a topographic study was created in AutoCAD Civil 3D. Other applications used in the project were SketchUp and Navisworks. The final BIM model was created in Autodesk Revit.

Data for the case study of the historical building Kurşunlu Khan in Turkey [12] were photographs, textual data on architectural and spatial characteristics, and 2D digital drawings and alterations created during construction and reconstructions. Another source was point clouds from TLS. The tool for 2D drafting was AutoCAD 2011, while for BIM modeling it was Revit Architecture 2013.

The authors of [13], who used the Mobile Mapping System to document cultural heritage, revealed that despite its great potential, human intervention is still needed to achieve the desired results, with technical and methodological limitations causing skepticism about the mobile mapping system for three-dimensional surveys.

Digital 3D modeling and visualization technologies have been widely used for more than 30 years. Despite the enormous efforts made to establish information technologies and especially 3D technologies for digital 3D modeling and visualization, the current situation is still ambiguous and the knowledge and skills in practice concerning 3D technologies pose a major challenge [14,15].

Since literary sources do not clearly identify exact reverse engineering [16,17] methods recommended for the creation of a 3D model of cultural heritage, it is necessary to consider the utilization of several methods in a specific case study.

This paper demonstrates the potential of reverse engineering methods such as terrestrial laser scanning (TLS), terrestrial (ground) (DSLRL), aerial (UAV) photogrammetry, BIM, as-built documentation for cultural heritage conservation, and scientifically examines the impact and assessment of these modern technologies' benefits throughout the process. This is important, since the combination of these technologies can contribute to saving time, maintaining security and providing high-precision digital archiving.

The advantages are explored over traditional ways of preserving cultural heritage. There may be limitations in both methods of data acquisition, so space and lighting conditions need to be considered. For photogrammetry, it is necessary to consider a sufficient degree of overlap to avoid deformation of the corners of the object. With TLS, it is important to optimize the number of scan positions to avoid unnecessary extension of the registration process of scans in the postprocessing phase and thus the achievement of an excessively dense point cloud.

The aim of this article was to examine currently used technologies and their role in the digitization workflow, and present a detailed historical building information model (HBIM) developed during the digitization project at the historic Kunerad Mansion (Slovakia).

This work is organized as follows: in Section 2, the subject of the case study and scientific problem are discussed. Then, in Section 3, the used methodology is presented, detailing three methods. TLS is described in Section 4, including the knowledge base, planning and realization phases. Section 5 deals similarly with photogrammetry, including ground and aerial data processing. In Section 6 follows data integration from TLS and both photogrammetry methods. The BIM is described in Section 7 with the resulting 3D model and as-built documentation. Finally, we draw conclusions in Section 8.

## 2. Subject of Case Study and Scientific Problem

The Kunerad Mansion National Cultural Monument was chosen for the case study and impact and benefit assessment. The castle was built in 1914 by Count Valentín Balestrém (1860–1920). The construction was inspired by the Art Nouveau architecture style of castles. During the Slovak National Uprising in 1944, it served as headquarters for the Second Partisan Staff of Milan Rastislav Štefánik. It was burned down on 25 September 1944. After the end of World War II, it was confiscated and became the property of the state forests department. Subsequently, in the years 1945–1948, it underwent extensive reconstruction according to the project of Dipl. Acad. Arch. Ferdinand Čapek and became a medical institute for the treatment of respiratory diseases. In 1959, the manor became part of the Rajecké Teplice spa. On 25 May 1967, it was declared a national cultural monument together with the adjoining park. During the repair of the roof on 11 March 2010, the manor house was engulfed in a large fire. Since then, it has remained closed and dilapidated. On 20 October 2018, eight years after the devastating fire, the dilapidated mansion burned down again (Figure 1) [18].

At the very beginning of the case study process, our first goal was to determine the level of detail (LOD). LOD defines the amount and degree of building information that needs to be placed in a BIM model. The determination of the LOD was complicated, as the monument was in a desolate state and was surrounded by lush vegetation. Based on the inspection and technical capabilities of the technologies we had at our disposal, the LOD value was determined to be 300.



**Figure 1.** Terrestrial photo of the Kunerad Mansion, captured by the authors.

One of the set goals was to create a 3D model and subsequently a photorealistic model, which is one of the basic pillars for visualization of unique architecture resulting from the requirements of the monument office. This 3D model is to be used for presentation purposes as well as to document the state of the building before the actual reconstruction of the monument. It was necessary to digitally record all the necessary visual aspects.

The next goal was to create a HBIM model of the building from the outputs obtained from modern technologies used during the process, where the identified materials of the building were documented and described, as well as the information related to the building itself.

The final goal was to create new detailed project documentation in the shortest possible time. It is important to note that the original project documentation did not exist and in order to follow the rules of the monument office, it was necessary to visualize as much of the historical details of the cultural monument as possible.

### 3. Methods

The used methodology is divided into 5 phases: planning, data collection, data processing, data integration and 3D model construction. Three methods were used within the methodology: TLS, photogrammetry and BIM. Each of the defined methods was included in the individual phases of the methodology according to the implemented project research. Some phases also interacted, while the as-built documentation was created from a geometric model. The scheme of the methodology is shown in Figure 2.

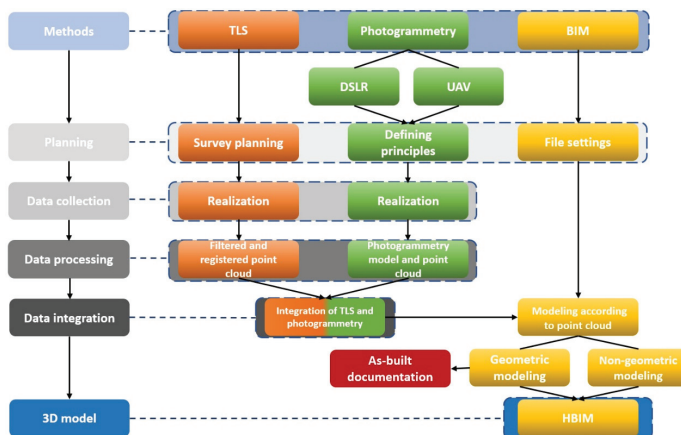


**Figure 2.** The methodology.

#### 4. 3D Laser Terrestrial Scanning: Knowledge Base

Utilization of 3D laser scanners is nowadays one of the most accurate, fastest and most efficient ways of obtaining 3D data (models) of existing objects. Obtained data are the source of information for real objects' transformation into an accurate 3D digital copy, which can capture spatial geometry and can be used for various types of analysis and further processing on a computer [19–21].

Terrestrial laser scanning, also known as terrestrial LiDAR (light detection and ranging) or topographic LiDAR, works by the XYZ coordinate system for many points on the ground. Laser pulses are projected to these points and the device–target distance is computed.

Laser scanning provides high accuracy when recording real-world objects. The scan result is a point cloud that represents a 3D image of the scanned objects. This technology is used in many areas of industry, but also in architecture [22].

The 3D model obtained by this process helps architects in the renovation planning of buildings and structures and brings the possibility of testing various design variants. These options are very effective in civil engineering too [23]. Designers can access data from different parts of the world and work simultaneously on new projects without the need for traveling and manual measurement in the case of potential changes evaluation.

Three-dimensional laser scanning is one of the reverse engineering techniques, which is also used in the digitization of cultural heritage objects. Reverse engineering (RE) is a way by which is possible to obtain the shape and the geometry of a given object and thus create its 3D digital model based on a physical model. The scientific and technical development of these methods brings many advantages applicable in almost the entire field of protection and visualization of cultural heritage. The possibilities of using the methods are, for example, digital twin creation, computer-aided repair, new educational tools (virtual tours and virtual museums) and much more [24].

According to the authors of [25], research and new technologies in the field of image processing, computer graphics and virtual reality have significantly progressed in creation of 3D computer images of real objects.

##### 4.1. Selection of Appropriate Digitization Technology

There are several sources [26,27] that indicate frequently used types of digitization technologies. They enable the acceleration of the selection of a suitable technology, based on defined selection criteria. The chosen technology can influence some important parameters such as the results of digitization, time, overall price, etc.

Figure 3 shows the selection of digitization technology depending on the criteria of accuracy range and object size. Since the accuracy is an important criterion when creating project documentation, the dependence of these criteria is relevant to us. The object was measured at the beginning of the process with a Leica DISTO D510 laser distance meter, where approximate measures of 53.94 m × 27.35 m × 11.610 m (width × depth × height) were determined. Based on the specified size of the object and the accuracy we had to achieve, we have chosen the most suitable digitization technologies that met our requirements:

- Terrestrial laser scanning;
- Terrestrial (ground) photogrammetry;
- Aerial photogrammetry.



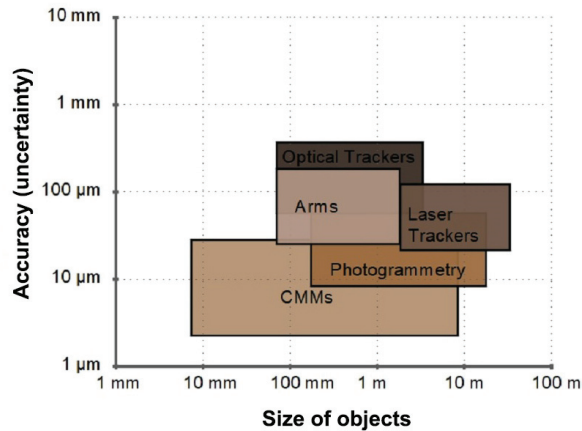


Figure 3. Accuracy ranges of EFR hardware technologies.

4.2. Terrestrial Laser Scanning: Planning Phase

This phase can also be called the preliminary phase of the 3D laser scanning process. It is necessary to obtain all available information about the object and its surroundings. The following requirements, listed in Table 1, had to be considered.

Table 1. Requirements for the implementation of the case study and the planned estimate.

Case Study Requirements	Description	Planning Estimation
Project location	It is necessary to consider the influence of weather in given locality, availability, density of vegetation around the object, lighting and area conditions.	Kunerad Castle 2106, 013 13 Kunerad. The building has an access road; there is vegetation in the area that will not interfere with data collection and there is no electricity or lighting in the building.
Project type	It can determine the required level of detail, cost, time, etc.	Reverse engineering, cultural heritage, LOD 300.
Time required for the project	Thorough planning and estimation of time consuming can contribute to efficiency in solving a project.	Outside–7 h 0 Floor–7 h 1 Floor–5 h 2 Floor–6 h Basement–10 h Total: 35 h. The need to divide the scanning process into several days.
Scanning accuracy	Scanning accuracy is determined by the type of scanner.	<2 mm
Scanning object	The subjects of scanning are objects and areas respectively scanning scenery.	Outside area of the object, 2 floors with ground floor and basement.

Planned estimation of study requirements is always performed after the physical inspection of the object, which is necessary before the start of the scanning. The inspection was realized in October 2019. For high efficiency, it is important to plan the correct placement of reference points, estimate the number of scan positions and plan their correct placement to achieve the expected results. It can be very helpful if there is project documentation for the object, from which it is possible to draw the mentioned facts. In our case, however, it was necessary to create project documentation and therefore we created only a so-called site sketch, which is helpful for the registration and postprocessing process when we can get quick information about the relationship between the scanner

positions. Depending on the size of the object and its complexity, the scanner positions were determined for each scenario separately. As mentioned above, the cultural heritage site was in a dilapidated state after fires and weather conditions (collapsed parts of the floor, collapsed roof, unstable parts, etc.) and it was also necessary to adjust the scanning positions accordingly. From the position of the scanner, the fact that reconstruction work will take place during the digitization was also considered. Other influences that could affect the scan quality were the dusty environment and safety.

#### 4.3. Terrestrial Laser Scanning: Realization Phase

To create 2D project documentation, it is necessary to set two important parameters, resolution and quality. These two parameters are the most important for the whole process, because they affect the level of detail captured and the time required to obtain data from one scanner position, which is adequately reflected in the total time required to obtain all data and help in the correct process of registering individual scans in postprocessing. The first parameter, resolution, determines the point distance, which then determines the level of detail. By increasing this parameter, we will achieve the capture of a larger number of points and, at the same time, reduce their distance. Otherwise, lowering this parameter results in a smaller number of points being captured while increasing the distance between them. For our purposes, based on the required level of detail and time saving in calculating the available distance to the object of interest, a resolution of 1/4 was chosen. This represented the distance of the point 6.136 mm at 10 m from the scanner.

The quality setting primarily determines the measurement speed and ‘noise’ reduction level, i.e., increased quality value increases the measurement time that the scanner spends on each scan point, while performing multiple measurements to confirm the information and then averaging the result. In addition to the above, this parameter also uses a noise reduction algorithm that determines whether the differences in the scan points are an accurate representation of detail or noise. The algorithm compares the scanned points at a certain distance to each other and determines whether their difference is in the tolerance specified by the quality setting. If not, the scan point is removed, resulting in noise reduction. The setting of this parameter also largely depends on the scanning conditions, such as interior or exterior spaces, weather conditions, etc. To meet the condition of saving time, we tried to achieve optimal conditions and thus achieve the quality setting parameter—2×.

Based on preliminary on-site measurements, it was necessary to determine the distance between the scanner positions and the distance of the reference points from the scanner position.

Table 2 shows a comparison of the settings of various parameters (quality and resolution) and the resulting achieved number of scan points on reference objects (spheres) at a given setting. Green values represent higher accuracy, yellow values represent lower accuracy and gray values represent low (<20) or insufficient number of acquired scan points required in the registration process. The minimum value for achieving green values is 80 captured scan points. The following columns represent the average time required to record data from a single scan position when scanning with RGB and when scanning without RGB. Each area of scenery that was scanned (see Table 1) required specific settings depending on the conditions. When scanning exterior scenery, it is always necessary to consider weather conditions at a given time. These measurements also show that in ideal weather it is sufficient to use the quality setting 2× at a resolution 1/4 and the location of reference points and targets at a distance up to 10 m.

**Table 2.** Comparison of quality and resolution parameters and average scan times.

Quality Settings	Reference Point Distance			Average Scan Time		
	Resolution Setting	5 m	15 m	30 m	with RGB (min)	without RGB (min)
2×	1/4	1150	120	25	5:01	2:47
	1/8	235	22	-	3:40	1:26
3×	1/4	1175	126	27	6:48	4:34
	1/8	239	25	-	4:07	1:53
4×	1/4	1390	135	25	10:23	8:09
	1/8	200	27	-	5:01	2:47

Scanning was performed in November 2019 with the terrestrial laser scanner Faro Focus X 330, with the possibility of scanning to a distance of 330 m and accuracy of 2 mm.

To achieve the highest possible accuracy, a combination of 140 mm reference balls (spheres) and targets (checkboards) was used. When using this type of terrestrial laser scanner, it is possible to scan without the use of reference spheres and targets, which can ultimately save time and money, but at the expense of scanning accuracy of the object. To achieve higher accuracy by scanning without reference balls and targets, it would be necessary to place the scanning positions at a very short distance, which would require a much larger number of final scanner positions and much more time spent on site. On the other hand, the use of reference balls and targets will only slightly prolong the time spent on site compared to the aforementioned previous case, and will also simplify the registration process in the software environment.

Ball positions are used in data processing, where the software automatically recognizes them as reference elements. Based on them, it automatically combines scans from different angles and thus creates a complex point cloud of the scanned object. It is also important to note that there had to be at least three common reference points between two scan positions. The harmonization and coordination of individual scans within the postprocessing is enabled by the integrated GPS receiver.

The most challenging scenery in terms of terrestrial laser scanning within the entire building was the basement of the castle. There were several reasons for this, such as the unavailability of electric power, very poor lighting conditions, high humidity, areas of fragmentation, transitions between light and dark parts of the building, the occurrence of dangerous shafts, surface condensation, falling plaster, etc. It was necessary to reduce the time required to obtain data. The scanner settings were adjusted and scanning was performed without RGB to ensure that the time required for data collection was minimal. Due to the fragmentation of the premises, 61 scanning positions were performed in the mansion basement. Figure 4 shows the correspondence view and the specific locations of the scan positions after the individual scans were registered in the postprocessing. Correspondence is the relationship between the same common reference object in multiple scans. Faro Scene software (version 2019.1, FARO Technologies, Inc., Sarasota, FL, USA) uses these objects to create correspondences. The result can then be visualized and evaluated in the Correspondence View, the 3D View or the Structure View tool. Postprocessing took place also in the FARO SCENE software environment, where the individual scenarios were registered separately in individual clusters. Then, these clusters were registered in the final point cloud. Finally, filters were applied in the software environment, and unwanted points in the point clouds of individual scenarios were removed. During the scanning itself, cleaning work also took place on the object and its surroundings, which led to minor time plan changes and various noises. These externalities had to be filtered out in the final process, as shown in Figure 5. It is important to mention that during the use of the technology of terrestrial laser scanning, so-called death spots arise where the laser beam does not hit the measured point on the object. These places must be added later in the following photogrammetry process. The resulting point cloud in this phase met the requirement of LOD 300 in terms of shape, orientation and location.



**Figure 4.** Correspondence view of Kunerad Mansion basement in FARO SCENE software.



**Figure 5.** Comparison of raw (a) and denoised/filtered (b) point clouds.

### 5. Photogrammetry: Knowledge Base

Photogrammetry is the art, science and technology of obtaining reliable information about physical objects and the environment through processes of recording, measuring and interpreting photographic images and patterns of recorded radiant electromagnetic energy and other phenomena [28]. Photogrammetry is divided according to:

1. Positions;
2. Method of evaluation;
3. Number of pictures taken;
4. Evaluations.

Figure 6 shows the scheme of photogrammetry organization.

Modern photogrammetry technologies, which are used to create a variety of environments and tools, have undergone tremendous development in recent decades. During this period, they have passed several milestones from the visual side through the quality of textures to large-scale 3D models. The basic principle of photogrammetry [29], which also results from the above scheme, is convergent imaging. When a photogrammetric image is taken, a central projection is created. The relationship between the subject and its captured image at the time of exposure is given by a photogrammetric beam passing through the center of the projection.

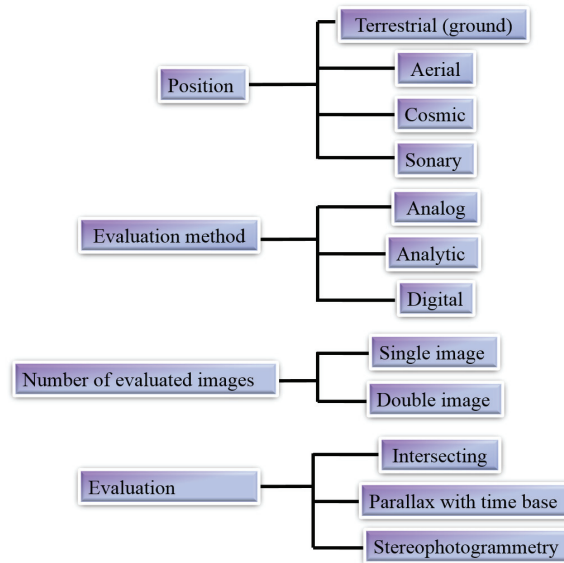


**Figure 6.** Scheme of photogrammetry organizations.

The shape of these rays is determined mainly by the elements of the internal orientation [30] and their position in space is determined by six rays from the external orientation. With respect to the elements of internal and external orientation and the sufficient offset, it is possible to create a point cloud representing the digitized object. Further processing of these points results in the creation of a triangulated irregular network (TIN) model, which forms the basis for further postproduction to achieve required details. Finally, the obtained texture based on the quality of the image is applied. It is important to note that the quality of the data will significantly affect the result. The main advantages of photogrammetry are high accuracy and massive collection of special data.

Like laser scanning, photogrammetry can be used in reverse engineering. Sufficient photographs in ground and aerial photogrammetry form a good spatial model, but also more detailed information about the individual details of the object [31]. The technology can also be used in hard-to-reach and inaccessible places. Created photorealistic 3D models (PR3DM) [32] find further application in the field of construction, architecture, medicine and also in the gaming industry. Within the already mentioned architectural [33] and cultural heritage digitization [34], sufficient interoperability is ensured, which allows integral use of photogrammetry in the digitization process as one of the basic tools.

### 5.1. Photogrammetry General Principles: Planning Phase

During the digital processing of Kunerad manor house using the photogrammetric method, it was necessary to consider that the 3D model itself had to be created in combination with laser scanning. This meant that the model was emphasized not only in terms of visual details but also in terms of accuracy by the qualitative output of data from laser scanning. This implies that in order to achieve the required outputs from the model, basic recommendations have to be followed, based on the previous experience and knowledge of the authors:

1. When capturing the subject, there is no relationship between the size of the subject and the number of shots. If there are enough photos available, more details can be captured and there is no need to return to the place and take a new picture of the object.

2. If possible, capturing should be performed at the highest possible resolution and without using zoom during shooting. Our advice is to create captured images in RAW format in terms of the larger range of adjustments.
3. Time, lighting, weather, haze and spatial conditions need to be considered so that the object can be captured from every possible angle and under consistent lighting conditions in the digitization process. This data can be used in combination with laser scanning.
4. Try to avoid shadows, because the RGB information is lost during the 3D model creation process and the model shape is incorrectly rendered.
5. When applying the convergent capturing method, it is necessary to ensure a sufficient degree of image overlap. If the overlap level does not reach the value of at least 80%, the detailing process may not be accurate. To ensure sufficient overlap between the individual pictures and adjust for their distortion, the horizontal angle should be in the range  $(-45^\circ, 45^\circ)$  and the vertical angle  $(-30^\circ, 30^\circ)$  [35].
6. Pictures should not show any signs of blur due to hand movement or instability of the body and should also be taken with minimal noise. If there is the need for focus only on the subject, shooting is then performed in automatic mode. In manual mode, we gain control over the basic parameters of the camera (ISO, F, f) and a balance is sought between them through the exposure triangle.
7. Capturing should be in the loop and with the same distance around the whole object if possible due to the spatial arrangement. The shooting distance should copy the shape of the subject throughout the loop. From the point of view of the vertical displacement, these loops should be made at intervals, respecting the value of the overlap. The aim is to achieve an even level of detail throughout the building.
8. Try to avoid panoramic shots because with these the depth information of each point in the picture is not obtained. Therefore, it is necessary to take pictures at small distances.
9. When using unmanned aerial vehicles (UAV), it is necessary to perform a control flight over and next to the building in the initial phase. Based on this flight, places where additional detailed scanning is required are identified.
10. Evaluate the situation in terms of setting the UAV selection of individual modes, both automatic and manual. It is also possible to create a combination of individual modes when it is necessary to consider the time of flight, weather conditions, space conditions or the phase of reconstruction carried out at the time.
11. In terms of flight speed in automatic flight mode, set the shutter speed and autofocus points so that pictures are not blurred.
12. For accurate parameterization of the object, it is suitable to use alignment points with known spacing distances, or to use a measuring tape or other tool of known size.
13. In order not to degrade the images, it is necessary to avoid moving objects, dust and smoke during the whole digitization process.
14. The subject should be as large as possible in the photo.

According to the recommendations, it can be stated that during the processing of all available pictures, the process of postproduction is minimized, such as adjusting white balance, noise reduction, over/under exposure, and other settings. Another piece of advice is to take some time for the sorting process, when you will create separate folders that contain slides to align the object and the remaining folders to create textures.

The result of the interconnection and achieving LOD 300 is a sufficient acquisition of information about the object such as shape, articulation and structure RGB.

### 5.2. Terrestrial (Ground) Photogrammetry: Realization Phase

It is possible to determine dimensions, positions and properties of objects and phenomena from photographic images produced by ground photogrammetry. Capturing is done from a stable position on the ground. Secured elements of the internal and external orientation of the images allow determining the 3D position of each point [36].

After the 3D laser scanning phase, terrestrial photogrammetry of the Kunerad manor house was started (December 2019). Capturing was performed on a DSLR CANON EOS 60D with an APS-C sensor, the resolution of 18 Mpx, and EPS 18–75 mm lens. The output format was RAW format for subsequent postprocessing to achieve image consistency (exposure, shadows, overexposure or underexposure). By the combination of requirements for accuracy and spatial arrangement from the project definition, the maximum distance of 5 m from the object was specified. At the maximum resolution and distance, a pixel size value of 2 mm was determined. This parameter guaranteed sufficient additional points to the laser scan point cloud.

From the basic setting parameters, the ISO value was fixed at 100 throughout the shooting, the aperture was F8.0, and the shutter speed changed during the position and orientation of the camera.

The ISO 100 value guaranteed that the sensor would not be too sensitive to light, and at the higher value the remaining two parameters would not be compensated for and the images would not produce higher noise intensity, which would result in a significant deterioration of the 3D model [37]. The aperture number was based on the spatial arrangement, as mentioned above. The relationship between the depth of field and the distance to the object was also considered, which means that the shortest distance from the object could be at a maximum 2.5 m. The hyperfocal distance, based on the well-known parameters of the camera, lens, and distance, was 1.93 m, which ensured that all images would be sufficiently focused.

Due to weather conditions, the capturing was performed during cloudy weather and in almost no wind. These conditions ensured that the lighting of the object would be diffuse, without significant sharp shadows. During the photo shoot, image checks were performed, because, as already mentioned, the photo shoot took place during the winter and in the proximity of the building. Moreover, there was snow on the building in certain places. Snow in combination with daylight affected the camera's basic parameters. Therefore, it was necessary to change these values and at the same time to follow mentioned recommendations when taking photos [38].

From the point of view of photography limitations, the same problem occurred as for the laser scanning, when both reconstruction and cleaning work took place during the process. It was necessary to avoid the mechanisms present during the capturing and at the same time monitor them so that they were not captured in the images.

The combination of data from laser scanning and ground photogrammetry was ensured by targets that were on the object and in its proximity range.

The total number of images created during the day with the emphasis on even coverage of the object was 1500. Photography was performed both by hand and using a monopod. Figure 7 shows the detail from ground photogrammetry.



**Figure 7.** Detail from terrestrial (ground) photogrammetry.

### 5.3. Aerial Photogrammetry: Realization Phase

Aerial photogrammetry [39] deals with the interpretation and evaluation of digital images that have been created from aircraft or other UAVs. The term UAV photogrammetry defines a remote measurement platform, which can be partially dependent or independent, does not contain a pilot and is equipped with photogrammetric measurement systems. These include small and medium video cameras, thermal or infrared camera systems and LIDAR aeronautical systems. Within the UAV standard, it is possible to monitor and record the position and direction of sensors that are applied in a local or global coordinate system.

In our case, to create a 3D model of the Kunerad manor it was necessary to implement not only ground but aerial photogrammetry as well. The DJI Mavic 2 PRO drone with an integrated Hasselblad L1D-20c camera with resolution of 20 Mpx and 1 inch CMOS sensor was used for this phase. Captured photos were saved in DNG format for further postprocessing.

To achieve the same pixel size (GSD) [40] as with the terrestrial photogrammetry, the maximum distance between the UAV and the object was determined to be 20 m. Again, the spatial conditions were considered, where part of the forest was in this radius. For this reason, the object was captured in manual mode for the outer perimeter and from above in automatic mode.

The photography was performed in a fully automatic mode, since the histogram images were evaluated as uniform during the control flight. A total of eight images was taken from each side, from above the building, and for details at the terraces.

Since it was not possible to combine two methods of photogrammetry in one day, the weather forecast was monitored for upcoming days and the lighting conditions were evaluated for the same parameters. It was not necessary to change the flight modes and the way of flying, because the wind conditions were very favorable (approx. 5 m/s).

During the flight, attention was paid to the degree of capture details on terraces, tower, external staircase, main entrance and individual details of the architecture. The essential part was capturing of common goals for the combination of the two methods of digitization.

The total number of images created during the flight, with the emphasis on even coverage of the object, was 670. Figure 8 shows the UAV positions in which the images were taken.



**Figure 8.** Aerial photogrammetry positions.

### 5.4. Photogrammetry Data Processing

Having outputs from ground and aerial photogrammetry, image processing was started. For each of the methods, it was necessary to check the output quality of each image. The inspection was performed in Lightroom software (version 8.0, Adobe, San Jose, CA, USA). Overexposed and underexposed images, exposure, shadows, chromatic aberration and profile correction were monitored. Edited images created the base dataset for generating high-quality model textures. Produced slides were then sorted and the subset was used



to align the object and the rest to texture the model. The processing of images into the 3D model was carried out in the RealityCapture software environment [41,42]. After importing folders containing slides to align the object, the first component that formed a point cloud was created. Another component included folders containing image information for textures. Both components were then merged into the form of a point cloud (60.7 mil. points), representing the object's shapes. The maximum deviation reprojection was set at 2.0 pixels, with a resulting component average re-projection deviation of 0.36 pixels. This parameter represented the LOD for the individual object details. The secondary task was to supplement the information from already mentioned dead spots. The point cloud model reached the LOD 300 and formed the basis for additional information involvement, such as cracks, deformations, etc.

Based on Figure 9, it can be stated that if the images were completely output, the point cloud also represented the quality of the obtained data. This means that the quality of the output model for further work depends on the quality of the result obtained at the beginning.



**Figure 9.** Point cloud of the Kunerad manor.

## 6. Integration of Terrestrial Scanning, Terrestrial Photogrammetry and Aerial Photogrammetry

The next processing step was the integration of point clouds from both 3D laser scanning, ground scanning and aerial photogrammetry. Point cloud outputs from the laser scanner contained so-called dead spots. This means that the model was not complete, since the scanning laser beam did not receive all the information for each location in the object during the scanning process. This was caused by both the angle and the position of the scanner. However, these dead spots can be supplemented with information from ground and aerial photogrammetry. Based on this fact, there were two cloud points that needed to be combined. Exported point clouds data were imported into the open source CloudCompare environment, where the process of cleaning and alignment was performed. During the importing, the position of data was adjusted to the local coordinate system with smaller coordinates [43]. Trimming of point clouds of gross errors was performed by the segmentation function. The tool used allowed us to choose segmentation of individual entities through polygons or rectangles. If the rotation was used, it was necessary to define the polygon, since it is available only for 2D. Individual entities were represented by surrounding vegetation, fencing, mechanisms (in photogrammetry) and paved areas. Subsequently, the statistical outlier removal (SOR) noise filter was applied to each point cloud [44]. The SOR algorithm calculates the average distance to each nearest neighbor point selected. It evaluates as the noise points those points that are further than the average distance and  $n$ -times the standard deviation. In this case, the basic settings defined by the software were sufficient. Segmented point clouds could then be combined (interconnected).

The reason for this was the difference in the coordinate systems of the software from which data were originally exported. CloudCompare has several ways to align boundaries, including bounding box alignment, manual point-to-point transformation and automatic alignment. Mutual points between laser scanning and photogrammetry had already been defined, so we applied alignment by using these points. To precisely specify individual common points, it is advisable that each of them carries an RGB value for each point, which will facilitate the search for points. The result of the alignment of the individual point clouds is shown in Figure 10. The histogram shows that the largest part consisted of the interconnection points with the smallest distance. The increasing distance was mostly formed by data from photogrammetry, where the laser device was unable to digitize the object. The created point cloud was exported in the structured E57 format and returned to the PR3DM generation process.

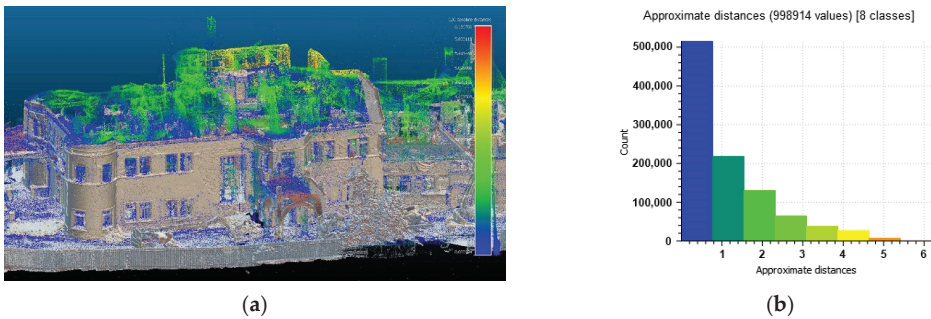


**Figure 10.** Denoised and filtered point cloud connected with terrestrial and aerial photogrammetry (a) and histogram of interconnection points (b).

The exported point cloud was reimported into the RealityCapture software environment. The interconnection created a sufficiently detailed model represented by the mean projection deviation of 0.35 pixels for mesh formation. It should be noted that in the case of 3D model creation, the point cloud from laser scanning is used without RGB and from photogrammetry with RGB for texturing the model (function provided by the software). The point cloud forms the mesh that needs to be optimized. Performing this step is necessary since the mesh itself also contains invalid points resulting from too thick a point cloud. In this process, the predefined distance between two points was 2 mm, which, despite sufficient detail, affected the size of the object itself. With the integrated simplification function, the degree of optimization of the mesh model is considered until there is a significant loss of details. The resulting number of triangles that contained the model was 29.7 mil. Finally, unwrap was performed and the texture was applied in 4 K resolution and texture quality at the level of 80%, which gives the object a photorealistic look. The texture quality value informs us about the maximum detail that can be obtained from the images.

The result is a 3D model that met the required output quality criteria, including LOD 300, color and photorealism. The final model, shown in Figure 11, serves mainly for presentation purposes as the digital twin of the real object, but also defined the basis for further analysis and required outputs.



**Figure 11.** The Kunerad Castle model connected with terrestrial and aerial photogrammetry.

## 7. Building Information Modeling: Knowledge Base

Building information modeling (BIM) is used to design and document building and infrastructure designs. Every detail of the building is modeled in BIM. The model can be used for analysis to explore design options and to create visualizations that help stakeholders understand what the building will look like before it is built. The model is then used to generate the design documentation for construction [45].

As mentioned, digitization brings benefits [46] in time and cost savings. The same is true for BIM modeling. In our case, we used HBIM.

HBIM can be divided into two categories. The first category is the simplified model that contains elements only defined as geometric shapes. The second category includes modeling using repetitive parametric elements. The problem of creating HBIM models is the absence of these elements and libraries, but also the mapping of the real state and identification in the creation of these libraries. A combination of these methods is used to make a HBIM.

This type of documentation is significantly more accurate than traditional, manually created documentation (using measurement tape or a laser distance meter), since the elements are captured in 3D space. In the case of historic buildings, it is very important that all structures, including those that lie outside the section plane in 2D drawings, are included in the project documentation.

### 7.1. Building Information Modeling: Planning Phase

The planning was divided into the three stages. During the first stage it was necessary to achieve the required LOD, since it determines the quality of the other two stages and respective goals. There are several levels of LOD in the field of cultural heritage, depending on the purpose for which they are used [47]. In our case, the requested level was closely related to its utilization in HBIM model creation and project documentation.

The second stage comprised the HBIM model's creation with the required LOD. An exported point cloud was created in the REVIT software, as it proved to be an effective tool with number of libraries that can be used in the creation of BIM [48] and in facility management (FM). In the next phase, segmentation took place for individual objects from the point cloud model. This segmentation was divided according to standard primitives integrated in the software environment.

Subsequently, the individual segments were modeled to the required level. In this process, there were two modeling subprocesses, namely the already mentioned simple shapes or using modeling tools. During this process, information from the texture of the component (cracks, deformations, etc.) was added to the model.

The final goal was to create a new project documentation of the existing state with the capture of the necessary details for the monument office and architects, to serve as a basis for the development of a project for the reconstruction of the Kunerad Mansion.

### 7.2. Building Information Modeling: Realization Phase

For the creation of the HBIM model, a point cloud from terrestrial laser scanning and photogrammetry was registered and cleaned. Since the target was the historical building, there were various ornaments on the facade, decorative casings, columns and other structures. The scan-to-BIM method was used, i.e., a point cloud served directly as the basis for the software in which the HBIM model was created. It was not appropriate to create the mesh or solid model from a point cloud in the CAD environment, since such modeling would only be time consuming and would not bring any benefits. Such a procedure is suitable for buildings such as production halls or industrial buildings. As mentioned several times, the emphasis was on both the accuracy of the data and the reliable capture of the existing condition of the object. Therefore, in cases when the basic dimensions of the object were directly modeled, it was no longer possible to simplify the structures either in the dimensions or in the direction (i.e., there are no parallel walls in the building).

To add more information to the HBIM, two more geomagnetic and ferromagnetic scanners were used during object scanning and photography. One scanned and determined the material composition of individual structures, the other, ferromagnetic one, scanned and determined the distribution and diameter of the reinforcement of load-bearing walls and ceiling boards (decks). Due to the poor technical condition of the aboveground floors of the building and factors such as humidity, and building materials containing metal, substrates with cavities or tiles, the required data could not be obtained.

Due to the high year-round humidity, it was not even possible to scan the basement using a geomagnetic scanner. Nevertheless, during scanning with a non-humidity-sensitive ferromagnetic scanner, the results in specific areas of the basement were very skewed. We assume that the entire measured area of the basement was made of reinforced concrete in combination with steel elements, and the data were distorted due to the high content of ferromagnetic metals. Therefore, invasive methods for the material composition determination were finally chosen (performed during the reconstruction). To conclude, at the time of the HBIM model creation, it was not possible to bring this information into the design of the model itself.

The system families of software were fully used in the creation of reinforced concrete slabs and floors. These constructions were relatively easy to identify from the scan. This was because of the fact that most of them were exposed by fire and the accuracy of technologies used in construction at beginning of the last century.

A special group of objects examined during the creation of the HBIM model was formed by walls, where it was not possible to determine their material composition, for the same reason as already mentioned. Based on experience of similar projects, it was possible to estimate with significant certainty the material composition of individual walls, and a new wall type was created for each wall thickness. The walls of the building were made of solid fired bricks and in the combination of their connections they differed only in the thickness of the plaster.

From the architectural point of view, high-precision shapes were required for vaults, so it was not possible to create a group for repetitive elements, as each vault differed in details. Therefore, vaults were created by the model-in-place system. This is a problem of HBIM where the ideal model is not achieved, but the process is reversed, and the model is an abstraction of reality [49].

Windows were defined as a group of families. Despite the fact that they were destroyed and only parts of them were preserved, it was possible to create a window with casing on a facade frontage. Casings were categorized as the wall additions and fully parametric. The door constructions were not sufficiently preserved and therefore it was not possible to capture them sufficiently into the HBIM.

The degree to which groups of objects were created reflects the level of detail (LOD). Table 3 shows the level of detail for individual modeled structures. The roof and door structures were devastated by the fire and therefore it was not possible to reliably capture their shapes. The pillars and railings were made of reinforced concrete, fire resistant, and could be modeled reliably. In the case of windows, it was possible to model them in a higher LOD, because during extinguishing of several fires in the building, some parts of their construction were revealed. In particular, the components of the wooden parts' connection (expansion joints for window linings), point-precise places of windows' attachment to the main structure and the interconnection of the wooden peripheral part of the window and the masonry structure were preserved.

**Table 3.** Level of detail of individual object structures.

Type of Construction/LOD	LOD 100	LOD 200	LOD 300	LOD 350	LOD 400	LOD 500
Wall			x			
Floor			x			
Roof		x				
Windows				x		
Doors			x			
Railings balusters			x			
Columns			x			

A fully usable HBIM model using parametric families was a good choice, especially for elements and structures such as railings, windows and various ornaments on the facade.

After the creation of the geometric HBIM model, the creation of as-built documentation followed, in which the building object was captured in the actual state. As-built documentation captures changes in the design compared to the planned documentation. This type of documentation contains the exact dimensions of the object as in the reality. The content of the documentation is:

1. Changes in individual units in the dispositional solution of the building, including changes in individual parts of structures, materials and location;
2. Unexpected complications that occurred during the construction and appropriate solutions applied, including notes and dates of resolved changes;
3. Attached with all related shop drawings and appendices [50].

In our case study of the Kunerad Mansion, where the mentioned documentation of construction drawings was not available, new, accurate as-built documentation was created from the HBIM model as the result of the basic specified goal. This documentation represents a digital model and is recognized as the main initial documentation. As shown in Figure 12, the documentation is highly accurate, because errors from manual measurements were eliminated. There are visible architectural elements, such as vaults, as well as the basic characteristic dimensions of the building, including the floor level.

Finally, the HBIM model of the real condition was created, together with the drawing documentation. The final situation shown in Figure 13 represents a built-up area of 736.97 m<sup>2</sup> and including the area of the terrace, the overall area is 1012.67 m<sup>2</sup>. The combination of the photorealistic model and the west view from the project documentation demonstrates the achievement of a high degree of accuracy in object modeling.

Within the creation of the HBIM model, it was also possible to complete the phase that represented the reconstructed state of some parts of the manor. As the example, we present a reconstructed baluster in Figure 14, while Figure 15 shows parts of the baluster with dimensions and numbers of pieces. This information was also used for the investor and other professions involved in the reconstruction.

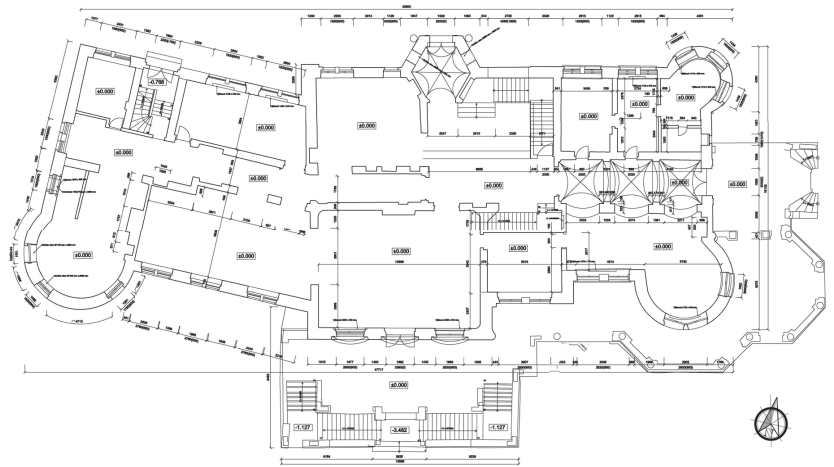


Figure 12. As-built documentation floor plan.

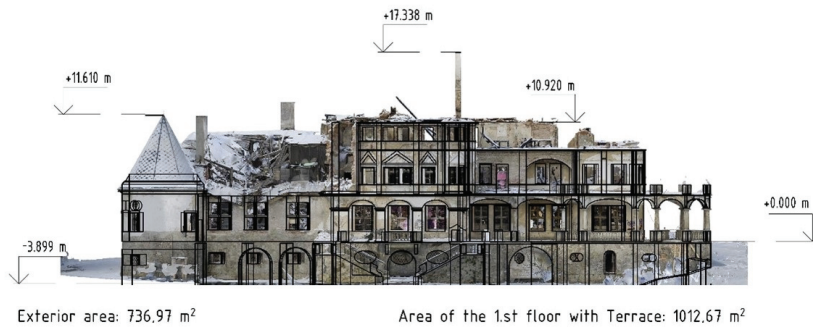


Figure 13. West view of the researched object.

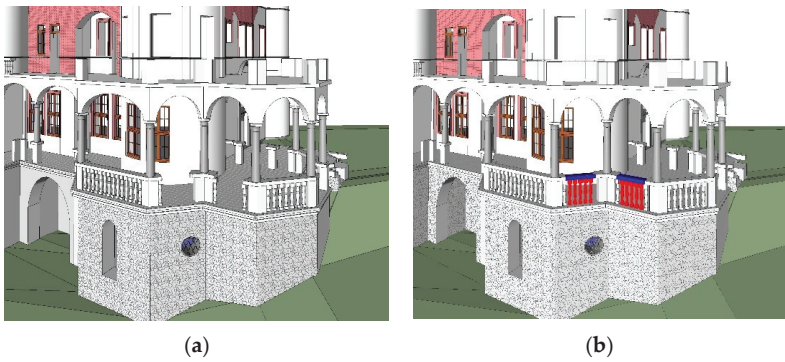
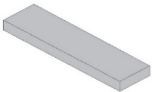


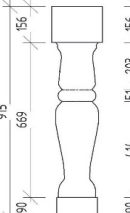


Figure 14. Original (a) and refurbished (b) baluster.

Table of New Railings Components			
DESCRIPTION	PICTURE		COUNT
Railing			2
Baluster			10

**Figure 15.** New parts of the baluster.

The HBIM model can be exported to IFC format. IFC is the universal interchange file used between individual software packages that serve only as browsers. Many of them are also available online. By using IFC, it is possible to constantly inspect the project not only in the design phase, but also in the reconstruction phase, and there is a possibility to inspect the construction from anywhere in the world. Construction companies can make notes to the HBIM/IFC model to intervene and solve problems with investors and architects. Another use is in the management of the building where the model is, whether in HBIM or IFC format, a valuable source of information.

## 8. Conclusions

Preservation of cultural heritage is one of the basic pillars of a country's history and intellectual wealth. In addition to storytelling, modern technology is currently contributing to this effort to pass information from generation to generation. Cultural heritage buildings and nearby objects are often notable parts of a city and transport infrastructure. It is important to mention that the terrestrial laser scanning and photogrammetry approach has a significant impact on other research and application areas. For example, laser scanning is one of the fundamental technologies for smart mobility solutions, which integrate operation of transport systems, overall sustainability [51], and safety of traffic. Vehicles with a specific level of automation require precise information about nearby objects to make real-time decision during driving, too [52]. Approaches and technologies mentioned in this paper are substantial for creating data which can be further used within the intelligent, digital infrastructure.

The presented paper demonstrates the utilization of the specific methods of terrestrial laser scanning, terrestrial (ground) and aerial photogrammetry and BIM. The methodology of digitization is divided into five steps: planning, data collection, data processing, data integration and 3D modeling.

The individual partial goals of the Kunerad manor digitization project were reached. Results were obtained by specific steps and integrated into the solution. The main part of the result was a 3D photorealistic model, created by the combination of TLS, ground and air photogrammetry. It has become a digital twin of the real object and is used mainly for presentation purposes. It is important to mention that the defined level of detail (LOD) of 300 was reached for each method applied during the project. Another part of the result was a HBIM model, using parametric families, especially for elements and structures such as railings, windows and various ornaments on the facade. Finally, as-built documentation was created reflecting the current state of the manor, and changes in individual units of structure, materials and locations.

Based on the implemented case study and experience gained by authors during the project, some advantages and disadvantages were identified regarding the methods and workflow used.

The advantages of the presented TLS approach are high accuracy and detailed object capture, which did not require return and additional measurement. Disadvantages, on the other hand, are expensive technology, high financial risk if the technology is damaged during the project, and limited ability to use equipment in a highly dusty environment, which is typical for construction sites.

For the photogrammetry, advantages come with the use of less expensive technology, higher quality of details presented by textures, and ability to capture whole object completely (terrestrial and aerial scanning). Disadvantages include the time factor, as the photogrammetry approach requires more time to digitize objects (capture details and specific individual parts), that the process needs to be performed by a person sufficiently trained in the basic photogrammetry principles, and higher inaccuracy.

The following is a recommendation summary applicable for similar projects:

- (1) If a monument is devastated by fire, a documentary safety analysis of the monument is always required;
- (2) Interior spatial conditions can be a limiting factor in the case of a devastated object and it is necessary to consider which method to use for data collection (TLS or photogrammetry);
- (3) A 3D model obtained from aerial photogrammetry helps in the planning of reconstruction works in terms of machines and mechanisms' location;
- (4) A BIM model becomes a necessary part of construction management for its monitoring but also for other works associated with reconstruction or renovation;
- (5) A HBIM model allows understanding of the state of the monument, the decay of individual materials, and identifies cracks and deformations.

The digitization of the building contributed not only to archiving with an emphasis on high accuracy, but also to the future direction in the field of NFT (non-fungible tokens). The creation of the HBIM model of the Kunerad manor created a basis for individual professions, so that they did not clash in the design and, finally, the pricing object was parameterized.

The outputs processed by proposed methodology fulfilled the achievement of research tasks with a comprehensive view of the issue. In conclusion, we can state that the methodology and chosen procedures can be applied to similar cultural heritage buildings in order to preserve them, whether in physical or digital form, for future generations.

**Author Contributions:** Conceptualization, M.P., P.K., M.F.; methodology M.P.; validation, M.F., M.P.; formal analysis, M.F.; investigation M.P., P.K.; resources, M.P., P.K., M.F., J.K.; scanner data acquisition, M.P.; data acquisition from photogrammetry, P.K.; data connectivity, M.F.; BIM modeling, J.K.; writing—original draft preparation, M.P., P.K., M.F., J.K.; writing—review and editing, M.P., P.K., M.F.; funding acquisition, P.K. All authors have read and agreed to the published version of the manuscript.

**Funding:** This publication was realized with support of Operational Program Integrated Infrastructure 2014–2020 of the project: Innovative Solutions for Propulsion, Power and Safety Components of Transport Vehicles, code ITMS 313011V334, co-financed by the European Regional Development Fund.



EUROPEAN UNION  
European Regional Development Fund  
OP Integrated Infrastructure 2014 – 2020



MINISTRY  
OF TRANSPORT  
AND CONSTRUCTION  
OF THE SLOVAK REPUBLIC

**Institutional Review Board Statement:** Not applicable.

**Informed Consent Statement:** Not applicable.

**Acknowledgments:** Special thanks to University Science Park UNIZA for support during the writing of this paper.



**Conflicts of Interest:** The authors declare no conflict of interest.

## References

1. Tornincasa, S.; Di Monaco, F. The future and the evolution of CAD. In Proceedings of the 14th International Research/Expert Conference, “Trends in the Development of Machinery and Associated Technology”, Mediterranean Cruise, Online, 11–18 September 2010.
2. Logothetis, S.; Stylianidis, E. BIM Open Source Software (OSS) for the documentation of cultural heritage. *Virtual Archeol. Rev.* **2016**, *7*, 28–35. [CrossRef]
3. Volk, R.; Stengel, J.; Schultmann, F. Building Information Modeling (BIM) for existing buildings—Literature review and future needs. *Autom. Constr.* **2014**, *38*, 109–127. [CrossRef]
4. Manjrekar, S.; Sandilya, S.; Bhosale, D.; Kanchi, S.; Pitkar, A.; Gondhalekar, M. CAVE: An Emerging Immersive Technology—A Review. In Proceedings of the UKSim-AMSS 16th International Conference on Computer Modelling and Simulation, Cambridge, UK, 26–28 March 2014; ISBN 978-1-4799-4923-6.
5. Gizzi, F.T.; Biscione, M.; Danese, M.; Maggio, A.; Pecci, A.; Sileo, M.; Potenza, M.R.; Masini, N.; Ruggeri, A.; Sileo, A.; et al. School-Work Alternation (SWA) Working Group (WG), Students Meet Cultural Heritage: An Experience within the Framework of the Italian School-Work Alternation (SWA)—From Outcomes to Outlooks. *Heritage* **2019**, *2*, 1986–2016. [CrossRef]
6. The Europeana Platform. Available online: <https://digital-strategy.ec.europa.eu/en/policies/europeana> (accessed on 16 March 2022).
7. Summary Report of the Public Consultation on Europeana, Europe’s Digital Platform for Cultural Heritage. 2018. Available online: <https://digital-strategy.ec.europa.eu/en/summary-report-public-consultation-europeana-europes-digital-platform-cultural-heritage> (accessed on 16 March 2022).
8. Toz, G.; Duran, Z. Documentation and Analysis of Cultural Heritage by Photogrammetric Methods and GIS: A Case Study. Commission V, WG V/4. 2019. Available online: <https://www.isprs.org/PROCEEDINGS/XXXV/congress/comm5/papers/593.pdf> (accessed on 16 March 2022).
9. Tobiasz, A.; Markiewicz, J.; Łapiński, S.; Nikel, J.; Kot, P.; Muradov, M. Review of Methods for Documentation, Management, and Sustainability of Cultural Heritage. Case Study: Museum of King Jan III’s Palace at Wilanów. *Sustainability* **2019**, *11*, 7046. [CrossRef]
10. Grussenmeyer, P.; Landes, T.; Voegtle, T.; Ringle, K. Comparison Methods of Terrestrial Laser Scanning, Photogrammetry and Tacheometry Data for Recording of Cultural Heritage Buildings. *Int. Arch. Photogramm. Remote Sens. Spat. Inf. Sci.* **2008**, *37*, 213–218. Available online: [https://www.researchgate.net/profile/Tania-Landes/publication/228645072\\_Comparison\\_Methods\\_of\\_Terrestrial\\_Laser\\_Scanning\\_Photogrammetry\\_and\\_Tacheometry\\_Data\\_for\\_Recording\\_of\\_Cultural\\_Heritage\\_Buildings/links/0fcfd50afe2b3011ba000000/Comparison-Methods-of-Terrestrial-Laser-Scanning-Photogrammetry-and-Tacheometry-Data-for-Recording-of-Cultural-Heritage-Buildings.pdf](https://www.researchgate.net/profile/Tania-Landes/publication/228645072_Comparison_Methods_of_Terrestrial_Laser_Scanning_Photogrammetry_and_Tacheometry_Data_for_Recording_of_Cultural_Heritage_Buildings/links/0fcfd50afe2b3011ba000000/Comparison-Methods-of-Terrestrial-Laser-Scanning-Photogrammetry-and-Tacheometry-Data-for-Recording-of-Cultural-Heritage-Buildings.pdf) (accessed on 16 March 2022).
11. Fai, S.; Graham, K.; Duckworth, T.; Wood, N.; Attar, R. Building information modelling and heritage documentation. In Proceedings of the XXIII CIPA International Symposium, Prague, Czech Republic, 11–16 September 2011.
12. Saygi, G.; Agugiano, G.; Hamamcioglu-Turan, M.; Remondino, F. Evaluation of gis and bim roles for the information management of historical buildings. In Proceedings of the ISPRS Annals of the Photogrammetry, Remote Sensing and Spatial Information Sciences, Volume II-5/W1, XXIV International CIPA Symposium, Strasbourg, France, 2–6 September 2013.
13. Di Stefano, F.; Chiappini, S.; Gorreja, A.; Balestra, M.; Pierdicca, R. Mobile 3D scan LiDAR: A literature review. *Geomat. Nat. Hazards Risk* **2021**, *12*, 2387–2429. [CrossRef]
14. Muenster, S. Digital 3D Technologies for Humanities Research and Education: An Overview. *Appl. Sci.* **2022**, *12*, 2426. [CrossRef]
15. Parfenov, V.; Igoshin, S.; Masaylo, D.; Orlov, A.; Kuliashou, D. Use of 3D Laser Scanning and Additive Technologies for Reconstruction of Damaged and Destroyed Cultural Heritage Objects. *Quantum Beam Sci.* **2022**, *6*, 11. [CrossRef]
16. Buonamici, F.; Carfagni, M.; Furferi, R.; Governi, L.; Lapini, A.; Volpe, Y. Reverse engineering modeling methods and tools: A survey. *Comput.-Aided Des. Appl.* **2018**, *15*, 443–464. [CrossRef]
17. Saiga, K.; Ullah, S.; Kubo, A.; Tashi, A. Sustainable Reverse Engineering Process. In Proceedings of the 28th CIRP Conference on Life Cycle Engineering, Jaipur, India, 10–12 March 2021; pp. 517–522.
18. History of Kunerad Castle. Available online: <https://www.zamokkunerad.sk/> (accessed on 20 October 2021).
19. Wu, C.; Yuan, Y.; Tang, Y.; Tian, B. Application of Terrestrial Laser Scanning (TLS) in the Architecture, Engineering and Construction (AEC) Industry. *Sensors* **2022**, *22*, 265. [CrossRef]
20. Monego, M.; Fabris, M.; Menin, A.; Achilli, V. 3-D survey applied to industrial archaeology by tls methodology. *Int. Arch. Photogramm. Remote Sens. Spat. Inf. Sci.* **2017**, *5*, 449–455. [CrossRef]
21. Marín-Buzón, C.; Pérez-Romero, A.M.; León-Bonillo, M.J.; Martínez-Álvarez, R.; Mejías-García, J.C.; Manzano-Agugliaro, F. Photogrammetry (SfM) vs. Terrestrial Laser Scanning (TLS) for Archaeological Excavations: Mosaic of Cantillana (Spain) as a Case Study. *Appl. Sci.* **2021**, *11*, 11994. [CrossRef]
22. Vosselman, G.; Maas, H.G. *Airborne and Terrestrial Laser Scanning*, 1st ed.; CRC Press: Boca Raton, FL, USA, 2010; ISBN 978-1904445-87-6.
23. Arayici, Y. An approach for real world data modelling with the 3D terrestrial laser scanner for built environment. *Autom. Constr.* **2007**, *16*, 816–829. [CrossRef]

24. Segreto, T.; Caggiano, A.; D'Addona, D.M. Assessment of laser-based reverse engineering systems for tangible cultural heritage conservation. *Int. J. Comput. Integr. Manuf.* **2013**, *26*, 857–865. [CrossRef]
25. Bradley, C.; Currie, B. Advances in the field of reverse engineering. *Comput. Aided Des. Appl.* **2005**, *2*, 697–706. Available online: <https://www.scopus.com/record/display.uri?eid=2-s2.0-36249012143&origin=inward&txGid=d567d36d5445d66d28ce5948b33ee117> (accessed on 11 January 2022). [CrossRef]
26. Sniderman, D. How to Choose Digitizing Technologies, 3D Scanning 101—Digital Engineering. 2010. Available online: <https://www.digitalengineering247.com/article/3d-scanning-101/> (accessed on 11 January 2022).
27. Boehler, W.; Marbs, A. The potential of noncontact close range laser scanners for cultural heritage recording. In Proceedings of the CIPA XIX International Symposium, XVIII-2001, Potsdam, Germany, 18–21 September 2001; p. 34. Available online: [https://www.researchgate.net/publication/265425255\\_The\\_potential\\_of\\_non-contact\\_close\\_range\\_laser\\_scanners\\_for\\_cultural\\_heritage\\_recording](https://www.researchgate.net/publication/265425255_The_potential_of_non-contact_close_range_laser_scanners_for_cultural_heritage_recording) (accessed on 12 January 2022).
28. Wolf, P.; Dewitt, B.; Wilkinson, B. *Elements of Photogrammetry with Application in GIS*, 4th ed.; McGraw-Hill Education: Maidenhead, UK, 2014.
29. McGlone, J.C. *Manual of Photogrammetry*, 5th ed.; American Society for Photogrammetry and Remote Sensing; Bethesda: Rockville, MA, USA, 2004; ISBN 978-1570830716.
30. Alan, A.; Bill, B.; Cathy, T. Digital camera self-calibration. *ISPRS J. Photogramm. Remote Sens.* **1997**, *52*, 149–159.
31. Acosta, E.; Spettu, F.; Fiorillo, F. A procedure to import a complex geometry model of a heritage building into bim for advanced architectural representations. *Int. Arch. Photogramm. Remote Sens. Spat. Inf. Sci.* **2022**. [CrossRef]
32. Rademacher, P.; Lengyel, J.; Cutrell, E.; Whitted, T. Measuring the perception of visual realism in images. In *Rendering Techniques*; Gortler, S.J., Myszkowski, K., Eds.; Springer Science and Business Media: Berlin/Heidelberg, Germany, 2001; pp. 235–247. [CrossRef]
33. Papadopoulou, A.; Kontos, D.; Georgopoulos, A. Developing a vr tool for 3d architectural measurements. *Int. Arch. Photogramm. Remote Sens. Spat. Inf. Sci.* **2022**, 421–427. [CrossRef]
34. Dostal, C.; Yamafune, K. Photogrammetric texture mapping: A method for increasing the Fidelity of 3D models of cultural heritage materials. *J. Archaeol. Sci. Rep.* **2018**, *18*, 430–436. [CrossRef]
35. Huang, S.; Zhang, Z.; Ke, T.; Tang, M.; Xu, X. Scanning Photogrammetry for Measuring Large Targets in Close Range. *Remote Sens.* **2015**, *7*, 10042–10077. [CrossRef]
36. Dudoň, J. Návrh Učebného Textu v Predmete Fotogrametria a DPZ. SPŠS Žilina. 2009. Available online: <http://www.pkgeo.eu/files/fotogrametria-a-DPZ.pdf> (accessed on 20 February 2022).
37. Photogrammetry Workflow Using a DSLR Camera. Available online: <https://scholarslab.lib.virginia.edu/blog/documentation-photogrammetry/> (accessed on 21 January 2022).
38. Srnec, K. M—Manuálny Expozičný Režim. Available online: <https://www.ephoto.sk/fotoskola/clanky/zaciname-s-fotografovanim/manualny-expozicny-rezim/> (accessed on 21 January 2022).
39. Marčíš, M. *Automatizované Fotogrametrické Metódy v Procese Digitalizácie Kultúrneho Dedičstva*; Slovak Technical University: Bratislava, Slovakia, 2019; Available online: [https://www.svf.stuba.sk/buxus/docs/dokumenty/skripta/Marcis-automatizovane\\_fotogrametricke\\_metody\\_v\\_procese\\_digitalizacie\\_kulturalneho\\_dedicstva\\_konecna.pdf](https://www.svf.stuba.sk/buxus/docs/dokumenty/skripta/Marcis-automatizovane_fotogrametricke_metody_v_procese_digitalizacie_kulturalneho_dedicstva_konecna.pdf) (accessed on 21 January 2022).
40. Ground Sampling Distance (GSD) in Photogrammetry. Available online: <https://support.pix4d.com/hc/en-us/articles/202559809-Ground-sampling-distance-GSD-in-photogrammetry> (accessed on 20 January 2022).
41. Eisenbeiss, H. UAV photogrammetry in plant sciences and geology. In Proceedings of the 6th ARIDA Workshop on Innovations in 3D Measurement, Modeling and Visualization, Povo, Italy, 25–26 February 2008.
42. Alan, A.; Bill, B.; Cathy, A. Comparative Analysis of Different Software Packages for 3D Modelling of Complex Geometries. In Proceedings of the 8th European-Mediterranean Conference, EuroMed, Online, 2–5 November 2020; Volume 12642, pp. 228–240.
43. CloudCompare—User Manual. Available online: <http://www.cloudcompare.org/doc/qCC/CloudCompare%20v2.6.1%20-%20User%20manual.pdf> (accessed on 16 March 2022).
44. Daniel Girardeau-Montaut, D. CloudCompare. 2022. Available online: [https://www.cloudcompare.org/doc/wiki/index.php?title=SOR\\_filter](https://www.cloudcompare.org/doc/wiki/index.php?title=SOR_filter) (accessed on 16 March 2022).
45. Autodesk. Benefits of BIM. Available online: <https://www.autodesk.com/solutions/bim/benefits-of-bim> (accessed on 11 February 2022).
46. Craggs, D.; Crilly, M.; Dawood, N. REALITY CAPTURE for BIM—Application, evaluation and integration within an architectural plan of works. In Proceedings of the 16th International Conference on Construction Applications of Virtual Reality, Hong Kong, China, 11–13 December 2016.
47. Fai, S.; Rafeiro, J. Establishing an appropriate level of detail (LOD) for a building information model (BIM)—West Block, Parliament Hill, Ottawa, Canada. *ISPRS Ann. Photogramm. Remote Sens. Spat. Inf. Sci.* **2014**, *2*, 123. [CrossRef]
48. Plata, A.R.M.D.L.; Franco, P.A.C.; Franco, J.C.; Gibello Bravo, V. Protocol Development for Point Clouds, Triangulated Meshes and Parametric Model Acquisition and Integration in an HBIM Workflow for Change Control and Management in a UNESCO's World Heritage Site. *Sensors* **2021**, *21*, 1083. [CrossRef] [PubMed]

49. Capone, M.; Lanzara, E. Scan-to-bim vs 3d ideal model hbim: Parametric tools to study domes geometry. *Int. Arch. Photogramm. Remote Sens. Spat. Inf. Sci.* **2019**, *42*, 219–226. Available online: <https://pdfs.semanticscholar.org/80be/7ea503e7f187658b4c20ed9dd617b295c26c.pdf> (accessed on 11 February 2022). [CrossRef]
50. Ellis, G. *What Are as Built Drawings?* *Digital Builder Blog, Autodesk Construction Cloud*. 2022. Available online: <https://constructionblog.autodesk.com/as-built-drawings/> (accessed on 15 February 2022).
51. Cingel, M.; Čelko, J.; Drličiak, M. Analysis in modal split. *Transp. Res. Procedia* **2019**, *40*, 178–185. [CrossRef]
52. Bučko, B.; Michálek, M.; Papierniková, K.; Zábovská, K. Smart Mobility and Aspects of Vehicle-to-Infrastructure: A Data Viewpoint. *Appl. Sci.* **2021**, *11*, 10514. [CrossRef]

## Article

# Photogrammetry (SfM) vs. Terrestrial Laser Scanning (TLS) for Archaeological Excavations: Mosaic of Cantillana (Spain) as a Case Study

Carmen Marín-Buzón <sup>1</sup>, Antonio Miguel Pérez-Romero <sup>1</sup>, Manuel J. León-Bonillo <sup>1</sup>, Rubén Martínez-Álvarez <sup>1</sup>, Juan Carlos Mejías-García <sup>2</sup> and Francisco Manzano-Agugliaro <sup>3,\*</sup>

<sup>1</sup> Graphic Engineering Department, University of Sevilla, 41013 Sevilla, Spain; carmenmarin@us.es (C.M.-B.); tao@us.es (A.M.P.-R.); leonbo@us.es (M.J.L.-B.); rbnmaral@us.es (R.M.-Á.)

<sup>2</sup> Prehistory and Archaeology Department, University of Sevilla, 41003 Sevilla, Spain; jcmejas@us.es

<sup>3</sup> Department of Engineering, CEIA3, University of Almeria, 04120 Almeria, Spain

\* Correspondence: fmanzano@ual.es

**Abstract:** The discovery of a Roman mosaic from the 2nd century AD in Cantillana (Seville) generated interest and the need for exhaustive documentation, so that it could be recreated with real measurements in a 3D model, not only to obtain an exact replica, but with the intention of analyzing and studying the behavior of two main geomatics techniques. Thus, the objective of this study was the comparative analysis of both techniques: near object photogrammetry by SfM and terrestrial laser scanner or TLS. The aim of this comparison was to assess the use of both techniques in archaeological excavations. Special attention was paid to the accuracy and precision of measurements and models, especially in altimetry. Mosaics are frequently relocated from their original location to be exhibited in museums or for restoration work, after which they are returned to their original place. Therefore, the altimetric situation is of special relevance. To analyze the accuracy and errors of each technique, a total station was used to establish the real values of the ground control points (GCP) on which the comparisons of both methods were to be made. It can be concluded that the SfM technique was the most accurate and least limiting for use in semi-buried archaeological excavations. This manuscript opens new perspectives for the use of SfM-based photogrammetry in archaeological excavations.

**Keywords:** archaeology; photogrammetry; SfM; scanner; TLS; mosaic; marble

**Citation:** Marín-Buzón, C.; Pérez-Romero, A.M.; León-Bonillo, M.J.; Martínez-Álvarez, R.; Mejías-García, J.C.; Manzano-Agugliaro, F. Photogrammetry (SfM) vs. Terrestrial Laser Scanning (TLS) for Archaeological Excavations: Mosaic of Cantillana (Spain) as a Case Study. *Appl. Sci.* **2021**, *11*, 11994. <https://doi.org/10.3390/app112411994>

Academic Editor: Tung-Ching Su

Received: 25 November 2021

Accepted: 13 December 2021

Published: 16 December 2021

**Publisher's Note:** MDPI stays neutral with regard to jurisdictional claims in published maps and institutional affiliations.



**Copyright:** © 2021 by the authors. Licensee MDPI, Basel, Switzerland. This article is an open access article distributed under the terms and conditions of the Creative Commons Attribution (CC BY) license (<https://creativecommons.org/licenses/by/4.0/>).

## 1. Introduction

In the 1980s, the Total Station without reflector (TPS) was introduced; in the 1990s GPS (Global Positioning System) [1] was introduced; at the beginning of the century, in the 2000s, LiDAR (Light Detection And Ranging or Laser Imaging Detection And Ranging) [2] was introduced. In the following decade, HDS (High Definition Surveying) emerged as a powerful technology in terms of speed, accuracy, accuracy, detail, and cost. This system is also often referred to as Terrestrial Laser Scanning (TLS), or sometimes as terrestrial LiDAR. However, it has yet to prove its advantages over current technologies.

The first commercial TLS system was built by Cyra Technologies in 1998 and was later acquired by Leica in 2001 [3]. TLS hardware has improved rapidly over the past two decades [4]. The price, size, and weight of laser scanners have fallen at a rapid rate, and the improvement of spatial resolution and measurement speed has also improved [5].

Instruments now classically known as TPS basically record single points individually, while TLS systems involve three-dimensional laser scanning that can record thousands of points per second of measurement [6]. With TLS, a point cloud is obtained that is similar to a photograph, but each point has coordinates (X, Y, Z) and an associated color in the well-known RGB (Red, Green, Blue) format [7]. The main advantages of TLS systems are the high speed of data acquisition and the high level of detail linked to a very high

theoretical accuracy. In summary, current TLS systems usually have a high millimeter spatial resolution, with an observation distance of tens of meters from the station, and the standard error is usually  $\pm 2$  mm at 25 m [8].

The first manuscript on the application of TLS for archaeology was fairly recent, according to the Scopus database, and dates from 2007 [9], where its possible use was suggested, but no archaeological work was performed. Later, in 2008, it was applied in an archaeological excavation in Egypt, and the results were combined with aerial photogrammetry [10]. These applications are slowly starting to be used, as is shown in the related literature. One application in 2009 [11] related to point cloud modeling, and demonstrated that it is a complex task to extract its unstructured information, requiring powerful software tools. In the 2010s, TLS was mostly used for archaeological applications in caves, such as in the Upper Paleolithic cave of Parpalló in Gandía [12], or in the Bronze Age cave “les fraux”, in Perigord (France) [13].

Regarding the comparison between both methods, it is worth mentioning studies carried out in 2002 comparing TLS and SfM photogrammetry, usually in optimal conditions for the recording of cultural heritage, and that both methods obtained similar results [14]. Only in 2012 was TLS compared with terrestrial photogrammetry in archaeological applications [15], in particular with measurements made on a part of the Palace of Phaistos on the island of Crete. In this case, results showed that in the recording of the data set, there were average differences of the order of a few centimeters, highlighting the superior ability of TLS applied on surfaces to describe the undulating portions of the walls of that settlement. On the other hand, recent studies have shown the advantage of SfM over TLS in the study of archaeological sites on surfaces such as petroglyphs [16].

A study comparing TLS with SfM for the evaluation of bulk densities of bulk samples [17] showed the validity of both methods with a less than 4.5% variation, but the authors of the study do not recommend either of the two methods. However, in recent modeling applications for building structures, a comparison between the two techniques has been performed on the ruins of the Church of the Annunciation of the Blessed Virgin Mary on Mount Carmel in Zagórz (Poland) [18]. Here, the authors show the advantages of the TLS technique over SfM in the following aspects: TLS needs less GCP; with SfM, the interior and exterior of the building must be processed separately (with the subsequent consumption of time spent on processing); TLS can be employed in low or no visibility situations (even at night). It should also be noted that the studies on heritage conservation used TLS to compare different methods performed with SfM, i.e., TLS was used as a control method, where 99.99% of the points have an accuracy of 1.2 cm. Therefore, these authors considered TLS a more accurate technique than SfM [19]. This approach has also been claimed by authors comparing the two techniques for bridge inspection and monitoring [20]. Where all authors agree is that the SfM technique is cheaper than TLS. Up to now, no comparison has been made for archaeological mosaics. For this reason, this case study presents a comparison of the results of both methods, TLS and SfM, applied to a Roman mosaic for its 3D virtual re-creation.

## 2. Materials and Methods

### 2.1. Mosaic of Cantillana

The Cantilla mosaic was found in November 2017 in the village of Cantillana (Seville), Figure 1, in southern Spain. The exact coordinates were UTM ETRS89 H30 (250502.350 W, 4165806.514 N), equivalent to EPSG25830.



**Figure 1.** Location of the Mosaic of Cantillana (Spain).

The mosaic is part of the pavement of an interior courtyard of a Roman domus from the 2nd century AD. This was surrounded by an arcaded gallery, supported by columns, and there was the rim of a well, also decorated with the mosaic technique, and a marble drain for the evacuation of rainwater. The mosaic decoration represents an aquatic environment, a marine bottom with a large number of marine species with bright colors on a white background of tesserae and black lines that simulate the movement of the fish (see Figure 2).



**Figure 2.** Detail of the Cantillana mosaic (Spain).

This mosaic, crowned by a well, is also decorated and surrounded by other structures in the Roman building to which it belongs, was extracted and restored in the Museum of Local History, where it is currently on permanent exposition until it is returned to the site where it was found after it has been adapted as an archaeological enclosure or crypt. It is, therefore, of the utmost importance to know with the utmost precision its geometry and relative positions.

## 2.2. Methods

The methods evaluated in this study, TLS and SfM, are shown in Figure 3. Previous works have been carried out for both methods, such as georeferencing and acquisition of ground control points (GCP) in the field.

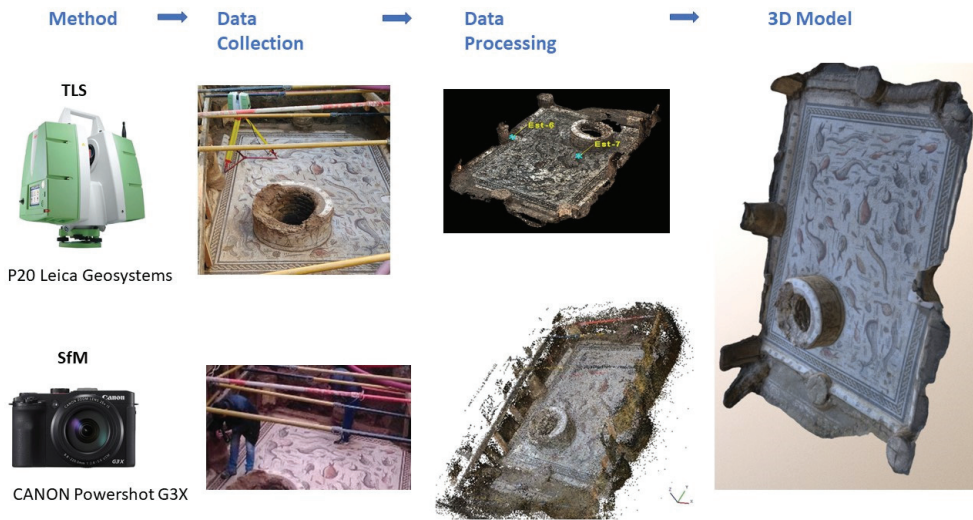


Figure 3. Methodology: TLS and SfM.

### 2.2.1. Georeferencing

Currently, all archaeological excavations must be georeferenced in order to have absolute coordinates in the official reference frame (UTM ETRS89) and to be able to proceed with their protection [21]. In this study, Leica GPS equipment, model 1200 with GX1230 antenna and RX1250 control unit on a pole, was used. The technical specifications of this equipment have been described in a previous manuscript [22].

### 2.2.2. Ground Control Points (GCP)

One of the factors that can significantly improve the quality of the results is the use of accurate and well distributed ground control points (GCP) [23]. This will allow us to properly correlate the generated model to the values of the terrain or the object. To ensure overall and internal accuracy, the location, distribution, and number of ground control points must be taken into account when establishing them in the area of interest [24].

The GCPs taken were the corners of the mosaic and significant points of some fish that appear as drawings in the mosaic, and of the well rim (see Figures 4 and 5). Table 1 lists the coordinates of the GCPs and the errors made in each of them once validated, in distance and pixel.



Figure 4. GCP surveying with the TCR705 total station.

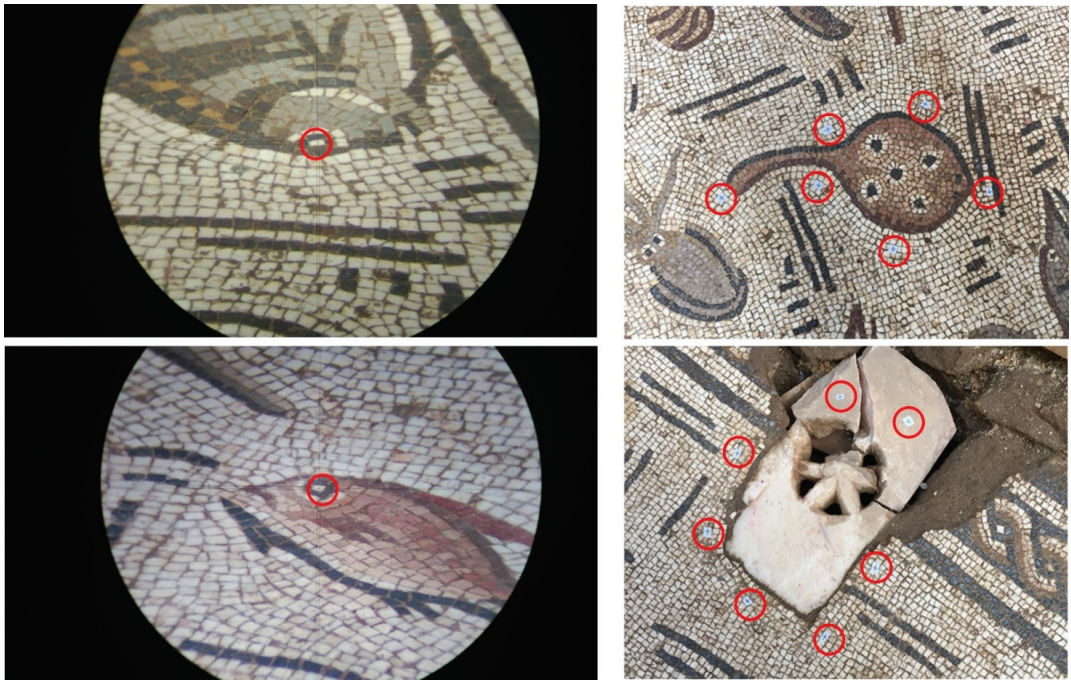


Figure 5. Example of Ground Control Points recorded (O).

Table 1. GCP Coordinates (UTM ETRS89) and errors.

GCP	X	Y	Z	E <sub>distance</sub> (mm)	E <sub>pixel</sub>
1	250,501.239	4,165,808.807	30.225	1.7	0.352
2	250,503.802	4,165,808.644	30.201	0.9	0.285
3	250,504.121	4,165,808.976	30.199	0.7	0.175
4	250,504.042	4,165,806.570	30.134	0.6	0.313
5	250,504.003	4,165,805.965	30.148	3.6	0.265
6	250,503.921	4,165,804.518	30.208	1.5	0.424
7	250,501.001	4,165,804.747	30.251	0.6	0.559
8	250,500.937	4,165,805.000	30.252	08	0.308
9	250,503.342	4,165,807.727	30.177	04	0.213
10	250,501.945	4,165,807.384	30.204	04	0.198
11	250,502.596	4,165,806.482	30.185	24	0.289
12	250,503.031	4,165,804.971	30.201	15	0.463
13	250,502.005	4,165,805.997	30.748	02	0.275
14	250,502.448	4,165805.860	30.756	17	0.500
15	250,502.529	4,165805.234	30.747	15	0.600

A total station, model Leica TCR705, of angular precision 15 cc. and 2 mm + 2 ppm linear, was used [25], (see Figure 4). The use of the total station is due to the fact that it has greater precision than the methodologies analyzed in this study, SfM and HDS. The points were marked with adhesive targets to fix with better precision the points to be taken with the mini prism (see Figure 5).

### 2.2.3. Photogrammetry (SfM)

The photographs were taken from the ground with a CANON Powershot G3X camera, focal length 8.8 mm and pixel size 2.4 × 2.4 microns. The cost of this equipment is usually around EUR 500. Data acquisition was carried out following a displacement similar to



that used in the programming of a photogrammetric flight, i.e., nadir shots (see Figure 6), maintaining the necessary overlap both in rows and columns.

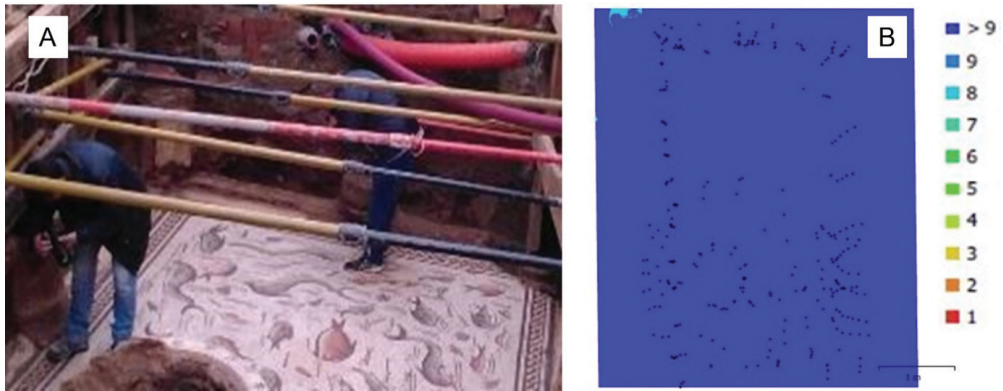


**Figure 6.** Data acquisition with SfM: (A) Taking photographs; (B) Overlapping of photographs.

The conditions for data collection using SfM techniques at the Cantillana site were excellent, since, due to the characteristics of the environment, there was diffuse light and consequently few shadows were produced. Likewise, the features of the object of study, due to its rough texture and varied colors, made it possible to obtain potentially high quality results. A total of 305 photos were taken within 30 min. The result obtained was an overlap of more than 80% (see Figure 6), where the whole mosaic had an overlap of more than 9 photographs. It should be remembered that the usual structure-from-motion (SfM) techniques need, at the least, trifocal overlaps to calibrate the cameras and reconstruct a scene [26].

Once all the photos had been taken, they were dumped and processed with the Agisoft Metashape program, which is based on a series of automatic algorithms. The processing time for the 305 photos was 14 h. Of these photos, only 15% needed technician assistance, and the others were processed automatically by the software (see Figure 7).

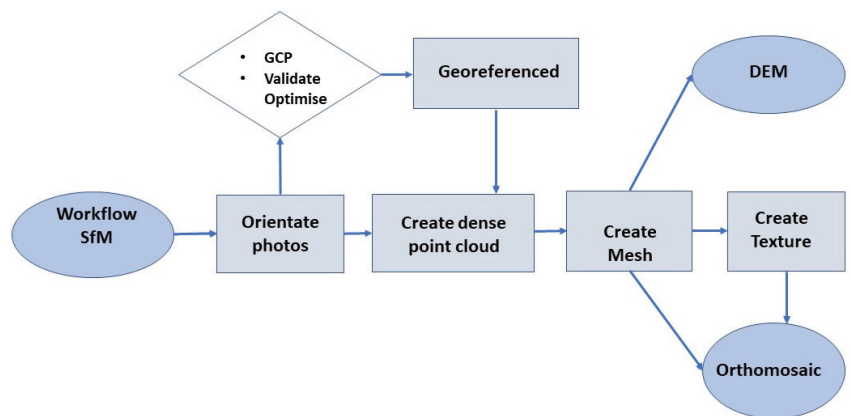


**Figure 7.** SfM Processing workflow.

A virtual 3D representation of the mosaic done with SfM can be found at the link <https://sketchfab.com/3d-models/mosaico-terramar-o-de-los-delfines-9d38178adae4403384f938cf25cbc51c> (accessed on 11 December 2021).

#### 2.2.4. Terrestrial Laser Scanning (TLS)

The TLS methodology aimed to obtain 3D information of the mosaic to reconstruct the scanned object. This methodology has, a priori, a number of drawbacks in relation to accuracy. These are due to internal and external factors. The internal ones are due to the type of equipment model used [27]. The external factors are due to the type of object surface, i.e., the material itself, which mainly affects the angle of incidence of the TLS laser [28].

Laser scanners use different technologies for their performance. Some are time-of-flight processors, i.e., they measure the time it takes for the emitted laser beam to travel from the scanner to the object and back, also known as pulse processors. Others work by phase difference, which implies that they have a periodic base signal which is modified depending on the object upon which it hits, and the existing modular difference between the emitted and received phase is then used to determine the distance traveled by the laser. The latest technological advances in TLS have allowed for the development of a technique called Wave Form Digitization (WFD), which is based on mixing pulse and phase difference measurement technology [29]. Lasers with WFD technology emit a multitude of pulses to record a single point, from all the records of that single point they eliminate those whose signal is very different from the majority. The signals that are optimal are added together, thus obtaining the measured point [30].

A Leica Geosystems P20 based on WFD technology with linear accuracy  $\pm 1$  mm and angular, vertical and horizontal 8" accuracy was used in this study. This equipment is able to record between 50,000 and 1,000,000 points per second (see Figure 8). The cost of this equipment is around EUR 20,000.



**Figure 8.** Data acquisition with TLS from different points of view.

There were three parking points with the TLS scanner, two inside the mosaic and one on the outside, since all the devices in the area related to the safety of the excavation, such as struts and structure fastenings to keep the mosaic as stable as possible (see Figure 8).

The TLS parking points (Est-6 and Est-7) were at the level of the mosaic. The third scan was made from the upper part (Est-5), that is to say at the street floor level, in order to have a record from above, although a posteriori all the errors produced by the mosaic excavation support props had to be eliminated. Figure 9 shows the location of the parking lots for the three scans and that of the four targets used. The targets model GZT21, Figure 9 (D-01, D-02, D-03, D-04), were installed on their corresponding magnetic supports. The

coordinates of these targets are listed in Table 2. The resolution was programmed to capture points at a step of 3 mm at 10 m. Scanning conditions are listed in Table 3.

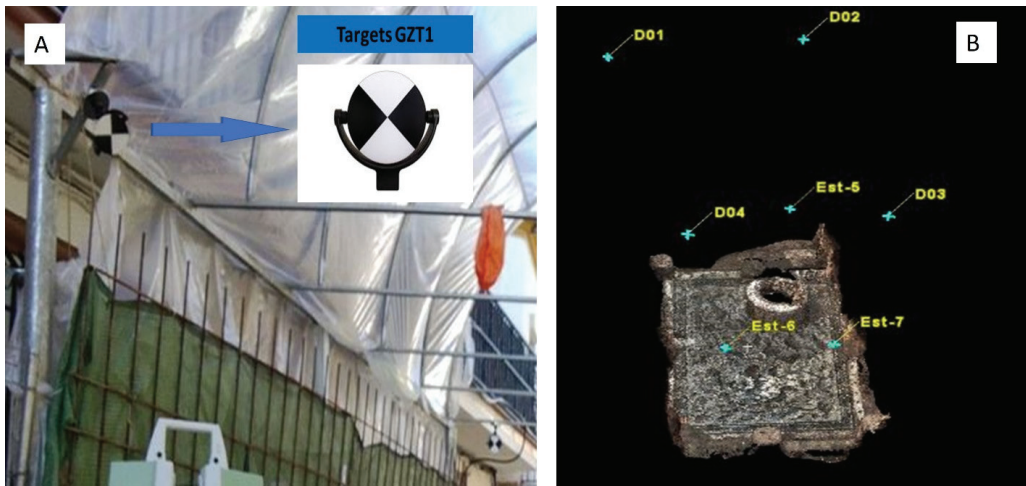


Figure 9. Target: (A) Target example; (B) Target positions.

Table 2. Coordinates of targets: D-01, D-02, D-03, D-04.

Target	X	Y	Z
D01	250,504.887	4,165,802.485	34.710
D02	250,501.280	4,165,802.133	34.706
D03	250,500.799	4,165,807.835	34.615
D04	250,503.795	4,165,808.125	34.728

Table 3. Scanning conditions.

Parameter	Value
Field of view	Full vault
Hz/V Area (°)	90°/55°
Scan Mode	Scan Only
Resolution	25.0 mm @ 10 m
Quality	3
Number of Dots (Hz × V)	2514 × 1013
Image Exposure	Auto
White Balance	Cold Light
Image Resolution	1920 × 1920
HDR Image	No
Estimated Time	7 min 22 s

Once the point acquisition was finished, the points were loaded into Leica’s Cyclone program. This software merges the point clouds taken from the different positions with the support of the control points, i.e., the four targets already mentioned. After all the data had been grouped into a single point cloud and correctly georeferenced, it was exported in a format readable by other programs to allow for its management and analysis.

### 3. Results

#### 3.1. SfM

The dense point cloud obtained with SfM were 8,246,650 points with RGB (Red, Green, Blue) color. The results achieved with photogrammetry were: a dense point cloud (see Figure 10A), mesh without texture (see Figure 10B), mesh with texture (see Figure 10C), and a digital elevation model (see Figure 10D). A virtual 3D representation of the mosaic done with SfM can be found at the link <https://sketchfab.com/3d-models/mosaico-terramar-ode-los-delfines-9d38178adae4403384f938cf25cbc51c> (accessed on 11 December 2021).

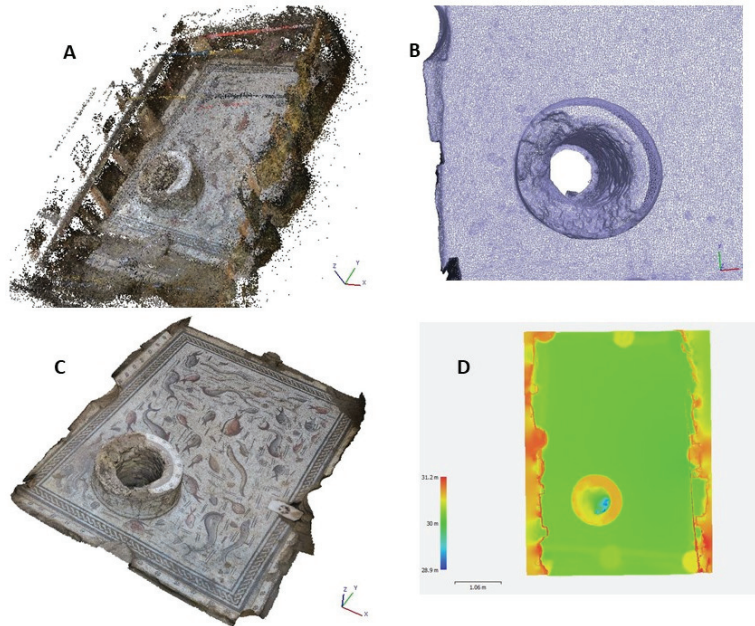


**Figure 10.** Results from SfM (A–D).

#### 3.2. TLS

A cloud of 99,821 points with RGB (Red, Green, Blue) color was obtained with the TLS once the scanning area was completed (see Figure 11). A virtual 3D representation of the mosaic done with TLS can be found at the link <https://www.pointbox.xyz/clouds/61b1d56d99e6e097d35c48ba> (accessed on 11 December 2021).

#### 3.3. SfM vs. TLS

Figure 12 shows an overlay between the 3D model generated by SfM and the point cloud obtained with TLS (in red). It reveals areas in which there is no representation of the points obtained with TLS or, more precisely, that they remain hidden under the SfM model. It is observed in Figure 12 that all the points measured by TLS on the smooth marble surface corresponding to the sump of the mosaic are not shown in the model. Figure 13A shows an enlargement of this area. Figure 13B shows an elevation showing that the points taken with TLS are located below the model, with GCP406 located on the surface of the sink as a reference.

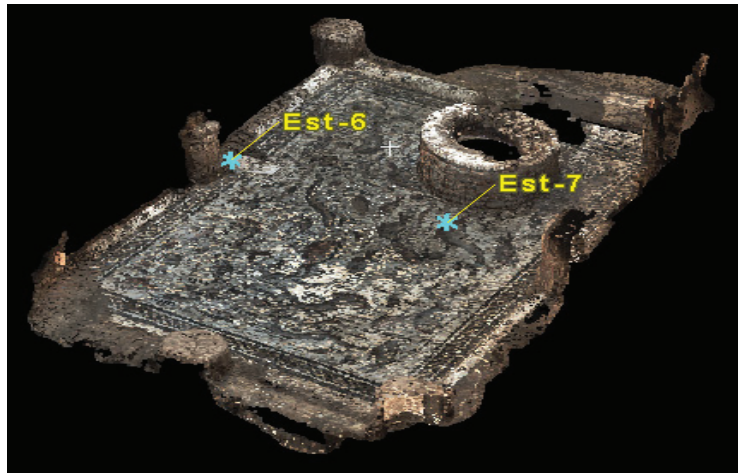


Figure 11. Point cloud obtained with TLS.

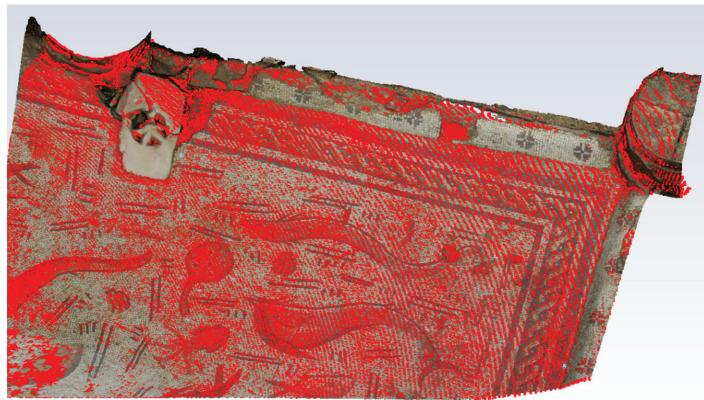


Figure 12. SfM model vs. TLS point cloud.

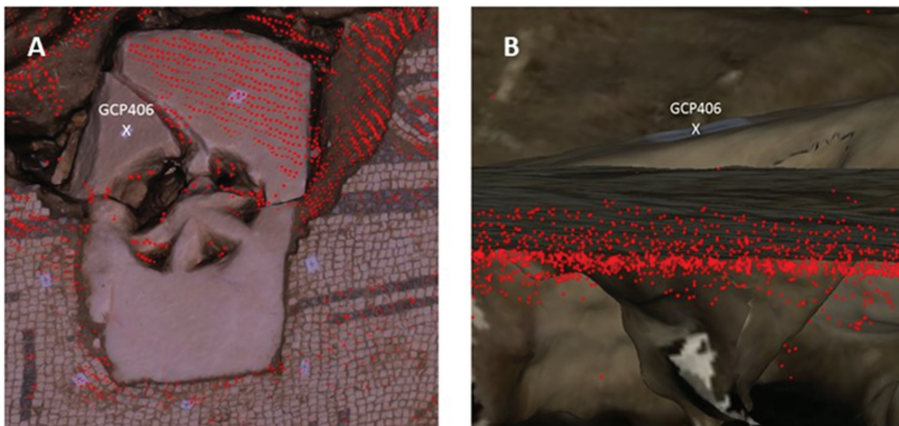


Figure 13. TLS points representation on SfM model on marble sink area. (A) 2D representation; (B) Altimetric profile.

It is clear that there is a difference in elevation in several areas, so it was considered necessary to perform a control measurement using a method that was not influenced by materials or geometric layout. For this purpose, the same TCR705 total station used for the georeferencing of the model was used. This total station was used to measure points of the mosaic with the help of a mini prism, so that the orientation or characteristics of the materials would not affect the measurement in any case. A total of 233 points were taken with a wide variety in location, material, degree of inclination, and color, due to the difference between shades represented in the tesserae of the mosaic. This method offered an accuracy within the range provided by the total station used, i.e.,  $\pm 2 \text{ mm} + 2 \text{ ppm}$ .

The comparison was made with a selected reduced area of the mosaic, (see Figure 13), which contains all the elements where the main divergences were found (sump, base-board, etc.).

To obtain the required area from the data obtained with TLS, the area of interest was simply cut out of the point cloud obtained from the whole mosaic. In order to present the chosen mosaic area with SfM, a new project with a total of 69 photographs was made. Of the 233 GCPs measured with the total station, 18 were used, as they were marked with stickers, so that identification was quick and accurate in the photographs (see Figure 14).



**Figure 14.** SfM model of the selected area with GCPs represented.

#### 4. Discussion

The 3DReshaper software was used to analyze the accuracy of the points between TLS and SfM. Figure 15 shows a comparison between both models analyzed, where 96% of the points presented an error in the range of +3 mm to  $-5 \text{ mm}$  (see Figure 15). The other 3.8% of the points varied within a range of  $-5 \text{ mm}$  and  $-17 \text{ mm}$ . These results are not a priori relevant and need to be compared with more precise data, such as the GCP taken with a total station.

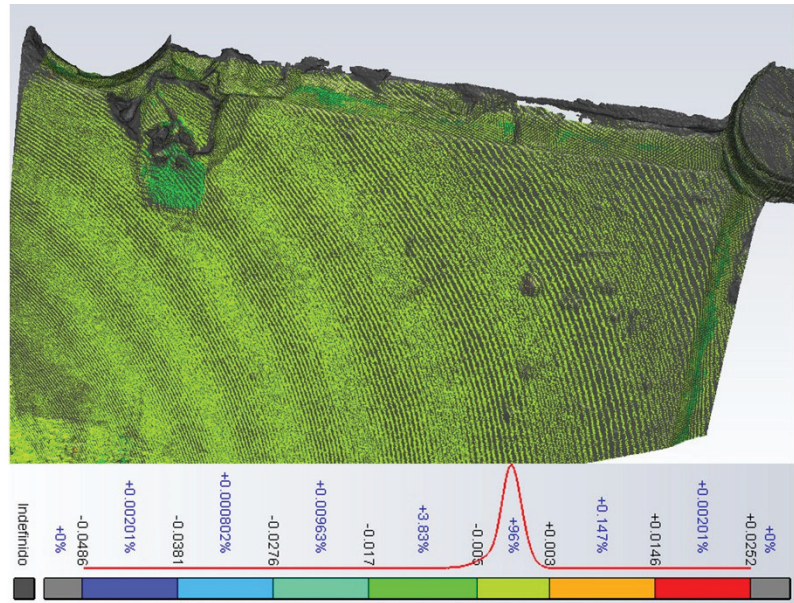


**Figure 15.** TLS vs. SfM.

The analysis of the SfM with the GCPs using 3DReshaper is shown in Figure 16A. The results show that the points had an absolute error greater than 1 mm, and that in no cases did the error reach 2 mm. Considering the features of the total station used to take the control points, where the error range is  $\pm 2$  mm + 2 ppm in the determination of coordinates, it can be concluded that the errors are below those seen in the reference materials.

By superimposing the GCPs on the high-definition mesh generated from the TLS points, it can be observed in Figure 16B that 88.5% of the points have an error between 5 mm and  $-0.7$  mm, while only 2.39% are between  $-0.7$  mm and  $-2$  mm. In addition, 9.17% of the points were between 5 mm and 13 mm. In this section, it can be observed that these are the points of the marble sink. The cyan and red tones are where the largest range of errors (between 5 mm and 1 cm) have appreciated, and it is there where the biggest differences can be observed, likely because of the materials that compose the sump, such as marble. The green tones of the baseboard are due to the angle of incidence, which in the baseboard is different from the rest of the points of the mosaic.

Table 4 summarizes the error ranges of each method regarding the control points. It can be observed that the technique that obtains the best results with respect to the GCPs is SfM photogrammetry. This does not mean that the TLS method does not meet the expectations of the GCPs, but that in the range of  $<2$  mm, the percentage of points is higher. In addition, it was found that there is a significant percentage of points that exceed the threshold of  $\geq 5$  mm, in particular 9.17%, because they are points taken on the clean part of the sink. The increase in error in this area is due to the material from which the sink is composed, which is marble. It has been proven in the literature that the laser in materials such as marble, goes through part of the surface and generates erroneous information in the points measured [31]. Specifically, marble, being a porous material on its surface, causes the laser to pass through the surface, generating an error in the altimetry of the points.

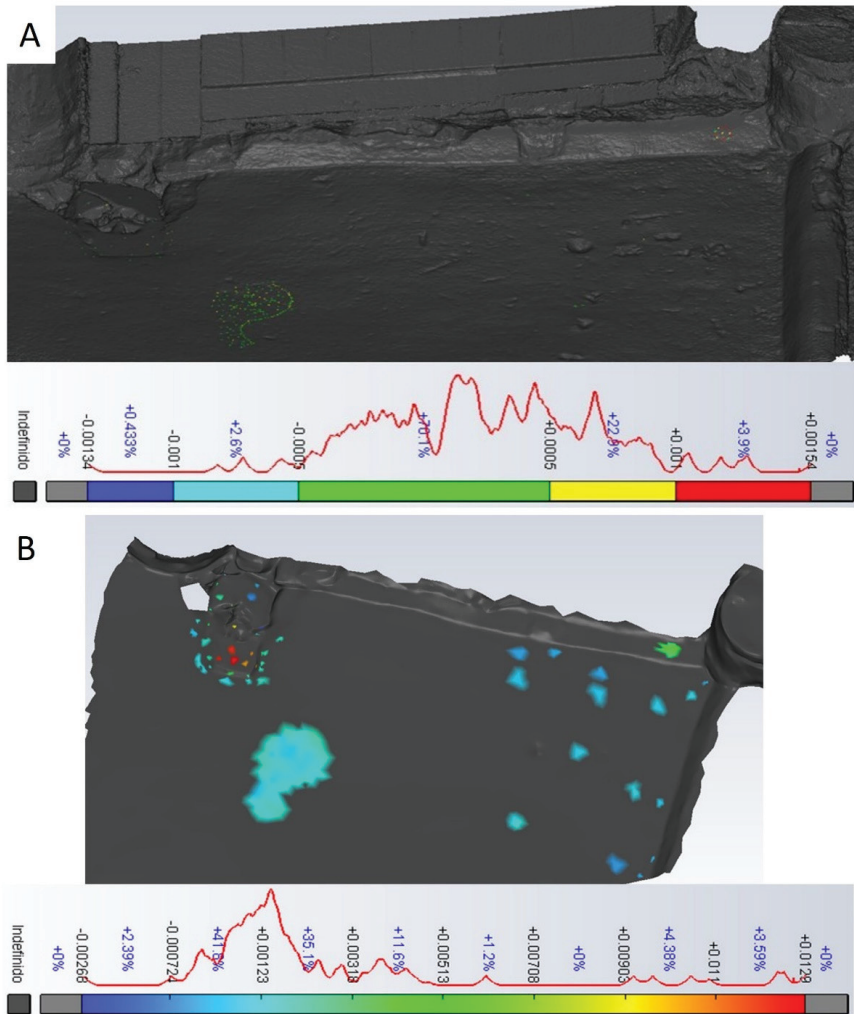


Figure 16. Accuracy analysis. (A) GCP vs. SfM. (B) GCP vs. TLS.

Table 4. Absolute range of error.

	≥5 mm	<5 mm	<2 mm	<1 mm	<0.5 mm
GCP vs. SfM	-	-	4.3%	95.6%	70.1%
GCP vs. TLS	9.17%	88.5%	2.39%	-	-

## 5. Conclusions

In this research, two geomatics techniques have been compared for the study of a Roman mosaic in its original location for its transfer to a restoration area or museum, and with the possibility of it being relocated in the future back to its original location. In the present study, photogrammetry based on SfM and low-cost cameras, and terrestrial scanner or TLS have been used, which are very widespread in archaeological excavations due to the high precision obtained from their results and the massive collection of point clouds. These have been compared with a more accurate method of obtaining coordinates, but that



is limited in terms of production or amount of information, i.e., the total station, which has, therefore, served as a control method.

In particular, it was observed that the marble area, that of the sink, was the one area that was influenced the most in the data acquisition with TLS, obtaining points below the elevation determined by the total station, probably because the porosity of the material produced a slight delay in the reflection of the signal emitted by the scanner. It can be concluded that the SfM technique is the one that comes closest to the optimal values generated by the total station. This is not to say that TLS is not an accurate technique since its accuracy values are very close.

In addition, the experiments performed in this study demonstrated the higher performance level and simplicity of the SfM technique with respect to TLS performance. In addition, the SfM technique is accessible to non-specialized personnel as it involves taking photographs using a certain strategy but without the need for technical preparation. The TLS technique, on the other hand, requires several stations and the measurement of control points from all stations. When equipment costs are considered alongside these factors, where the TLS technique is 40 times more expensive, but the SfM obtained 10 times more points, photogrammetry techniques with SfM presented a clear advantage over TLS for the accurate documentation of mosaics in archaeological excavations.

However, there are constraints to the technique of photogrammetry using SfM if it is to be extended to other types of archaeological excavations, e.g., when the distance at which the photographs are taken is not close to the object. In this case, the distance would be the equivalent to the flight altitude of a photogrammetric flight. Another important limitation is when environmental lighting conditions are not suitable; here, the TSL technique is clearly better, for example, in caves or inside buildings.

**Author Contributions:** Conceptualization, F.M.-A. and C.M.-B.; methodology, A.M.P.-R.; M.J.L.-B.; R.M.-Á.; J.C.M.-G.; F.M.-A. and C.M.-B.; software, C.M.-B. and A.M.P.-R.; validation, C.M.-B. and A.M.P.-R.; formal analysis, C.M.-B. and A.M.P.-R.; data curation, J.C.M.-G.; C.M.-B. and A.M.P.-R.; writing—original draft preparation, F.M.-A., C.M.-B. and A.M.P.-R.; writing—review and editing, A.M.P.-R.; M.J.L.-B.; R.M.-Á.; J.C.M.-G.; F.M.-A. and C.M.-B.; supervision, F.M.-A.; project administration C.M.-B. and A.M.P.-R.; funding acquisition, C.M.-B. and A.M.P.-R. All authors have read and agreed to the published version of the manuscript.

**Funding:** This research received no external funding.

**Institutional Review Board Statement:** Not applicable.

**Informed Consent Statement:** Not applicable.

**Data Availability Statement:** Not applicable.

**Acknowledgments:** The authors would like to thank CIAIMBITAL (University of Almeria, Ceia3) for its support.

**Conflicts of Interest:** The authors declare no conflict of interest.

## References

1. Marín-Buzón, C.; Pérez-Romero, A.; López-Castro, J.; Ben Jerbania, I.; Manzano-Agugliaro, F. Photogrammetry as a new scientific tool in archaeology: Worldwide research trends. *Sustainability* **2021**, *13*, 5319. [\[CrossRef\]](#)
2. Cheng, L.; Chen, S.; Liu, X.; Xu, H.; Wu, Y.; Li, M.; Chen, Y. Registration of laser scanning point clouds: A review. *Sensors* **2018**, *18*, 1641. [\[CrossRef\]](#) [\[PubMed\]](#)
3. Liang, X.; Kankare, V.; Hyypä, J.; Wang, Y.; Kukko, A.; Haggrén, H.; Yu, X.; Kaartinen, H.; Jaakkola, A.; Guan, F.; et al. Terrestrial laser scanning in forest inventories. *ISPRS J. Photogramm. Remote Sens.* **2016**, *115*, 63–77. [\[CrossRef\]](#)
4. Large, A.R.G.; Heritage, G.L.; Charlton, M.E. Laser scanning: The future. *Laser Scanning Environ. Sci.* **2009**, *262*, 262–271. [\[CrossRef\]](#)
5. Gressin, A.; Mallet, C.; Demantké, J.; David, N. Towards 3D lidar point cloud registration improvement using optimal neighborhood knowledge. *ISPRS J. Photogramm. Remote Sens.* **2013**, *79*, 240–251. [\[CrossRef\]](#)
6. Yang, B.; Dong, Z.; Liang, F.; Liu, Y. Automatic registration of large-scale urban scene point clouds based on semantic feature points. *ISPRS J. Photogramm. Remote Sens.* **2016**, *113*, 43–58. [\[CrossRef\]](#)

7. Weinmann, M.; Hinz, S.; Jutzi, B. Fast and automatic image-based registration of TLS data. *ISPRS J. Photogramm. Remote Sens.* **2011**, *66*, S62–S70. [[CrossRef](#)]
8. Puttonen, E.; Lehtomäki, M.; Kaartinen, H.; Zhu, L.; Kukko, A.; Jaakkola, A. Improved sampling for terrestrial and mobile laser scanner point cloud data. *Remote Sens.* **2013**, *5*, 1754–1773. [[CrossRef](#)]
9. Kang, D.; Lee, H.; Park, H.S.; Lee, I. Computing method for estimating strain and stress of steel beams using terrestrial laser scanning and FEM. In *Key Engineering Materials*; Trans Tech Publications Ltd.: Freienbach, Switzerland, 2007; Volume 347, pp. 517–522. [[CrossRef](#)]
10. Brechtken, R.; Przybilla, H.J.; Wahl, D. Visualisation of a necropolis on the basis of a portable aerial photogrammetric system and terrestrial laser scanning. In Proceedings of the ISPRS Congress Beijing 2008, Beijing, China, 3–11 July 2008; Volume XXXVII, pp. 667–672. Available online: [https://www.researchgate.net/profile/Rainer-Brechtken/publication/242142584\\_VISUALISATION\\_OF\\_A\\_NECROPOLIS\\_ON\\_THE\\_BASIS\\_OF\\_A\\_PORTABLE\\_AERIAL\\_PHOTOGRAMMETRIC\\_SYSTEM\\_AND\\_TERRESTRIAL\\_LASER\\_SCANNING/links/5e4bbde6a6fdccd965af1d57/VISUALISATION-OF-A-NECROPOLIS-ON-THE-BASIS-OF-A-PORTABLE-AERIAL-PHOTOGRAMMETRIC-SYSTEM-AND-TERRESTRIAL-LASER-SCANNING.pdf](https://www.researchgate.net/profile/Rainer-Brechtken/publication/242142584_VISUALISATION_OF_A_NECROPOLIS_ON_THE_BASIS_OF_A_PORTABLE_AERIAL_PHOTOGRAMMETRIC_SYSTEM_AND_TERRESTRIAL_LASER_SCANNING/links/5e4bbde6a6fdccd965af1d57/VISUALISATION-OF-A-NECROPOLIS-ON-THE-BASIS-OF-A-PORTABLE-AERIAL-PHOTOGRAMMETRIC-SYSTEM-AND-TERRESTRIAL-LASER-SCANNING.pdf) (accessed on 11 December 2021).
11. Boochs, F.; Kern, F.; Schütze, R.; Marbs, A. Approaches for geometrical and semantic modelling of huge unstructured 3D point clouds. *Photogramm. Fernerkund. Geoinf.* **2009**, *2009*, 65–77. [[CrossRef](#)]
12. Lerma, J.L.; Navarro, S.; Cabrelles, M.; Villaverde, V. Terrestrial laser scanning and close range photogrammetry for 3D archaeological documentation: The Upper Palaeolithic Cave of Parpalló as a case study. *J. Archaeol. Sci.* **2010**, *37*, 499–507. [[CrossRef](#)]
13. Grussenmeyer, P.; Landes, T.; Alby, E.; Carozza, L. High resolution 3D recording and modelling of the Bronze Age cave “Les Fraux” in Périgord (France). In Proceedings of the Conference ISPRS Commission V Symposium, Newcastle, UK, 2020; Volume 38, pp. 262–267. Available online: [https://hal.archives-ouvertes.fr/hal-03099460/file/ISPRS\\_2010\\_Gruss\\_Land\\_Alby\\_Carozza.pdf](https://hal.archives-ouvertes.fr/hal-03099460/file/ISPRS_2010_Gruss_Land_Alby_Carozza.pdf) (accessed on 11 December 2021).
14. Lichte, D.D.; Gordon, S.J.; Stewart, M.P.; Franke, J.; Tsakiri, M. Comparison of digital photogrammetry and laser scanning. In Proceedings of the Proceedings: CIPA W6 International Workshop, Corfu, Greece, 1–2 September 2002; pp. 39–47.
15. Fabris, M.; Achilli, V.; Artese, G.; Bragagnolo, D.; Menin, A. High resolution survey of phaiostos palace (Crete) by Tls and terrestrial photogrammetry. *Int. Arch. Photogramm. Remote Sens. Spat. Inf. Sci.* **2012**, *39*, B5. [[CrossRef](#)]
16. Peña-Villasenín, S.; Gil-Docampo, M.; Ortiz-Sanz, J. Professional SfM and TLS vs a simple SfM photogrammetry for 3D modelling of rock art and radiance scaling shading in engraving detection. *J. Cult. Heritage* **2018**, *37*, 238–246. [[CrossRef](#)]
17. Blistan, P.; Jacko, S.; Kovanič, L.; Kondela, J.; Pukanská, K.; Bartoš, K. TLS and SfM approach for bulk density determination of excavated heterogeneous raw materials. *Minerals* **2020**, *10*, 174. [[CrossRef](#)]
18. Lewińska, P.; Róg, M.; Żądło, A.; Szombara, S. To save from oblivion: Comparative analysis of remote sensing means of documenting forgotten architectural treasures-Zagórz Monastery complex, Poland. *Measurement* **2021**, *13*, 110447. [[CrossRef](#)]
19. Moyano, J.; Nieto-Julian, J.E.; Bienvenido-Huertas, D.; Marín-García, D. Validation of close-range photogrammetry for architectural and archaeological heritage: Analysis of point density and 3d mesh geometry. *Remote Sens.* **2020**, *12*, 3571. [[CrossRef](#)]
20. Mohammadi, M.; Rashidi, M.; Mousavi, V.; Karami, A.; Yu, Y.; Samali, B. Quality evaluation of digital twins generated based on UAV photogrammetry and TLS: Bridge case study. *Remote Sens.* **2021**, *13*, 3499. [[CrossRef](#)]
21. Verhoeven, G.; Doneus, M.; Briese, C.; Vermeulen, F. Mapping by matching: A computer vision-based approach to fast and accurate georeferencing of archaeological aerial photographs. *J. Archaeol. Sci.* **2012**, *39*, 2060–2070. [[CrossRef](#)]
22. Méndez, V.; Pérez-Romero, A.; Sola-Guirado, R.; Miranda-Fuentes, A.; Manzano-Agugliaro, F.; Zapata-Sierra, A.; Rodríguez-Lizana, A. In-field estimation of orange number and size by 3D laser scanning. *Agronomy* **2019**, *9*, 885. [[CrossRef](#)]
23. Villanueva, J.K.S.; Blanco, A.C. Optimization of ground control point (GCP) configuration for unmanned aerial vehicle (UAV) survey using structure from motion (SfM). *Int. Arch. Photogramm. Remote Sens. Spat. Inf. Sci.* **2019**, *42*. [[CrossRef](#)]
24. Oniga, V.-E.; Breaban, A.-I.; Pfeifer, N.; Chirila, C. Determining the suitable number of ground control points for UAS images georeferencing by varying number and spatial distribution. *Remote Sens.* **2020**, *12*, 876. [[CrossRef](#)]
25. Marín-Buzón, C.; Pérez-Romero, A.; Tucci-Álvarez, F.; Manzano-Agugliaro, F. Assessing the orange tree crown volumes using google maps as a low-cost photogrammetric alternative. *Agronomy* **2020**, *10*, 893. [[CrossRef](#)]
26. Salaun, Y.; Marlet, R.; Monasse, P. Line-Based Robust SfM with Little Image Overlap. In Proceedings of the 2017 International Conference on 3D Vision (3DV), Qingdao, China, 10–12 October 2017; pp. 195–204.
27. Cabo, C.; Del Pozo, S.; Rodríguez-González, P.; Ordóñez, C.; Aguilera, S.D.P. Comparing terrestrial laser scanning (TLS) and wearable laser scanning (WLS) for individual tree modeling at plot level. *Remote Sens.* **2018**, *10*, 540. [[CrossRef](#)]
28. Marčič, M. Quality of 3D models generated by SfM technology. *Slovak J. Civ. Eng.* **2013**, *21*, 13–24. [[CrossRef](#)]
29. Truong-Hong, L.; Gharibi, H.; Garg, H.; Lennon, D. Equipment considerations for terrestrial laser scanning for civil engineering in urban areas. *J. Sci. Res. Rep.* **2014**, *3*, 2002–2014. [[CrossRef](#)]
30. Large, A.R.; Heritage, G.L. Laser scanning—Evolution of the discipline. In *Laser Scanning for the Environmental Sciences*; Wiley-Blackwell: Oxford, UK, 2009; pp. 1–20.
31. Lerma García, J.L.; Van Genechten, B.; Santana Quintero, M. *3D Risk Mapping. Theory and Practice on Terrestrial Laser Scanning. Training Material Based on Practical Applications*; Universidad Politecnica de Valencia Editorial: Valencia, Spain, 2008; Available online: <https://lirias.kuleuven.be/1773517?lmo=0> (accessed on 11 December 2021).



## Article

# GPR and Digital Survey for the Diagnosis and the 3D Representation of the Battle of Issus Mosaic from the House of the Faun, Pompeii (Naples, Italy)

Marilena Cozzolino <sup>1,\*</sup>, Antonio De Simone <sup>2</sup>, Vincenzo Gentile <sup>1</sup>, Paolo Mauriello <sup>1</sup> and Amanda Piezzo <sup>3</sup>

<sup>1</sup> Department of Agricultural, Environmental and Food Sciences, University of Molise, Via De Sanctis Snc, 86100 Campobasso, Italy; vincenzo.gentile86@gmail.com (V.G.); mauriello@unimol.it (P.M.)

<sup>2</sup> Department of Human Sciences, University Suor Orsola Benincasa, Corso Vittorio Emanuele 292, 80135 Napoli, Italy; desimone.prof@gmail.com

<sup>3</sup> National Archaeological Museum of Naples (MANN), Ministry of Culture, Piazza Museo 19, 80135 Napoli, Italy; amanda.piezzo@beniculturali.it

\* Correspondence: marilena.cozzolino@unimol.it

**Abstract:** The application of non-invasive geophysical techniques and digital surveys to explore cultural heritage is becoming a very important research field. The capability to detect inner and superficial changes in the inspected surfaces allows for imaging spatial inhomogeneity and material features and planning targeted conservation and restoration interventions. In this work, the results of a research project carried out on the famous Battle of Issus Mosaic, also known as the “Alexander Mosaic”, are presented. It is a masterpiece of ancient art that was found in 1831 in the House of Faun, the most luxurious and spacious house in Pompeii. It is notable for its size (3.41 × 5.82 m), the quality of workmanship and the subject that represents the culminating phase of the battle between Alexander Magno’s army and the Persian one of Darius. In 1916, it was moved inside the National Archaeological Museum of Naples, where the original horizontal location was changed with a vertical arrangement supported by an inner wooden structure, whose exact manufacture is unclear. Today, the mosaic is affected by important instability phenomena highlighted by the appearance of the significant detachment of tiles, superficial lesions and swelling of the surface. Given the important need to preserve it, a high-detail diagnostic study was realized through a digital survey and non-invasive geophysical surveys using ground-penetrating radar (GPR). The investigation was repeated after two years, in 2018 and 2020, with the aim of verifying the evolution of degradation. The work provided a high-resolution estimate of the state of the health of the mosaic and allowed for obtaining a three-dimensional reconstruction of the internal mosaic structure, including the formulation of hypotheses on the engineering supporting works of the twentieth century; this provides an essential tool for the imminent conservation project, which also implies restoring the original horizontal position.

**Keywords:** mosaic of alexander; GPR; digital survey; pre-conservation diagnosis

**Citation:** Cozzolino, M.; De Simone, A.; Gentile, V.; Mauriello, P.; Piezzo, A. GPR and Digital Survey for the Diagnosis and the 3D Representation of the Battle of Issus Mosaic from the House of the Faun, Pompeii (Naples, Italy). *Appl. Sci.* **2022**, *12*, 6965. <https://doi.org/10.3390/app12146965>

Academic Editor: Tung-Ching Su

Received: 7 June 2022

Accepted: 6 July 2022

Published: 9 July 2022

**Publisher’s Note:** MDPI stays neutral with regard to jurisdictional claims in published maps and institutional affiliations.



**Copyright:** © 2022 by the authors. Licensee MDPI, Basel, Switzerland. This article is an open access article distributed under the terms and conditions of the Creative Commons Attribution (CC BY) license (<https://creativecommons.org/licenses/by/4.0/>).

## 1. Introduction

In recent years, the use of non-invasive geophysical and geomatic techniques has assumed an increasingly important role in the field of cultural heritage, especially by supporting conservation and restoration projects. Geophysical methods are very useful for assessing the presence of underground structures in preventive archeology at different scales [1–6]; addressing conservation and stability issues of architectural monuments by inspecting soil foundations; assessing the mechanical properties of structural elements [7–13]; and exploring internal and superficial structures of precious and delicate targets, such as statues, wall paintings and mosaics [7,14–18]. Among these techniques, ground-penetrating radar (GPR) is widely used thanks to the miniaturization of the instrumentation, the high

investigation resolution and the minimal impact on the analyzed surfaces. For example, Masini et al. [7] presented GPR prospecting on three different constructive elements that are typical of historical buildings (a wall, a masonry pillar and a marble column), allowing for the characterization of the masonry, the detection of cracks and the imaging of metallic reinforcement bars. The obtained information was relevant for providing better knowledge of the history of the monuments and their current internal state to be evaluated for in any possible restoration intervention. Matias et al. [14] used GPR combined with seismic transmission tomography to provide important results in an investigation of columns and walls of a 14th-century UNESCO monument by giving information on the quality and spatial distribution of the materials used in the construction of the monument. Manataki et al. [15] applied different GPR systems with frequencies of 1600 MHz, 500 MHz and 250 MHz to study the mosaics of Delos island, which holds a significant body of ancient Greek art of the Hellenistic period that is on UNESCO's World Heritage List. The 1600 MHz system allowed for identifying the boundaries of the mosaic layers, as well as problematic areas, such as bulges and high levels of moisture that may cause deterioration.

For the same topics, geophysical methods can also be applied jointly with geomatic techniques that, thanks to the advances in data collection, processing and visualization, represent an important source of knowledge regarding diagnostics and documentation [19–26]. Cozzolino et al. [20] conducted a 3D metric survey through photogrammetry and ground-penetrating radar (GPR) tests applied to the study of the trapezophoros with two griffins attacking a doe of Ascoli Satriano, which is a masterpiece of ancient art that needs to be protected. The work provided information on both visible and hidden defects, such as numerous cracks that affect the sculpture. Arias et al. [21] showed the usefulness of a multidisciplinary approach to heritage documentation involving close-range photogrammetry and ground-penetrating radar techniques, as well as the development of finite-element-based structural models. The study was focused on the documentation of a medieval bridge concerning the geometric shape, the building material, and the current damage and its causes. Danese et al. [25] showed a spatial-analysis-based protocol for the interpretation of data coming from different non-invasive tests to improve the extraction process of the pattern's decay. The case study was a frescoed wall of a Gymnasium in Pompeii, which was investigated with the following non-invasive techniques: structure-from-motion photogrammetry (SfM), ground-penetrating radar and multitemporal infrared thermography. This approach enabled the extraction of decay patterns to construct a 3D model that constituted the deformation map of the painting analysis methodology and to establish the first step for the restoration of an important multilevel characterization of a fresco that is useful for the protection and mitigation of its deterioration risk.

In this study, a high-detail diagnostic investigation was realized through a digital survey and non-invasive geophysical survey using ground-penetrating radar (GPR) on the Battle of Issus Mosaic, also known as the "Alexander Mosaic". It was found on 24 October 1831 in the exedra of the peristyle of the House of the Faun (Regio VI, 12, 2) in Pompeii, which was the ancient city destroyed by the eruption of Vesuvius in 79 AD (Figures 1 and 2) [27]. In 2018, the National Archaeological Museum of Naples (MANN), where the mosaic is exposed, set up a working group, mainly composed of personnel within the institute, which is collaborating with the Central Institute for Restoration, as well as the University of Molise and the Center for Research on Archaeometry and Conservation Science (University of Naples Federico II and University of Sannio) for surveys and diagnostic investigations. The study determining the state of conservation of the mosaic was aimed at supporting the restoration project and the change of its placement. To this end, a high-detail survey was realized by the University of Molise in 2018, and it was repeated in 2020 to verify the evolution of degradation in compliance with the following workflow:

- (1) The creation of a high-resolution 3D model and orthophotos of the external surfaces through a photogrammetry digital survey in order to highlight the decay and even the type of decay, which is not perceivable by direct sight.

- (2) An analysis of the inner surfaces through the implementation of non-invasive GPR surveys with the purpose of detecting anomalies indicating voids or fractures.
- (3) An analysis of the photographic documentation produced between 1916 and 1917 in relation to the GPR data to understand the type of internal structure of support and carefully calculate its weight. This information is useful for facilitating the organization of the movement of the mosaic.
- (4) The production of new and detailed documentation, which has been non-existent so far and is useful for the imminent conservation actions.



**Figure 1.** Location of Pompeii on the map of Italy (a), plan of the city with the position of the House of Faun (b) and the exedra of the peristyle where the mosaic was found (c).



**Figure 2.** A close-up picture of the Battle of Issus Mosaic.

## 2. Test Site: The Battle of Issus Mosaic

The Battle of Issus Mosaic represents the triumph of Alexander the Great over Darius III of Persia in 333 BC during the Battle of Issus in Turkey. The masterpiece was created at the end of the second century BC in the opus vermiculatum technique with about 1,800,000 millimetric tesserae. In the left portion, Alexander the Great is depicted with his horse

Bucephalus. Medusa is represented on the cuirass with her wavy hair. On the right, there is Dario on a chariot as he tries to launch an assault with his men while the coachman is already whipping the horses. We also note Dario Oxyathres, who sacrifices himself to allow his brother Darius III to save himself by letting himself be pierced by the Macedonian leader. The spears, the crowding of men and horses, the fallen horse and the Persian soldier in the foreground who looks at himself in agony in a mirror bring to mind the dramatic moment of the battle.

From the moment of its discovery, there was a debate between the court, the academicians, the archaeologists, the architects and the mosaicists regarding its state of conservation and the choice of keeping it at Pompeii in its original location or detaching and transferring it to the Royal Bourbon Museum. The conservation events of the Alexander Mosaic from the House of the Faun to its current location are described in detail in [28]: “At the end, after many uncertainties, the King resolved to transfer the Mosaic in Naples and on 16 November 1843, under pouring rain, the crate containing the Mosaic of Alexander was placed on a railway wagon coming from Maddaloni, near Caserta, pulled by sixteen oxen and escorted by armed soldiers, and after a grueling journey of nine days finally came in the Royal Museum where it was exhibited, not without controversy, in the ground floor of the Gallery, in the so-called Room of the Balbi. The Mosaic remained in this place until 1916 when it was moved to the western mezzanine where Vittorio Spinazzola, Director of the National Archaeological Museum of Naples between 1910 and 1924, picked up the mosaics in a new independent collection and where it still is exposed. A detailed documentation on photographic plates, made between 1916 and 1917, is preserved in the Historical Photo Archive of Special Superintendence for the Archaeological Heritage of Naples and Pompeii. The photographs gather information relative to all phases of the moving and the final installation”. However, the type of structure created at the base of the mosaic to support it in a vertical position is not well understood as there are no shots of it.

The events briefly explained profoundly affected the state of conservation of the work, which is currently affected by important instability phenomena highlighted by the appearance of significant detachments of tiles (the occurrence is emphasized by the vibrations transmitted by car and railway traffic outside the museum), superficial lesions and swelling of the surface. In addition, it must be considered that the mosaic was designed and built to be placed on the floor, and consequently, the detachment from the site of discovery produced a significant alteration. In fact, the almost complete, albeit brief, removal of the rudus (the layer of lime, sand and aggregates, such as gravel or pebbles, which formed a concrete of consistent thickness) and the transport from the lower to the upper floor significantly affected the nucleus (the layer of mortar mixed with fragments of bricks that served as a support for the floor made of tiles). This procedure unnaturally transformed a floor mosaic into a wall mosaic [29].

### 3. Material and Methods

#### 3.1. Photogrammetric Digital Survey

The production of the three-dimensional model of the mosaic surface was carried out through two photogrammetric surveys carried out in 2018 and 2020. The frames were acquired along horizontal bands (ensuring an average overlap of 80% both horizontally and vertically) at a distance of about 0.5 m from the mosaic surface using a Nikon D80 reflex camera (CCD sensor (23.6 × 15.8 mm) with 12.2 million pixels and a fixed focal length of 24 mm). The camera was set in aperture priority mode ( $f/9$  value) and with an ISO sensitivity equal to 100. In order to reference the 3D model in Cartesian space in real metric units, a survey with a total station was also created using 163 clearly recognizable elements on the mosaic surface as markers. Therefore, a reference system was set up with an origin ( $P = 0,0,0$ ) located in the lower-left corner of the mosaic and all the project data were implemented in an information system managed with Quantum GIS software (Version 3.16.11 Hannover, Open Source Geospatial Foundation, Beaverton, OR, USA).

Data processing was carried out using the Photoscan software (Agisoft Metashape Pro, Version 1.6.4, Agisoft LLC, St. Petersburg, Russia) through the following operations:

- (1) Alignment of frames using the structure-from-motion (SfM) technique [30]. Three datasets were generated: a discrete point cloud describing the object's starting geometry, the positions of the camera at the time of the acquisition of the frames and the internal calibration parameters of the camera (focal length and three radial and two tangential distortion coefficients relative to the main point).
- (2) Geometry construction through the generation of a dense cloud.
- (3) Positioning of the 3D model in Cartesian space. The points detected with the total station were entered as ground control points (GCPs) within the software. The result was the processing of a dense metric and georeferenced cloud, obtaining an average registration error of 0.007 m for the 2018 survey and 0.005 m for the 2020 survey.
- (4) Mesh generation by transforming the three-dimensional model from a point cloud to the surface of triangulated points. In order to recognize and adapt the discontinuities in the model, a "multi-resolution model" routine based on automated algorithms was used. Furthermore, an "optimization method" and a "decimation filter" were applied to reorganize and smooth the nodes of the triangles and to simplify the model and generate a multi-resolution model, respectively.
- (5) Construction of the texture through the application of digital images to the model and the creation of metric and geo-referenced orthophotos exported in the GeoTIFF format.
- (6) Generation and export in GeoTIFF format of the digital elevation model (DEM).

### 3.2. Ground-Penetrating Radar (GPR)

GPR is based on the diffusion of electromagnetic pulses into the soil and the recording of those re-radiated by buried targets characterized by sufficient dimensions and electromagnetic properties different from those of the surrounding ground. The quantities that are measured are the time required for the wave to travel the path from the transmitting antenna to a discontinuity and return to the surface (double time or two-way time) and the amplitude of the reflected wave. The double travel time depends on the speed with which the wave propagates within the material and provides information on the depth at which the reflectors are located. However, the amplitude, which represents how much energy returns to the surface after reflection, depends on the initial energy of the sent wave, the quantity that is dissipated along the way and the contrast of the electromagnetic properties of the materials that comprise the surface of the reflection. A complete description of the method is available in textbooks, such as [31–35].

The factors that influence the performance of the system in terms of the detectability of existing targets are the electromagnetic properties of the propagation medium, which determine the depth of investigation that can be reached, which varies from point to point. Since the attenuation of the means is a function of the radiated frequency, the use of high-frequency antennas generally allows for enhancing the resolution power, but at the expense of the penetration depth of the signals.

The georadar surveys were carried out on the entire surface of the mosaic in its actual vertical position. An IDS georadar RIS-K2 with a 3000 MHz high-resolution antenna was used for the data acquisition, whose features were considered sufficient and suitable for an overall assessment of the conservation status of the mosaic with respect to the type of target to be investigated and the thicknesses of surfaces to be analyzed.

Technically, data acquisition took place on 114 lines, from top to bottom every 5 cm, where instrumental readings were executed in continuous mode (Figure 3). In addition, several horizontal profiles and some profiles on the sides of the mosaic were acquired.





**Figure 3.** Grid data acquisition (a) with an IDS georadar (b).

Raw data were processed using GPR-SLICE 7.0 software (Screening Eagle Technologies Ag, Zurich, Switzerland) [36] using standard methodological approaches. In the first step, data and trace editing were executed, inserting information such as the temporal and spatial sampling intervals (time window, 20 ns; samples/scan, 512; scan/mark, 25; unit/marker, 1). Data were recorded and processed as 16-bit data and were converted by subtracting out the DC drift (wobble) in the data and, at the same time, adding a gain with time. A time-zero correction was determined to designate the starting point of the wave and the center frequency of the antenna was matched. Then, a bandpass filter and background removal were respectively applied to reduce noise from the oscillating components that had a regular frequency cycle in the frequency domain and to remove striation noises that occurred at the same time. Processed radargrams were subsequently corrected with an automatic gain control (ACG) function [37] that was applied to each trace based on the difference between the mean amplitude of the signal in the time window and the maximum amplitude of the trace. In the final step, the resulting filtered radargrams were inserted into a three-dimensional matrix from which sections were obtained at a particular double-time interval (measured in nanoseconds). Considering the complex layering and the reduced length of the profiles, we preferred to not apply the migration filter and we avoided presenting results converting time to depth using a mean value with the possibility to obtain an arbitrary and inaccurate estimate.

#### 4. Results and Discussion

Figure 4 shows the DEMs obtained in 2018 and 2020 and Figure 5 shows some details of the last one transparently overlaid onto the processed orthophoto. The DEM analysis in 2018 (Figure 3a,b) highlighted depressions and reliefs relative to a hypothetical plane passing through the point of origin of the reference system ( $P = 0,0,0$ ) in a spatial range of 3.66 cm. The reliefs were mainly located on the frame of the panel where the swellings responsible for the detachment of some mosaic tiles were clearly highlighted. The depressions, on the other hand, affected the central and right portions of the mosaic. The presence of an internal iron frame at the edges of the panel could, on the one hand, have favored the onset of bubbles and swelling as a consequence of the natural oxidation processes of the metal; on the other hand, it could have resisted deformations due to volumetric variations of the mortars in response to changes in temperature and humidity and/or deformations triggered by kinematic stresses (natural or artificial). This could explain the existence of depressions detected in the central part and the onset of lesions, especially on the edges (most resistant points) and the points of greatest weakness of the panel (central and right part). In order to identify the surface variations from 2018 to 2020, the point clouds of the surveys were metrically compared through the CloudCompare software (Verison 2.11 beta, Telecom ParisTech and the R&D division of EDF, Villeurbanne, France). Figure 6 shows the absolute distances between the point cloud obtained by subtracting the 2020 data from

those of 2018. On a global scale, a uniform swelling of the central part of the mosaic was estimated to be in the range of about 4 mm.

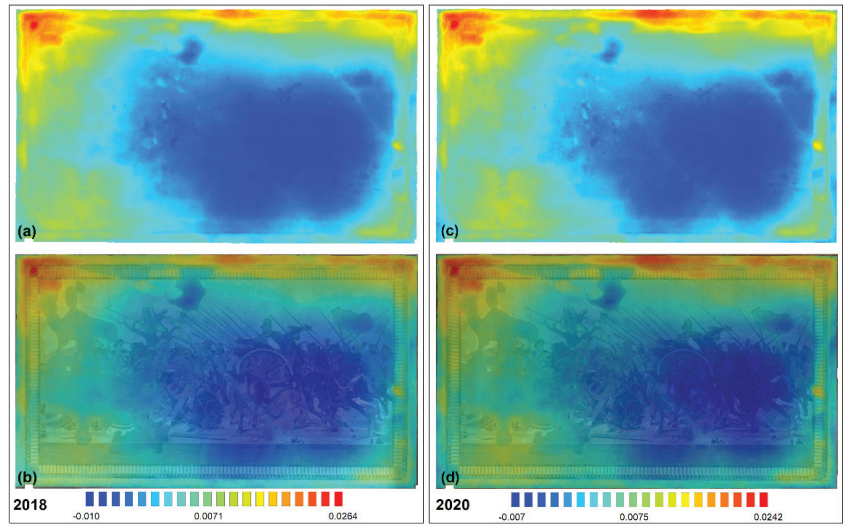


**Figure 4.** DEMs obtained in 2018 (a) and 2020 (c) and the same drawings transparently placed on the orthophoto (b,d). The values in the legend are expressed in meters.



**Figure 5.** Details of the orthophoto obtained in 2020 (a–c) and DEMs transparently overlaid on them (d–f).

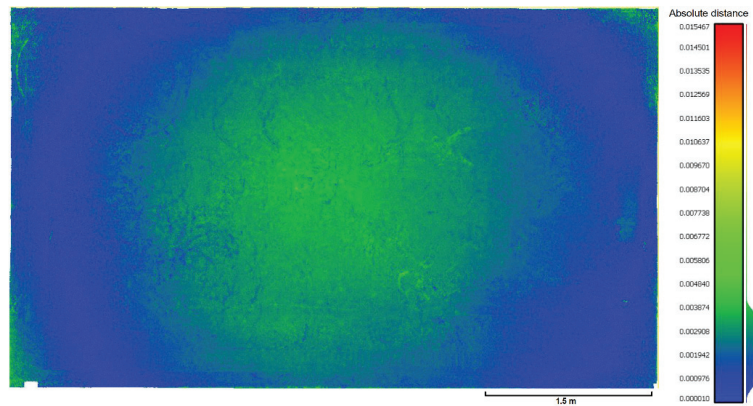


**Figure 6.** Absolute distance obtained by subtracting the 2020 data from 2018 data.

Figure 7 shows the images obtained in 2018 from the visual analysis of the orthophoto in which the areas affected by restorations, the detachment of tesserae and fractures are highlighted. The indication of the fractures was just quantitative and therefore they were not classified by taking into account the elevation, thickness and dimensions. The visual analysis of the orthophoto made it possible to detect in detail every single fracture and the detachment of tesserae present on the surface. The latter phenomenon, caused by multiple factors, was aggravated by the vertical position of the mosaic, which, compared with the original horizontal position, determined the displacement on the ground and the irreversible loss of the individual tiles or portions of the mosaic. The fractures had two main alignments: one vertical/horizontal, which mainly affected the edges of the mosaic, and one diagonal to the mosaic, which concerned the central/right portion of the panel. The latter was particularly relevant and fell into the areas of greatest depression recorded in the digital surface elevation model. The presence of restored and consolidated areas on the left side may have increased the resistance of the surfaces, avoiding the onset of superficial lesions.

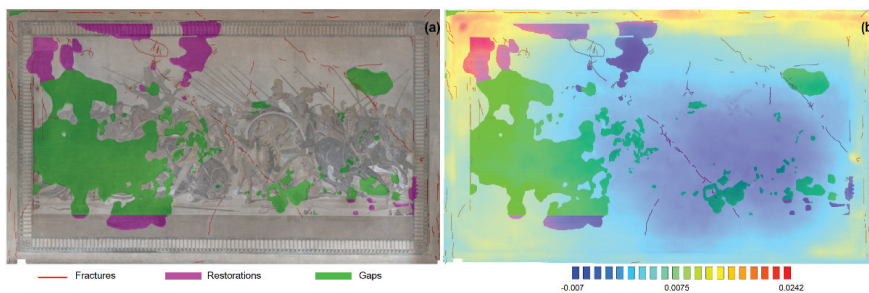


**Figure 7.** Restorations, detachments of tesserae and fractures reported on the orthophoto (a) and the DEM (b).

Regarding the GPR results, anomalies due to the presence of the iron support reinforcement present under the frame stood out in the different time slices (Figure 8). The degrees of amplitude variation in the time-slices were assigned a color scale that was chosen in order to show sufficient contrast to make the anomalies easily recognizable: light green corresponded to low amplitudes, while red corresponded to high amplitudes. The anomalies visible in these representations depicted the spatial distribution of the amplitudes of the reflections at specific depths within the grid. Within the sections, low amplitude variations expressed small reflections that indicated the presence of homogeneous material. High

amplitudes, on the other hand, denoted significant discontinuities in the investigated surface. In the most superficial part, we saw some anomalies of high amplitude that denoted a variation in the consistency of the materials (Figure 8b), which were located mainly on the left side of the mosaic. This aspect could be related to the presence of depressions and diagonal fractures in the central area and right side of the panel. The anomaly on the right side, near the border, was located at the point where there was swelling.

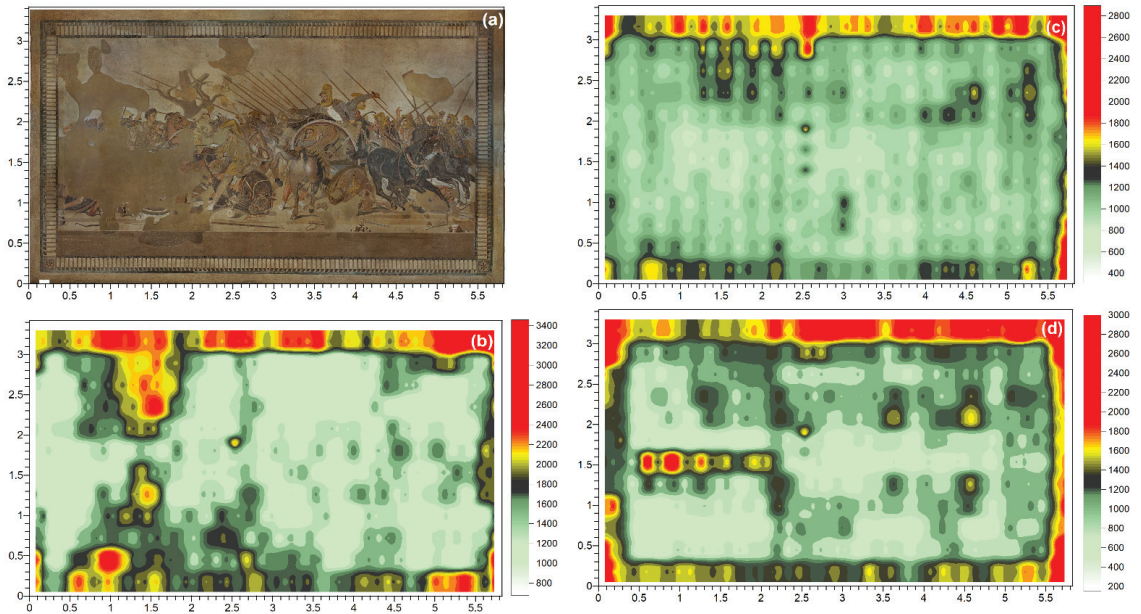


**Figure 8.** Details of the orthophoto obtained in 2020 (a) and slices relating to the time slices of 0.35–0.88 ns (b), 1.88–2.4 ns (c) and 3.34–3.87 ns (d).

In order to understand the inner structure, in the following part, the analysis of photographic documentation, made between 1916 and 1917, which records all phases of the moving and the final vertical installation, was jointly analyzed with GPR radargrams and slices. Following the images, it is known that the mosaic was housed on some blocks of rock. In Figure 9a, it is possible to note the original stratigraphy by recognizing, from top to bottom, the nucleus, the rudus and the screed covering the stone beams. Subsequently, the section was cleaned, the screed was removed and the stone structure was brought to light. Some wedges separated the rudus from the blocks of rock (Figure 9b). Then, the surface of the section was leveled and the rudus was cleaned of residual lime for the realization of the support frame (Figure 9c). In the next phase, equally spaced holes were drilled in the rudus, three of which are visible in Figure 9d.

From the analysis of the georadar results, it was assumed that these holes were drilled to anchor the rudus to the frame under construction by means of pins. Figure 10b shows the acquired radargram at the edge of the frame, as indicated by the green arrow on the mosaic orthophoto (Figure 10d). With red circles, the positions of the holes visible in the photos are indicated. At those points, hyperbolas are attributable to the presence of iron pins. However, there are other anomalies (indicated with yellow arrows) of the same nature. At the edges, the close hyperbolas reflected the positions of the nails used to fix the iron L-bars (blue arrows) installed in the following stages. Figure 10c shows the radargram acquired at the edge of the original frame, as indicated by the magenta arrow on the mosaic. The anomalies persisted and another one was highlighted on the left (red arrow). There were no more anomalies in the upper band. Then, the pins penetrated the mosaic by at least

15 cm (a few cm in the original one). The radargram acquired in the upper band, again at the edge of the original mosaic, highlighted the same anomalies found below (Figure 10a). Here, the pins are still visible from the top of the frame.

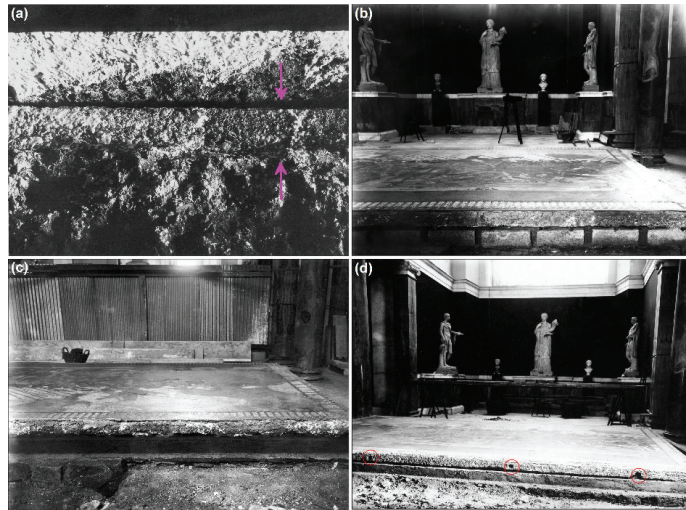


**Figure 9.** Photo no. 4138-1916-EX 306 (a), photo no. 4131-1916-EX 299 (b), photo no. 4129-1917-EX 297 (c) and photo no. 4130-1916-EX 298 (d).

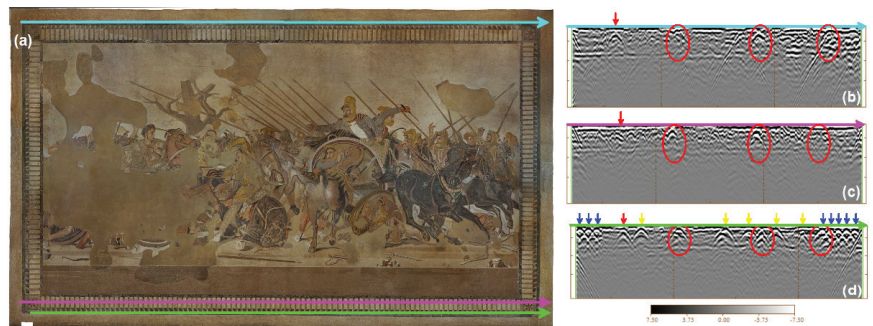


**Figure 10.** Location of the anchor pins (indicated by red circles) and further anomalies on three horizontal radargrams (b–d) located at the positions of the colored arrows (a).

The same situation is found on the sides where two hyperbolas are visible (Figure 11), in addition to the pins visible with the naked eye.

Figure 12 shows the digital model of the processes followed before applying the frame and removing the stone.

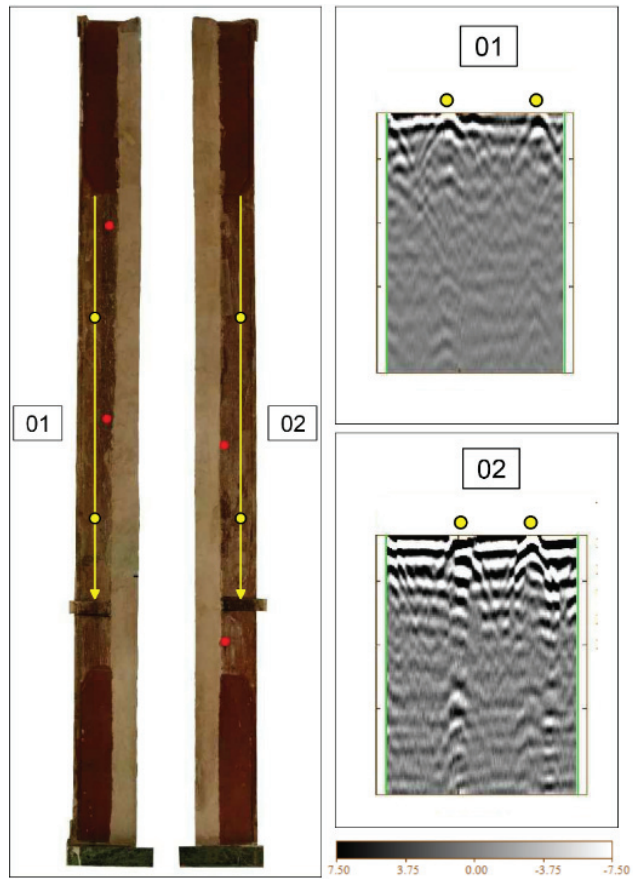


**Figure 11.** Orthophoto of the left and right sides of the mosaic and radargrams labeled 01 and 02. Red dots indicate visible pins.

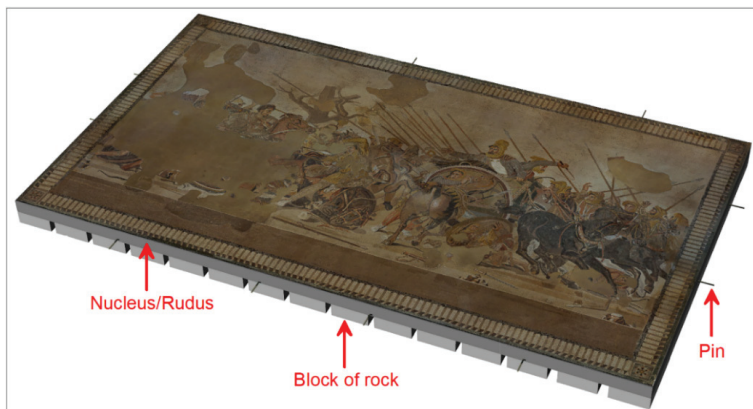


**Figure 12.** Digital model with the locations of the blocks of rock and the anchor pins.

The external frame was probably made using wooden crosspieces measuring  $25 \times 13$  cm. Figure 13a shows a detail of Figure 9d (photo no. 4130-1916-EX 298), where in the background,

a wooden crosspiece appears with regular carvings. They were assumed to be about 10 cm wide and placed at intervals of about 22 cm. Figure 13b shows the digital model of the carved frame. It was assumed that this element is related to the underlying part of the longitudinal crosspiece that was specially prepared to house the elements of the internal filling.

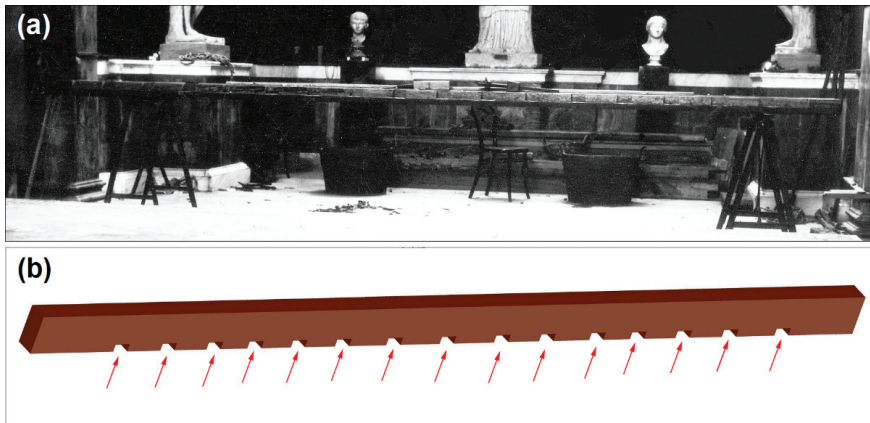


**Figure 13.** Photo no. 4130-1916-EX 298 (a) and digital model of the frame with indication of the notches using red arrows (b).

The anchoring of the wooden crosspieces with the mosaic is described in the previous section. To reinforce the structure, four angular iron bars were added (Figure 14). Holes were also drilled to position the protective covering of the front part of the mosaic. A 2 cm board was placed under the wooden crosspieces, which were placed under the stone crosspieces (Figure 14a). This table was probably removed in the next phases.

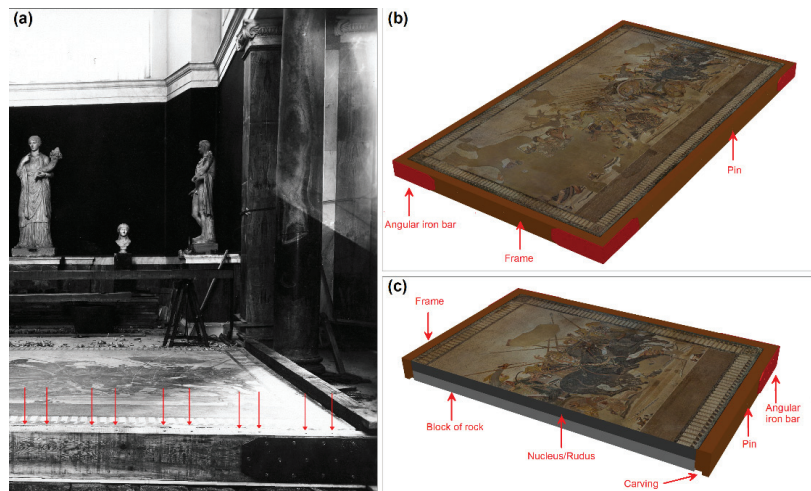


**Figure 14.** Photo no. 4132-1916-EX 300 (a), a digital model with the anchoring of the frame and addition of iron angles (b) and a cross-section (c).

A protective sheet was added to the surface, which was blocked with a board on the edge by means of nails in the pre-drilled points in the previous step (Figure 15a). Some sides were added (10 cm wide and 5 cm high) in between where the wide boards were to be placed (Figure 15b). The gaps were subsequently sealed with mortar (Figure 15c). After

which, the lifting of the recessed mosaic began (Figure 14d), which was placed in a vertical position on a support (Figure 15e).

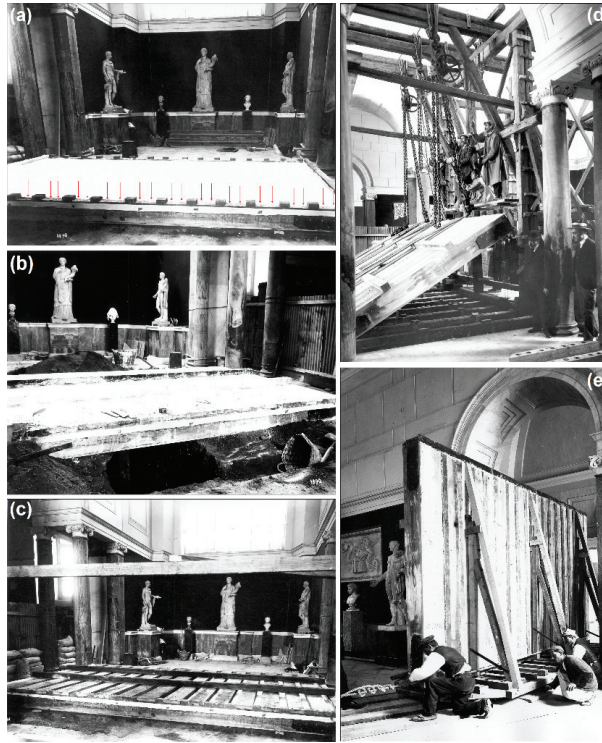


**Figure 15.** Photo no. 4133-1916-EX 301 (a), photo no. 4134-1916-EX 302 (b), photo no. 4135-1916-EX 303 (c), photo no. 4157-1917-EX 325 (d) and photo no. 4173-1917-EX 341 (e).

On the back, from a historical photo, an alternation of narrow dark boards and wide light boards, 10 cm and 22 cm wide, respectively, can be noted (Figure 16a). In the GPR slice relating to the time window 1.88–2.4 ns (Figures 8b and 16b), a series of vertical anomalies were highlighted that began directly in contact with the rudus. It was plausible that the wooden structure placed at the rear of the mosaic traced this structure in some way. In particular, it is likely that the narrow boards were actually beams or murals 10 cm wide (with a maximum length of 14 cm, depending on the thickness of the shaving made under the rudus), which rested directly under the mosaic. As can be seen from many of the radargrams, some profiles seemed to be characterized by the presence of metal elements as brackets to block the vertical wooden beams from the rudus. An example is shown in Figure 17, where three identifiable hyperbolas emerged clearly with the rudus, the filling lime and the closing table. Hyperbolas 1 and 2 (Figure 17a) often penetrated the mosaic and probably represented a system for anchoring the possible wooden beam (vertical georadar anomalies) directly to the mosaic. At approximately hyperbola 3, a sort of reinforcement was evident under the vertical structures (Figure 18). The spaces were probably filled with plaster and closed everything with the boards that were visible on the back. The slice (Figure 17b), which was related to the time window between 3.34 ns and 3.87 ns, was enhanced to visualize the three anomalies jointly, even if detected at different depths.



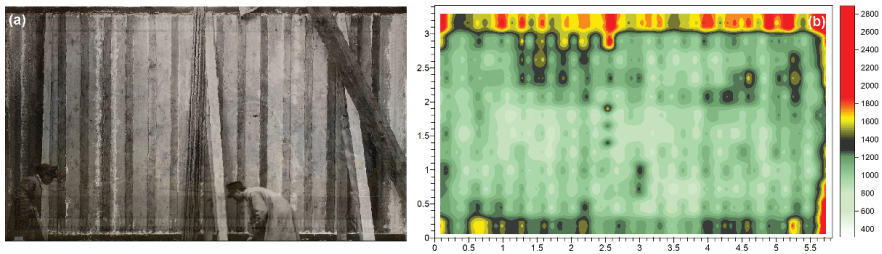


**Figure 16.** Historical photo (photo no. 4172-1917-EX 340) straightened and positioned on the back of the mosaic (a) and time slice relating to the time window 1.88–2.4 ns (b).

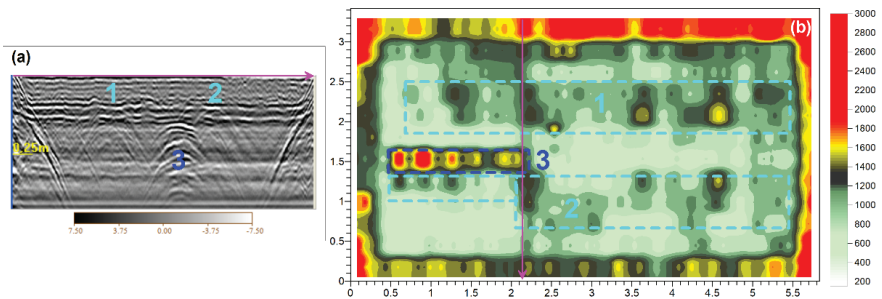


**Figure 17.** Main anomalies, labeled 1, 2 and 3, indicated on the radargram (acquired as indicated by the magenta arrow) (a) and on the slice relating to the time window 3.34–3.87 ns (b).

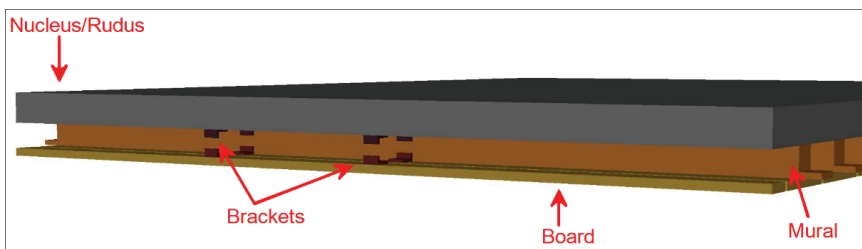


**Figure 18.** Anchor system digital model.

Therefore, after the removal of the blocks of rock, the vertical beams would have been housed (directly or indirectly) thanks to the notches located at the base of the longitudinal beams of the frame. In this system, it is possible to make four hypotheses based on the presumed depth of the notch, the location of the vertical beams and the closing plank. The hypotheses in question took into account the position and shape of the acquired georadar anomalies:

**Hypothesis 1.** (Figure 19): Support boards (25 × 12 cm) were inserted at regular intervals under the rudus. The boards were closed in the lower part with boards (10 × 2 cm) that protrude by 2 cm outside. The empty space between the support boards was filled with plaster. We consider this hypothesis the least probable, as it does not explain the presence of the georadar anomalies previously discussed.

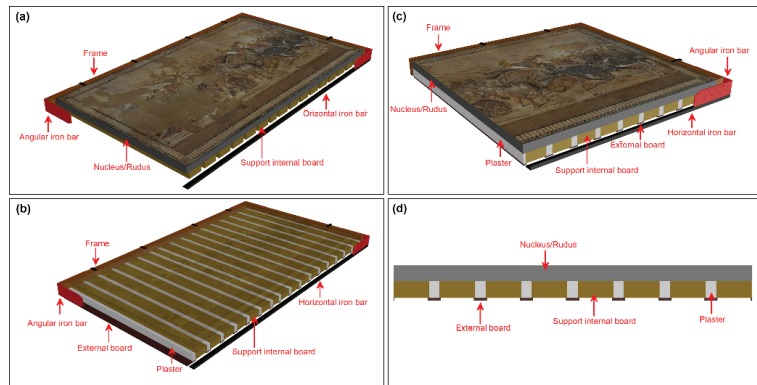


**Figure 19.** Hypothesis 1 digital model: locations of support boards under the rudus (a), complete support system (b), cross-section (c) and longitudinal section (d).

**Hypothesis 2.** (Figure 20): The vertical beams inserted at regular intervals were worked to be housed and nailed to the frame. Between one beam and the other, closing tables were inserted through brackets. The gaps left empty between the beams were filled with plaster.

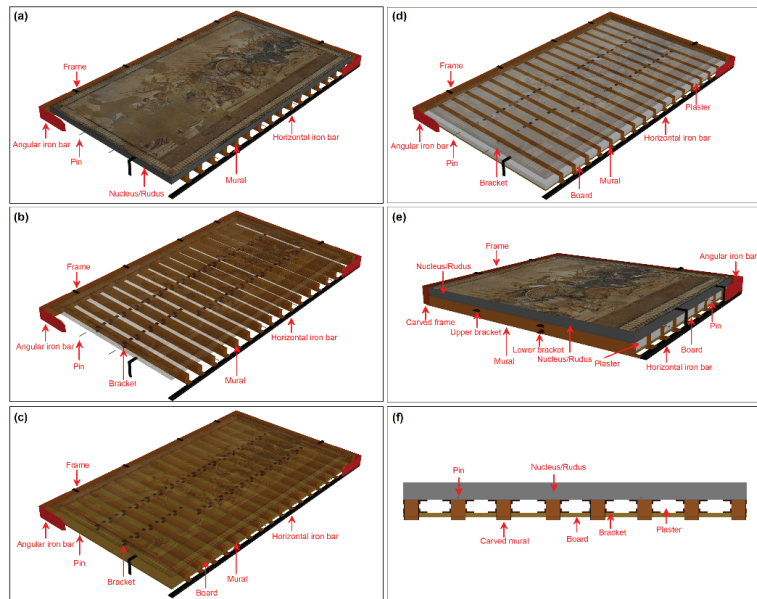


**Figure 20.** Hypothesis 2: locations of vertical beams (a), locations of anchoring brackets (b), locations of closing boards (c), complete support system (d), cross-section (e) and longitudinal section (f).

**Hypothesis 3.** (Figure 21): This differs from hypothesis 2 in that the incision was made to be 12 cm in order to completely contain the vertical beam that rests directly under the rudus and protrudes 2 cm outside.

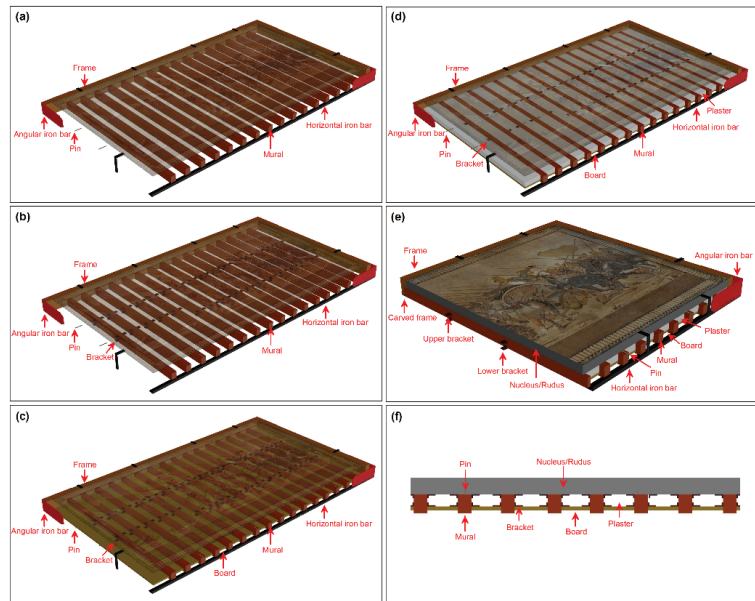


**Figure 21.** Hypothesis 3 digital model: positions of vertical beams (a), locations of anchoring brackets (b), arrangement of closing tables (c), complete support system (d), cross-section (e) and longitudinal section (f).

**Hypothesis 4.** (Figure 22): The planks were anchored to the vertical beams by means of brackets according to a “T” system. Closing tables were inserted between one plank and the other. The gaps left empty between the beams were filled with plaster. This is the hypothesis that best matches the shape and position of the georadar anomalies.

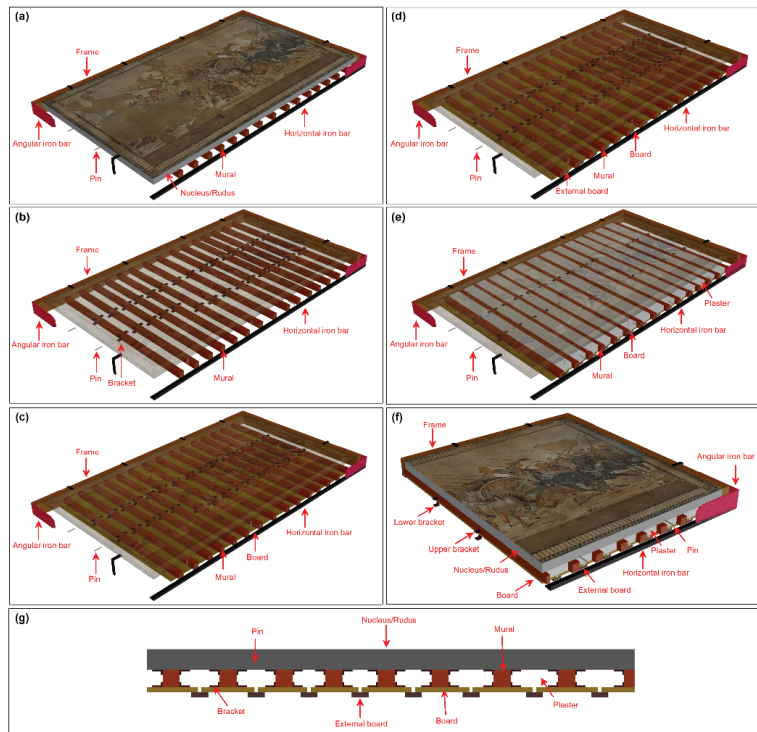


**Figure 22.** Hypothesis 4 digital model: vertical beam positions (a), anchoring bracket locations (b), board arrangements (c), external board positions (d), complete support system (e), cross-section (f) and longitudinal section (g).

### 5. Conclusions

In this study, the issue connected to the conservation of the Alexander Mosaic was investigated in an organic and exhaustive way, starting from the analysis of the available knowledge framework. From an operational point of view, the adopted research methodology provided for the recognition of all available documentation, an accurate survey of the current state from the morphological point of view and non-invasive diagnostic investigations. This allowed for obtaining a further preliminary and in-depth knowledge phase of the asset to also provide a framework for comparison with what emerged from previous studies and, therefore, data on any changes in the state of conservation of the asset. In detail, in addition to a slight progression of the degradation phenomena already recorded in 2018, regarding the lesions, anomalies in the support emerged from the diagnostic results, which suggested the presence of discontinuities in the background mortar. This could have probably been due to the presence of different materials, with particular reference to the mosaic embedding system put in place during the transfer in 1916, consisting of a wooden frame placed along the perimeter, with interposed wooden joists reinforced with metal elements. However, to date, insufficiently exhaustive data has emerged regarding the state of conservation of the support that is not visible and cannot be inspected directly and the actual state will be fully detected only after moving the mosaic from its current position, making the back accessible. Currently, the first phase of the restoration can now be considered completed, which was limited to interventions to make the mosaic surface safe, which was necessary in the face of the detected degradation phenomena and limited only to the elimination of the conditions that can generate critical issues during movement (loose tiles, presence of continuity solutions between the layers, etc.). Subsequently, the mosaic will be overturned, following which it will be possible to access the support to

promptly check its conservation status, fine-tune the subsequent conservation interventions and possibly provide for the construction of a new collection system should the existing one prove to be no longer suitable. Subsequently, the mosaic will be placed in a horizontal position that will allow for the restoration of the mosaic surface and the final rearrangement to be carried out. The restoration operations, which will also affect the rear parts, will be preceded by further diagnostic analyzes once the mosaic is overturned. In this way, at the end of the project, a complete model will be obtained, which will integrate all the results and will represent a precious source of knowledge on this important artifact.

**Author Contributions:** Conceptualization, M.C., P.M., A.D.S. and A.P.; Data curation, M.C., P.M. and V.G.; Methodology M.C., P.M. and V.G.; Validation, M.C., P.M., A.D.S., A.P. and V.G.; Writing—original draft, M.C., P.M. and V.G.; Writing—review and editing, M.C., P.M. and V.G. All authors have read and agreed to the published version of the manuscript.

**Funding:** This research received no external funding.

**Institutional Review Board Statement:** Not applicable.

**Informed Consent Statement:** Not applicable.

**Acknowledgments:** Special thanks to Paolo Giulierini for having involved us in this important project and for having been a constant guide, always demonstrating the greatest passion and dedication to the protection of this very important masterpiece. We are also very thankful to the company “Boviar. Integrated systems for diagnostics and monitoring”, in particular Filippo Bovio, for the technical-scientific support during the data acquisition and processing phases.

**Conflicts of Interest:** The authors declare no conflict of interest.

## References

1. Cozzolino, M.; Bakovic, M.; Borovinic, N.; Galli, G.; Gentile, V.; Jabucanin, M.; Mauriello, P.; Merola, P.; Živanovic, M. The Contribution of Geophysics to the Knowledge of the Hidden Archaeological Heritage of Montenegro. *Geosciences* **2020**, *10*, 187. [[CrossRef](#)]
2. Fassbinder, J.W.E.; Reindel, M. Magnetometer prospection as research for pre-Spanish cultures at Nasca and Palpa, Perú. In Proceedings of the 6th International Archaeological Prospection Conference, Rome, Italy, 14–17 September 2005; Piro, S., Ed.; CNR: Roma, Italy, 2005; pp. 6–10.
3. Tsokas, G.N.; Giannopoulos, A.; Tsourlos, P.; Vargemezis, G.; Tealby, J.M.; Sarris, A.; Papazachos, C.B.; Savopoulou, T. A large scale geophysical survey in the archaeological site of Europos (northern Greece). *J. Appl. Geophys.* **1994**, *32*, 85–98. [[CrossRef](#)]
4. Papadopoulou, N.G.; Tsourlos, P.; Tsokas, G.N.; Sarris, A. Two-dimensional and three-dimensional resistivity imaging in archaeological site investigation. *Archaeol. Prospect.* **2006**, *13*, 163–181. [[CrossRef](#)]
5. Cozzolino, M.; Calì, L.M.; Gentile, V.; Mauriello, P.; Di Meo, A. The Discovery of the Theater of Akragas (Valley of Temples, Agrigento, Italy): An Archaeological Confirmation of the Supposed Buried Structures from a Geophysical Survey. *Geosciences* **2020**, *10*, 161. [[CrossRef](#)]
6. Cozzolino, M.; Gentile, V.; Giordano, C.; Mauriello, P. Imaging Buried Archaeological Features through Ground Penetrating Radar: The Case of the Ancient Saepinum (Campobasso, Italy). *Geosciences* **2020**, *10*, 225. [[CrossRef](#)]
7. Masini, N.; Persico, R.; Rizzo, E. Some examples of GPR prospecting for monitoring of the monumental heritage. *J. Geophys. Eng.* **2010**, *7*, 190–199. [[CrossRef](#)]
8. Tsourlos, P.I.; Tsokas, G.N. Non-destructive electrical resistivity tomography survey at the south walls of the Acropolis of Athens. *Archaeol. Prospect.* **2011**, *18*, 173–186. [[CrossRef](#)]
9. Catapano, I.; Ludeno, G.; Soldovieri, F.; Tosti, F.; Padeletti, G. Structural assessment via ground penetrating radar at the Consoli Palace of Gubbio (Italy). *Remote Sens.* **2018**, *10*, 45. [[CrossRef](#)]
10. Pirinu, A.; Balia, R.; Piroddi, L.; Trogu, A.; Utzeri, M.; Vignoli, G. Deepening the knowledge of military architecture in an urban context through digital representations integrated with geophysical surveys. The city walls of Cagliari (Italy). In Proceedings of the 2018 IEEE International Workshop on Metrology for Archaeology and Cultural Heritage, Cassino, Italy, 22–24 October 2018; pp. 211–215.
11. Angelis, D.; Tsourlos, P.; Tsokas, G.; Zacharopoulou, G.; Power, C. Combined application of GPR and ERT for the assessment of a wall structure at the Heptapyrgion fortress (Thessaloniki, Greece). *Appl. Geophys.* **2018**, *152*, 208–220. [[CrossRef](#)]
12. Pérez-Gracia, V.; Caselles, J.O.; Clapes, J.; Osorio, R.; Martínez, G.; Canas, J.A. Integrated near-surface geophysical survey of the Cathedral of Mallorca. *J. Archaeol. Sci.* **2009**, *36*, 1289–1299. [[CrossRef](#)]
13. Cozzolino, M.; Gentile, V.; Mauriello, P.; Peditrou, A. Non-Destructive Techniques for Building Evaluation in Urban Areas: The Case Study of the Redesigning Project of Eleftheria Square (Nicosia, Cyprus). *Appl. Sci.* **2020**, *10*, 4296. [[CrossRef](#)]

14. Matias, M.; Almeida, F.; Moura, R.; Barraca, N. High resolution NDT in the characterization of the inner structure and materials of heritage buildings walls and columns. *Constr. Build. Mater.* **2021**, *267*, 121726. [CrossRef]
15. Manataki, M.; Maris, C.; Sarris, A.; Vafidis, A. Using GPR to Evaluate the Stratigraphic Condition of the Mosaic of the Dolphins in Delos Island, Greece, in order to Adopt the necessary Conservation measures. In Proceedings of the 10th International Workshop on Advanced Ground Penetrating Radar, The Hague, The Netherlands, 9–11 September 2019; pp. 1–7.
16. Piroddi, L.; Vignoli, G.; Trogu, A.; Deidda, G.P. Non-destructive Diagnostics of Architectonic Elements in San Giuseppe Calasanzio's Church in Cagliari: A Test-case for Micro-geophysical Methods within the Framework of Holistic/integrated Protocols for Artefact Knowledge. In Proceedings of the 2018 IEEE International Conference on Metrology for Archaeology and Cultural Heritage, Cassino, Italy, 22–24 October 2018; pp. 17–21.
17. Urban, T.M.; Bennett, M.R.; Bustos, D.; Manning, S.W.; Reynolds, S.C.; Belvedere, M.; Odess, D.; Santucci, V.L. 3-D radar imaging unlocks the untapped behavioral and biomechanical archive of Pleistocene ghost tracks. *Sci. Rep.* **2019**, *9*, 16470. [CrossRef] [PubMed]
18. Wiewel, A.; Conyers, L.; Piroddi, L.; Papadopoulos, N. An Experimental Use of Ground-Penetrating Radar to Identify Human Footprints. *Archeosciences* **2021**, *45*, 143–146. [CrossRef]
19. Donadio, E.; Spanò, A.; Sambuelli, L.; Picchi, D. Three-Dimensional (3D) modelling and optimization for multipurpose analysis and representation of ancient statues. In *Latest Developments in Reality-Based 3D Surveying and Modelling*; Remondino, F., Georgopoulos, A., Gonzalez-Aguilera, D., Agrafiotis, P., Eds.; MDPI: Basel, Switzerland, 2018; pp. 95–118. ISBN 978-3-03842-684-4.
20. Cozzolino, M.; Di Meo, A.; Gentile, V.; Mauriello, P.; Zullo, E. Combined Use of 3D Metric Survey and GPR for the Diagnosis of the Trapezophoros with Two Griffins Attacking a Doe of Ascoli Satriano (Foggia, Italy). *Geosciences* **2020**, *10*, 307. [CrossRef]
21. Arias, P.; Armesto, J.; Di-Capua, D.; González-Drigo, R.; Lorenzo, H.; Pérez-Gracia, V. Digital photogrammetry, GPR and computational analysis of structural damages in a mediaeval bridge. *Eng. Fail. Anal.* **2007**, *14*, 1444–1457. [CrossRef]
22. Oses, N.; Dornaika, F.; Moujahid, A. Image-based delineation and classification of built heritage masonry. *Remote Sens.* **2014**, *6*, 1863–1889. [CrossRef]
23. Costanzo, A.; Minasi, M.; Casula, G.; Musacchio, M.; Buongiorno, M.F. Combined use of terrestrial laser scanning and IR thermography applied to a historical building. *Sensor* **2015**, *15*, 194–213. [CrossRef] [PubMed]
24. Barrile, V.; Bilotta, G.; Meduri, G.M.; De Carlo, D.; Nunnari, A. Laser Scanner technology, ground-penetrating radar and augmented reality for the survey and recovery of the artistic, archaeological and cultural heritage. *ISPRS Ann. Photogramm. Remote Sens. Spat. Inf. Sci.* **2017**, *4*, 123–127. [CrossRef]
25. Danese, M.; Sileo, M.; Masini, M. Geophysical Methods and Spatial Information for the Analysis of Decay frescoes. *Surv. Geophys.* **2018**, *39*, 1149–1166. [CrossRef]
26. Cozzolino, M.; Gabrielli, R.; Galatà, P.; Gentile, V.; Greco, G.; Scopinaro, E. Combined use of 3D metric surveys and non-invasive geophysical surveys for the determination of the state of conservation of the Stylite Tower (Umm ar-Rasas, Jordan). *Ann. Geophys.* **2019**, *61*, 72. [CrossRef]
27. Bonucci, C. Scavi romani di Pompei, Ercolano, Boscotrecase, luglio a dicembre. *BullInst* **1832**, *1*, 11.
28. Melillo, L. Das Alexandermosaik aus der Casa del Fauno in Pompeji—Die fruhren Bergungsmassnahmen. In *Alexander der Grosse und die Offnung der Welt Asiens Kulturen im Wandel*, 1st ed.; Hansen, S., Wiczorek, A., Tellenbach, M., Eds.; Schnell & Steiner: Mannheim, Germany, 2009; pp. 61–65. ISBN 978-3795421779.
29. De Simone, A.; Piezzo, A. Il restauro del mosaico di Alessandro tra immagine e materia: Ultimi studi e prime ipotesi di intervento. In *Atti del XXVII Colloquio Dell'associazione Italiana per lo Studio e la Conservazione del Mosaico*, 27th ed.; Angelelli, C., Erba, M.E., Massara, D., Zulini, E., Eds.; Quasar: Rome, Italy, 2022; pp. 5–10. ISBN 987-88-5491-248-9.
30. Remondino, F.; El-Hakim, S. Image-based 3-D modelling: A review. *Photogramm. Rec.* **2006**, *21*, 269–291. [CrossRef]
31. Conyers, L.B. *Interpreting Ground-Penetrating Radar for Archaeology*; Left Coast Press: Walnut Creek, CA, USA, 2012.
32. Everett, M.E. *Near-Surface Applied Geophysics*; Cambridge University Press: Cambridge, UK, 2013.
33. Goodman, D.; Piro, S. *GPR Remote Sensing in Archaeology*; Springer: Berlin/Heidelberg, Germany, 2013.
34. Reynolds, J.M. *An Introduction to Applied and Environmental Geophysics*, 2nd ed.; John Wiley & Sons: Oxford, UK, 2011.
35. Cozzolino, M.; Di Giovanni, E.; Mauriello, P.; Piro, S.; Zamuner, D. *Geophysical Methods for Cultural Heritage Management*; Geophysics Series; Springer: Cham, Switzerland, 2018.
36. GPR-SLICE Software. Available online: <http://www.gprsurvey.com/practice/GPR-SLICE> (accessed on 13 May 2022).
37. Jol, H. *Ground Penetrating Radar: Theory and Applications*; Elsevier: Amsterdam, The Netherlands, 2009; ISBN 978-0-444-53348-7.



## Article

# Style Recognition of Door God Paintings by Hypothesis Testing for Texture Features of Painting Patterns

Tung-Ching Su \*, Tsung-Chiang Wu, Ming-Hung Wun and Cheng-Wei Wang

Department of Civil Engineering and Engineering Management, National Quemoy University, Kinmen 89250, Taiwan; tsung\_chiang@nqu.edu.tw (T.-C.W.); ji394su3love20@gmail.com (M.-H.W.); joswawagiga@gmail.com (C.-W.W.)

\* Correspondence: spcyj@nqu.edu.tw

**Abstract:** Many studies in the literature have presented multiple remote sensing techniques for defect inspection of paintings. At present, however, papers on defect inspection and restoration of oriental architectural arts—such as door god paintings—are still rare. If an aged and damaged door god painting needs a restoration, then following the style and treatment skill of the original artist as much as possible is important for the restoration. Unfortunately, it is usually difficult to access the original artists for some of the aged door god paintings. This paper considers the texture features of auspicious patterns of armors on warrior door gods as useful information to recognize styles of door god paintings by unknown artists. First, a two-level two-dimensional discrete wavelet transform coupled with co-occurrence matrix calculation was adopted to analyze the texture features, based on the descriptors of angular second moment (ASM), entropy (ENT), contrast (CON), homogeneity (HOM), dissimilarity (DIS), correlation (COR), and cluster tendency (CLU), in the four orientations of 0° (horizontal), 45° (vertical), and 90° and 135° (double diagonal). Second, a two-tailed *t*-test based on the analyzed texture features was introduced into the hypothesis testing for demonstrating the master and apprentice relationships between the surveyed artists, and for recognizing the door god painting styles of unknown artists as well. The experimental results show that the proposed method effectively describes the texture features of the auspicious patterns of the surveyed door god paintings, and is able to determine the useful co-occurrence features for recognizing unknown artists' painting styles.

**Keywords:** door god paintings; texture features; discrete wavelet transform; two-tailed *t*-test; painting style recognition

**Citation:** Su, T.-C.; Wu, T.-C.; Wun, M.-H.; Wang, C.-W. Style Recognition of Door God Paintings by Hypothesis Testing for Texture Features of Painting Patterns. *Appl. Sci.* **2022**, *12*, 2637. <https://doi.org/10.3390/app12052637>

Academic Editor: Asterios Bakolas

Received: 16 February 2022

Accepted: 1 March 2022

Published: 3 March 2022

**Publisher's Note:** MDPI stays neutral with regard to jurisdictional claims in published maps and institutional affiliations.



**Copyright:** © 2022 by the authors. Licensee MDPI, Basel, Switzerland. This article is an open access article distributed under the terms and conditions of the Creative Commons Attribution (CC BY) license (<https://creativecommons.org/licenses/by/4.0/>).

## 1. Introduction

Door god paintings are frequently seen on the gates of traditional residences or temples, and belong to one kind of Chinese architectural artworks (see Figure 1 [1]). Because of Chinese people's worship of animism in ancient times, some of the door god characters are imaginary. Today, there are several pairs of door gods representing faith in home safety and evil avoidance. The noun "door god" can be seen in the period as early as before the Qin Dynasty [2]. Essentially, the door god characters can be separated into two categories: warrior, and civil official. The greatest difference between warriors and civil officials is that a set of armor is necessary for a warrior, but unnecessary for a civil official. Shen Tu (Chinese transliteration: 神荼) and Yu Lei (Chinese transliteration: 鬱壘) are the earliest warrior door gods and prevailed in the Han Dynasty [3]. In addition to Shen Tu and Yu Lei, Chin Shu Pao (Chinese transliteration: 秦叔寶) and Yu Chih Kung (Chinese transliteration: 尉遲恭) are also frequently seen warrior door gods in the temples of Taiwan. Several auspicious patterns—such as lock chain, turtle back, fish scales, flowers, clouds, and the Chinese characters of "回" and "卍" (see Figure 2)—have been adopted to decorate warriors' armor. For each of the above auspicious patterns, the displayed texture features



may be different due to the creativity of different artists. The different texture features mean that every artist has his/her own unique painting style via his/her special treatment or skill with door god paintings [4].

Any famous door god painting generally has a long history, but that long history may result in the impossibility of identifying the original artist. Additionally, door god paintings use residence or temple gates as their support materials, and so the placed locations of door god paintings belong to a semi-outdoor environment, where door god paintings are apt to suffer as a result of climate factors—such as temperature, relative humidity, and wind—or human factors, such as ritual activities and inadvertent collisions. Hence, the conservation and maintenance of door god paintings are more challenging than for other paintings or artworks collected in a well-controlled, indoor environment, such as an art gallery or museum. When restoring an aged and damaged door god painting, the treatment skill and the procedure must follow its original style as best as possible in order to preserve the unique style of the door god painting. In case of the original artist being unknown, the original style cannot be correctly followed by the painting restoration.



**Figure 1.** A pair of door god paintings: (a) Yu Chih Kung (Chinese transliteration: 尉遲恭): warrior on the left door; (b) Chin Shu Pao (Chinese transliteration: 秦叔寶): warrior on the right door [1].

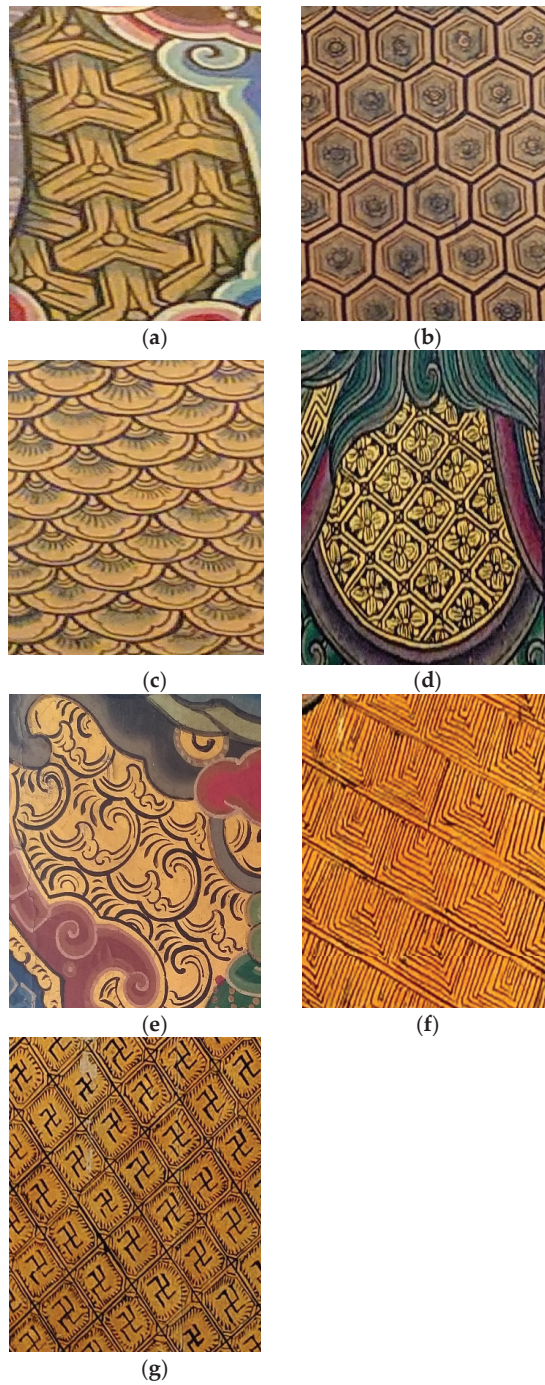


**Figure 2.** Example images of auspicious patterns on paintings of warriors' armor: (a) lock chain pattern; (b) turtle back pattern; (c) fish scales pattern; (d) flowers pattern; (e) clouds pattern; (f) Chinese character pattern: “回”; (g) Chinese character pattern: “卍”.

## 2. Research Aim

The types of deterioration of door god paintings usually include lifting, cracks, shrinkage, atomization, chalking, etc. As far as we know, the current literature discussing restorations of door god paintings is quite scarce. Related image processing methods have also demonstrated their effectiveness in artwork defect detection by providing useful information for artwork restoration [5–7]. This paper’s main contributions are as follows: First, to apply an image-processing-based texture analysis method to extract the texture features from the acquired auspicious pattern images. Second, hypothesis testing is implemented on the texture feature dataset to see the similarity of the auspicious patterns between the surveyed artists, and to demonstrate the master and apprentice relationship as well. Finally, hypothesis testing also is applied to the texture feature dataset to see to which painting style(s) among the surveyed artists the door god painting style(s) of the unknown artist(s) are the closest. In this way, a door god painting restoration can retain its originality as much as possible.

## 3. Backgrounds

### 3.1. Artists of Door God Paintings in Taiwan

Since around the 1960s, there have been certain famous artists who created door god paintings for traditional residences or temples in Taiwan. However, most of these famous artists are now deceased, and so their created door god paintings are regularly restored by their apprentices, some of whom are even members of the famous artists’ family. For instance, the two famous artists of door god paintings—Yu-Feng Chen (Chinese transliteration: 陳玉峰, 1900–1964) and Chun-Yuan Pan (Chinese transliteration: 潘春源, 1891–1972)—were both apprentices to an artist from Quanzhou, Fujian, China, and most of their door god paintings are distributed over temples in southern Taiwan. Shou-Yi Chen (Chinese transliteration: 陳壽彝, 1934–2012, the eldest son of Yu-Feng Chen) and his cousin, Tsao-Ju Tsai (Chinese transliteration: 蔡草如, 1919–2007), were both apprentices of door god painting to Yu-Feng Chen. Among the door god paintings of Yu-Feng Chen, Shou-Yi Chen, and Tsao-Ju Tsai, there is a special painting style belonging to their family genre. Similarly, Chun-Yuan Pan, Li-Shui Pan (Chinese transliteration: 潘麗水, 1914–1995, the son of Chun-Yuan Pan), and Yueh-Hsiung Pan (Chinese transliteration: 潘岳雄, 1943–present, the eldest son of Li-Shui Pan) also created door god paintings with a special painting style belonging to their family genre. Consequently, a mentorship genealogy concerning the creation of door god paintings in southern Taiwan can be established. As for artists in other areas of Taiwan, Hung [2] established a mentorship genealogy for a famous artist in Hsinchu, Taiwan, and compiled a list of the door god paintings created by the artist and his apprentices.

There have been a few cases of door god painting restoration in Taiwan in the past. In 1968, S.-Y. Chen cooperated with two other artists to refurbish aged door god paintings of the Qingshui Zushi (Divine Ancestor) Temple in New Taipei City, Taiwan [4]. Another artist, Lien-Cheng Hsu (Chinese transliteration: 許連成, 1919–2002), created door god paintings for a historic temple in northern Taiwan in 1975, and Hsu’s door god paintings were refurbished in 1989 by Chia-Cheng Liu (Chinese transliteration: 劉家正, 1955–present). In fact, C.-C. Liu refurbished many of Hsu’s door god paintings, but Liu’s painting style belongs to the family genre of Pan rather than Hsu, and so there is a little controversy about the restoration approach.

The original artists of the door god paintings in Taiwan can almost always be identified but, unfortunately, in Kinmen and Penghu—which are the outlying islands of Taiwan—the original artists of door god paintings are mostly difficult to ascertain. Along with the immigration of ancestors from southern Fujian (China) to Taiwan, Kinmen and Penghu were selected as the relay stops. Therefore, there certainly should be some kind of master and apprentice relationships between the artists in southern Fujian and Taiwan, including the outlying islands.

### 3.2. Texture Feature Analysis for Paintings

An image showing a frequency of tonal change, such as zebra crossings and knitting, can be regarded as one with texture features [8]. Similarly, an auspicious pattern image also shows the frequency of tonal change. Several studies in the literature have discussed the applications of texture feature analysis to painting restoration [9–11], painting classification by artistic genre [12–14], painting style recognition [15,16], and raw material investigation [11,17]. Cai and Siegel [9] explored two texture features—energy (or homogeneity) and entropy (or disorderliness)—to model the visual appearance of paintings before and after surface varnishing. Based on a calculation of the gray-level co-occurrence matrix (GLCM), energy and entropy demonstrated that they are sensitive to the effect of varnishing—especially as entropy shows the increase in a painting’s contrast by varnishing. The statistic calculation of GLCMs is a common approach, and has been used to extract texture features for the classification of traditional Chinese paintings based on the painters [18].

Wavelet-based analysis, where multiscale and multiorientation image decomposition is performed, has been applied to a collection of high-resolution digital scans of drawings or paintings to describe the painting characteristics [19]. Cetinic and Grgic [20] introduced various classifiers into automated painter recognition based on the texture features extracted by GLCM and discrete wavelet transforms (DWTs). Undoubtedly, the statistical properties of wavelet coefficients have demonstrated that they are successful in the stylistic analysis of paintings [21,22]. Referring to related research [23,24], the process of texture feature extraction first conducts image decomposition using DWT to obtain sub-band images that are multiscale and multiorientation. Secondly, GLCMs are generated from sub-band images, and finally the texture descriptors—such as energy, entropy, contrast, correlation, and others—are calculated from GLCMs.

## 4. Research Material

Based on the investigations of Lee [25] and Kang [26] on door god paintings in Taiwan, some of their investigated temples and other temples in Taiwan were selected as the study sites, and smartphones (model ASUS\_Z01HDA or Sony\_J9110) were used to acquire the auspicious pattern images. In total, 52 temples were visited and 453 auspicious pattern images were acquired (see the zip folder in the Supplementary Materials). Table 1 lists the number of acquired auspicious pattern images, which involve fish scales, lock chain, turtle back, and “回” patterns by the 31 artists. Among the four auspicious patterns, lock chain and fish scales are the most common patterns adopted in door god paintings, and so they have a much greater number of acquired images than the others. Moreover, the stronger the artist’s reputation, the greater the number of auspicious pattern images acquired.

In addition to the 453 auspicious pattern images of the surveyed artists, we also acquired 12 auspicious pattern images of unknown artists from temples in Kinmen for the study of painting style recognition. In order to avoid blurred imaging of the door god paintings, support of the smartphones by a tripod instrument instead of a handheld approach was necessary. Considering the different sizes of the door god paintings, the appropriate instrument height and object distance had to be determined by trial and error during the imaging process. Most of the trial and error results in the field indicate that the appropriate instrument height and object distance are ~1.5 m and 1–2 m, respectively. Because the door god paintings are located in semi-outdoor environments, sometimes the imaging process suffers as a result of the structures of the temples, the azimuths of sunshine, or the weather, leading to an inappropriate illuminated image. An inappropriate illumination will result in an image with low quality in contrast and brightness. The f-stop numbers (apertures) of the ASUS\_Z01HDA and Sony\_J9110 are  $f/1.7$  and  $f/1.6$  ( $f$ : lens focal length), respectively. Thus, an automated adjustment of lens focal length was adopted in order to acquire the auspicious pattern images with appropriate contrast and brightness.

**Table 1.** Numbers of auspicious pattern images, with their corresponding artists.

Artist	Auspicious Pattern				Total
	Fish Scales	Lock Chain	Turtle Back	“回”	
Lee, H.-C. (李漢卿)	6	-	-	-	6
Wang, H.-H. & Hung, C.-S. (王錫河 & 洪純宋)	5	-	-	-	5
Lin, C.-H. (林中信)	8	3	-	-	11
Chang, C.-K. (張劍光)	5	2	-	-	7
Yu, C.-H. (游景賢)	3	3	-	-	6
Liu, C.-C. (劉家正)	14	16	-	-	30
Pan, Y.-H. (潘岳雄)	12	3	-	-	15
Mei, Y.-S. (梅月杉)	4	2	-	-	6
Hsu, M.-Y. (許明義)	6	5	-	-	11
Tsai, M.-H. (蔡孟學)	4	1	-	-	5
Tsai, H.-Y. & Tsai, W.-C. (蔡海永 & 蔡文傑)	3	4	-	-	7
Yen, W.-P. (顏文伯)	4	2	-	-	6
Su, T.-F. (蘇天福)	8	10	-	-	18
Chung, Y.-S. (鐘銀樹)	4	1	-	-	5
Cho, F.-T. (卓福田)	2	-	-	-	2
Chen, C.-S. (陳秋山)	5	1	-	-	6
Wang, H.-H. (王錫河)	6	5	1	-	12
Chu, Y.-L. (朱銀)	5	4	1	-	10
Lu, S.-W. (呂石旺)	4	3	2	-	9
Kuo, F.-T. (郭佛賜)	12	7	4	-	23
Chen, Y.-C. (陳陽春)	11	11	4	-	26
Pan, L.-S. (潘麗水)	67	35	2	3	107
Chuang, W.-N. (莊武男)	5	11	1	-	17
Wang, J.-Y. (王瑞瑜)	2	4	-	2	8
Dragon (鹿港小龍)	1	4	-	1	6
Chang, H.-L. (張火爐)	2	3	-	3	8
Huang, M.-S. (黃名樹)	1	2	-	1	4
Tsai, L.-C. (蔡龍進)	15	5	-	-	20
Hsu, L.-C. (許連成)	8	-	1	5	14
Chen, S.-Y. (陳壽彝)	13	20	6	4	43
Total	245	167	22	19	453

## 5. Methodology

### 5.1. Texture Feature Extraction

Figure 3 shows a diagram of the texture feature extraction proposed in this paper. Before performing the 2-level 2-dimensional (2D) DWT, each RGB-wise auspicious pattern image is transformed into a grayscale one. In other words, the color information is not taken into consideration for our DWT operation. After the 2-level 2D DWT, an approximation image and three detailed images in horizontal ( $0^\circ$ ), vertical ( $90^\circ$ ), and diagonal ( $45^\circ$  or  $135^\circ$ ) orientations are derived. Based on the three detailed images, the GLCMs in the 4 orientations are calculated. Hereafter, each GLCM calculates the co-occurrence features, consisting of angular second moment (ASM), entropy (ENT), contrast (CON), homogeneity (HOM), dissimilarity (DIS), correlation (COR), and cluster tendency (CLU). In this research, the co-occurrence features in a certain orientation can be expressed as a  $1 \times 7$  vector, and so the co-occurrence features in the 4 orientations are finally integrated into a  $4 \times 7$  matrix.

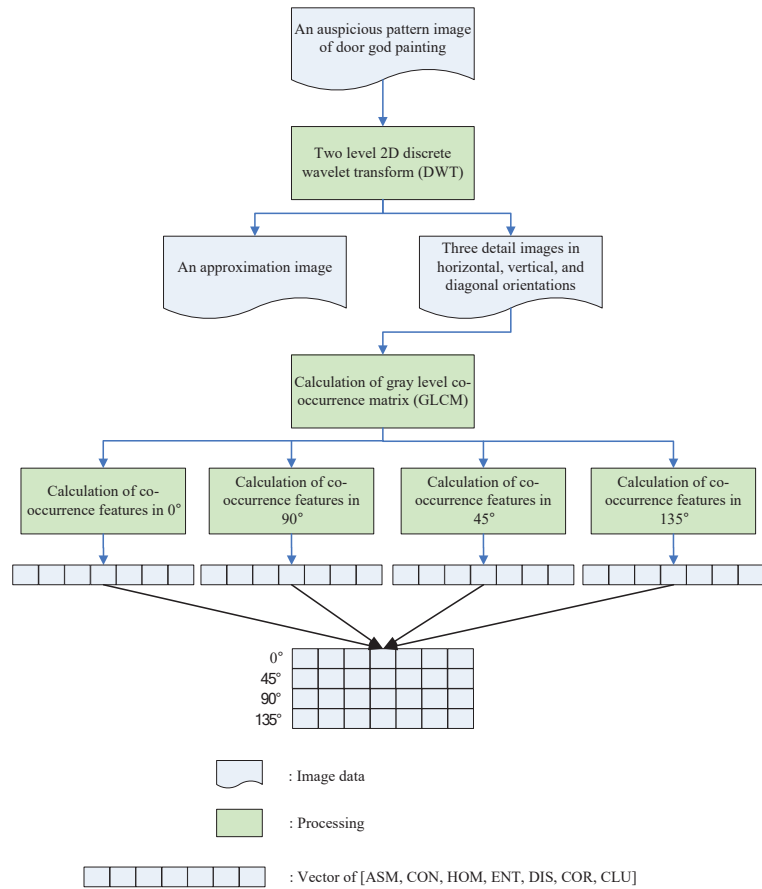


**Figure 3.** Scheme of texture feature extraction from auspicious pattern imagery.

### 5.1.1.1. Two-Level 2D DWT

Wavelet transform (WT) is a linear transform developed from Fourier transform, where the basic functions are sinusoids, but the wavelet functions vary with frequency and limit duration, thus offering better resolutions along the frequency scale [27,28]. In the beginning, the development of WT was for signal processing, but not for image processing, until Daubechies and Mallat provided the discretization of WT and established the connection between WT and the multiresolution theory, respectively. This paper regards an auspicious pattern image as the change in a discrete signal along a 2D scale. A 2D DWT can decompose the auspicious pattern image into many scales, which range from the roughest scale to the finest [29–31]. Through a decomposition of 2D DWT, which is implemented by consecutive low-pass (L) and high-pass (H) filtering through one-dimensional convolution, the auspicious pattern image  $I(m, n)$  can be divided into sub-band images, including an approximation image (LL) and three detailed images in horizontal (HL), vertical (LH), and diagonal (HH) orientations [28]. The parameters of  $m$  and  $n$  denote the number of pixels of the image in the row and column directions, respectively.

The approximation image (LL) can be further decomposed in the next level to obtain the images of LL, HL, LH, and HH, with the sizes of  $(m/2, n/2)$ . For the decomposition of each level, the alternative convolutions of the approximation image and the low-pass or high-pass filters in the column or row directions are operated using a downsampling function by 2. Thus, the 2D DWT finally produces the pyramid representations of the

sub-band images, which occupy the same amount of storage as the original auspicious pattern image [32].

Several studies in the literature indicate that the 2-level 2D DWT (i.e., 2D DWT in the second level) can robustly extract the details of the image texture features from the original images [23,24,28,33]. After decomposition in the second level, the 7 sub-band images, including 6 detailed images (HL1, LH1, HH1, HL2, LH2, and HH2) and one approximation image (LL2), are obtained. The indices of “1” and “2” signify the first and second levels, respectively. Among the above 6 detailed images, HL2, LH2, and HH2 were chosen to calculate the paper’s GLCMs.

### 5.1.2. Calculation of the Gray-Level Co-Occurrence Matrix (GLCM)

A GLCM is a one-dimensional square matrix, where each element in the row ( $i$ ) and column ( $j$ ) directions records a relative occurrence frequency ( $M_{ij}$ ) of a pair of pixels with the same element value, separated by a certain pixel distance ( $D$ ) in one orientation ( $\theta$ ) [23,28]. Figure 4 shows an illustration of GLCM production at different orientations and pixel distances for a pixel of interest in the square matrix, along with an example of statistics for  $M_{ij}$  at  $90^\circ$  (vertical direction) and one pixel distance. Figure 4b shows the GLCM of an example detailed image, where the image size is 7-by-7 (but not limited to square) and the number of gray levels is 8. In the GLCM, the element (3, 0) has a value of 1, because there is only one instance in the example detailed image where the vertically adjacent pixels (2, 1) and (1, 1) have gray-level values of 3 and 0, respectively.

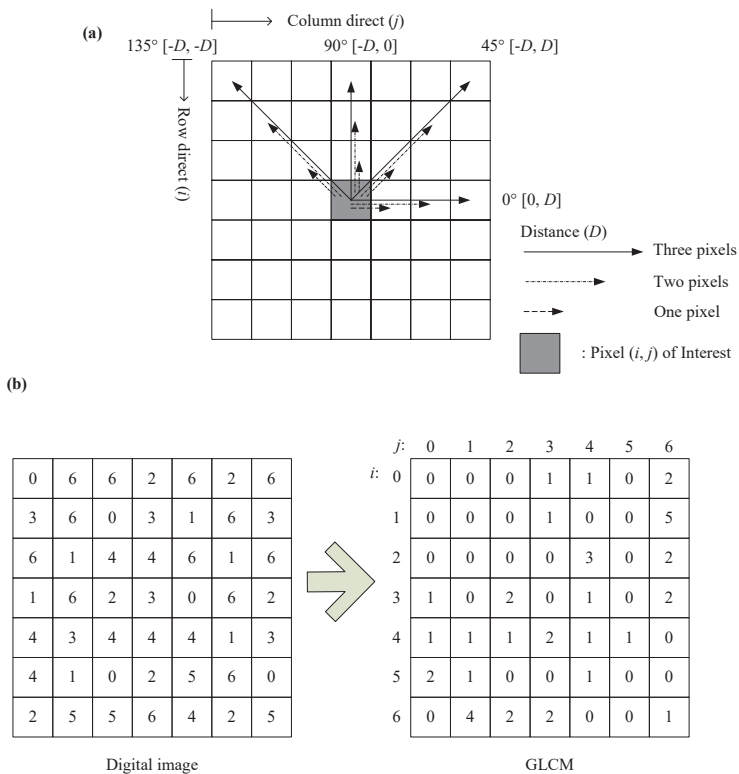


**Figure 4.** Illustration of GLCM production: (a) A pair of pixels with the same element value separated by the different pixel distances in 4 orientations. (b) Relative occurrence frequency recording of gray levels of digital images, using a GLCM with  $D = 1$  and  $\theta = 90^\circ$ .

Except for the four necessary orientations of 0°, 45°, 90°, and 135°, several studies have indicated that the different pixel distances ( $D$ ) have a great influence on the accuracy of GLCM-based texture description, and demonstrated that one pixel distance ( $D = 1$ ) can lead to better accuracy of the feature extractions [23,34]. This paper introduces an adjacent distance of bordering on pixels instead of striding over pixels into the calculation of the GLCMs.

### 5.1.3. Calculation of Co-Occurrence Features

The GLCMs obtained from the detailed images of HL2 and LH2 further calculate the co-occurrence features in 0° and 90°, respectively. Both of the GLCMs in 45° and 135° obtained from the detailed image of HH2 further calculate the co-occurrence features in the double-diagonal orientations. The 7 aforementioned co-occurrence features can be obtained using the following texture descriptors:

Angular Second Moment (ASM): The uniformity of distribution of the gray level in an auspicious pattern image can be represented thus [35]. The texture descriptor of ASM is expressed as follows:

$$\sum_{i=1}^n \sum_{j=1}^n P_{ij}^2 \tag{1}$$

The value of ASM ranges from  $1/n^2$  to 1. When the value is 1, it means a constant image. Here,  $P_{ij}$  is calculated as  $\frac{M_{ij}}{\sum_{i=1}^n \sum_{j=1}^n M_{ij}}$ .

Entropy (ENT): A statistical measure of randomness determines the textural interference in an auspicious pattern image [24,35]. The texture descriptor of ENT is obtained as follows:

$$-\sum_{i=1}^n \sum_{j=1}^n P_{ij} \cdot \log_{10} P_{ij} \tag{2}$$

The larger the ENT value, the higher the textural complexity of the auspicious pattern. Thus, there should be a highly negative correlation between ASM and ENT.

Contrast (CON): The local variations in an auspicious pattern image can be measured by this descriptor, which is calculated as follows:

$$\sum_{i=1}^n \sum_{j=1}^n (i - j)^2 \cdot P_{ij} \tag{3}$$

The higher the CON, the higher the image contrast will be. Hence, a CON of 0 means a constant image.

Homogeneity (HOM): HOM can also be called an inverse differential moment, which measures the similarity between the distributions of elements in a GLCM and those in the diagonal GLCM [24]. The textural descriptor is defined as follows:

$$\sum_{i=1}^n \sum_{j=1}^n \frac{P_{ij}}{1 + (i - j)^2} \tag{4}$$

The representation of HOM is contrary to that of CON—the higher the HOM, the lower the image contrast (or the more the image homogeneity) will be.

Dissimilarity (DIS): The degree of dissimilarity of the gray levels in an auspicious pattern image is now measured. DIS is very sensitive to the arrangement of gray-level values or tones in an imagery space, and is expressed as follows:

$$\sum_{i=1}^n \sum_{j=1}^n |i - j| P_{ij} \tag{5}$$

A higher DIS value means a greater dissimilarity of gray levels in the image.



Correlation (COR): The spatial dependencies between the image pixels can be defined [24] to indicate the textural directionalities of the auspicious patterns [36] by this textural descriptor, which is calculated as follows:

$$\frac{\sum_{i=1}^n \sum_{j=1}^n (i \cdot j) P_{ij} - \mu_x \mu_y}{\sigma_x \sigma_y} \tag{6}$$

In other words, COR is a correlation coefficient of GLCM. The higher the COR is, the greater is the spatial dependency of gray levels in a certain direction.

Cluster tendency (CLU): The degree of the textural clustering in an auspicious pattern image is measured and can be obtained as:

$$\sum_{i=1}^n \sum_{j=1}^n (i - \mu_x + j - \mu_y)^2 \cdot P_{ij} \tag{7}$$

It should be noted that a lower CLU value means higher textural clustering. Moreover, there is an interrelationship between CLU and COR. When the values of CLU and COR are large, there will be an indefinite textural directionality or a wide distribution of gray levels. Here,  $\mu_x$ ,  $\mu_y$ ,  $\sigma_x$ , and  $\sigma_y$  are calculated as follows:

$$\left\{ \begin{array}{l} \mu_x = \sum_{i=1}^n \sum_{j=1}^n i \cdot P_{ij} \\ \mu_y = \sum_{i=1}^n \sum_{j=1}^n j \cdot P_{ij} \\ \sigma_x = \sqrt{\sum_{i=1}^n \sum_{j=1}^n (i - \mu_x)^2 \cdot P_{ij}} \\ \sigma_y = \sqrt{\sum_{i=1}^n \sum_{j=1}^n (j - \mu_y)^2 \cdot P_{ij}} \end{array} \right. \tag{8}$$

### 5.2. Statistical Testing

This paper adopted a two-tailed *t*-test to test the similarity between any two auspicious patterns, the similarity of an auspicious pattern between any two surveyed artists, or the similarity of an auspicious pattern between the surveyed and unknown artists. The hypotheses of the *t*-tests are described as follows:

#### 5.2.1. Testing for Similarity between Any Two Auspicious Patterns

This paper aims to examine the similarities and differences between the auspicious patterns in door god paintings in Taiwan by applying hypothesis testing to the obtained co-occurrence features. As shown in to Figure 3, we calculated the co-occurrence feature values for each auspicious pattern image, which were recorded as a 4-by-7 matrix. Thus, the obtained co-occurrence feature values in a certain orientation can be arranged as an *n*-by-7 matrix, where *n* is the number of auspicious pattern images. In the fish scales pattern, for example, the data size of its obtained co-occurrence feature values in one orientation is 245-by-7. The arrangement of the 245-by-7 matrix also means that the hypothesis testing does not consider the different painting styles between the artists. For each orientation, any 2 of the 4 auspicious patterns performed a two-tailed *t*-test, where the null ( $H_0$ ) and alternative ( $H_1$ ) hypotheses were expressed as follows:

$$\left\{ \begin{array}{l} H_0 : D_i = D_j \\ H_1 : D_i \neq D_j \end{array} \right. \tag{9}$$

and  $D_i$  and  $D_j$  are the *n*-by-7 data matrices of the extracted co-occurrence features of auspicious patterns *i* and *j*, respectively. Thus, there is a total of  $C_2^4 = 6$  combinations for the two-tailed *t*-test.

### 5.2.2. Testing for Similarity of an Auspicious Pattern between Any Two Surveyed Artists

This paper demonstrates whether any two surveyed artists have a master and apprentice relationship by applying hypothesis testing to the extracted co-occurrence features of the auspicious patterns of their door god paintings. For some artists, unfortunately, there are extremely few images accessibly acquired, resulting in a non-normal distribution for the number of tested samples. In order to control the risk of accepting a false hypothesis, both  $\alpha$  and  $\beta$ —which are the probabilities of rejecting and accepting the null hypothesis, respectively—must be considered. For this paper, the values of  $\alpha/2 = 0.05$  and  $\beta = 0.1$  were introduced into the calculation of the minimum sample size ( $N$ ) from the National Institute of Standards and Technology [37]:

$$N \geq \left( t_{1-\frac{\alpha}{2}} + t_{1-\beta} \right)^2 \left( \frac{s}{\delta} \right)^2 \quad (10)$$

where  $s$  and  $\delta$  denote the standard deviations of the samples and the population, respectively. In this paper,  $s$  is equal to  $\delta$ , so Equation (10) can be rewritten as  $\left( t_{1-\frac{\alpha}{2}} + t_{1-\beta} \right)^2$ . Considering the degrees of freedom as 30, the values of  $t_{1-\frac{\alpha}{2}}$  and  $t_{1-\beta}$  are 1.6973 and 1.3104, respectively; thus, the  $N$  value approximates to 9.

According to the above estimation for the minimum size of samples, this paper considers the surveyed artists, from whom we can acquire more than 10 images (including 10 images) for some auspicious patterns, using a two-tailed  $t$ -test. Therefore, from Table 1, only the fish scales and lock chain patterns satisfy the above condition, and there is a total of  $C_2^{n_a}$  ( $n_a$ : number of considered artists) combinations for the two-tailed  $t$ -test. In this paper, the  $n_a$  values are 7 and 6 for the fish scales and lock chain patterns, respectively. The co-occurrence features of the fish scales and lock chain patterns in an orientation are arranged as an  $m$ -by-7 data matrix, where  $m$  ( $m \geq 10$ ) is the number of acquired auspicious pattern images for a certain considered artist. Based on Equation (9), here  $D_i$  and  $D_j$  represent the  $m$ -by-7 data matrices of artists  $i$  and  $j$ , respectively.

### 5.2.3. Testing for Similarity of an Auspicious Pattern between Surveyed and Unknown Artists

The two-tailed  $t$ -test was applied to the extracted co-occurrence features of the fish scales or lock chain patterns of the unknown artists' door god paintings to determine whether there was a similar painting style between the surveyed and unknown artists. Among the acquired 12 auspicious pattern images of the unknown artist(s), the number of fish scales and lock chain pattern images was half each. Hence, the sample of just 6 images is able to control the risk of accepting a false hypothesis by the two-tailed  $t$ -test, with  $\alpha/2 = 0.05$ ,  $\beta = 0.05$ , and  $\delta = 1.5s$ . In the two-tailed  $t$ -test, an  $l$ -by-7 ( $l = 6$  in this paper) data matrix was built for recording the co-occurrence features of the fish scales or lock chain patterns in an orientation, where  $l$  is the number of acquired fish scales or lock chain pattern images for the unknown artist(s). Based on Equation (9), here  $D_i$  and  $D_j$  represent the  $m$ -by-7 and  $l$ -by-7 data matrices of surveyed artist  $i$  and unknown artist  $j$ , respectively.

## 6. Results and Discussion

### 6.1. Texture Features of Surveyed Auspicious Patterns

The four auspicious patterns in Table 1, including fish scales, lock chain, turtle back, and “回”, were surveyed and calculated for their co-occurrence features (texture features), as shown in Figure 5. Here, each co-occurrence feature plotted in Figure 5 is a mean of all of the calculated co-occurrence features of the acquired images for the auspicious pattern. Figure 5 shows that for any auspicious pattern the co-occurrence features in the double-diagonal orientations are approximately equal. This result demonstrates that all four of the auspicious patterns have texture symmetry in the double-diagonal orientations. The co-occurrence features of the four auspicious patterns are discussed as follows:

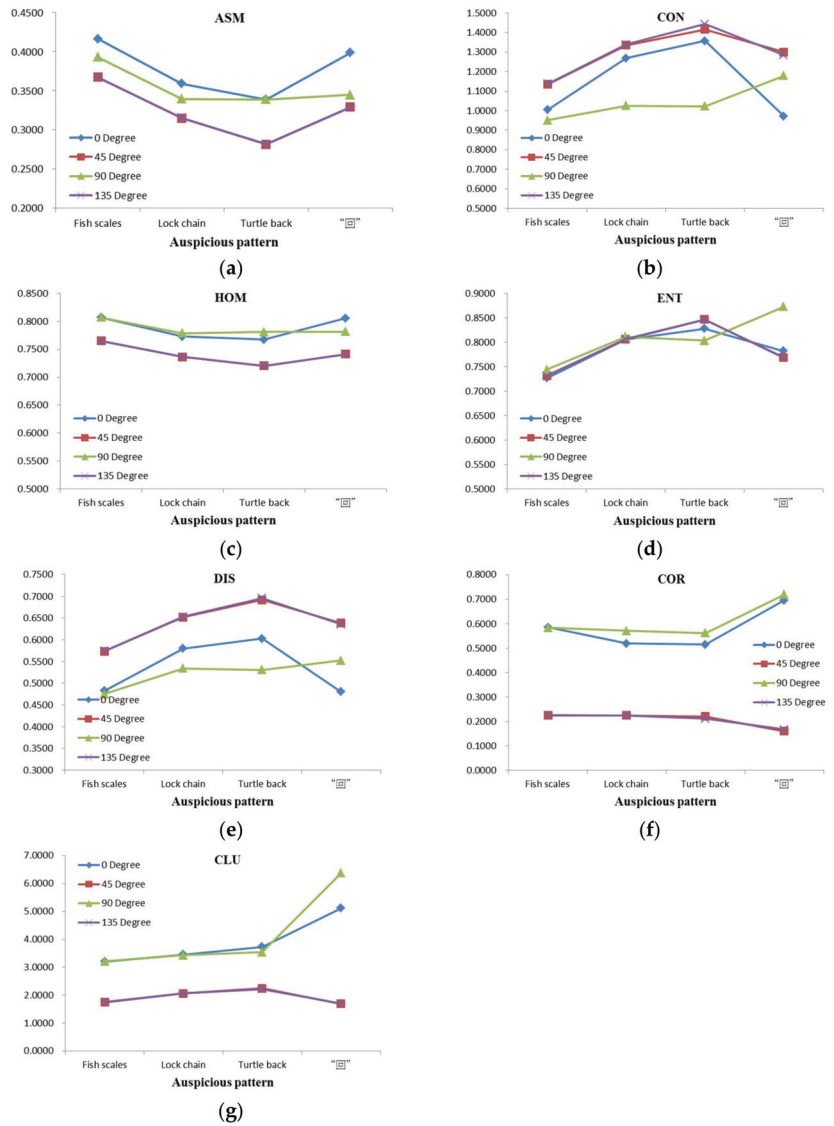


**Figure 5.** Texture features of auspicious pattern examples in different orientations: (a) ASM. (b) CON. (c) HOM. (d) ENT. (e) DIS. (f) COR. (g) CLU.

In ASM the fish scales and turtle back patterns obtained the highest and lowest co-occurrence feature values, respectively. This result demonstrates that the fish scales pattern images are more constant than the others. For any auspicious pattern, the distribution of gray levels in the horizontal orientation is more uniform than those in the other orientations.

In CON, Figure 5b illustrates that the imagery contrasts of the auspicious patterns in the double-diagonal orientations are higher than those in the horizontal or vertical orientations. Except for the “回” pattern, the co-occurrence feature values in the vertical orientation are lower than those in the other orientations, where the co-occurrence feature values of the turtle back pattern are the highest. Thus, compared with the other patterns, the turtle back pattern usually has the highest imagery contrast. Figure 5b,c illustrate that the concave shapes of the obtained curves in HOM run contrary to the convex ones in CON.

Due to the slightly higher HOM values of the fish scales pattern, the textural descriptor of HOM demonstrates that the fish scales pattern has a lower contrast than the other patterns. The lower imagery contrast also means a greater imagery constant.

In addition to CON and HOM, the shapes of the obtained curves between ENT and ASM are also contrary. The ENT value of the “回” pattern in the vertical orientation is clearly much larger than that of the other patterns in the different orientations. This result shows that, compared with the other patterns, the “回” pattern in the vertical orientation has the highest textural complexity. Excluding the vertical orientation, the turtle back pattern has the highest textural complexity. However, there are similar shapes of the obtained curves between CLU and COR. In COR, the values in the horizontal and vertical orientations are far higher than those in the double-diagonal orientations. Among the auspicious patterns, the “回” pattern has an extreme difference in the COR values between the horizontal or vertical orientations and the double-diagonal ones. Thus, this paper demonstrates that greater spatial dependency of gray levels in the auspicious pattern images means higher CLU values, i.e., higher textural clustering.

In DIS, Figure 5e shows that the auspicious pattern images have higher dissimilarity of the gray levels in the double-diagonal orientations than in the horizontal or vertical orientations. It is noticeable that the shapes of the obtained curves between CON and DIS are similar (see Figure 5b,e). Hence, textural analysis demonstrates that there is an interrelationship between CON and DIS for the four auspicious patterns. A higher contrast of an auspicious pattern image means a higher dissimilarity of the gray levels in the image.

### 6.2. Similarity between Any Two Auspicious Patterns

A two-tailed *t*-test was applied to the calculated co-occurrence features to see the similarity between any two of the four auspicious patterns, and the results of the six combinations are shown in Table 2. The results confirm that there is the most textural difference between the fish scales and lock chain patterns, and the most textural similarity between the lock chain and turtle back patterns. This result indicates that it is easy to distinguish the fish scales patterns from lock chain patterns, but very difficult to distinguish the lock chain patterns from turtle back patterns. In spite of that, the textures of the fish scales and lock chain patterns were sometimes confused when considering some of the textural descriptors in certain orientations, e.g., CON in the vertical orientation.

Table 2 also indicates that the fish scales and turtle back patterns in the horizontal and vertical orientations almost have a significant texture similarity. However, applying the textural descriptors of ASM, HOM, ENT, and DIS to the texture features in the double-diagonal orientations confirms that there is a significant difference between the fish scales and turtle back patterns. In other words, the four above textural descriptors in the double-diagonal orientations are useful in recognition of the fish scales and turtle back patterns. Finally, most of the textural descriptors in any orientation are inadequate to distinguish the “回” pattern from the others unless one considers the textural descriptor of COR.

**Table 2.** Two-tailed *t*-test results for similarity between any two auspicious patterns.

Tested Patterns	Orientation	Co-Occurrence Feature						
		ASM	CON	HOM	ENT	DIS	COR	CLU
Fish scales vs. Lock chain	0°	H <sub>1</sub>	H <sub>1</sub>	H <sub>1</sub>	H <sub>1</sub>	H <sub>1</sub>	H <sub>1</sub>	H <sub>0</sub>
	45°	H <sub>1</sub>	H <sub>1</sub>	H <sub>1</sub>	H <sub>1</sub>	H <sub>1</sub>	H <sub>0</sub>	H <sub>1</sub>
	90°	H <sub>1</sub>	H <sub>0</sub>	H <sub>1</sub>	H <sub>1</sub>	H <sub>0</sub>	H <sub>0</sub>	H <sub>0</sub>
	135°	H <sub>1</sub>	H <sub>1</sub>	H <sub>1</sub>	H <sub>1</sub>	H <sub>1</sub>	H <sub>0</sub>	H <sub>1</sub>
Fish scales vs. Turtle back	0°	H <sub>1</sub>	H <sub>0</sub>	H <sub>0</sub>	H <sub>0</sub>	H <sub>0</sub>	H <sub>0</sub>	H <sub>0</sub>
	45°	H <sub>1</sub>	H <sub>0</sub>	H <sub>1</sub>	H <sub>1</sub>	H <sub>1</sub>	H <sub>0</sub>	H <sub>0</sub>
	90°	H <sub>0</sub>	H <sub>0</sub>	H <sub>0</sub>	H <sub>0</sub>	H <sub>0</sub>	H <sub>0</sub>	H <sub>0</sub>
	135°	H <sub>1</sub>	H <sub>0</sub>	H <sub>1</sub>	H <sub>1</sub>	H <sub>1</sub>	H <sub>0</sub>	H <sub>0</sub>
Fish scales vs. “回”	0°	H <sub>0</sub>	H <sub>0</sub>	H <sub>0</sub>	H <sub>0</sub>	H <sub>0</sub>	H <sub>1</sub>	H <sub>1</sub>
	45°	H <sub>0</sub>	H <sub>0</sub>	H <sub>0</sub>	H <sub>0</sub>	H <sub>0</sub>	H <sub>1</sub>	H <sub>0</sub>
	90°	H <sub>0</sub>	H <sub>0</sub>	H <sub>0</sub>	H <sub>0</sub>	H <sub>0</sub>	H <sub>1</sub>	H <sub>1</sub>
	135°	H <sub>0</sub>	H <sub>0</sub>	H <sub>0</sub>	H <sub>0</sub>	H <sub>0</sub>	H <sub>1</sub>	H <sub>0</sub>
Lock chain vs. Turtle back	0°	H <sub>0</sub>	H <sub>0</sub>	H <sub>0</sub>	H <sub>0</sub>	H <sub>0</sub>	H <sub>0</sub>	H <sub>0</sub>
	45°	H <sub>0</sub>	H <sub>0</sub>	H <sub>0</sub>	H <sub>0</sub>	H <sub>0</sub>	H <sub>0</sub>	H <sub>0</sub>
	90°	H <sub>0</sub>	H <sub>0</sub>	H <sub>0</sub>	H <sub>0</sub>	H <sub>0</sub>	H <sub>0</sub>	H <sub>0</sub>
	135°	H <sub>0</sub>	H <sub>0</sub>	H <sub>0</sub>	H <sub>0</sub>	H <sub>0</sub>	H <sub>0</sub>	H <sub>0</sub>
Lock chain vs. “回”	0°	H <sub>0</sub>	H <sub>0</sub>	H <sub>0</sub>	H <sub>0</sub>	H <sub>0</sub>	H <sub>1</sub>	H <sub>0</sub>
	45°	H <sub>0</sub>	H <sub>0</sub>	H <sub>0</sub>	H <sub>0</sub>	H <sub>0</sub>	H <sub>1</sub>	H <sub>0</sub>
	90°	H <sub>0</sub>	H <sub>0</sub>	H <sub>0</sub>	H <sub>0</sub>	H <sub>0</sub>	H <sub>1</sub>	H <sub>1</sub>
	135°	H <sub>0</sub>	H <sub>0</sub>	H <sub>0</sub>	H <sub>0</sub>	H <sub>0</sub>	H <sub>1</sub>	H <sub>0</sub>
Turtle back vs. “回”	0°	H <sub>0</sub>	H <sub>0</sub>	H <sub>0</sub>	H <sub>0</sub>	H <sub>0</sub>	H <sub>1</sub>	H <sub>0</sub>
	45°	H <sub>0</sub>	H <sub>0</sub>	H <sub>0</sub>	H <sub>0</sub>	H <sub>0</sub>	H <sub>1</sub>	H <sub>0</sub>
	90°	H <sub>0</sub>	H <sub>0</sub>	H <sub>0</sub>	H <sub>0</sub>	H <sub>0</sub>	H <sub>1</sub>	H <sub>1</sub>
	135°	H <sub>0</sub>	H <sub>0</sub>	H <sub>0</sub>	H <sub>0</sub>	H <sub>0</sub>	H <sub>0</sub>	H <sub>0</sub>

H<sub>0</sub>: supports the hypothesis that the texture features between the two auspicious patterns are similar; H<sub>1</sub>: supports the hypothesis that the texture features between the two auspicious patterns are dissimilar. Confidence level  $\alpha$ : 0.05.

### 6.3. Similarity of an Auspicious Pattern between Any Two Surveyed Artists

Figure 6 shows a diagram of master and apprentice relationships for the surveyed artists, who acquired more than 10 auspicious pattern images for the fish scales or turtle back patterns. Some of the artists shown in Figure 6 were not surveyed for this paper, but they are/were the teachers of the surveyed artists, and are necessary to display in the diagram of the master and apprentice relationships. Figure 6 illustrates that the surveyed artists can be approximately separated into two family genres, i.e., Y.-F. Chen and C.-Y. Pan. Indeed, C.-C. Liu not only apprenticed to his uncle (belonging to the family genre of Pan), but also learned from S.-Y. Chen (belonging to the family genre of Chen) and the other artists by observing their treatment skills with the door god paintings. Thus, the theory is that the painting style of C.-C. Liu should involve those of the two family genres. On the other hand, F.-T. Kuo (Chinese transliteration: 郭佛賜) and Y.-C. Chen (Chinese transliteration: 陳陽春) do not have any master and apprentice relationships with the other surveyed artists, including with one another. Therefore, the theory is that there should be a great difference in the painting styles of F.-T. Ku or Y.-C. Chen from the others, including one another.

The two-tailed *t*-test results for the similarities between any two surveyed artists' fish scales and lock chain patterns in the four orientations are recorded in the symmetric matrices as shown in Tables 3 and 4, respectively. Excluding the diagonal elements of the matrices, each element uses a vector to record the two-tailed *t*-test result. In a vector of [], the elements express the acceptances of the hypotheses based on the co-occurrence features of ASM, CON, HOM, ENT, DIS, COR, and CLU in sequence, and the symbols of “0” and “1” indicate confirmation of the H<sub>0</sub> and H<sub>1</sub> hypotheses, respectively.

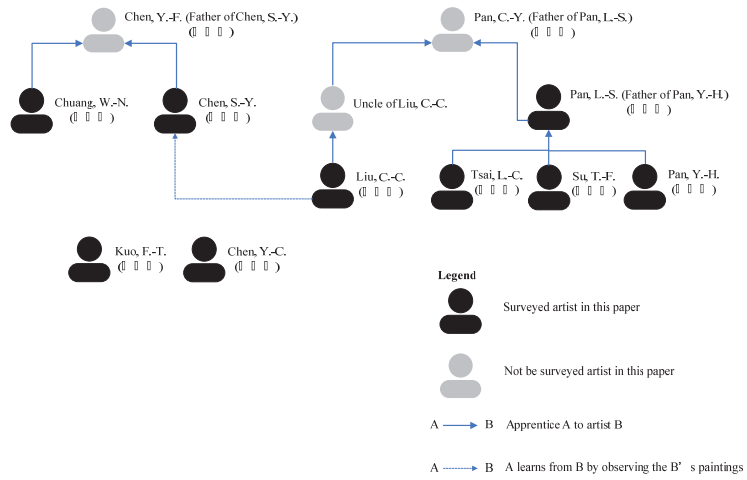


**Figure 6.** A diagram of master and apprentice relationships between the surveyed artists (black coloring) and their mentors (gray coloring).

**Table 3.** Two-tailed *t*-test results for similarity between any two surveyed artists’ fish scales patterns in the orientations.

Orientation	Artist	Liu, C.-C.	Kuo, F.-T.	Chen, Y.-C.	Pan, L.-S.	Tsai, L.-C.	Chen, S.-Y.	Pan, Y.-H.
0°	Liu, C.-C.		[1,1,1,1,1,0,1]	[1,0,0,1,0,1,0]	[1,1,1,1,1,1,0]	[1,1,1,1,1,0,1]	[0,0,0,0,0,1,0]	[0,1,1,0,1,1,0]
	Kuo, F.-T.			[1,1,1,1,1,1,0]	[1,1,1,1,1,1,1]	[0,0,0,0,0,1,0]	[1,0,1,1,1,1,0]	[1,1,1,1,1,1,0]
	Chen, Y.-C.				[1,1,1,1,1,1,1]	[1,1,1,1,1,0,1]	[0,0,0,0,0,0,0]	[1,1,1,1,1,1,0]
	Pan, L.-S.					[1,1,1,1,1,1,1]	[1,1,1,1,1,1,0]	[1,1,0,1,0,1,1]
	Tsai, L.-C.						[1,0,1,1,0,0,0]	[1,1,1,1,1,1,1]
	Chen, S.-Y.							[0,1,1,0,1,1,0]
45°	Liu, C.-C.		[1,0,1,1,1,0,1]	[0,0,0,0,0,0,0]	[1,1,1,1,1,1,1]	[1,0,1,1,0,1,1]	[0,0,0,0,0,1,0]	[0,1,1,1,1,1,1]
	Kuo, F.-T.			[1,1,1,1,1,0,1]	[1,1,1,1,1,1,1]	[0,0,0,0,0,0,0]	[1,0,1,1,1,0,0]	[1,1,1,1,1,1,1]
	Chen, Y.-C.				[1,1,1,1,1,1,1]	[1,1,1,1,1,0,1]	[0,0,0,0,0,0,0]	[1,1,1,1,1,1,1]
	Pan, L.-S.					[1,1,1,1,1,0,1]	[1,1,1,1,1,0,1]	[1,0,0,1,0,1,1]
	Tsai, L.-C.						[1,0,0,1,0,0,0]	[1,1,1,1,1,1,1]
	Chen, S.-Y.							[1,1,1,1,1,1,1]
90°	Liu, C.-C.		[1,1,1,1,1,0,1]	[0,0,0,0,0,0,1]	[0,1,1,1,1,1,0]	[1,1,1,1,1,0,1]	[0,0,0,0,0,1,0]	[0,1,1,0,1,1,1]
	Kuo, F.-T.			[1,1,1,1,1,0,1]	[1,1,1,1,1,1,1]	[0,0,0,0,0,0,0]	[1,1,1,1,1,1,1]	[1,1,1,1,1,1,0]
	Chen, Y.-C.				[1,1,1,1,1,1,1]	[1,1,1,1,1,1,1]	[0,0,0,0,0,1,0]	[0,1,1,0,1,1,1]
	Pan, L.-S.					[1,1,1,1,1,1,1]	[0,1,1,0,1,1,0]	[1,1,0,1,0,1,1]
	Tsai, L.-C.						[1,1,1,1,1,0,1]	[1,1,1,1,1,1,0]
	Chen, S.-Y.							[0,1,1,0,1,1,1]
135°	Liu, C.-C.		[1,0,1,1,1,0,1]	[0,0,0,0,0,0,0]	[1,1,1,1,1,1,1]	[1,0,1,1,1,0,1]	[0,0,0,0,0,0,0]	[0,1,1,1,1,1,1]
	Kuo, F.-T.			[1,1,1,1,1,0,1]	[1,1,1,1,1,1,1]	[0,0,0,0,0,1,0]	[1,0,1,1,1,0,0]	[1,1,1,1,1,1,1]
	Chen, Y.-C.				[1,1,1,1,1,0,1]	[1,1,1,1,1,0,1]	[0,0,0,0,0,0,0]	[1,1,1,1,1,1,1]
	Pan, L.-S.					[1,1,1,1,1,1,1]	[1,1,1,1,1,0,1]	[1,0,0,1,0,1,1]
	Tsai, L.-C.						[1,0,1,1,0,0,0]	[1,1,1,1,1,1,1]
	Chen, S.-Y.							[1,1,1,1,1,1,1]

Confidence level  $\alpha$ : 0.1. The elements in a vector of [] indicate the hypotheses supported based on the co-occurrence features of ASM, CON, HOM, ENT, DIS, COR, and CLU, in sequence, and “0” and “1” denote  $H_0$  and  $H_1$ , respectively.

**Table 4.** Two-tailed *t*-test results for similarity between any two surveyed artists’ lock chain patterns in the orientations.

Orientation	Artist	Liu, C.-C.	Su, T.-F.	Chen, Y.-C.	Pan, L.-S.	Chuang, W.-N.	Chen, S.-Y.
0°	Liu, C.-C.		[1,0,1,1,1,0,1]	[0,0,0,0,1,0]	[1,1,1,1,1,0]	[1,1,1,1,0,1]	[0,0,0,0,1,0]
	Su, T.-F.			[1,1,1,1,1,0,1]	[1,1,1,1,1,1]	[0,0,0,0,0,0]	[1,0,1,1,1,0,1]
	Chen, Y.-C.				[1,1,1,1,1,0]	[1,1,1,1,0,1]	[0,0,0,0,0,0]
	Pan, L.-S.					[1,1,1,1,1,1]	[1,1,1,1,1,1]
	Chuang, W.-N.						[1,0,1,1,1,0,1]
	Chen, S.-Y.						
45°	Liu, C.-C.		[1,0,0,1,0,0,0]	[0,0,0,0,1,0]	[1,1,1,1,1,1]	[1,0,1,1,1,1]	[0,0,0,0,1,0]
	Su, T.-F.			[0,0,0,0,0,0]	[1,1,1,1,1,0,1]	[0,0,0,0,0,0]	[0,0,0,0,0,0]
	Chen, Y.-C.				[1,1,1,1,1,0,1]	[1,1,1,1,0,1]	[0,0,0,0,0,0]
	Pan, L.-S.					[1,1,1,1,1,0,1]	[1,1,1,1,1,0,1]
	Chuang, W.-N.						[1,0,0,0,0,0]
	Chen, S.-Y.						
90°	Liu, C.-C.		[1,1,1,1,1,0,1]	[0,0,0,0,1,0]	[1,1,1,1,1,0]	[1,1,1,1,0,1]	[1,0,0,1,0,1,1]
	Su, T.-F.			[1,1,1,1,1,1]	[1,1,1,1,1,1]	[0,0,0,0,0,0]	[0,1,1,0,1,0,0]
	Chen, Y.-C.				[1,1,1,1,1,0]	[1,1,1,1,1,1]	[0,0,0,0,1,1]
	Pan, L.-S.					[1,1,1,1,1,1]	[1,1,1,1,1,1]
	Chuang, W.-N.						[1,1,1,1,1,0]
	Chen, S.-Y.						
135°	Liu, C.-C.		[1,0,0,1,0,0,0]	[0,0,0,0,0,0]	[1,1,1,1,1,1]	[1,1,1,1,0,1]	[0,0,0,0,0,0]
	Su, T.-F.			[0,0,0,0,0,0]	[1,1,1,1,0,1]	[0,0,0,0,0,0]	[0,0,0,0,0,0]
	Chen, Y.-C.				[1,1,1,1,1,0,1]	[1,1,1,1,0,1]	[0,0,0,0,0,0]
	Pan, L.-S.					[1,1,1,1,0,1]	[1,1,1,1,0,1]
	Chuang, W.-N.						[1,0,0,0,0,0]
	Chen, S.-Y.						

Confidence level  $\alpha$ : 0.1. The elements in a vector of [] indicate the hypotheses supported based on the co-occurrence features of ASM, CON, HOM, ENT, DIS, COR, and CLU, in sequence, and “0” and “1” denote  $H_0$  and  $H_1$ , respectively.

Based on the diagram of the master and apprentice relationships in Figure 6, the two-tailed *t*-test results in Tables 3 and 4 are discussed. Most of the two-tailed *t*-test results successfully indicate the differences in the painting styles between the two main family genres of Chen and Pan. For instance, Table 3 demonstrates that the painting style of S.-Y. Chen is significantly different from those of L.-S. Pan, L.-C. Tsai, and Y.-H. Pan. Moreover, Table 4 shows that the painting style of L.-S. Pan is robustly different from those of S.-Y. Chen and W.-N. Chuang. However, there is an unreasonable result of recognizing the painting styles between the two main family genres of Chen and Pan as W.-N. Chuang versus T.-F. Su (see Table 4); W.-N. Chang and T.-F. Su belong to the family genres of Chen and Pan, respectively, but the two-tailed *t*-test result indicates that they have a robust similarity in painting style.

In the same family genre, this paper notes that the painting styles of the direct relatives of master and apprentice—such as L.-S. Pan versus L.-C. Tsai, T.-F. Su, or Y.-H. Pan—should be extremely similar. Unfortunately, Tables 3 and 4 cannot effectively demonstrate that a similar painting style exists among the above direct relatives of master and apprentice. For the collateral relatives of apprentices, Table 4 shows in the family genre of Chen that the painting styles of S.-Y. Chen and W.-N. Chuang have higher textural similarity in the double-diagonal orientations than in the horizontal and vertical orientations. The above characteristic also exists in the family genre of Pan, such as with C.-C. Liu versus T.-F. Su, but excludes L.-C. Tsai versus C.-C. Liu or Y.-H. Pan.

For the fish scales pattern, the co-occurrence features of ASM, HOM, ENT, and DIS have higher applicability to demonstrate the master and apprentice relationships in Figure 6 than the others. Based on the four above co-occurrence features, however, L.-C. Tsai and Y.-C. Chen, relative to the other surveyed artists in Table 3, seem to obtain fewer

reasonable demonstrations of master and apprentice relationships between them and the other artists. For the lock chain pattern, except for COR, the other co-occurrence features have approximate applicability to demonstrate the master and apprentice relationships. Furthermore, among the surveyed artists in Table 4, T.-F. Su shows the fewest reasonable demonstrations of master and apprentice relationships between him and the other artists. Consequently, in this paper the three artists L.-C. Tsai, Y.-C. Chen, and T.-F. Su were excluded from the following two-tailed *t*-test to observe the similarity of the fish scales and lock chain patterns between the surveyed and unknown artists. Moreover, ASM, HOM, ENT, and DIS were considered in the two-tailed *t*-test based on the fish scales pattern, and in addition to the four above co-occurrence features, CON and CLU were considered in the test based on the lock chain pattern.

6.4. Similarity of Auspicious Patterns between Surveyed and Unknown Artists

The two-tailed *t*-test was also used to assist in the painting style recognition of the unknown artists' door god paintings in Kinmen. If a robust similarity of an auspicious pattern between the surveyed and unknown artists is obtained, this suggests that the door god paintings of the unknown artist(s) could be restored by referring to the painting style of the surveyed artist. Tables 5 and 6 show the two-tailed *t*-test results for the similarities of the fish scales and lock chain patterns between the surveyed and unknown artists, respectively, and demonstrate that F.-T. Kuo and W.-N. Chuang have the most similar painting styles to the unknown artists' fish scales and lock chain patterns, respectively.

To further observe the painting styles of each surveyed artist, we performed an interquartile range calculation for the co-occurrence features extracted from the acquired auspicious pattern images. Therefore, one co-occurrence feature in the four orientations can calculate four medians via the interquartile range analysis, and this paper adopts a mean value of the four medians of the co-occurrence feature to describe the painting style. The charts shown as Figure 7 plot the means of the medians of the extracted co-occurrence feature values for the surveyed artists' fish scales and lock chain patterns, respectively. By discussing Figure 7, the painting styles of the fish scales and lock chain patterns of the unknown artists in Kinmen could be surmised.

**Table 5.** Two-tailed *t*-test results for similarity between surveyed and unknown artists' fish scales patterns in the orientations.

Orientation	Artist	Liu, C.-C.	Kuo, F.-T.	Pan, L.-S.	Chen, S.-Y.	Pan, Y.-H.
0°	Unknown	[1,1,1,1]	[0,0,0,0]	[1,1,1,1]	[1,1,1,1]	[1,1,1,1]
45°		[1,1,1,1]	[0,0,0,0]	[1,1,1,1]	[1,1,1,1]	[1,1,1,1]
90°		[1,1,1,1]	[1,0,0,0]	[1,1,1,1]	[1,1,1,1]	[1,1,1,1]
135°		[1,1,1,1]	[0,0,0,0]	[1,1,1,1]	[1,1,1,1]	[1,1,1,1]

Confidence level  $\alpha$ : 0.1. The elements in a vector of [] indicate the hypotheses supported based on the co-occurrence features of ASM, HOM, ENT, and DIS, in sequence, and "0" and "1" denote  $H_0$  and  $H_1$ , respectively.

**Table 6.** Two-tailed *t*-test results for similarity between surveyed and unknown artists' lock chain patterns in the orientations.

Orientation	Artist	Liu, C.-C.	Pan, L.-S.	Chuang, W.-N.	Chen, S.-Y.
0°	Unknown	[1,1,1,1,1,1]	[1,1,1,1,1,1]	[0,0,0,0,0,0]	[1,1,1,1,1,0]
45°		[1,1,1,1,1,1]	[1,1,1,1,1,1]	[0,1,1,0,1,0]	[1,1,1,1,1,1]
90°		[1,1,1,1,1,1]	[1,1,1,1,1,1]	[0,0,0,0,0,0]	[0,1,1,0,1,1]
135°		[1,1,1,1,1,1]	[1,1,1,1,1,1]	[0,1,0,0,1,0]	[1,1,1,1,1,1]

Confidence level  $\alpha$ : 0.1. The elements in a vector of [] indicate the hypotheses supported based on the co-occurrence features of ASM, CON, HOM, ENT, DIS, and CLU, in sequence, and "0" and "1" denote  $H_0$  and  $H_1$ , respectively.



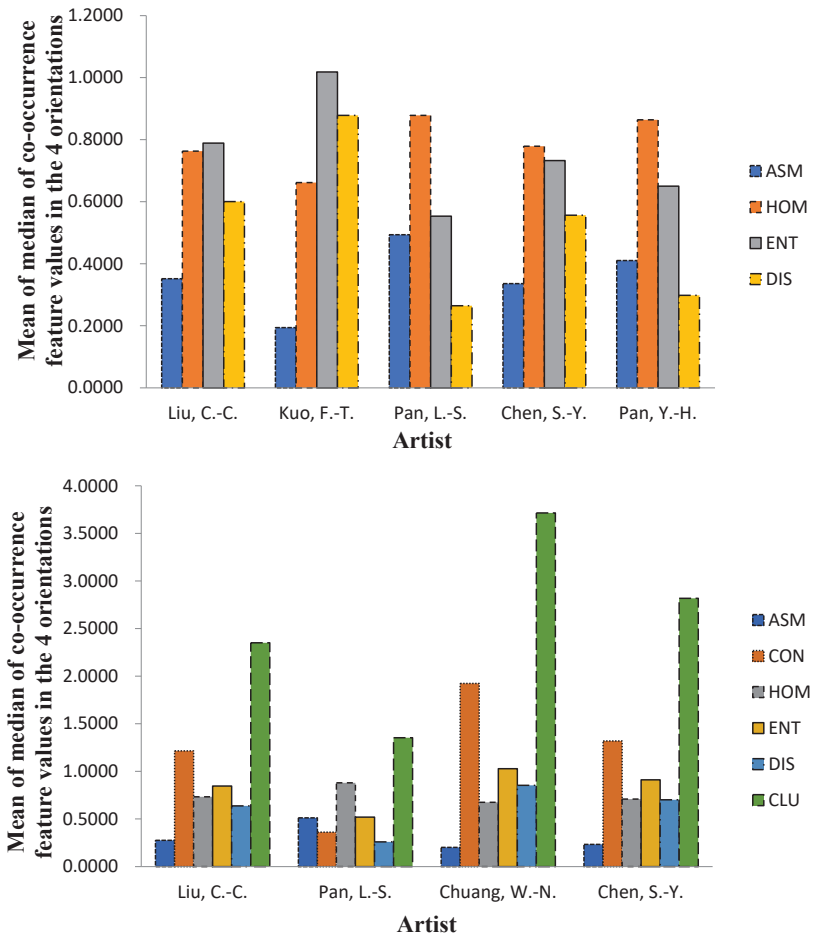


**Figure 7.** Means of medians of co-occurrence feature values in four orientations extracted from acquired auspicious pattern images of surveyed artists: fish scales pattern (**upper chart**); lock chain pattern (**lower chart**).

The upper chart of Figure 7 shows that F.-T. Kuo’s fish scales patterns have lower ASM and HOM and higher ENT and DIS than those of the other surveyed artists. The lower ASM and HOM mean that the acquired fish scales pattern images of F.-T. Kuo exhibit lower images constancy, leading to a higher image contrast. Based on the higher ENT and DIS, this paper finds that F.-T. Kuo’s fish scales patterns (or the unknown artists’ fish scales patterns in Kinmen) have higher textural complexity and higher hue gradient than those of the other surveyed artists.

In addition to ASM, HOM, ENT, and DIS, CON and CLU can help describe the painting style of W.-N. Chuang’s lock chain patterns (or the unknown artists’ lock chain patterns in Kinmen). The lower chart of Figure 7 shows that W.-N. Chuang’s lock chain patterns also have lower ASM and HOM and higher ENT and DIS than those of the other surveyed artists. Because the representation of HOM is contrary to that of CON, the lower chart illustrates that W.-N. Chuang’s lock chain patterns have higher CON than those of the other surveyed artists. The lower chart also shows that W.-N. Chuang’s lock chain patterns have the highest CLU among the surveyed artists. Thus, this result indirectly explains why

the unknown artists' lock chain patterns in Kinmen have higher textural clustering than the surveyed artists.

From the above discussion, this paper finds that there should be a similar door god painting style between F.-T. Kuo and W.-N. Chuang, because both of their auspicious patterns have the same characteristics of lower ASM and HOM and higher ENT and DIS. Thus, the door god paintings in Kinmen could be restored by referring to the painting styles of F.-T. Kuo or W.-N. Chuang.

## 7. Conclusions

Based on a two-level two-dimensional DWT and gray-level co-occurrence matrix calculation, this research proposes a texture feature extraction procedure and, coupled with a two-tailed *t*-test to analyze the door god painting styles, demonstrates the master and apprentice relationships between the surveyed artists so as to recognize unknown artists' painting styles. In total, 52 temples in Taiwan were visited to acquire 453 images for the auspicious patterns—including fish scales, lock chain, turtle back, and “回”—on the armor of door god warriors created by the surveyed artists. Additionally, 12 auspicious pattern images of unknown artists' door god paintings in Kinmen, which is an outlying island of Taiwan, were also acquired.

In the door god painting style analysis, the result indicates that all four auspicious patterns have texture symmetry in the double-diagonal orientations. The texture of the fish scales patterns is more constant (i.e., lower contrast) than that of the other patterns. For any auspicious pattern, the textural contrast in the double-diagonal orientations is higher than those in the horizontal or vertical orientations and, among the four auspicious patterns, the turtle back pattern usually has the highest textural contrast. Except in the vertical orientation, the turtle back pattern has the highest textural complexity. In the vertical orientation, the highest textural complexity exists in the “回” pattern. Generally, there is the most textural difference between the fish scales and lock chain patterns, and the most textural similarity between the lock chain and turtle back patterns. The analysis herein also successfully demonstrates the interrelationships between the seven co-occurrence features.

The results of our analysis effectively demonstrate the differences in the painting styles between the family genres of Chen and Pan. In a family genre, however, the results of our analysis fail to indicate that artists with a direct relationship of master and apprentice are expected to have a similar painting style. As for the collateral relatives of apprentices, our findings confirm that the artists' auspicious patterns seem to have higher textural similarity in the double-diagonal orientations than in the horizontal and vertical orientations. Through the two-tailed *t*-test, based on the fish scales pattern, we found that the co-occurrence features of ASM, HOM, ENT, and DIS are useful to demonstrate the apprentice relationships between the five artists of C.-C. Liu et al. Based on the lock chain pattern, except for COR, the other six co-occurrence features are useful to demonstrate the apprentice relationships between the four artists of C.-C. Liu et al.

Among the surveyed artists, F.-T. Kuo and W.-N. Chuang have the most similar painting styles to the unknown artists' fish scales and lock chain patterns, respectively. Thus, the door god paintings in Kinmen could be restored by referring to the painting styles of F.-T. Kuo or W.-N. Chuang. According to the analyzed painting styles of Kuo and Chuang, this paper surmises the painting styles of unknown artists in Kinmen, indicating that the unknown artists' fish scales patterns exhibit higher textural contrast, textural complexity, and hue gradient than those of the surveyed artists. Furthermore, the unknown artists' lock chain patterns also have higher textural contrast and clustering than those of the surveyed artists.

The hypothesis testing method can currently determine the useful co-occurrence features for recognizing the unknown artists' painting styles. In the future, the useful co-occurrence features will be input into neural networks in order to recognize the style of every single door god painting. We also believe that deep learning convolutional neural

networks based on the human visual system would be useful in recognizing the style of every single door god painting.

**Supplementary Materials:** The following supporting information can be downloaded at: <https://drive.google.com/file/d/1ax76s22qelbdEmsi5ILhCKe3HlrVhAoP/view?usp=sharing> (accessed on 1 December 2021).

**Author Contributions:** Conceptualization, T.-C.S. and T.-C.W.; methodology, T.-C.S.; software, T.-C.S. and M.-H.W.; validation, T.-C.S. and T.-C.W.; formal analysis, M.-H.W. and C.-W.W.; investigation, T.-C.S., M.-H.W. and C.-W.W.; data curation, M.-H.W.; writing—original draft preparation, T.-C.S.; writing—review and editing, T.-C.S. and T.-C.W.; project administration, T.-C.S.; funding acquisition, T.-C.S. All authors have read and agreed to the published version of the manuscript.

**Funding:** This research was funded by the Ministry of Science and Technology, Taiwan, grant number MOST 108-2410-H-507-013-MY2. The APC was funded by the Ministry of Science and Technology, Taiwan.

**Conflicts of Interest:** The authors declare no conflict of interest.

## References

1. Wu, S. *A Report of Restoration Project for Tsao-Ju Tsai's Door God Paintings in the Pei Tian Temple, Chiayi, Taiwan*; Tainan National University of the Arts: Tainan, Taiwan, 2016. (In Chinese)
2. Hung, H.-S. A study on architecture Du Tou painting of Li Jin Cyuan and his apprentices. *Collect. Pap. Arts Res.* **2013**, *20–21*, 21–47. (In Chinese)
3. Wang, X.-G. Analysis of the door-god painting pattern in Zhangzhou. *J. Jimei Univ.* **2011**, *14*, 16–22. (In Chinese)
4. Lee, Y.-Y. Appreciation of painted door gods and armours in temples. *Art Apprec.* **2009**, *5*, 15–20. (In Chinese)
5. Kawanaka, H.; Kosaka, S.; Iwahori, Y.; Sugiyama, S. Image reproduction based on texture image extension with traced drawing for heavy damaged mural painting. *Procedia Comput. Sci.* **2013**, *22*, 968–975. [[CrossRef](#)]
6. Ortiz, R.; Ortiz, P.; Colao, F.; Fantoni, R.; Gómez-Morón, M.A.; Vázquez, M.A. Laser spectroscopy and imaging applications for the study of cultural heritage murals. *Constr. Build. Mater.* **2015**, *98*, 35–43. [[CrossRef](#)]
7. Pan, N.; Hou, M.; Lv, S.; Hu, Y.; Zhao, X.; Ma, Q.; Li, S.; Shaker, A. Extracting faded mural patterns based on the combination of spatial-spectral feature of hyperspectral image. *J. Cult. Herit.* **2017**, *27*, 80–87. [[CrossRef](#)]
8. Lillesand, T.M.; Kiefer, R.W.; Chipman, J.W. *Remote Sensing and Image Interpretation*, 6th ed.; John Wiley & Sons, Inc.: Hoboken, NJ, USA, 2008.
9. Cai, Y.; Siegel, M. Texture Characterization of the Visual Appearance of Paintings. In Proceedings of the 19th IEEE Instrumentation and Measurement Technology Conference, Anchorage, AK, USA, 21–23 May 2002.
10. El-Rifai, I.; Mahgoub, H.; Ide-Ektessabi, A. Multi-spectral Imaging System (IWN) for the Digitization and Investigation of Cultural Heritage. In Proceedings of the Part I of EuroMed: Euro-Mediterranean Conference, Nicosia, Cyprus, 31 October–5 November 2016.
11. Ricca, M.; Alberghina, M.F.; Randazzo, L.; Schiavone, S.; Donato, A.; Albanese, M.P.; La Russa, M.F. A combined non-destructive and micro-destructive approach to solving the forensic problems in the field of cultural heritage: Two case studies. *Appl. Sci.* **2021**, *11*, 6951. [[CrossRef](#)]
12. Zujovic, J.; Gandy, L.; Friedman, S.; Pardo, B.; Pappas, T.N. Classifying Paintings by Artistic Genre: An Analysis of Features & Classifiers. In Proceedings of the IEEE International Workshop on Multimedia Signal Processing, Rio de Janeiro, Brazil, 5–7 October 2009.
13. Keshvari, S.; Chalechale, A. Classification of Iranian Paintings Using Texture Analysis. In Proceedings of the 2016 6th International Conference on Computer and Knowledge Engineering (ICCKE), Mashhad, Iran, 20–20 October 2016.
14. Lee, S.-G.; Cha, E.-Y. Style classification and visualization of art painting's genre using self-organizing maps. *Hum.-Cent. Comput. Inf. Sci.* **2016**, *6*, 7. [[CrossRef](#)]
15. Gultepe, E.; Conturo, T.E.; Makrehchi, M. Predicting and grouping digitized paintings by style using unsupervised feature learning. *J. Cult. Herit.* **2018**, *31*, 13–23. [[CrossRef](#)]
16. Narag, M.J.G.; Soriano, M.N. Identifying the Painter Using Texture Features and Machine Learning Algorithms. In Proceedings of the 3rd International Conference on Cryptography, Security and Privacy, Kuala Lumpur, Malaysia, 19–21 January 2019.
17. Crupi, V.; Fazio, B.; Fiocco, G.; Galli, G.; La Russa, M.F.; Licchelli, M.; Majolino, D.; Malagodi, M.; Ricca, M.; Ruffolo, S.A.; et al. Multi-analytical study of Roman frescoes from Villa dei Quintili (Rome, Italy). *J. Archaeol. Sci. Rep.* **2018**, *21*, 422–432. [[CrossRef](#)]
18. Lu, G.; Gao, Z.; Qin, D.; Zhao, X.; Liu, M. Content-based Identifying and Classifying Traditional Chinese Painting Images. In Proceedings of the 2008 Congress on Image and Signal Processing, Sanya, China, 27–30 May 2008.
19. Lyu, S.; Rockmore, D.; Farid, H. A digital technique for art authentication. *Proc. Natl. Acad. Sci. USA* **2004**, *101*, 17006–17010. [[CrossRef](#)] [[PubMed](#)]

20. Cetinic, E.; Grgic, S. Automated Painter Recognition based on Image Feature Extraction. In Proceedings of the International Symposium on Electronics in Marine (ELMAR-2013), Zadar, Croatia, 25–27 September 2013.
21. Johnson, C.R.; Hendriks, E.; Bereznoy, I.J.; Brevdo, E.; Hughes, S.M.; Daubechies, I.; Li, J.; Postma, E.; Wang, J.Z. Image Processing for artist identification. *IEEE Signal Process. Mag.* **2008**, *25*, 37–48. [[CrossRef](#)]
22. Jafarpour, S.; Polatkan, G.; Brevdo, E.; Hughes, S.; Brasoveanu, A.; Daubechies, I. Stylistic Analysis of Paintings Using Wavelets and Machine Learning. In Proceedings of the 2009 17th European Signal Processing Conference, Glasgow, UK, 24–28 August 2009.
23. Ji, Y.; Sun, L.; Li, Y.; Ye, D. Detection of bruised potatoes using hyperspectral imaging technique based on discrete wavelet transform. *Infrared Phys. Technol.* **2019**, *103*, 103054. [[CrossRef](#)]
24. Ghahfarrokhi, S.S.; Khodadadi, H. Human brain tumor diagnosis using the combination of the complexity measures and texture features through magnetic resonance image. *Biomed. Signal Process Control* **2020**, *61*, 102025. [[CrossRef](#)]
25. Lee, Y.-H. *Amazing Gods on Doors: Door God Paintings in Taiwan from 1821 to 1970*; Bureau of Cultural Heritage, Ministry of Culture (BOCH): Taichung, Taiwan, 2013. (In Chinese)
26. Kang, N.-H. *Catalogue of Door God Paintings in Taiwan*; Owl Publishing House Co., Ltd.: Taipei, Taiwan, 2012. (In Chinese)
27. Lu, W.; Gao, X.; Tao, D.; Li, X. A wavelet-based image quality assessment method. *Int. J. Wavelets Multiresolution Inf. Process.* **2008**, *6*, 541–551. [[CrossRef](#)]
28. Yang, M.-D.; Su, T.-C.; Pan, N.-F.; Liu, P. Feature extraction of sewer pipe defects using wavelet transform and co-occurrence matrix. *Int. J. Wavelets Multiresolution Inf. Process.* **2011**, *9*, 211–225. [[CrossRef](#)]
29. Beura, S.; Majhi, B.; Dash, R. Mammogram classification using two dimensional discrete wavelet transform and gray-level co-occurrence matrix for detection of breast cancer. *Neurocomputing* **2015**, *154*, 1–14. [[CrossRef](#)]
30. Sudarshan, V.K.; Ng, E.Y.K.; Acharya, U.R.; Chou, S.M.; Tan, R.S.; Ghista, D.N. Computer-aided diagnosis of Myocardial Infarction using ultrasound images with DWT, GLCM and HOS methods: A comparative study. *Comput. Biol. Med.* **2015**, *62*, 86–93.
31. Yang, D.-W.; Wu, H. Three-dimensional temperature uniformity assessment based on gray level co-occurrence matrix. *Appl. Therm. Eng.* **2016**, *108*, 689–696. [[CrossRef](#)]
32. Canty, M.J. *Image Analysis, Classification, and Change Detection in Remote Sensing with Algorithms for ENVI/IDL*, 2nd ed.; CRC Press, Taylor & Francis Group: Boca Raton, FL, USA, 2010.
33. Yang, M.-D.; Su, T.-C. Automated diagnosis of sewer pipe defects based on machine learning approaches. *Expert Syst. Appl.* **2008**, *35*, 1327–1337. [[CrossRef](#)]
34. Arebey, M.; Hannan, M.A.; Begum, R.A.; Basri, H. Solid waste bin level detection using gray level co-occurrence matrix feature extraction approach. *J. Environ. Manag.* **2012**, *104*, 9–18. [[CrossRef](#)] [[PubMed](#)]
35. O’Byrne, M.; Ghosh, B.; Pakrashi, V.; Schoefs, F. Texture Analysis based Detection and Classification of Surface Features on Ageing Infrastructure Elements. In Proceedings of the Bridge and Concrete Research in Ireland Conference, Dublin, Ireland, 6–7 September 2012.
36. Fu, K.-L.; Chen, C.-T.; Chen, S.-C. Texture analysis on SPOT images for detecting illegal use of regulated slopeland. *J. Soil Water Conserv.* **2004**, *36*, 201–214. (In Chinese)
37. National Institute of Standards and Technology (NIST). SEMATECH e-Handbook of Statistical Methods, Department of Commerce, US. Available online: <https://itl.nist.gov/div898/handbook/prc/section2/prc222.htm> (accessed on 16 March 2021).



Article

# An Improved Shoulder Line Extraction Method Fusing Edge Detection and Regional Growing Algorithm

Haoyang Jiao <sup>1,2,3</sup>, Fayuan Li <sup>1,2,3,\*</sup>, Hong Wei <sup>1,2,3</sup> and Wei Liu <sup>1,2,3</sup><sup>1</sup> School of Geography, Nanjing Normal University, Nanjing 210023, China<sup>2</sup> Key Laboratory of Virtual Geographic Environment, Nanjing Normal University, Ministry of Education, Nanjing 210023, China<sup>3</sup> Jiangsu Center for Collaborative Innovation in Geographical Information Resource Development and Application, Nanjing 210023, China

\* Correspondence: lifayuan@njnu.edu.cn

**Abstract:** Shoulder lines can best depict the morphological characteristics of the Loess Plateau. Moreover, a shoulder line depicts the external appearance of spatial differentiation of loess landforms and the internal mechanism of loess landform evolution. The efficient and accurate extraction of shoulder lines can help to deepen the re-understanding of the morphological structure and differentiation of loess landforms. However, the problem of shoulder line continuity in the extraction process has not been effectively solved. Therefore, based on high-resolution satellite images and digital elevation model (DEM) data, this study introduced the regional growing algorithm to further correct edge detection results, thereby achieving complementary advantages and improving the accuracy and continuity of shoulder line extraction. First, based on satellite images, the edge detection method was used to extract the original shoulder lines. Subsequently, by introducing the regional growing algorithm, the peaks and the outlet point extracted with the DEM were used as the growth points of the positive and negative (P-N) terrains to grow in four-neighborhood fields until they reached a P-N terrain boundary or a slope threshold. Finally, the P-N terrains extracted by the regional growing method were used to correct the edge detection results, and the “burr” was removed using a morphological image-processing method to obtain the shoulder lines. The experimental results showed that the method proposed in this paper can accurately and effectively complete the extraction of shoulder lines. Furthermore, the applicability of this method is better and opens new ideas for quantitative research on loess landforms.

**Keywords:** satellite images; shoulder line; edge detection; regional growing algorithm; positive and negative (P-N) terrain

**Citation:** Jiao, H.; Li, F.; Wei, H.; Liu, W. An Improved Shoulder Line Extraction Method Fusing Edge Detection and Regional Growing Algorithm. *Appl. Sci.* **2022**, *12*, 12662. <https://doi.org/10.3390/app122412662>

Academic Editor: Tung-Ching Su

Received: 26 October 2022

Accepted: 7 December 2022

Published: 10 December 2022

**Publisher’s Note:** MDPI stays neutral with regard to jurisdictional claims in published maps and institutional affiliations.



**Copyright:** © 2022 by the authors. Licensee MDPI, Basel, Switzerland. This article is an open access article distributed under the terms and conditions of the Creative Commons Attribution (CC BY) license (<https://creativecommons.org/licenses/by/4.0/>).

## 1. Introduction

One of the most significant recent discussions has been the study of spatial differentiation in the Loess Plateau [1–5]. Shoulder lines are the topographic structural lines that best depict loess landform characteristics. The shape, grade, spatial distribution, development trend, and other characteristics of shoulder lines reflect the regional variations in loess landforms, as shown in Figure 1. However, due to the complexity of the Loess Plateau, the effective extraction of shoulder lines is influenced by a variety of factors, such as the accuracy of the source data, the local discontinuity of the lines, and the applicability of the method [6–10]. Consequently, a more efficient and accurate shoulder line extraction method is still needed. The traditional method of extracting shoulder lines is to use the contour lines of topographic maps or aerial images to directly delineate them [11–15]. Although the precision is excellent, the efficiency of this method is low, and the workload is heavy.

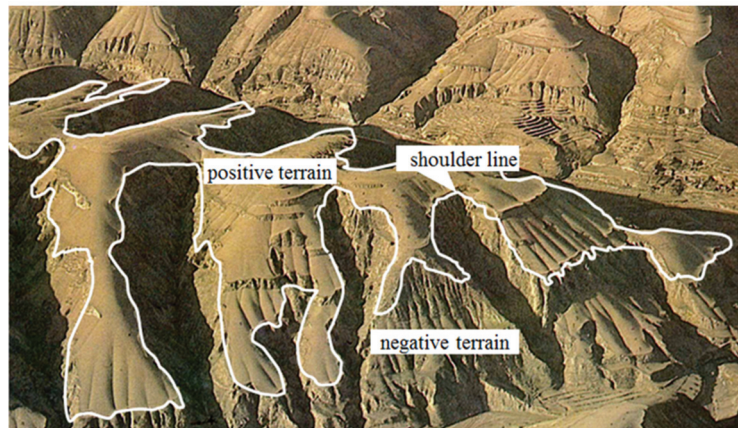


**Figure 1.** An illustration of shoulder line of the Loess Plateau.

In recent years, with the support of RS and GIS technologies, the characteristic terrain elements in a landform can be automatically extracted and analyzed, and the extraction of shoulder lines has become one of the hot spots for study [16–21]. Researchers have studied the automatic extraction of shoulder lines. The extraction methods can be classified into three types: The first method is the geometric morphological method. Terrain parameters, such as slope, slope aspect, and curvature, are used for regular judgment to obtain shoulder lines based on the given rule of shoulder lines in the geometric form. For example, Evans used DEM data as the basis for extracting shoulder lines by combining areas of low difference between mean elevation and high positive plan curvature [22]. Lei obtained shoulder lines by comparing the slopes of upstream and downstream grids on the same slopes [23]. Xiao proposed a method for extracting shoulder lines based on slope aspect orientation according to the slope-turning characteristics of loess landforms [24]. This method is simpler, faster, and easier to implement compared with the traditional approach. However, the actual effect obtained is not ideal. The second method is the hydro-geomorphologic method. The constraint and drawing of shoulder lines are achieved as a result of the interaction between the hydrological process and the landform and are based on the principle of a flow analysis of the terrain surface. For example, Lv applied a surface-flow digital simulation method and a contour vertical-line-tracking method to achieve shoulder line extraction based on the principle of a terrain surface flow analysis [25]. Liu used water flow paths for distributed water flow computation to extract shoulder lines [26]. Yang used the direction of confluence to determine the streamline of a slope and drew a shoulder line based on the inflection point of the streamline [27]. The shoulder lines obtained by this method have a certain geological significance compared with the geometric morphological method, and the problem of shoulder line continuity is overcome to a certain extent. However, the digital simulation of surface water is influenced by several factors, including water flow direction and catchment threshold, which increase the uncertainty of a slope's flow path, making judging points on a characteristic shoulder line difficult, lacking in precision, and necessitating substantial calculations. The third method is based on an image-processing method. The edge detection method achieves the purpose of detecting sudden edge change by comparing the changing characteristics in the image brightness value and detecting the sudden change point of the image brightness. For example, Vrieling used the supervised classification approach for the maximum likelihood classifier to classify gullies and non-gullies [28]. Yan used image binarization and various edge detection operators to extract shoulder lines [29]. Wang extracted a shoulder line by combining the P-N opening of the terrain and the threshold segmentation of a difference image [30]. Compared to the previous two methods, edge detection operators can quickly and effectively extract such changing features, and some operators can even extract weak mutation features to better

reflect details; this provides a method for indistinct shoulder line extraction. However, the shoulder lines extracted with edge detection methods tend to be less closed, and the line segments are fragmented and do not match the actual shoulder lines. In conclusion, the above methods share the same problem in that they require a means to effectively balance continuity and accuracy. Drawing on the advantages of the good applicability of the edge detection method, finding ways to further improve the integrity of shoulder lines is an urgent problem to be solved. The regional growing algorithm, a fundamental feature in image segmentation research, can produce continuous, closed regions with relatively little domain information [31,32]. The regional growing method has advantages for solving the continuity problem of shoulder lines based on DEM data [33]. However, the resolution of DEM data has a great influence on the extraction results, and it is difficult to obtain high-precision DEM data, especially in large areas. Hence, a shoulder line extraction method that combines the edge detection method and regional growing algorithm is proposed here to comprehensively improve the continuity and accuracy of shoulder lines. Based on high-resolution satellite images, this study uses the advantages of edge detection in highlighting details to complete the extraction of an original shoulder line. At the same time, based on DEM data, the regional growing algorithm is used to realize the determination of P-N terrain, to overcome the discontinuities of the original shoulder line, and to complete the accurate extraction of the shoulder line.

## 2. Materials and Methods

### 2.1. Study Areas

The study area is one of the key national governance regions for soil and water conservation and is located in Yijun and Luochuan counties, Shaanxi Province, China, with latitudes between  $35^{\circ}25' N$  and  $34^{\circ}42' N$  and longitudes between  $109^{\circ}20' E$  and  $109^{\circ}37' E$ , as shown in Figure 2. The topography of this place is the Loess Plateau. In this area, the elevation ranges from 85 m to 3719 m. The watershed unit is usually used as the basic landform analysis unit due to its relative internal homogeneity; hence, in this study, the extraction of shoulder lines was also presented with small watersheds as the sample area.

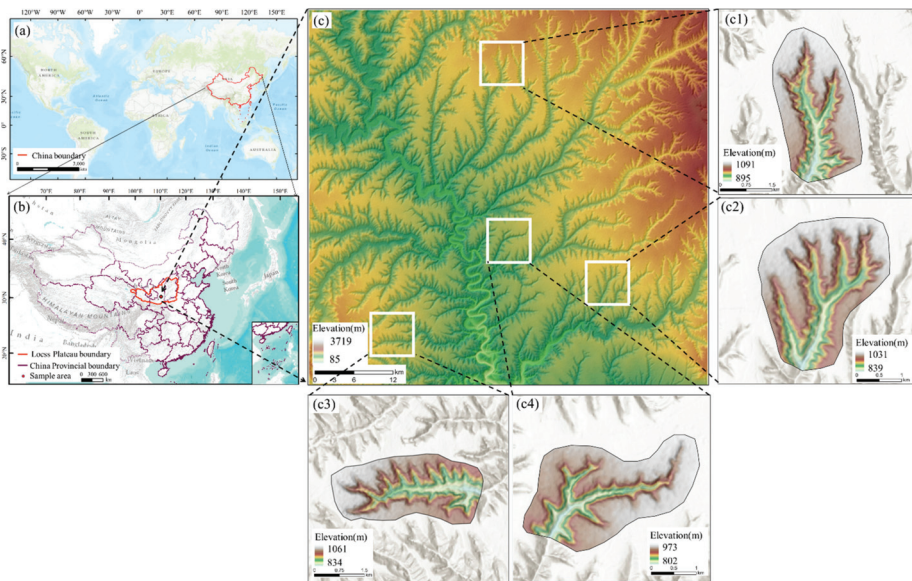


**Figure 2.** Location of the study area: (a,b) location of Loess Plateau; (c,c1–c4) hillshade map of the study area.



## 2.2. Data

In this study, high-resolution satellite images were used to produce higher-density spectral and textural information. Imagery of 3 m resolution downloaded from Planet Explorer (<https://www.planet.com/explorer/>, (accessed on 1 September 2021)) was used. The image data were mainly captured between June and September 2021. During this period, the images had less cloud content, and crops were harvested on the land surface; therefore, the boundaries of objects with loess morphologies were more obvious, which aided image edge detection and shoulder line extraction. The Advanced Land-Observing Satellite (ALOS) Digital Elevation Model with a spatial resolution of 12.5 m was used to calculate the peak point and outlet point of the sample area. The DEM data were downloaded from the National Aeronautics and Space Administration (NASA, <https://search.asf.alaska.edu/#/>, (accessed on 1 October 2016)). The horizontal and vertical accuracies of the elevation data could reach 12.5 m. These were the most accurate data from open-source DEM data. More details on the data are shown in Table 1.

**Table 1.** Details of data used in this study.

Data Name	Type	Resolution	Data Resource
Satellite images	Raster	3 m	<a href="https://www.planet.com/explorer/">https://www.planet.com/explorer/</a> (accessed on 1 September 2021)
DEM	Raster	12.5 m	<a href="https://search.asf.alaska.edu/#/">https://search.asf.alaska.edu/#/</a> (accessed on 1 October 2016)
Vector boundaries data	Vector	—	1:250,000 national basic geographic database

## 2.3. Edge Detection

In image-processing technology, commonly used edge detection operators include the Roberts operator, Sobel operator, Prewitt operator, Laplace operator [34], and Canny operator [35]. These operators have different edge detection capabilities for images with different characteristics. In an image, shallow gullies appear as linear features with weak feature information. The Canny operator has the characteristics of good anti-interference ability and accurate positioning and can effectively identify and locate edges on slope data. Compared with other edge detection operators, the Canny operator can seek the best solutions for anti-noise solutions and precise positioning. Therefore, this study selected the Canny operator to complete detection of the experimental sample area. To make the shoulder line features more obvious and to avoid image noise interference, the images needed to be preprocessed.

### 2.3.1. Image Grayscale

Performing grayscale operations on images can reduce the amount of computation needed. The maximum value of three image components is taken as the result of image grayscale processing, as shown in Formula (1):

$$Gray(i, j) = \max[R(i, j), G(i, j), B(i, j)] \quad (1)$$

where  $Gray(i, j)$  represents the gray value of an image, and  $R(i, j), G(i, j), B(i, j)$  represent the three components of the image.

### 2.3.2. Binary Image

A target image has a large difference in gray value from its background image, and it is partitioned according to the gray value. The gray value of a target image is marked as 0, and the gray value of a background image is marked as 1. If  $F(x, y)$  is the gray value of a pixel in the image, the transformation function of the gray threshold  $Th$  is as follows:

$$F(x, y) = \begin{cases} 1, & F(x, y) > Th \\ 0, & F(x, y) \leq Th \end{cases} \quad (2)$$

### 2.3.3. Canny Edge Detection

To perform edge detection on the preprocessed target images, the Canny edge detection method included the following four steps: The first step was to smooth the image. We constructed a filter with a Gaussian function, performed convolution filtering on the images, removed noise, and obtained smooth images. The second step was to calculate the gradient magnitude and gradient direction of the images. The gradient magnitude and gradient direction of the smoothed images were calculated by the finite difference in the first-order partial derivatives. The third step was to perform non-maximum suppression on the gradient amplitude. To determine the edge, it was necessary to keep the point with the largest local gradient and to suppress the non-maximum value, that is, we set the non-local maximum value point to zero in order to obtain a refined edge. If the gradient value of the neighborhood center point was larger than the value of the two adjacent points along the gradient direction, the current neighborhood center point was determined as a possible edge point. Otherwise, it was assigned a value of zero, and the pixel point was judged as a non-edge point. The fourth step was double threshold detection. After applying non-maximal suppression, the remaining edge pixels provided a more accurate representation of the true edges in the images. However, some edge pixels were still caused by noise and color variations. To account for these spurious responses, edge pixels must be filtered out with weak gradient values, as well as edge pixels with high gradient values. This was achieved by choosing high and low thresholds. If the gradient value of an edge pixel was higher than the high threshold, it was marked as a strong edge pixel. If the gradient value of an edge pixel was less than the high threshold and greater than the low threshold, it was marked as a weak edge pixel. If the gradient value of an edge pixel was less than the low threshold, it was suppressed.

### 2.4. Regional Growing Algorithm

The regional growing algorithm is a process of merging pixels or sub-regions into a larger area according to similarity criteria [36]. This algorithm is based on the theory that regions start with a group of growing points and that the same or similar adjacent pixels merge into new growing points. This process is continuously repeated until there are no more points to merge. The three steps are as follows: (1) choosing the appropriate growing points, (2) determining the similarity criteria, and (3) establishing the stop rules.

#### 2.4.1. Identifying Growing Points for P-N Terrain

Shoulder lines lie on the boundaries of P-N terrain. Accordingly, extracting the P-N terrain boundary is considered a premise of shoulder line extraction. Positive terrain is an area that is higher than the adjacent region or that is located in a tectonic uplift region. The P-N terrain method can be used to classify positive terrain. Errors in the positive terrain can be classified into two categories, as follows: (1) depressions, where the condition is caused by artificial modification or slight topographic relief in small regions, and (2) flatland, where a small difference can be observed between the original elevation and the elevation after smoothing when using a filter window slide on a nearly flat DEM. Slight elevation changes can affect the results. This phenomenon is especially evident in the Loess Plateau area, which means that peaks located in positive terrain must be correctly classified. Hence, peaks should be chosen as the growing points of positive terrain and should grow until there are no more points of the same type to merge. The above-mentioned positive terrain was extracted using the P-N terrain method. The size of the analysis window depended on the fragmentation of the landform. If the landform had more fragments, then we tended to choose a smaller analysis window. Negative terrain is an area that is lower than the adjacent region or an area that is located at a tectonic down-lift region. The test area was a complete watershed, and the negative terrain was connected. Accordingly, one growing point for negative terrain was enough. The outlet was the lowest elevation point and was located in negative terrain. On this basis, the outlet point was chosen as the growing point

of the negative terrain and grew until there were no more points of the same type to merge. The above-mentioned negative terrain was extracted using the P-N terrain method.

2.4.2. Growth Criteria

We assumed that the pixel with a gray value of 8 was the initial growth point, as shown in Figure 1, where the numbers in the figure indicate the gray levels of pixels. The growing criterion for the four neighborhoods of 8 was that the calculated result should be in the range between  $-1$  and  $1$  when the growing point was less than the neighbor point. If no difference could be found between the adjacent growing results, then the growing process stopped. Figure 3 illustrates four stages of the regional growing algorithm. Figure 3a depicts an original image, and the numbers are gray values. Figure 3b–d represents the growth process.

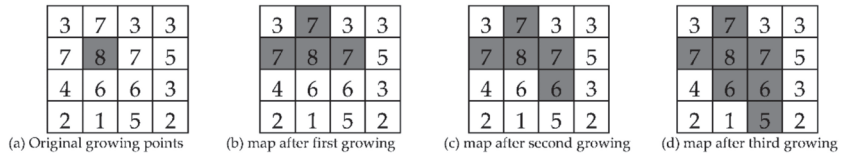


Figure 3. Illustration of regional growth: (a–d) represent the four steps of the regional growing algorithm, respectively.

The regional growing algorithm can avoid most misclassification areas. Still, for those regions that are connected to the correct area, it remains difficult to accurately identify them. This problem results in the inaccurate position of the shoulder line, and it is serious in the Loess Plateau area. To improve this concept, this study introduced slope gradient, and defined the following rules: if the slope gradient of the negative terrain was smaller than the given threshold and the negative terrain was adjacent to the positive terrain, then this negative terrain could be considered as positive terrain, as shown in Figure 4. The threshold of the slope gradient depended on the type of loess landform. This study tested different thresholds, compared the test results with the manual visual interpretation results, and chose  $7^\circ$  as the final slope threshold.

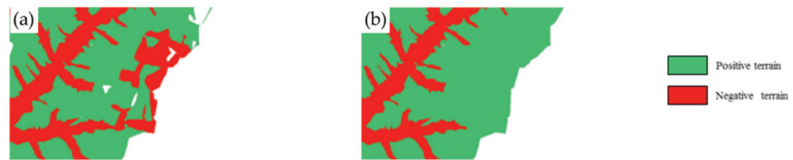


Figure 4. Slope’s influence on the positive and negative terrain classification results: (a) represents the classification map of positive and negative terrain; (b) represents the results after slope correction.

2.5. Burr Removal

The resulting shoulder line had some parasitic components in line corners, as shown in Figure 5. These parasitic components are called burrs. These burrs can lead to uncertain positions of the shoulder line. When the shoulder line was transformed from a grid to a vector, this defect became more prominent.



Figure 5. Contrast between before (a) and after (b) burr removal.

This study used a morphological image-processing method to remove burrs. The basic principle of this method was that fixed structure elements were used to detect and thin the endpoint (Equation (3)). Structure elements were used to detect and remove burrs. The algorithm was as follows: (1) The threshold of endpoint thinning was determined. We observed the image; if the length of a burr was less than 3 pixels, the threshold was set to 5 pixels to guarantee the reliability of the experimental results. (2) The structure elements were determined. The diagonal pixels could be ignored because the growing method only used four neighbor pixels. This study used the structure elements as shown in Figure 6. In these elements, “×” represents ignored pixels, “1” depicts shoulder line pixels, and “0” denotes background pixels. In an analysis window, if the image value agreed with any structure element in Figure 6, then “0” was set as the center pixel value (Equation (4)). The whole image was scanned using structure elements that could only remove one endpoint pixel at once. The above operation was repeated five times to ensure that the burrs were completely removed. The difference between before and after the above-mentioned steps is shown in Figure 5. (3) The correct end points were recovered. Given that this method processed all the end points, the correct end points were also removed, as were the burrs. The next step was to recover the correct end points. Structure elements were used to scan the whole image and remove the end points again. The burrs were already removed after the previous five scans. Accordingly, the pixels removed at this time were the correct end points. Thereafter, we performed four neighbor expansions and obtained the intersection with the original shoulder line (Equation (5)). The expansion time was the same as the thinning time. The complete process of this study method is shown in Figure 7.

$$X_1 = A \odot \{B\} \tag{3}$$

where  $A$  is the original shoulder line,  $B$  is the structure elements,  $\odot$  is the thinning, and  $X_1$  is the thinning result.

$$X_2 = \bigcup_{k=1}^8 (X_1 \odot B^k) \tag{4}$$

where  $X_2$  is the end point,  $B^k$  ( $k = 1, 2, 3, 4$ ) are the structure elements, and  $\odot$  is the hit-miss transformation.

$$X_3 = (X_2 \oplus H) \cap A \tag{5}$$

where  $X_3$  is the shoulder line,  $H$  is a four-neighborhood structure element,  $A$  is the original shoulder line, and  $\oplus$  is the expansion.

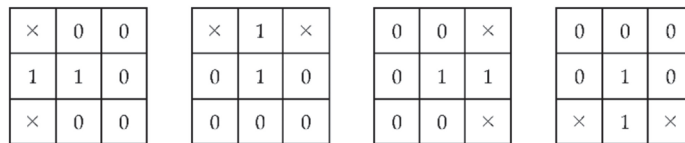


Figure 6. Structure elements.

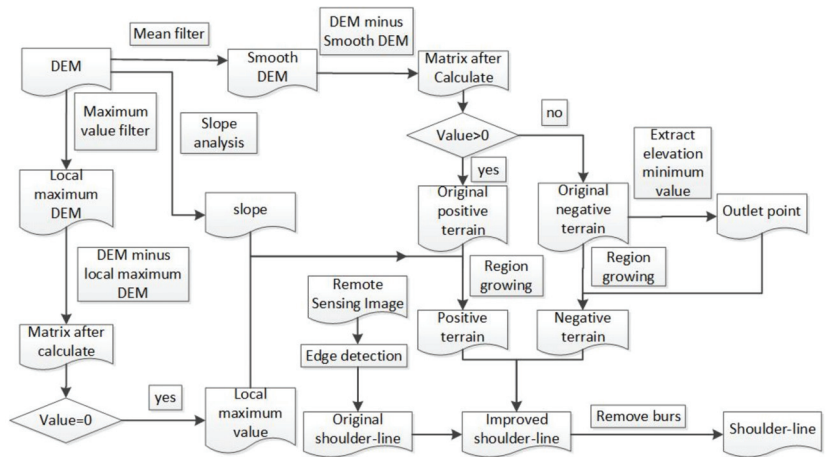


Figure 7. The complete process of our experiment.

### 2.6. Accuracy Assessments

To objectively evaluate and verify the superiority of the method in this paper, the following indicators were used to evaluate the edge detection method, the regional growing algorithm, and the method in this paper. Class pixel accuracy (CPA) is the percentage of correct pixels out of all the extracted result pixels; the closer the value is to 100%, the better. Pixel accuracy (PA) is the percentage of correctly extracted pixels in an image, that is, the proportion of correctly extracted pixels out of the total pixels; the larger the value, the better. The dice similarity coefficient (Dice) is a measure of set similarity, indicating the ratio of the area where two objects intersect the total area; the value range is (0, 1), and the effect is best when it is 1. Intersection over union (IOU) is the overlapping area between the extraction results and the real value divided by the joint area between the extraction results and the real value; the value is between (0, 1), and the larger the value, the better the effect. The formulas for each indicator are as follows:

$$CPA = \frac{TP}{(TP + FP)} \times 100\% \tag{6}$$

$$PA = \frac{(TP + TN)}{(TP + TN + FP + FN)} \times 100\% \tag{7}$$

$$Dice(A, B) = \frac{2|A \cap B|}{|A| + |B|} \tag{8}$$

$$IOU = \frac{|A \cap B|}{|A \cup B|} \tag{9}$$

where  $A$  is the method extraction result;  $B$  is the manual visual interpretation result;  $TP = (A \cap B)$  is the method correctly extracting the region;  $FN = A - (A \cap B)$  is the target area missed by the method;  $TN = I - A$  is the real background area; and  $I$  is the set of image pixels.

## 3. Results

### 3.1. Parameter Settings

When using edge detection to detect high-precision remote-sensing images, to identify the edges of gullies more accurately, it was necessary to set appropriate parameters for the Canny operator function. The Canny function had two parameters: The first parameter represented the first threshold, and the calculated boundary points were greater than this threshold to be the real boundary. The second parameter represented the second

threshold; the calculated boundary points below this threshold were discarded. Based on the understanding of the terrain features of the study sample area, the parameters were adjusted, and the final optimal first and second parameters were 50 and 210, respectively, when using the regional growing algorithm to generate positive and negative terrain based on DEM data. Based on the comparison of extraction results that used different window sizes, the window size of  $13 \times 13$  was the best size for shoulder line extraction [37]. Positive and negative terrain growth points were set as peaks and outlet points, respectively.

### 3.2. Results Analysis

In this study, the Canny operator was used to complete the detection of the gully range on high-resolution satellite images, and the extraction results were superimposed on the image data, as shown in Figure 8. Based on the DEM data, the regional growing algorithm was used to complete the extraction of positive and negative terrain for each sample area. This study chose peaks and outlets as P-N terrain growing points, respectively. The peak and outlet points could be detected through neighborhood analysis and the watershed boundary method. In the process of growing, the same values of pixels were merged until there were no points to merge. The generated results were also superimposed on hillshade data, as shown in Figure 9. Overall, compared with high-resolution satellite images and hillshade data, the extraction results of edge detection and the regional growing algorithm were better.

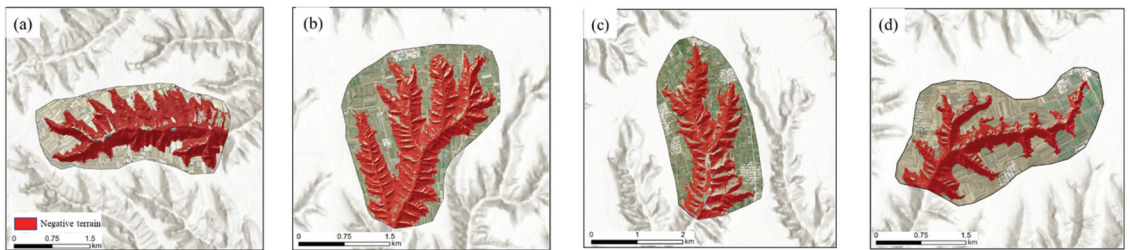


**Figure 8.** The result of extracting Negative terrain by edge detection method. (a–d) represent 4 sample areas.

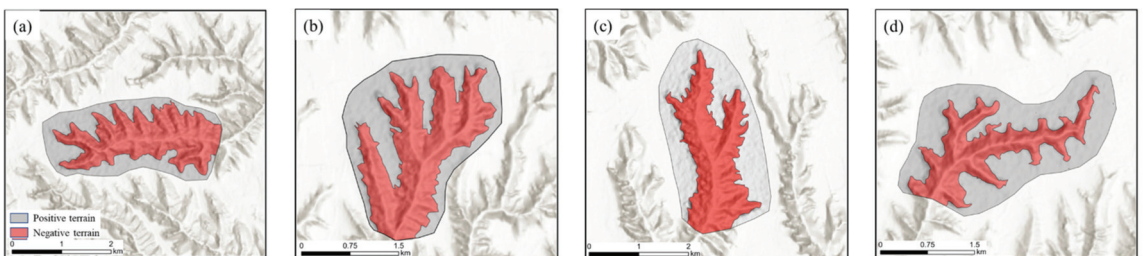


**Figure 9.** The results of extracting P-N terrain using the regional growing algorithm: (a–d) represent 4 sample areas.

To compare the performance of the regional growing and edge detection methods for the extraction of the shoulder line, the real shoulder line needed to be defined. In this paper, manual visual interpretation supported by expert knowledge was employed to extract the real shoulder line. The shoulder line extracted using the manual visual interpretation method based on high-resolution satellite images was used as the evaluation criterion. The extraction results of the regional growing and edge detection methods were evaluated by comparing the negative terrain areas of these two methods with the real shoulder line results. It can be seen from Table 2 that, for the four sample areas, the regional growing algorithm was generally better than the edge detection method when the negative terrain

areas were used as the evaluation indicator. For example, sample area a, the difference between the results obtained by the regional growing algorithm and the standard results was within 12 ha, and the error was within 5%; the difference between the results obtained by the edge detection method and the standard results was within 41 ha, and the error was within 13%. These results also showed that the results of shoulder line extraction are credible when studying the characteristic indicators related to area, such as gully erosion. However, in the details, we can find that there were still differences between the two methods. The specific analysis was as follows. It can be found from Figure 10 that the regional growing algorithm was more advantageous in the detailed expression of the shoulder line, such as the turning point of the shoulder line. However, it can be found from Figure 11 that, although the edge detection method could reflect more details, the extraction results were fragmented, resulting in inaccurate positioning of the shoulder line in some places, and the generated shoulder line was discontinuous. Although DEM data do not contain more information than high-resolution satellite images, they become an advantage for the positive and negative terrain generated by the regional growing method. This is because the core of the regional growing algorithm is the determination of the growing point. We could accurately find the lowest point (the outlet) and the highest point (the peak) as the positive and negative topographic growth points based on the DEM data using the digital terrain analysis method. Furthermore, for shoulder line continuity obtained through extraction, the regional growing algorithm had more advantages.

**Table 2.** Comparison of extracted negative terrain area with standard area differences.

Method	Indicator	Sample Area a	Sample Area b	Sample Area c	Sample Area d
Manual visual interpretation	negative terrain area (ha)	320.912	328.762	347.209	197.833
	negative terrain area (ha)	328.624	317.811	334.249	189.325
Regional growing algorithm	percent error	2.403%	3.331%	3.733%	4.301%
	absolute error	7.712	10.951	12.960	8.508
	negative terrain area (ha)	280.713	290.678	317.581	176.741
Edge detection	percent error	12.526%	11.584%	8.533%	10.662%
	absolute error	40.199	38.084	29.628	21.092

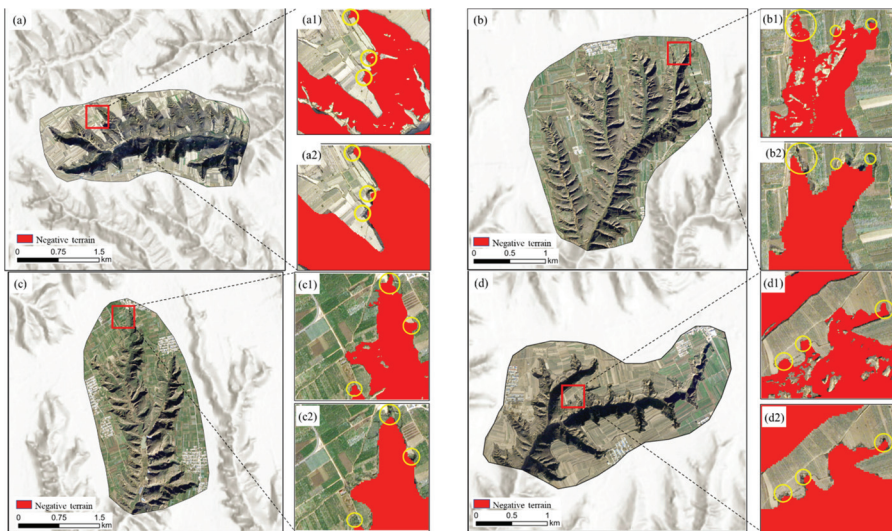


**Figure 10.** Results of edge detection compared to the regional growing algorithm: (a–d) represent 4 sample areas; (a1,b1,c1,d1) represent the results of the edge detection method; (a2,b2,c2,d2) represent the results of the regional growing algorithm.

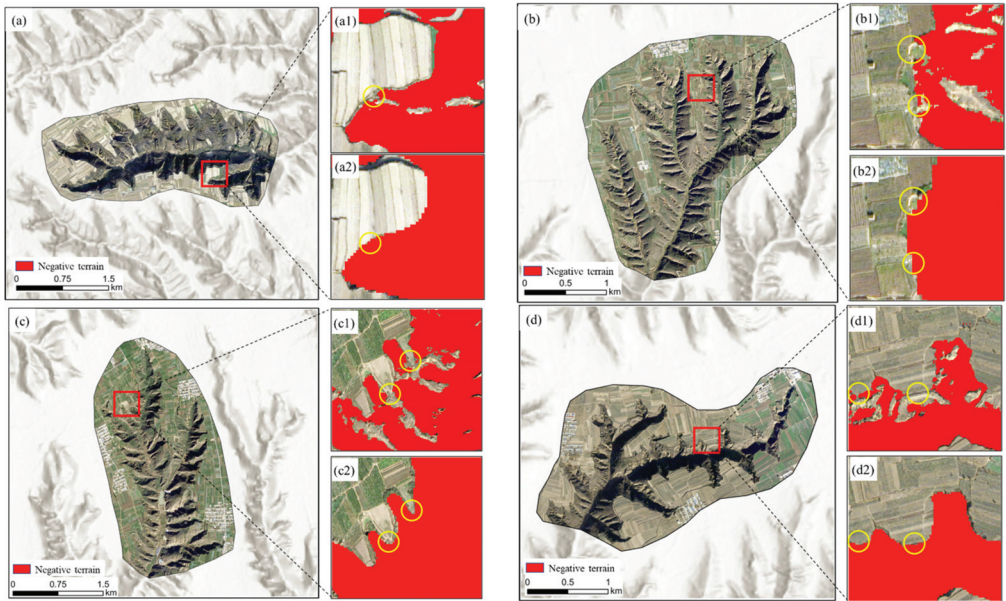


**Figure 11.** Results of the regional growing algorithm compared to edge detection: (a–d) represent 4 sample areas; (a1,b1,c1,d1) represent the results of the edge detection method; (a2,b2,c2,d2) represent the results of the regional growing algorithm.

By comparing and analyzing the shoulder line obtained by manual visual interpretation of the shoulder line based on high-resolution satellite images shown in Figure 12, we can see that the shoulder line extracted by edge detection under positive and negative terrain constraints was closer to the artificial shoulder line. Therefore, the advantages of edge detection in detail and the advantages of the regional growing algorithm in continuity were combined. By using the P-N terrain constrained edge detection results obtained by the regional growing method and removing the burrs, we could finally obtain better detailed and continuous shoulder line extraction results, as shown in Figure 13.

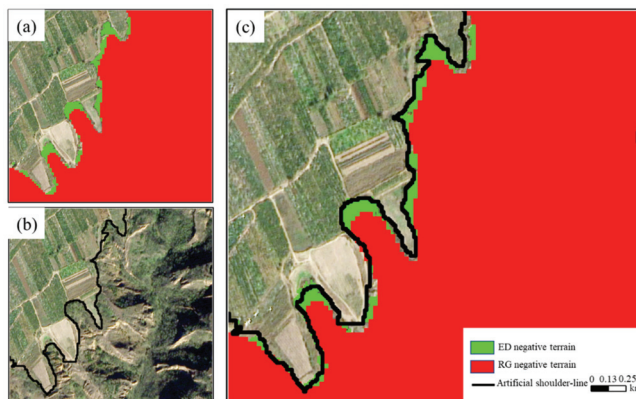


**Figure 12.** Comparison of shoulder lines between edge detection, regional growing algorithm, and manual visual interpretation. (a) represents the results of edge detection method and regional growing algorithm; (b) represents the results of manual visual interpretation; (c) represents the overlay of extraction results from different methods.



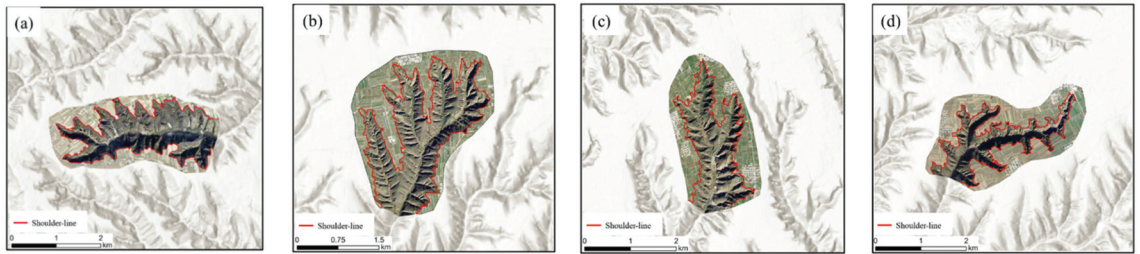


**Figure 13.** Results of improved shoulder line: (a–d) represent 4 sample areas.

### 3.3. Precision Evaluation

By comparing the CPA, PA, Dice, and IOU values, it can be seen from Table 3 that the extraction method in this study was better than edge detection and the regional growing algorithm. For example, in sample area a, the CPA value of the proposed method was 7.1% and 5.6% higher than those of the edge detection method and the regional growing algorithm, respectively. The largest PA value obtained was for the method proposed in this study, which was closer to 1, and the effect was better than those of the other methods. Similarly, both the Dice and IOU values were closer to 1, which was better than the other methods. Therefore, the reliability and accuracy of the method proposed in this study were verified.

**Table 3.** Comparison of accuracy evaluation index values of different algorithms.

Sample Area	Method	CPA	PA	Dice	IOU
a	Edge detection	0.814	0.791	0.818	0.734
	Regional growing algorithm	0.829	0.807	0.820	0.813
	Method in this study	0.885	0.864	0.877	0.907
b	Edge detection	0.837	0.797	0.820	0.828
	Regional growing algorithm	0.831	0.845	0.815	0.836
	Method in this study	0.897	0.858	0.871	0.891
c	Edge detection	0.776	0.801	0.843	0.794
	Regional growing algorithm	0.819	0.836	0.833	0.857
	Method in this study	0.867	0.917	0.866	0.897
d	Edge detection	0.801	0.799	0.791	0.747
	Regional growing algorithm	0.811	0.781	0.831	0.811
	Method in this study	0.873	0.911	0.859	0.909

## 4. Discussion

### 4.1. Comparison of Different Operators

For edge detection operators for different images, there are differences in edge detection. It is the premise of accurate shoulder line extraction to select an operator that is suitable for the study sample area from among many operators. Therefore, we chose sample area a to discuss the effects of common operators on the shoulder line extraction results, and the experimental results are shown in Figure 14. In this study, the line-related parameters of the shoulder line were used to further compare the detection results of each edge detection operator. These parameters were mainly used to describe the fineness of the line segment extracted by the operator. As shown in Table 4, the overall effect of the line segment extracted by the Canny operator was better than the other operators. We found that the Prewitt operator and the Sobel operator both performed differential and filtering operations on the image and only had some differences in the selection of weights for smoothing. However, the image was blurred to a certain extent, and some edges could not be detected. Therefore, the detection accuracy was relatively low, and this type of operator was deemed more suitable for situations where the gray value of an image edge is relatively obvious. The detection accuracy of the Roberts operator was relatively high,

but it was easy to lose part of the edge, which made the detection results incomplete. At the same time, the image was not smoothed, and the noise could not be suppressed; thus, this operator had the best response to images with steep, low noise. The Laplace operator smoothed the image through the Gaussian function and had a relatively obvious effect on noise suppression. However, the original edge could also be smoothed during processing, resulting in some edges that could not be detected. In addition, the noise had a great influence on it; the detected image details were very rich, but at the same time, false edges could appear. If the false edges were reduced, the detection accuracy could also be reduced; many true edges could be lost, and different parameters should be selected for different images. The Canny operator was more accurate than the Laplace operator in detecting edges. Although some edge information could be lost, this operator had the best effect among the above-mentioned edge detection operators and could identify small edges more clearly.

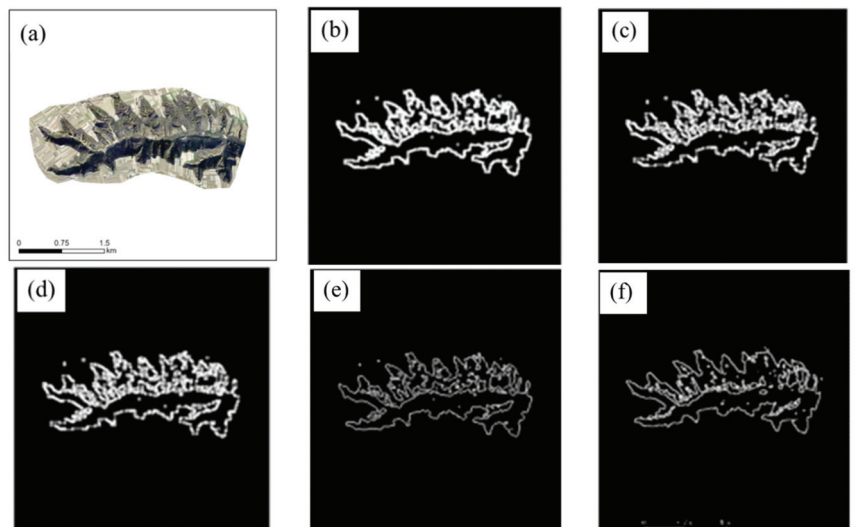


**Figure 14.** (a) represents sample area a; (b–f) represent the extraction results of the Roberts, Prewitt, Sobel, Laplace, and Canny operators, respectively.

**Table 4.** Comparison of evaluation index values of different edge detection operators.

Operator Type	Number of Lines	Maximum Length (m)	Total Length (m)
Prewitt	427	12,116	21,033
Sobel	514	6283	23,877
Robert's	441	9867	23,196
Laplace	154	17,421	22,966
Canny	87	19,308	22,393.8

#### 4.2. Applications and Future Research

The landform types of the Loess Plateau in northern Shaanxi show significant regional differences, and the dominant factors of landform influence vary for different landform types. Loess landform types are mainly divided into tableland, ridges, and hills [38–40], and there were challenges in realizing the fully automatic extraction of the Loess Plateau shoulder line. For the Loess Plateau, it can be seen from the previous accuracy evaluation results that the proposed method had good applicability. To further verify the applicability of this method in extracting shoulder lines, we selected a loess tableland area with an area of 35,975.531 ha. The results are shown in Figure 15. By superimposing the extracted results onto high-precision images, it can be seen that the extracted shoulder lines were

effective and reasonable, which verified that this method had good universality in Loess tableland area.

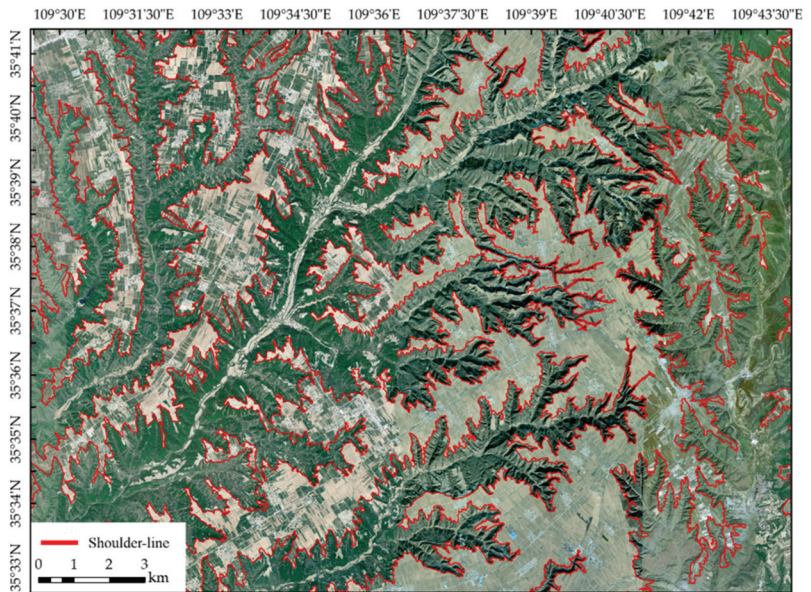


**Figure 15.** Shoulder lines extracted by applying the method proposed in this study.

In loess ridge and hill regions, the terrain was more complex. As shown in Figure 16, there were many seriously discontinuous shoulder lines due to occasional gravity erosion factors, such as landslides and scattering. Some areas were also affected by artificial landforms, such as terraced fields, dams, etc., resulting in the existence of multilevel shoulder lines (Figure 16a). At the same time, in loess ridge and hill regions, due to the influence of vegetation, the slope of the shoulder line's up- and down-slopes showed little change, and there were invisible shoulder lines (Figure 16b,c). Even if there is no interference from vegetation, in autumn and winter the continuity and visibility of shoulder lines are poor due to the impact of gravity, such as landslides, strays, and collapses, or even human factors (Figure 16d). Therefore, the application of this method in loess ridge and hill areas is also a problem that needs to be discussed and solved in the future. In future research, it is necessary to further analyze the applicability of this method for different data sources and different landform types. To better apply the method to different landform types over a large area, we could try to divide different areas according to the different land use characteristics (soil erosion characteristics and land use directions) of each landform type. On this basis, we could establish quantitative models of different shoulder lines to achieve the high-efficiency and high-precision extraction of shoulder lines.

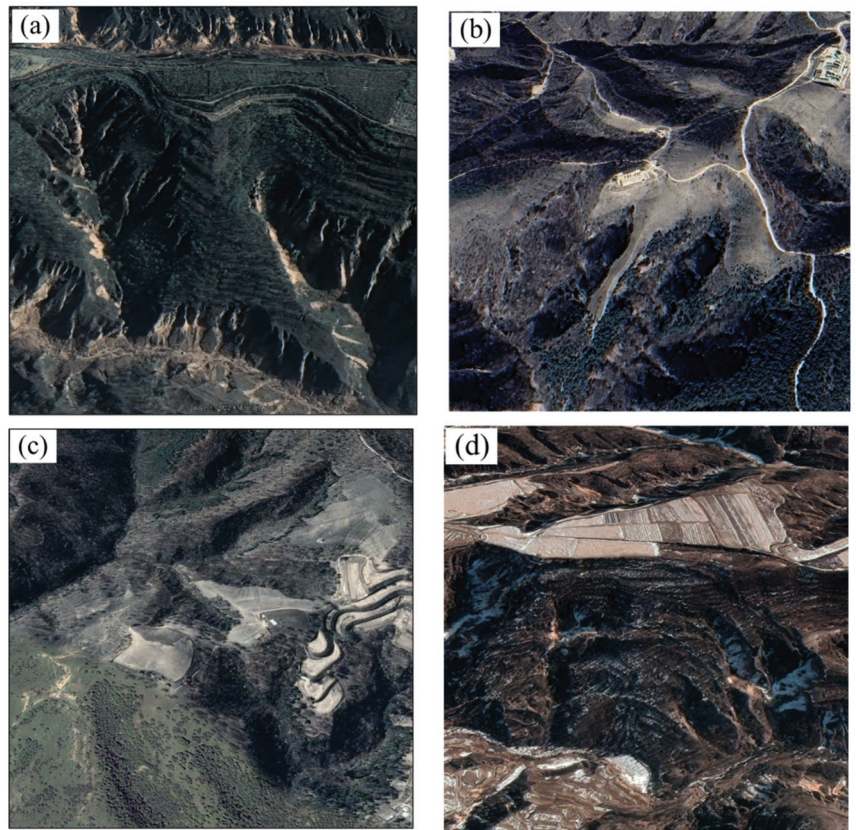


**Figure 16.** Examples of landforms in loess ridge and hill regions. (a–d) show the distribution of shoulder lines in loess ridge and hill regions, respectively

## 5. Conclusions

Aiming to improve the poor continuity and inaccuracy of extracted shoulder lines, this study proposed an extraction method that fused edge detection and the regional growing algorithm. The experimental results showed that the CPA and PA values of the edge detection method were in the ranges of 77.6–83.7% and 79.1–80.1%, respectively; the CPA and PA values of the regional growing algorithm were in the ranges of 81.1–83.1% and 78.1–84.5%, respectively; the CPA and PA values of the method proposed in this study were in the ranges of 86.7–89.7% and 85.8–91.7%, respectively. Moreover, the Dice and IOU values of the method studied in this paper were closer to 1 than those of the edge detection method and the regional growing algorithm. This method could guarantee shoulder line continuity and integrity. Meanwhile, burr removal reduced errors when the grid shoulder line was transformed into a vector.

Shoulder lines have obvious turning points above and below the line, and the terrain factors (slope, curvature, etc.) also change accordingly. The geomorphic mechanisms of the P-N terrain above and below the line are significantly different. The positive terrain above the line basically maintains the original slope state after loess accumulation, and slope erosion is mainly surface erosion. The negative terrain below the line is dominated by gully erosion and gravity erosion, and various gravity landforms are widely developed. In summary, shoulder lines can be used as an important topographic index for regional soil erosion intensity and landform division. The accurate extraction of shoulder lines can provide a

new perspective for the quantitative study of loess landforms and is very important for the study of Loess Plateau landforms, soil erosion characteristics, and ecological environments.

**Author Contributions:** Conceptualization, F.L. and H.J.; methodology, H.J.; validation, H.J., H.W. and W.L.; writing—original draft preparation, H.J., W.L. and H.W.; writing—review and editing, H.J., H.W. and W.L.; supervision, F.L.; funding acquisition, F.L. All authors have read and agreed to the published version of the manuscript.

**Funding:** This work was supported by the National Natural Science Foundation of China (grant number: 42271421).

**Institutional Review Board Statement:** Not applicable.

**Informed Consent Statement:** Not applicable.

**Data Availability Statement:** Data will be made available on reasonable request.

**Conflicts of Interest:** The authors declare no conflict of interest.

## References

- Li, S.; Xiong, L.; Tang, G.; Strobl, J. Deep Learning-Based Approach for Landform Classification from Integrated Data Sources of Digital Elevation Model and Imagery. *Geomorphology* **2020**, *354*, 107045. [\[CrossRef\]](#)
- Rokosh, D.; Bush, A.B.; Rutter, N.W.; Ding, Z.; Sun, J. Hydrologic and Geologic Factors That Influenced Spatial Variations in Loess Deposition in China during the Last Interglacial–Glacial Cycle: Results from Proxy Climate and GCM Analyses. *Palaeogeogr. Palaeoclimatol. Palaeoecol.* **2003**, *193*, 249–260. [\[CrossRef\]](#)
- Chen, L.; Wei, W.; Fu, B.; Lü, Y. Soil and Water Conservation on the Loess Plateau in China: Review and Perspective. *Prog. Phys. Geogr.* **2007**, *31*, 389–403. [\[CrossRef\]](#)
- Chen, Y. Types of valleys in the loess hilly area in the middle reaches of the Yellow River. *Sci. Geogr. Sin.* **1984**, *4*, 321–327.
- Zhao, G.; Mu, X.; Wen, Z.; Wang, F.; Gao, P. Soil Erosion, Conservation, and Eco-Environment Changes in the Loess Plateau of China. *Land Degrad. Dev.* **2013**, *24*, 499–510. [\[CrossRef\]](#)
- Perroy, R.L.; Bookhagen, B.; Asner, G.P.; Chadwick, O.A. Comparison of Gully Erosion Estimates Using Airborne and Ground-Based LiDAR on Santa Cruz Island, California. *Geomorphology* **2010**, *118*, 288–300. [\[CrossRef\]](#)
- Jiang, S.; Tang, G.; Liu, K. A New Extraction Method of Loess Shoulder Line Based on Marr-Hildreth Operator and Terrain Mask. *PLoS ONE* **2015**, *10*, e0123804. [\[CrossRef\]](#)
- Yang, X.; Li, M.; Na, J.; Liu, K. Gully Boundary Extraction Based on Multidirectional Hill-Shading from High-Resolution DEMs. *Trans. GIS* **2017**, *21*, 1204–1216. [\[CrossRef\]](#)
- Ke, W.; Cheng, W.; Qingfeng, Z.; Kailong, D. Loess Shoulder Line Extraction Based on Openness and Threshold Segmentation. *Acta Geod. Cartogr. Sin.* **2015**, *44*, 67–75.
- Dai, W.; Yang, X.; Na, J.; Li, J.; Brus, D.; Xiong, L.; Tang, G.; Huang, X. Effects of DEM Resolution on the Accuracy of Gully Maps in Loess Hilly Areas. *Catena* **2019**, *177*, 114–125. [\[CrossRef\]](#)
- Daba, S.; Rieger, W.; Strauss, P. Assessment of Gully Erosion in Eastern Ethiopia Using Photogrammetric Techniques. *Catena* **2003**, *50*, 273–291. [\[CrossRef\]](#)
- Castillo, C.; Pérez, R.; James, M.R.; Quinton, J.N.; Taguas, E.V.; Gómez, J.A. Comparing the Accuracy of Several Field Methods for Measuring Gully Erosion. *Soil Sci. Soc. Am. J.* **2012**, *76*, 1319–1332. [\[CrossRef\]](#)
- Fadul, H.M.; Salih, A.A.; Imad-eldin, A.A.; Inanaga, S. Use of Remote Sensing to Map Gully Erosion along the Atbara River, Sudan. *Int. J. Appl. Earth Obs. Geoinf.* **1999**, *1*, 175–180. [\[CrossRef\]](#)
- Shruthi, R.B.; Kerle, N.; Jetten, V. Object-Based Gully Feature Extraction Using High Spatial Resolution Imagery. *Geomorphology* **2011**, *134*, 260–268. [\[CrossRef\]](#)
- Seutloali, K.E.; Beckedahl, H.R.; Dube, T.; Sibanda, M. An Assessment of Gully Erosion along Major Armoured Roads in South-Eastern Region of South Africa: A Remote Sensing and GIS Approach. *Geocarto Int.* **2016**, *31*, 225–239. [\[CrossRef\]](#)
- Gafurov, A.M.; Yermolayev, O.P. Automatic Gully Detection: Neural Networks and Computer Vision. *Remote Sens.* **2020**, *12*, 1743. [\[CrossRef\]](#)
- Lv, G.; Xiong, L.; Chen, M.; Tang, G.; Sheng, Y.; Liu, X.; Song, Z.; Lu, Y.; Yu, Z.; Zhang, K. Chinese Progress in Geomorphometry. *J. Geogr. Sci.* **2017**, *27*, 1389–1412. [\[CrossRef\]](#)
- Cheng, W.; Liu, Q.; Zhao, S.; Gao, X.; Wang, N. Research and Perspectives on Geomorphology in China: Four Decades in Retrospect. *J. Geogr. Sci.* **2017**, *27*, 1283–1310. [\[CrossRef\]](#)
- Castillo, C.; Taguas, E.V.; Zarco-Tejada, P.; James, M.R.; Gómez, J.A. The Normalized Topographic Method: An Automated Procedure for Gully Mapping Using GIS. *Earth Surf. Process. Landf.* **2014**, *39*, 2002–2015. [\[CrossRef\]](#)
- Golosov, V.; Yermolaev, O.; Rysin, I.; Vanmaercke, M.; Medvedeva, R.; Zaytseva, M. Mapping and Spatial-Temporal Assessment of Gully Density in the Middle Volga Region, Russia. *Earth Surf. Process. Landf.* **2018**, *43*, 2818–2834. [\[CrossRef\]](#)

21. Wei, H.; Li, S.; Li, C.; Zhao, F.; Xiong, L.; Tang, G. Quantification of Loess Landforms from Three-Dimensional Landscape Pattern Perspective by Using DEMs. *ISPRS Int. J. Geo-Inf.* **2021**, *10*, 693. [[CrossRef](#)]
22. Evans, M.; Lindsay, J. High Resolution Quantification of Gully Erosion in Upland Peatlands at the Landscape Scale. *Earth Surf. Process. Landf.* **2010**, *35*, 876–886. [[CrossRef](#)]
23. Lei, X.; Zhou, Y.; Li, Y.; Wang, Z. Construction and characteristic analysis of loess landform approximation factor based on DEM. *J. Geo-Inf. Sci.* **2020**, *22*, 431–441.
24. Xiao, C.; Tang, G. Classification of valley shoulder line in Loess Relief. *Arid. Land Geogr.* **2007**, *30*, 646–653.
25. Lv, G.; Qian, Y.; Chen, Z. Research on automatic extraction of loess landform shoulder line based on grid digital elevation model. *Sci. Geogr. Sin.* **1998**, *18*, 567–573.
26. Liu, P.; Zhu, Q.; Wu, D.; Zhu, J.; Tang, X. Research on automatic extraction technology of loess area shoulder line based on grid DEM and water flow path. *J. Beijing For. Univ.* **2006**, *28*, 72–76.
27. Yang, F.; Zhou, Y.; Chen, M. Shoulder line constrained loess water-erodible gully extraction. *Mt. Res.* **2016**, *34*, 504–510.
28. Vrieling, A.; Rodrigues, S.C.; Bartholomeus, H.; Sterk, G. Automatic Identification of Erosion Gullies with ASTER Imagery in the Brazilian Cerrados. *Int. J. Remote Sens.* **2007**, *28*, 2723–2738. [[CrossRef](#)]
29. Yan, S.; Tang, G.; Li, F.; Dong, Y. Automatic extraction of loess landform lines using DEM edge detection. *Geomat. Inf. Sci. Wuhan Univ.* **2011**, *36*, 363–366.
30. Wang, K.; Wang, Z.; Zhang, Q.; Ding, K. A Loess Plateau shoulder line Extraction Method Combining Topographic Opening and Differential Image Threshold Segmentation. *Acta Geod. Cartogr. Sin.* **2015**, *44*, 67–75.
31. Lira, J.; Maletti, G. A Supervised Contextual Classifier Based on a Region-Growth Algorithm. *Comput. Geosci.* **2002**, *28*, 951–959. [[CrossRef](#)]
32. Ghule, A.G.; Deshmukh, P.R. Image Segmentation Available Techniques, Open Issues and Region Growing Algorithm. *J. Signal Image Process.* **2012**, *3*, 71–75.
33. Liu, W.; Li, F.Y.; Xiong, L.Y.; Liu, S.L.; Wang, K. Shoulder Line Extraction in the Loess Plateau Based on Region Growing Algorithm. *Int. J. Geogr. Inf. Sci.* **2016**, *18*, 220–226.
34. Basu, M. Gaussian-Based Edge-Detection Methods—a Survey. *IEEE Trans. Syst. Man Cybern. Part C Appl. Rev.* **2002**, *32*, 252–260. [[CrossRef](#)]
35. Canny, J. A Computational Approach to Edge Detection. *IEEE Trans. Pattern Anal. Mach. Intell.* **1986**, *PAMI-8*, 679–698. [[CrossRef](#)]
36. Zhang, Z.; Wang, Y.; Xue, G. *Digital Image Processing and Computer Vision—Visual C++ and Matlab Implementation*; People's Posts and Telecommunications Press: Beijing, China, 2010; 368p.
37. Xiong, L.; Tang, G.; Yan, S.; Zhu, S.; Sun, Y. Landform-Oriented Flow-Routing Algorithm for the Dual-Structure Loess Terrain Based on Digital Elevation Models: Flow-Routing Algorithms for the Dual-Structure Loess Terrain. *Hydrol. Process.* **2014**, *28*, 1756–1766. [[CrossRef](#)]
38. Xiong, L.-Y.; Tang, G.-A.; Li, F.-Y.; Yuan, B.-Y.; Lu, Z.-C. Modeling the Evolution of Loess-Covered Landforms in the Loess Plateau of China Using a DEM of Underground Bedrock Surface. *Geomorphology* **2014**, *209*, 18–26. [[CrossRef](#)]
39. McVicar, T.R.; Van Niel, T.G.; Li, L.; Wen, Z.; Yang, Q.; Li, R.; Jiao, F. Parsimoniously Modelling Perennial Vegetation Suitability and Identifying Priority Areas to Support China's Re-Vegetation Program in the Loess Plateau: Matching Model Complexity to Data Availability. *For. Ecol. Manag.* **2010**, *259*, 1277–1290. [[CrossRef](#)]
40. Wei, H.; Xiong, L.; Zhao, F.; Tang, G.; Lane, S.N. Large-Scale Spatial Variability in Loess Landforms and Their Evolution, Luohe River Basin, Chinese Loess Plateau. *Geomorphology* **2022**, *415*, 108407. [[CrossRef](#)]



Article

# Development of an Underground Tunnels Detection Algorithm for Electrical Resistivity Tomography Based on Deep Learning

Yin-Chun Hung <sup>1,\*</sup>, Yu-Xiang Zhao <sup>2</sup> and Wei-Chen Hung <sup>1</sup>

<sup>1</sup> Department of Civil Engineering and Engineering Management, National Quemoy University, Kinmen 89250, Taiwan; hungbarry1997@gmail.com

<sup>2</sup> Department of Computer Science and Information Engineering, National Quemoy University, Kinmen 89250, Taiwan; yxzhao@nqu.edu.tw

\* Correspondence: hij@nqu.edu.tw

**Featured Application:** Authors are encouraged to provide a concise description of the specific application or a potential application of the work. This section is not mandatory.

**Abstract:** Kinmen Island was in a state of combat readiness during the 1950s–1980s. It opened for tourism in 1992, when all troops withdrew from the island. Most military installations, such as bunkers, anti airborne piles, and underground tunnels, became deserted and disordered. The entries to numerous underground bunkers are closed or covered with weeds, creating dangerous spaces on the island. This study evaluates the feasibility of using Electrical Resistivity Tomography (ERT) to detect and discuss the location, size, and depth of underground tunnels. In order to discuss the reliability of the 2D-ERT result, this study built a numerical model to validate the correctness of in situ measured data. In addition, this study employed the artificial intelligence deep learning technique for reprocessing and predicting the ERT image and discussed using an artificial intelligence deep learning algorithm to enhance the image resolution and interpretation. A total of three 2D-ERT survey lines were implemented in this study. The results indicate that the three survey lines clearly show the tunnel location and shape. The numerical simulation results also indicate that using 2D-ERT to survey underground tunnels is highly feasible. Moreover, according to a series of studies in Multilayer Perceptron of deep learning, using deep learning can clearly show the tunnel location and path and effectively enhance the interpretation ability and resolution for 2D-ERT measurement results.

**Keywords:** Electrical Resistivity Tomography (ERT); deep learning; underground tunnel

**Citation:** Hung, Y.-C.; Zhao, Y.-X.; Hung, W.-C. Development of an Underground Tunnels Detection Algorithm for Electrical Resistivity Tomography Based on Deep Learning. *Appl. Sci.* **2022**, *12*, 639. <https://doi.org/10.3390/app12020639>

Academic Editor: Yosoon Choi

Received: 23 November 2021

Accepted: 5 January 2022

Published: 10 January 2022

**Publisher's Note:** MDPI stays neutral with regard to jurisdictional claims in published maps and institutional affiliations.



**Copyright:** © 2022 by the authors. Licensee MDPI, Basel, Switzerland. This article is an open access article distributed under the terms and conditions of the Creative Commons Attribution (CC BY) license (<https://creativecommons.org/licenses/by/4.0/>).

## 1. Introduction

Kinmen is a small island. During the 43 years of military control, the Kinmen government constructed various defence works and military camps, as well as many spiritual landmarks. Military installations, bunkers, and tunnels can be seen across the island. During the military administration, there were at least 1000 barracks, 22 large-scale monuments, 28 memorial pavilions, and 10 large underground Halls in the Kinmen area [1]. As it was in a state of combat readiness for an extended period, 120,000 soldiers were stationed in Kinmen. After the 1990s, the government regained local autonomy and democratic governance, and the original historical sites became the resources of local tourism development. In recent years, with the reduction of military garrison and opening of military spaces, the pace of development has accelerated. It is estimated that over 1000 vacant barracks will be released over the coming years. At least 300 barracks have been or are in the process of being released, and about 50 to 80 barracks are planned for annual release.

Although the vacant barracks are being released, the numerous underground bunkers are still closed or covered with weeds. In recent years, there have been frequent occurrences of collapsing underground bunkers that endanger private property [2]. Public works were frequently halted due to the discovery of underground bunkers during excavation [3] and



ammunition depots excavated during public works [4]. The original data on these underground bunkers, including their planimetric positions, massing sizes, and underground depths, are difficult to obtain or simply incorrect. These difficulties and inconsistencies result from frequent changes of documents keepers and mistakes in handover during army withdrawal. Therefore, the Kinmen County Government faces a challenge in providing a detailed report on underground bunker investigation necessary when planning public works, thus delaying the planning and design schedule. If an underground bunker is discovered during the construction, the works must be halted. Without such reports, the building schedule cannot resume, which significantly delays the construction progress and affects the efficiency of government administration. In addition, the army faces similar problems of unknown or unclear locations of underground bunkers when returning the land to private owners, thus affecting the military handover schedule. Civilians also worry about whether there are any underground bunkers nearby, endangering their homes and safety.

Over the past decades, despite societal progress, urban disasters occurred frequently. The collapse of underground bunkers across Kinmen is an example of such disasters. Detailed and correct geological data of the site can enhance the effectiveness of urban disaster prevention and reduce the potential damage these disasters may cause. The geotechnical engineering investigation targets the geological conditions of the site. The conventional geotechnical investigation uses mainly the geological drilling method, but the drilling cost is high and provides only a single point of information. Sometimes it needs to be combined with the geophysical exploration method to gain the complete geological picture.

In recent years, nondestructive geophysical technology has been gradually introduced in different underground environmental surveys. In combination with document information, the information of underground "surface and space" can be obtained [5]. In the past, geophysical exploration was used in the geotechnical investigation primarily for seismic detection (refraction, reflection, and surface wave techniques). The elastic wave velocity of strata is closely bound with the material engineering characteristics [6–8], but the seismic detection is likely to be influenced by ambient vibration noise. Moreover, seismic refraction detection cannot positively detect the low-velocity layer under the high-velocity one, and the shallow layer (less than 50 m) reflection seismic detection is challenging to implement. The surface wave seismic detection is mainly 1D and 2D probing technique, and the 3D detection method is still in the preliminary research stage. Ground-penetrating radar is an electromagnetic method similar to seismic reflection detection. Here detecting the distribution of bed boundary and the localisation of depth and the depth of investigation are limited. If a Bistatic antenna is used, it can increase the detection depth capability [9–12]. The ground-penetrating radar has been used in underground structure and archaeological investigations to a great extent, for instance, in underground tunnel mining [13,14], underground pit mining [15,16], and historical building mining [17,18]. However, the ground-penetrating radar only judges the location of possible tunnel structures derived from the discontinuity of radar wave velocity. The shape, size, depth, and distribution range of underground blockhouses are unknown.

Electrical Resistivity Tomography (ERT) is a geophysical method of mapping underground structures using electrodes placed in boreholes or electrical resistivity measurements from the surface. The present electrical resistivity tomography technique can explore 2D and even 3D resistivity distribution, and the depth of investigation can be adjusted easily by the length of the measuring line. The resistivity is highly correlated with the geomaterial and groundwater characteristics, so it has gradually become one of the primary geophysical methods of geotechnical investigation. In the past decade, the ERT has been extensively used in a variety of geotechnical and environmental engineering investigation and monitoring, for instance, in geologic surveys [19,20], fault line surveys [21–25], slipping plane survey and monitoring [26–28], groundwater investigation and pollution monitoring [29,30], reservoir/dam leakage investigation and monitoring [31,32], refuse landfill leakage investigation and monitoring [33–35], and underground tunnel mining [36–38].

Kinmen Island is located between Taiwan and China. The test site is located in an abandoned barracks area in the central region of Kinmen Island, shown in Figure 1. A large-scale military defensive infrastructure was built in this area, including multiple underground tunnels. The Shuangru Mountain Tunnel was built in 1949. It is 1142 m long, extending in all directions, and had a significant strategic position and value. After the troops' withdrawal, the Kinmen County Government declared this tunnel an important cultural heritage in 2019, as it had significant historical value. However, the site has been in disrepair; multiple tunnel intersections have collapsed, and it is difficult to determine the tunnel path and true underground location. This study attempts to evaluate the feasibility of using ERT to detect the basic data on the location, size, and depth of the underground tunnel.

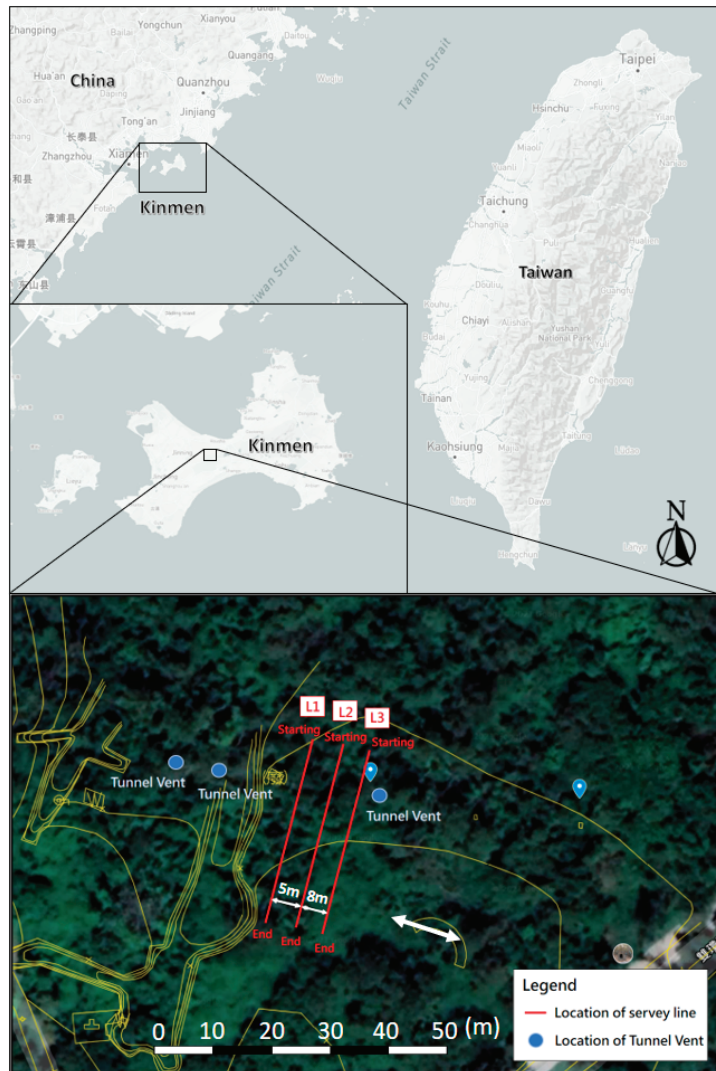


Figure 1. Test site location and measurement wiring diagram.

The measurement results of ERT in the geotechnical investigation is influenced by soil water content, geological structure, groundwater level, and ambient noise, among other

things. These factors affect the sensitivity of ERT measurement and spatial analysis, so this technology still faces problems in spatial resolution capability. Therefore, this study intends to construct a numerical model with the collected data to discuss the reliability of ERT results for detecting underground tunnels.

As all geologic configurations are essentially 3D, theoretically, the 3D resistivity survey is supposed to obtain the most accurate result [39]. At present, the 3D ERT survey has been studied by most scholars actively, but it is not yet as extensively used as 2D ERT. The main reason is that the Conduct 3D ERT test needs a larger area site, 3D ERT has a relatively higher cost, and field tests take a long time. Therefore, the use of the 3D ERT survey is not yet widespread.

In recent years, artificial intelligence has been extensively used in various domains [40]. This study uses the deep learning algorithm of artificial intelligence for reprocessing several 2D-ERT images from a field test. The Multilayer Perceptron (MLP) of the deep learning method is used to approximate resistivity value. More profiles are developed from the original 2D-ERT images, and the 3D resistivity value information is approximated by different profiles to establish the 3D resistivity model. This study aims to enhance the image resolution capability and interpretation capability of deep learning and discusses the feasibility of this type of artificial intelligence algorithm for enhancing 2D-ERT image resolution.

## 2. Research Method

### 2.1. Electrical Resistivity Tomography (ERT)

In terms of the measuring principle of ERT, the direct current or low-frequency alternating direct current is conducted to the ground through a pair of current electrodes, C1 and C2, to establish a man-made electric field. The electric field is measured using another pair of potential electrodes, P1 and P2, so as to measure the potential difference between P1 and P2, different configurations of electrodes (e.g., Wenner, pole-dipole, Schlumberger, dipole-dipole, and pole-pole), and the movement of electrodes that correspond to different space geometry factors. Thus, apparent resistivity can be obtained. The resistivity measured infield is not the true resistivity of the subsurface structures. Therefore, the apparent resistivity needs to be calculated via an inversion analysis to obtain the approximately real resistivity profile [39].

The direct current resistivity method includes 1D, 2D, and 3D detection methods. The advantage of a 1D survey is a rapid measurement, but the defect is that it cannot consider the transverse resistivity variation, thus affecting the reliability of measurement results and interpretation. In the last few decades, to enhance the accuracy of the electrical prospecting method in result interpretation, the researchers developed the 2D survey from the pseudo depth composed of the VES and profiling results of the 1D survey. As the 2D-ERT has a low cost and short test time, the apparent underground resistivity is obtained by wiring laid, and the resistivity of subsurface soil is obtained by appropriate inverse calculation. In recent years, more research has been devoted to the research on 3D measurement, leading to higher accuracy of 3D detection. However, the effectiveness of 3D detection is still under investigation and is limited to the measurement of space and time [41–45]. Thus, 2D detection is still the most economical and feasible measurement method at present.

To select the test site, several underground tunnel vent holes were found on the surface of a site according to the tunnel literature, indicating a possible presence of an underground tunnel. In order to evaluate the location, size, and depth data of this tunnel, this study attempted ERT detection.

Therefore, three survey lines, L1, L2, and L3, were laid in the Shuangru Mountain Barrack Field, as shown in Figure 1. The overall length of each survey line was 46 m, the electrode spacing was 2 m. The three survey lines were parallel with each other. The distance between L1 and L2 was 5 m, the distance between L2 and L3 was 8 m. The electrode configuration used Wenner Array for data collection infield measurement. This test used the SYSCAL PRO Switch 48 ground resistance instrument of France IRIS. In this experiment, the analysis software Res2dinv (version 3.54 z) [39] developed by Geotomo

was used for inverse analysis. The inverse analysis method used the optimal least square method (L2 norm). To ensure the measurement quality, each survey line was measured repeatedly to ensure the deviation was below 3%.

### 2.2. Reliability Analysis

To analyse the reliability of the 2D-ERT result, this study attempts to build a numerical model to validate the correctness of in situ measured data. The numerical model was built using RES2DMOD developed by Geotomo [46]. The in situ geologic configuration was simulated in the built mesh, and an appropriate resistivity value was given. The numerical solution was calculated using the finite element method to obtain apparent resistivity, and the apparent resistivity profile inverse calculation was carried out using the Optimal least square method (Res2dinv [47]). The numerical simulation resistivity profile can be obtained and compared with the in situ actual resistivity profile result.

The numerical model resistivity can be obtained from the collected geologic data, such as geologic maps, drilling data, the resistivity distribution range of geomaterial, and the preliminary detection result of ERT. Different depths, positions, or specific regions of the model are given appropriate resistivity values according to experience and professional judgment.

According to the analysis of the collected geologic data of the site, the geology around the Shuangru Mountain Tunnel mainly comprises two kinds of strata, which are silty sand within 15 m below the earth's surface and silty clay at 15–30 m below the earth's surface. This study referred to the geologic drilling data of the site and took the silty sand as background to build the numerical model of a tunnel and simulate the tectonics stratum of the tunnel.

### 2.3. Deep Learning

The MLP is one of the basic types of deep learning architecture. Its architecture follows the neural network system principle, learns, and predicts data. The MLP learns in the perceptron; the weight is changed after each data processing. The weight is adjusted using an algorithm, and the deviation in the training process is reduced to minimize the error in the amount of output and prediction results. The main advantage is the ability to solve complex problems rapidly. The MLP is a feedforward neural network composed of the multilayer structure of linear and nonlinear activation functions. Each layer is composed of basic elements of neurons, and each neuron is fully connected to all others in the previous and subsequent layers. Neurons in the network have a bias value  $b$  and an activation function  $f$ . The connection between neurons in different layers is defined by connection weight,  $w_i \in R$ ,  $i \in \{1, 2, \dots, n\}$ . These parameters are updated during the training of MLP. The general activation functions are ReLU, TANH, sigmoid, and softmax. The output value  $y$  of a neuron is defined as:

$$y = f\left(\sum_{i=1}^n w_i x_i + b\right) \quad (1)$$

where  $x_i$  is the output value of neuron  $i$  of the previous layer,  $i \in \{1, 2, \dots, n\}$ . The MLP network generally includes one input layer, one output layer, and one or more dense layers, detailed below.

1. Input layer: the number of neurons of the input layer is determined by the point  $k$  of input data.
2. Hidden layer: fully connected layer between the input layer and output layer.
3. Output layer: the neuron of the output layer is determined by the number of classes or the output of the approximation function.

In the training process of MLP, the weight  $w_i$  and offset parameter  $b$  are updated in every iteration, and the update target is a minimum loss function. After network training, it can be used for classification or function approximation. The architecture is shown in Figure 2 [48–52].

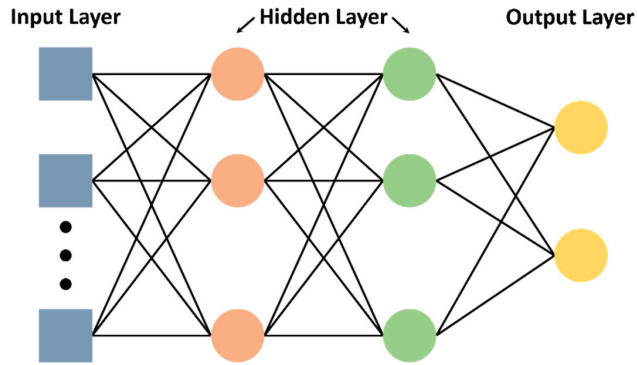


Figure 2. MLP architecture diagram.

In this study, we used Adaptive Moment Estimation (Adam) optimization to train MLP and minimize the Mean Squared Error (MSE). Adam optimization was applied to calculate the adaptive training rate of the parameters [53]. This method, in addition to storing the descending mean of the square of the past of the gradient or  $v_t$  and the mean of the descending of the past of the gradient or  $m_t$ , is kept as momentum. This is why the momentum can be seen as a ball sliding on a sloping surface with no friction and, therefore, can be placed at the minimum error level [54]. Both parameters of the mean descending average of the square of the gradient and the average of the descending of the past of the gradient can be calculated as follows:

$$m_t = \beta_1 m_{t-1} + (1 - \beta_1) g_t$$

$$v_t = \beta_2 v_{t-1} + (1 - \beta_2) g_t^2$$

where  $g_t$  is the gradients at subsequent time steps,  $m_t$  and  $v_t$  are estimates of the first moment (the mean) and the second moment (the uncentered variance) of the gradients, respectively (hence the name of the method). As  $m_t$  and  $v_t$  are initialized as vectors of zeros, the authors of Adam observe that they are biased towards zero, especially during the initial time steps, especially when the decay rates are low (i.e.,  $\beta_1$  and  $\beta_2$  are close to 1).

The prediction of unknown data has always been a complex problem, and it is also an important application in neural networks. The high-level network architecture of deep learning can more accurately predict and describe the distribution and changes of unknown data. The ERT profile is an inverted trapezoid; two sides are blank and short of resistivity data. This study used machine learning, data prediction, and computational ability to reduce the error between the actual value and prediction value of MLP for the blank in the field test ERT profile by MLP. The result was obtained after reiteration to convergence, forming a complete rectangular section. More profiles of different positions were developed from MLP, and the in situ 3D resistivity model was built last. In this study, we used only three-layer (discrete) 2D-ERT data to predict that multilayer (continuous) 3D ERT data is itself a complex and challenging problem. We hope that the 3D resistivity image predicted by MLP will enhance image resolution and interpretation capability.

### 3. Results and Discussion

#### 3.1. ERT Field Acquisition and Data Analysis

##### 3.1.1. L1 Survey Line

The result of the L1 survey line, according to Wenner, is shown in Figure 3 (RMS Error = 2.3%). The electrical property of the stratum is approximately divided into two layers, and the resistivity profile descends as the depth increases. There are two higher resistivity regions located at the survey line 10–18 m and 34–42 m, within 1.5 m depth from the surface. Because Kinmen Island had been free of rain for a long time in the measurement period, the topsoil was very dry. The other region shows low resistivity values at 3–18 m and 32–42 m of survey line and within 1.5–7.9 m underground. As the geology of this region is silty sand stratum, the geology is relatively loose and has higher water content. Notably, at 18–25 m of survey line and 2.5–6.5 m of depth, the resistivity value increases suddenly, the resistivity value of this region increases inwards, indicating this may be the tunnel location, according to preliminary analysis. According to Figure 3, the tunnel may be located at 2.5 m underground, with a height of about 2.5 m and a width of about 4 m, indicated by red dotted lines in Figure 3.

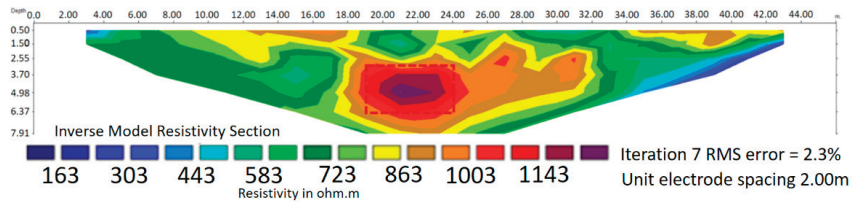


Figure 3. L1 result.

##### 3.1.2. L2 Survey Line

Figure 4 shows the result of the L2 survey line (RMS Error = 2.3%). It shows the same trend as Figure 3 because the L2 survey line is close to L1. The stratum is divided into two layers, in which the middle region has relatively high resistivity, while the rest is a stratum of lower resistivity. As the geology of this region is silty sand stratum, the geology is relatively loose and has higher water content. At 18–28 m of survey line and 2.5–5.5 m of depth, the resistivity value increases suddenly, the resistivity value of this region increases inwards, indicating this may be the tunnel location according to preliminary analysis. As shown in Figure, the tunnel may be located at 2.5 m underground, with a height of about 2.5 m and width of about 4 m, indicated by red dotted lines in Figure 4.

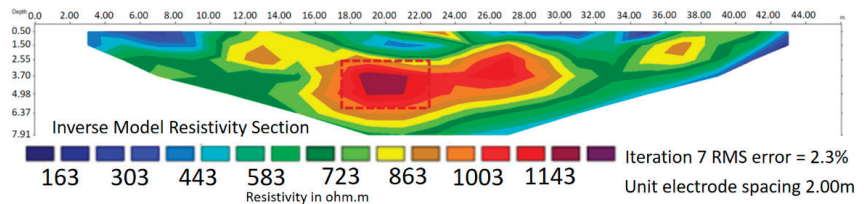


Figure 4. L2 result.

##### 3.1.3. L3 Survey Line

The result of the L3 survey line, according to Wenner, is shown in Figure 5 (RMS Error = 1.87%). It shows the same trend as Figure 4 because of the proximity of the L3 survey line to L2. The electrical property of the stratum is approximately divided into two layers. The resistivity profile descends as the depth increases, and there is a region of relatively high resistivity in the middle. At 3–14 m of survey line and within the earth’s surface to 1.5 m underground, this region showed higher resistivity. Because Kinmen

Island had been free of rain for an extended period during measurement, the topsoil was extremely dry. The other region showed a low resistivity value at 22–42 m of survey line and within the distance of 7.9 m from the earth’s surface. As the geology of this region is silty sand stratum, the geology is relatively loose and has higher water content. At 12–20 m of the survey line and 2–5 m of depth, the resistivity value increases suddenly, and the resistivity value of this region increases inwards. This indicates a possible tunnel location, according to preliminary analysis. As shown in Figure 5, the tunnel may be located at 2 m underground, the height is about 2.5 m, and the width is about 4 m, indicated by red dotted lines in Figure 5.

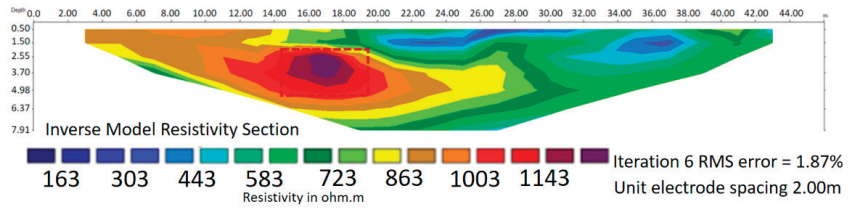


Figure 5. L3 result.

### 3.1.4. Comprehensive Interpretation

According to the measurement results of three survey lines, L1, L2, and L3, there is a high resistivity region in the earth resistivity profile. In order to analyse whether the high resistivities are correlated with each other in space, a 2.5D simulated diagram of the three survey lines in relative positions is drawn, as shown in Figure 6. It is observed that if the high resistivity regions of various profiles are selected and connected in line, the selected region and path correspond to the tunnel location and path in the literature.

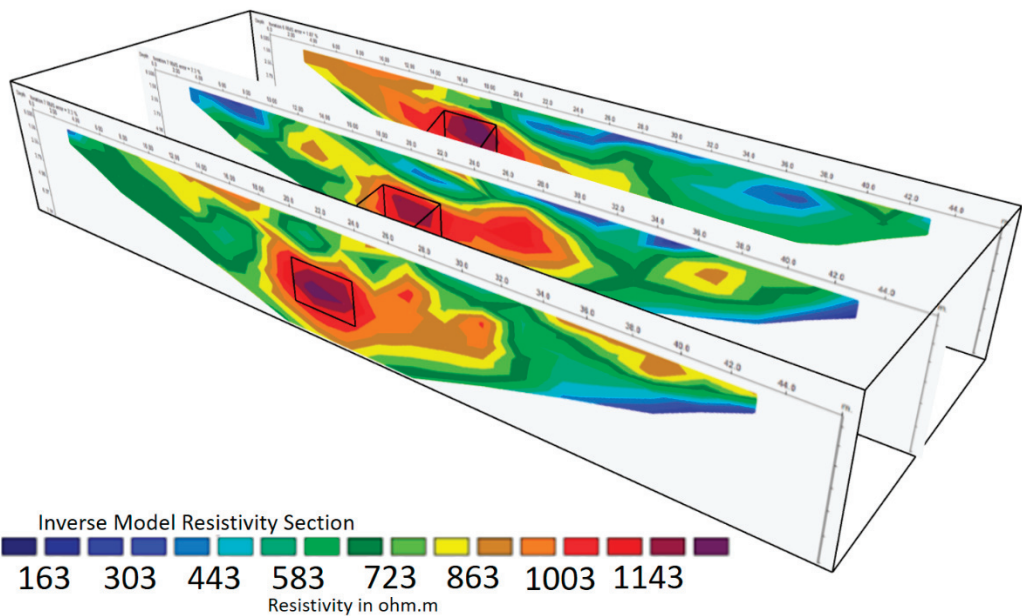


Figure 6. 2.5D simulated diagram of three survey lines.

### 3.2. Reliability Analysis

To verify the reliability of the 2D-ERT images, this study constructed a numerical model to validate the correctness of in situ measured data. To simulate the onsite strata condition, this study used the same measurement parameters as in situ measurement, referred to the geologic drilling data of site, and took the silty sand as background to build the numerical model of a tunnel to simulate the stratum tectonics of the tunnel in the stratum. Referring to the site concrete tunnel size, a 3 m high and 5 m wide square tunnel was built at 2 m underground, and the reasonable resistivity of each unit was assumed. The resistivity value of the concrete tunnel was assumed to be 1000 ohm-m, dry air inside a tunnel, the resistivity was assumed to be 2000 ohm-m, the resistivity of the soil layer covering the tunnel was assumed to be 400 ohm-m. The numerical model is shown in Figure 7.

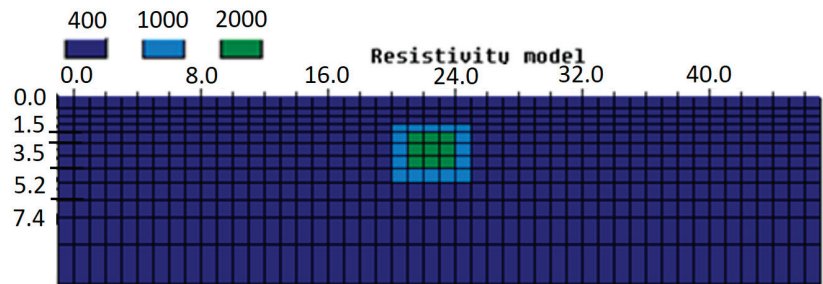


Figure 7. Numerical simulation model.

Figure 8 shows the numerical simulation result (RMS Error = 0.46%). As seen, the background silty sand shows low resistivity distribution, and relatively low resistivity values are shown at 2–18 m and 26–42 m of the survey line. Relatively high resistivity distribution is shown at 20–25 m of a survey line and 2–5 m of depth, indicated by red dotted lines in Figure 8. The numerical simulation result in Figure 8 is compared with the in situ test results in Figures 3–5. The four figures are very similar to each other, proving that the stratum tectonics in Figures 3–5 match the stratum tectonics assumed by numerical simulation, proving high reliability. Therefore, the high resistivity region is identified as the tunnel location and path.

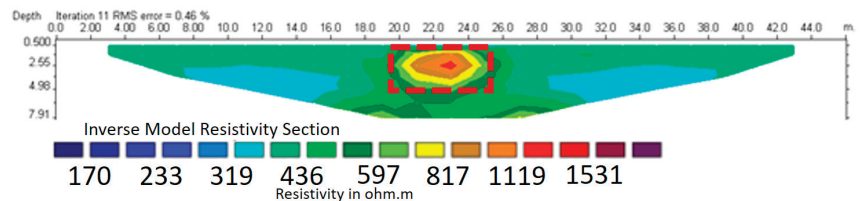


Figure 8. Numerical simulation result.

### 4. Deep Learning Prediction

The 2D ERT test result mainly shows a 2D profile; the tunnel location and path cannot be interpreted directly. To establish a 3D electrical resistivity model, this study used MLP for calculation. The computational ability of learning, data prediction, and reducing the error between the actual value and prediction value of MLP was used to build the in situ 3D electrical resistivity model.

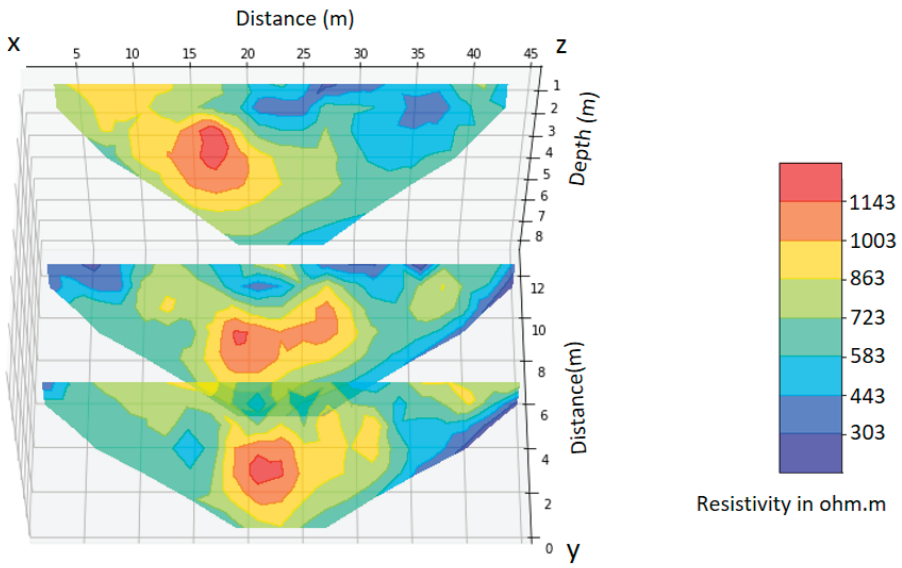


Figure 9a–g shows a series of results of deep learning prediction. Before artificial intelligence calculation, the measured data in this research must be converted into an MLP data format. The L1, L2, and L3 in situ measurement results are inputted to establish the graph of the relation of relative positions of L1, L2, and L3 for the initial model. Figure 9a shows the initial model of the original data of L1, L2, and L3; the result is similar to Figure 6. Table 1 shows the MLP network structure parameters. The MLP is a three-layer architecture, including two hidden and one output layer. Figure 9b shows the training result of the MLP network. The MLP is reiterated during training to reduce the error amount of output and prediction results and performs calculations until the network converges. Through the nonlinear iterative calculation of the MLP, as seen in Figure 9b, the error value is converged slowly after each iterative computation. Figure 9c shows the result of the original data after MLP data prediction. This is the output of the training data, which can be compared with the original data in Figure 9a. It can be seen that the training results can faithfully present the original data characteristics. Figure 9d shows the results of using the trained MLP to predict the unknown regions of L1, L2, and L3. Figure 9d shows the initially blank areas and without onsite measurement data, such as the lower left corner and the lower right corner, which can be predicted by the MLP network to predict the resistance value. Figure 9e shows the result of using the trained MLP to predict successive profiles. When the predicted number of profiles increases, the 3D resistivity model is built, and 14 profiles are predicted in this study. Due to the narrow scope of this study, the 14 layers of data are predicted by three layers of original data of the resistivity values predicted by the MLP network, which is sufficient to establish a 3D model. Figure 9f shows the 3D resistivity model result. The tunnel is a reinforced concrete structure; it is characterized by unlikely electrical conduction and high resistivity, especially in the 2D ERT result. In order to highlight the location of high resistivity, this study concealed the low resistivity colour of the 3D resistivity model in Figure 9f. After repeated tests and the resistivities are arranged, the 60% of the resistance value is taken as a boundary, the colour of resistivity value lower than 60% is hidden, and the colour of resistivity value higher than 60% is displayed. The result, after adjustment, is shown in Figure 9g; the tunnel location and path have been shown clearly.

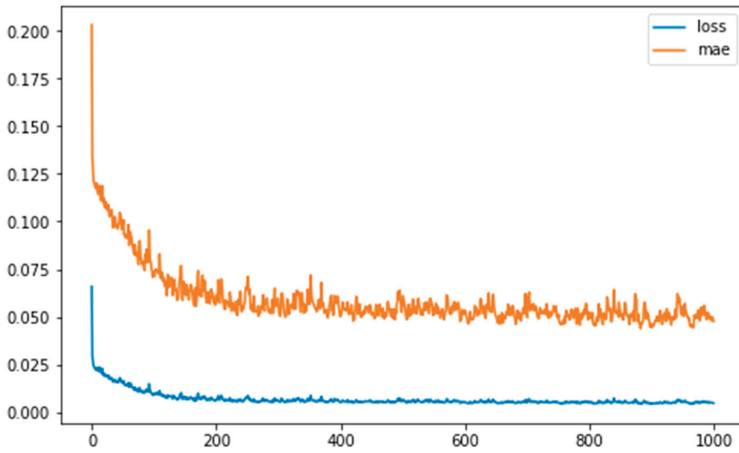
**Table 1.** MLP network structure parameter list.

Structure	Parameter
Number of layers	3
Number of Neurons in the layers	Input = 2, Hidden1 = 32, Hidden2 = 32 Output = 1
Initial weights and biases	Random
Activation function	Sigmoid
Optimization	Adam

From the existing literature, we already know the approximate location and direction of the underground tunnel in reality. The results of the MLP study show that a few (three layers) 2D-ERT data to predict the 3D ERT data can be seen and that the location of the tunnel is consistent with the actual location.

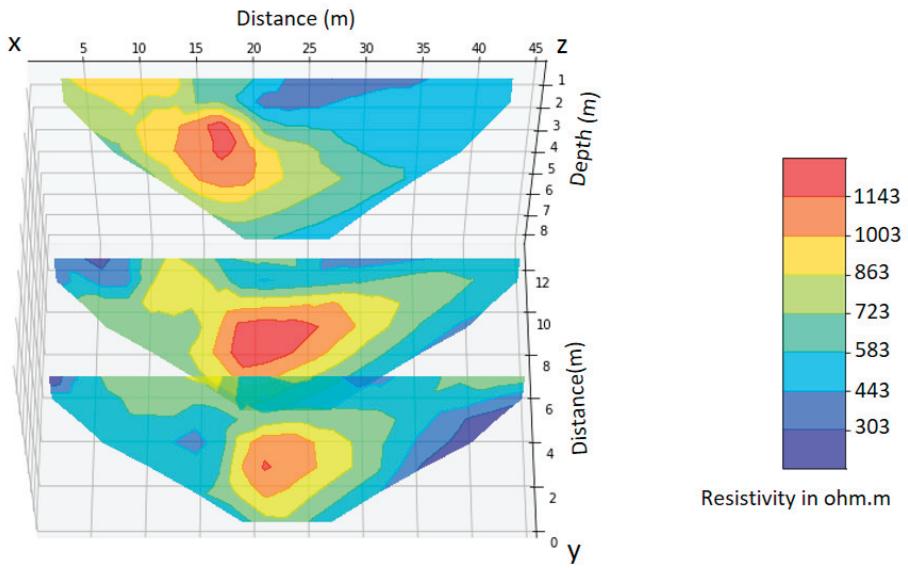


(a)

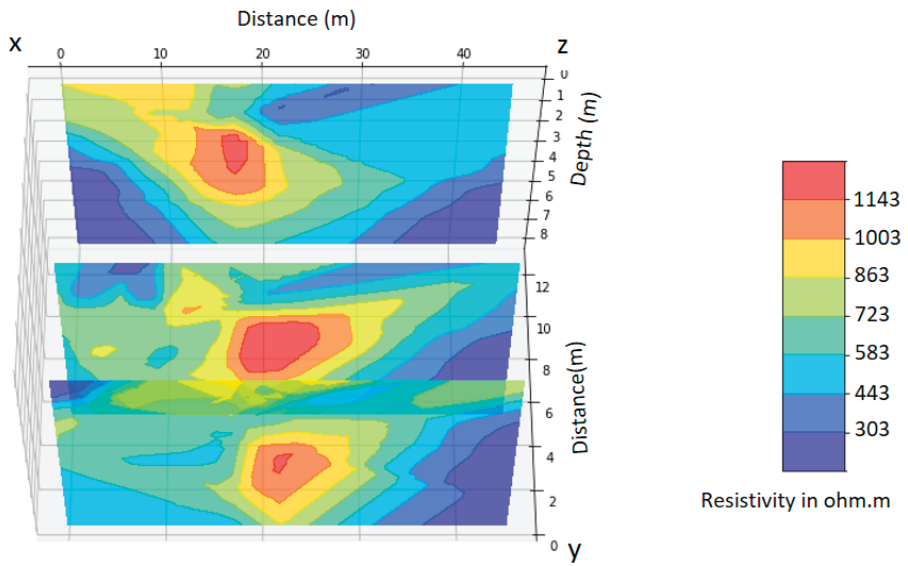


(b)

Figure 9. Cont.



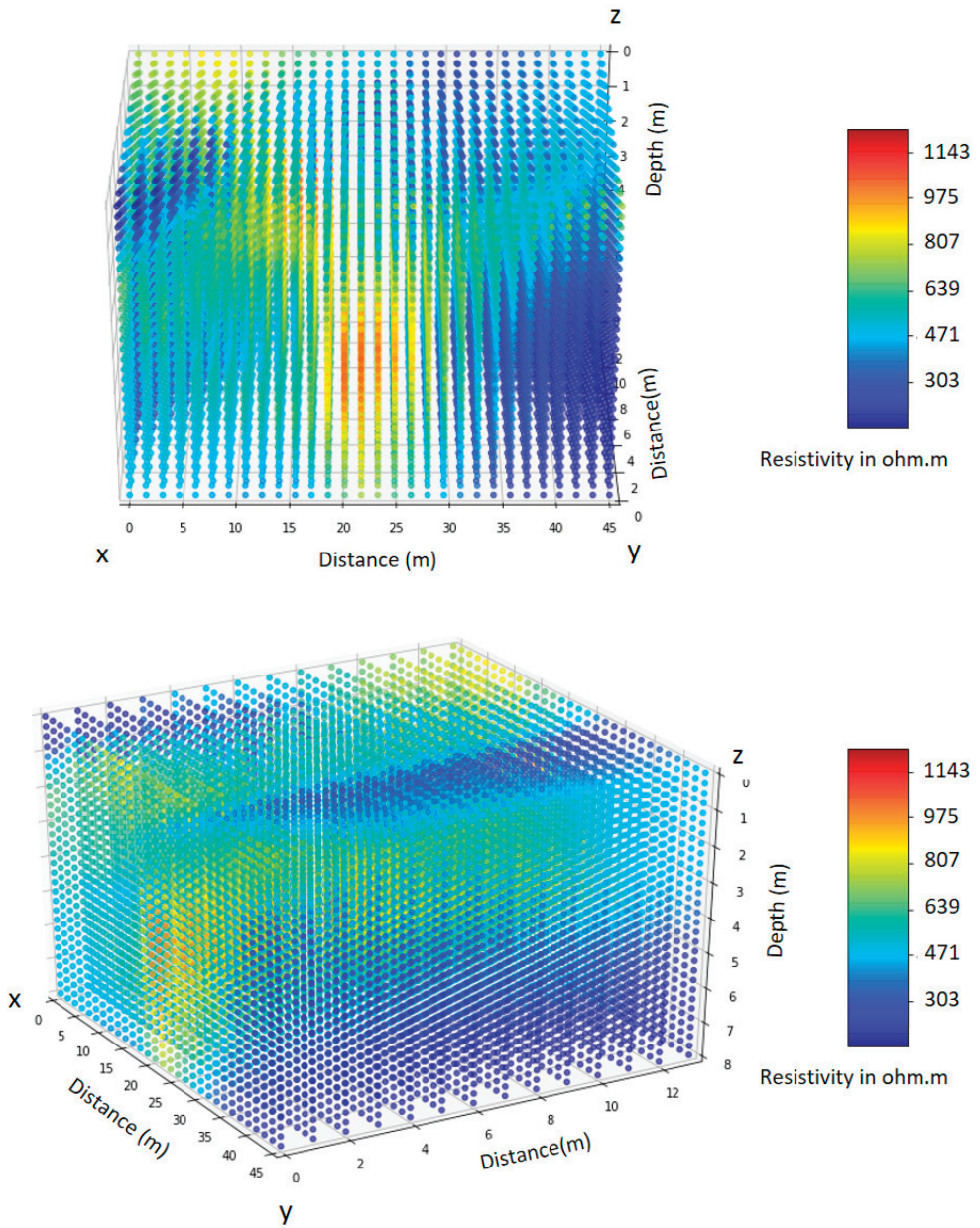
(c)



(d)

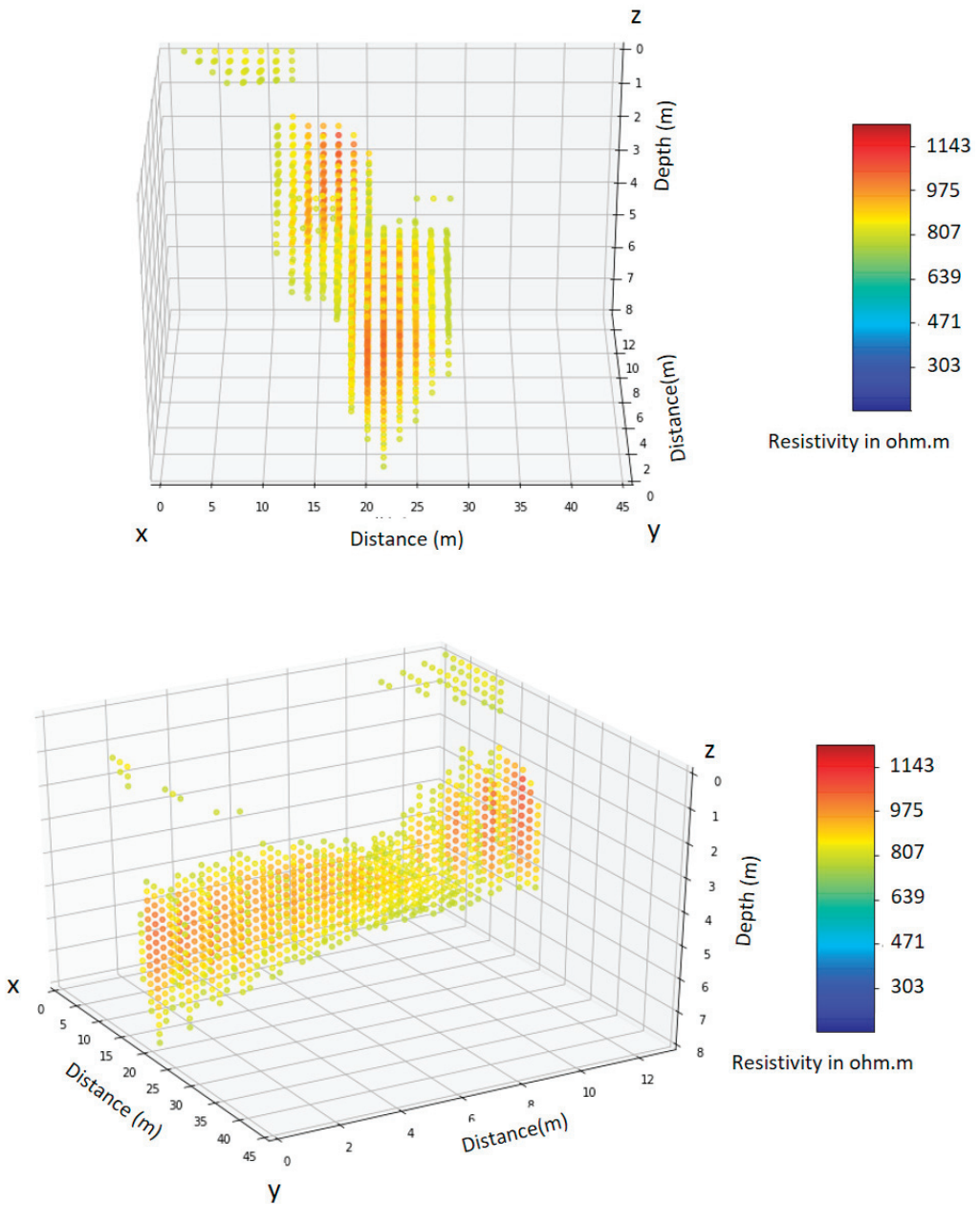
Figure 9. Cont.





(f)

Figure 9. Cont.



(g)

**Figure 9.** Deep learning prediction results (a–g). (a) Original data of L1, L2, and L3; (b) Error rate of MLP network training process; (c) Result of the original data of L1, L2, and L3 after MLP data prediction; (d) Result of unknown regions of L1, L2, and L3 after MLP data prediction; (e) Result of successive profiles after MLP data prediction; (f) Result of 3D resistivity model; (g) MLP predicted tunnel location and path.

## 5. Conclusions

Most of the extensively hidden underground tunnels in Kinmen Island have been abandoned and unoccupied to avoid the damage to human life and property caused by tunnel breakdown and prevent accidental destruction of the precious cultural heritage. This study used 2D-ERT for in situ measurement to find the location of tunnels hidden underground. To test the reliability of 2D-ERT in tunnel survey, a numerical model was built. The actual configuration of the onsite strata and the shape of the underground tunnel were simulated to analyze and validate the accuracy of in situ measurement. In addition, to enhance the measurement result interpretation ability and resolution to determine the actual position and path of the tunnel, this study used an artificial intelligence algorithm to estimate and build a 3D electrical resistivity model.

The results indicate that three survey lines were used for 2D ERT measurement in this study. As the tunnel is a reinforced concrete structure, it is characterized by unlikely electrical conduction and high resistivity, especially in the 2D ERT result. The three survey lines have high resistivity regions in the profiles. According to the numerical simulation result, this high resistivity region is highly likely to be the tunnel location, and the tunnel location, height, and width have been displayed clearly. The three survey lines are displayed in 2.5D mode. The high resistivity regions of various profiles are selected and connected in line, and the selected region and path are similar to in situ tunnel location and path. According to the results of this study, using 2D-ERT to survey underground tunnels is highly feasible.

With the 2D-ERT test result showing a 2D profile, the tunnel location and path cannot be interpreted directly. As the 3D electrical resistivity survey is limited by space, time, and economy, the measurement is not yet frequently used. In recent years, artificial intelligence has been extensively used in various domains. To establish a 3D resistivity map, this study used the MLP of artificial intelligence deep learning algorithm for calculation and used the computational ability of learning, data prediction. The error between the actual value and prediction value of MLP was reduced to complete the building of in situ 3D electrical resistivity model. According to a series of findings, the tunnel location and path can be displayed using an artificial intelligence algorithm. The measurement result interpretation ability and resolution are enhanced effectively. This study can further discuss different types of tunnels in the future to enhance the feasibility of 2D-ERT for underground tunnel surveys.

**Author Contributions:** Conceptualization, Y.-C.H.; methodology, Y.-C.H. and Y.-X.Z.; modelling, W.-C.H.; software, Y.-X.Z. and W.-C.H.; data analysis, Y.-X.Z., W.-C.H. and Y.-C.H.; conclusions, Y.-C.H. and Y.-X.Z.; Field test, W.-C.H. All authors have read and agreed to the published version of the manuscript.

**Funding:** The authors would like to thank the Ministry of Science and Technology of the Republic of China, Taiwan, for financially supporting this research under Project number MOST 109-2221-E-507-004.

**Institutional Review Board Statement:** Not applicable.

**Informed Consent Statement:** Not applicable.

**Data Availability Statement:** Not applicable.

**Conflicts of Interest:** The authors declare no conflict of interest.

## References

1. Chiang, B.W. *Investigation and Research of Kinmen Wars Records*; Kinmen National Park: Kinmen, Taiwan, 2005.
2. The Underground Tunnels Collapsed and Endangered the Houses, Kinmen Daily. 2014. Available online: <https://www.chinatimes.com/realtimenews/20140523003816-260402?chdtv> (accessed on 30 October 2021).
3. The Government Public Works Were Stopped Construction by Underground Tunnels during Excavation, Liberty Times. 2018. Available online: <https://www.kmdn.gov.tw/1117/1271/1272/136247/> (accessed on 30 October 2021).
4. The Government Public Works Were Found Ammunition Galleries during Excavation, Kinmen Daily. 2006. Available online: <https://www.kmdn.gov.tw/1117/1271/1272/136098/?cprint=pt> (accessed on 30 October 2021).

5. Raffaele Persico Salvatore Piro Neil Linford, *Innovation in Near Surface Geophysics*; Elsevier: Amsterdam, The Netherlands, 2018; ISBN 9780128124307.
6. Lin, C.P.; Lin, C.H.; Wu, P.L.; Liu, H.C.; Hung, Y.C. Applications and challenges of near surface geophysicals in geotechnical engineering. *Chin. J. Geophys.* **2015**, *58*, 2664–2680.
7. Lin, C.H.; Lin, C.P.; Hung, Y.C.; Chung, C.C.; Wu, P.L.; Liu, H.C. Application of geophysical methods in a dam project: Life cycle perspective and Taiwan experience. *J. Appl. Geophys.* **2018**, *158*, 82–92. [[CrossRef](#)]
8. Stokoe, K.H.; Joh, S.H.; Woods, R.D. Some contribution of in situ geophysical measurements to solving geotechnical engineering problems. In Proceedings of the 2nd International Geotechnical and Geophysical Site Characterization Conference, ISC-2, Porto, Portugal, 19–22 September 2004; pp. 97–132.
9. Geophysical Survey System, Inc. *Traning Notes*; GSSI Press: Nashua, NH, USA, 1992.
10. Geophysical Survey System, Inc. *RADAN for Windows Version 5.0 User's Manual*; GSSI Press: Nashua, NH, USA, 2003; pp. 1–132.
11. Ribolini, A.; Bini, M.; Isola, I.; Coschino, F.; Baroni, C.; Salvatore, M.C.; Zanchetta, G.; Fornaciati, A. GPR versus geoarchaeological findings in a complex archaeological site (Badia Pozzeveri, Italy). *Archaeol. Prospect.* **2017**, *24*, 141–156. [[CrossRef](#)]
12. Lee, D.H.; Lai, S.L.; Wu, J.H.; Chang, S.K.; Dong, Y.M. Detecting the remaining structure foundation using ground penetrating radar: The outer wall of small east gate of Taiwan FU, Taiwan. *J. GeoEng.* **2018**, *13*, 85–92. [[CrossRef](#)]
13. Baryshnikov, V.D.; Khmelin, A.P.; Denisova, E.V. GPR detection of inhomogeneities in concrete lining of underground tunnels. *J. Min. Sci.* **2014**, *50*, 25–32. [[CrossRef](#)]
14. Li, S.C.; Zhou, Z.Q.; Ye, Z.H.; Li, L.P.; Zhang, Q.Q.; Xu, Z.H. Comprehensive geophysical prediction and treatment measures of karst caves in deep buried tunnel. *J. Appl. Geophys.* **2015**, *116*, 247–257. [[CrossRef](#)]
15. Mochales, T.; Casas, A.M.; Pueyo, E.L.; Pueyo, O.; Román, M.T.; Pocióvi, A.; Soriano, M.A.; Ansón, D. Detection of underground cavities by combining gravity, magnetic and ground penetrating radar surveys: A case study from the Zaragoza area, NE Spain. *Environ. Geol.* **2008**, *53*, 1067–1077. [[CrossRef](#)]
16. Karlovsek, J.; Scheuermann, A.; Willimas, D.J. Investigation of voids and cavities in bored tunnels using GPR. In Proceedings of the 2012 14th International Conference on Ground Penetrating Radar (GPR), Shanghai, China, 4–8 June 2012; pp. 496–501.
17. Gracia, V.P.; Canas, J.A.; Pujades, L.G.; Clapés, J.; Caselles, O.; Garcia, F.; Osorio, R. GPR survey to confirm the location of ancient structures under the Valencian Cathedral (Spain). *J. Appl. Geophys.* **2000**, *43*, 167–174. [[CrossRef](#)]
18. Leucci, G.; Parise, M.; Sammarco, M.; Scardozzi, G. The Use of Geophysical Prospections to Map Ancient Hydraulic Works: The Triglio Underground Aqueduct (Apulia, Southern Italy): GPR and ERT Survey on Ancient Hydraulic Works. *Archaeol. Prospect.* **2016**, *23*, 195–211. [[CrossRef](#)]
19. Dahlin, T. The development of DC resistivity imaging techniques. *Comput. Geosci.* **2001**, *27*, 1019–1029. [[CrossRef](#)]
20. Hung, Y.C.; Chou, H.S.; Lin, C.P. Appraisal of the Spatial Resolution of 2D Electrical Resistivity Tomography for Geotechnical Investigation. *Appl. Sci.* **2020**, *10*, 4394. [[CrossRef](#)]
21. Suzuki, K.; Toda, S.; Kusunoki, K.; Fujimitsu, Y.; Mogi, T.; Jomori, A. Case studies of electrical and electromagnetic methods applied to mapping active faults beneath the thick quaternary. *Eng. Geol.* **2000**, *56*, 29–45. [[CrossRef](#)]
22. Demanet, D.; Renardy, F.; Vanneste, K.; Jongmans, D.; Camelbeeck, T.; Meghraoui, M. The use of geophysical prospecting for imaging active faults in the Roer Graben, Belgium. *Geophysics* **2001**, *66*, 78–89. [[CrossRef](#)]
23. Batayneh, A.; Barjous, M. A Case Study of Dipole-Dipole Resistivity for Geotechnical Engineering from the Ras en Naqab Area, South Jordan. *J. Environ. Eng. Geophys.* **2003**, *8*, 31–38. [[CrossRef](#)]
24. Rizzo, E.; Colellab, A.; Lapenna, V.; Piscitella, S. High resolution images of the fault controlled High Agri Valley basin (Southern Italy) with deep and shallow electrical resistivity tomographies. *Phys. Chem. Earth* **2004**, *29*, 321–327. [[CrossRef](#)]
25. Nguyen, F.; Garambois, S.; Jongmans, D.; Pirard, E.; Loke, M.H. Image processing of 2D resistivity data for imaging faults. *J. Appl. Geophys.* **2005**, *57*, 260–277. [[CrossRef](#)]
26. Pazzi, V.; Morelli, S.; Fanti, R. A Review of the Advantages and Limitations of Geophysical Investigations in Landslide Studies. *Int. J. Geophys.* **2019**, *2019*, 2983087. [[CrossRef](#)]
27. Batayneh, A.; Al-Diabat, A.A. Application of a two dimensional electrical tomography technique for investigating landslides along the Amman-Dead Sea highway, Jordan. *Environ. Geol.* **2002**, *42*, 399–403. [[CrossRef](#)]
28. Perrone, A.; Iannuzzi, A.; Lapenna, V.; Lorenzo, P.; Piscitelli, S.; Rizzo, E.; Sdao, F. High resolution electrical imaging of the Varco d'Izzo earthflow (southern Italy). *J. Appl. Geophys.* **2004**, *56*, 17–29. [[CrossRef](#)]
29. Chen, T.T.; Hung, Y.C.; Hsueh, M.W.; Yeh, Y.H.; Weng, K.W. Evaluating the Application of Electrical Resistivity Tomography for Investigating Seawater Intrusion. *Electronics* **2018**, *7*, 107. [[CrossRef](#)]
30. Nyquist, J.E.; Bradley, J.C.; Davis, R.K. DC resistivity monitoring of potassium permanganate injected to oxidize TCE in situ. *J. Environ. Eng. Geophys.* **1999**, *4*, 135–148. [[CrossRef](#)]
31. Lin, C.-P.; Hung, Y.-C.; Yu, Z.-H. Performance of 2D ERT in Investigation of Abnormal Seepage: A Case Study at the Hsin-Shan Earth Dam in Taiwan. *J. Environ. Eng. Geophys.* **2014**, *9*, 101–112. [[CrossRef](#)]
32. Hung, Y.C.; Chen, T.T.; Tsai, T.F.; Chen, H.X. A Comprehensive Investigation on Abnormal Impoundment of Reservoirs—A Case Study of Qionglin Reservoir in Kinmen Island. *Water* **2021**, *13*, 1463. [[CrossRef](#)]
33. Colucci, P.; Darilek, G.T.; Laine, D.L.; Binley, A. Locating Landfill Leaks Covered with Waste. In Proceedings of the International Waste Management and Landfill Symposium, Sardinia 99, Cagliari, Italy, 4–8 October 1999; Volume 3, pp. 137–140.



34. Binley, A.; Daily, W.; Ramirez, A. Detecting leaks from waste storage ponds using electrical tomographic methods. In Proceedings of the 1st World Congress on Process Tomography, Buxton, UK, 14 April 1999; pp. 6–17.
35. Daily, W.; Ramirez, A.; Binley, A. Remote Monitoring of Leaks in Storage Tanks using Electrical Resistance Tomography: Application at the Hanford Site. *J. Environ. Eng. Geophys.* **2004**, *9*, 11–24. [[CrossRef](#)]
36. Orfanos, C.; Apostolopoulos, G. 2D-3D resistivity and microgravity measurements for the detection of an ancient tunnel in the Lavrion area, Greece. *Near Surf. Geophys.* **2011**, *9*, 449–457. [[CrossRef](#)]
37. Mousavi, H.; Khazaei, S. Detection of underground tunnels using electrical resistivity and refraction seismic tomography methods. *J. Earth Space Phys.* **2016**, *42*, 578–606.
38. Lesparre, N.; Boyle, A.; Grychtol, B.; Cabrera, J.; Marteau, J.; Adler, A. Electrical resistivity imaging in transmission between surface and underground tunnel for fault characterization. *J. Appl. Geophys.* **2016**, *128*, 163–178. [[CrossRef](#)]
39. Loke, M.H. *Tutorial: 2-D and 3-D Electrical Imaging Surveys*; Geotomo Software: Penang, Malaysia, 2004.
40. Pouyanfar, S.; Sadiq, S.; Yan, Y.; Tian, H.; Tao, Y.; Reyes, M.P.; Shyu, M.L.; Chen, S.C.; Iyengar, S.S. A survey on deep learning: Algorithms, techniques, and applications. *ACM Comput. Surv. (CSUR)* **2018**, *51*, 1–36. [[CrossRef](#)]
41. Alile, O.M.; Aigbogun, C.O.; Enoma, N.; Abraham, E.M.; Ighodalo, J.E. 2D and 3D Electrical Resistivity Tomography (ERT) Investigation of Mineral Deposits in Amahor, Edo State, Nigeria. *Niger. Res. J. Eng. Environ. Sci.* **2017**, *2*, 215–231.
42. Alile, O.M.; Abraham, E.M. Three dimensional geoelectrical imaging of the subsurface structure of university of Benin-Edo state Nigeria. *Adv. Appl. Sci. Res.* **2015**, *6*, 85–93.
43. Bentley, L.R.; Gharibi, M. Resistivity Imaging at a Heterogeneous Two and Three Dimensional Electrical Remediation Site. *Geophysics* **2004**, *69*, 674–680. [[CrossRef](#)]
44. Chávez, R.E.; Cifuentes Nava, G.; Tejero, A.; Hernández Quintero, J.E.; Vargas, D. Special 3D electric resistivity tomography (ERT) array applied to detect buried fractures on urban areas: San Antonio Tecómilt, Milpa Alta, México. *Geofísica Int.* **2014**, *53*, 425–434. [[CrossRef](#)]
45. Osinowo, O.O.; Falufosi, M.O. 3D Electrical Resistivity Imaging (ERI) for subsurface evaluation in pre engineering construction site investigation. *NRIAG J. Astron. Geophys.* **2018**, *7*, 309–317. [[CrossRef](#)]
46. Geotomo Software 2002. RES2DMOD Ver. 3.01, Rapid 2D Resistivity forward Modelling Using the Finite Difference and Finite-Element Methods. Available online: <https://www.geotomosoft.com/index.php> (accessed on 30 October 2021).
47. Geotomo Software 2007. RES2DINV Ver. 3.56, Rapid 2D Resistivity and IP Inversion Using the Least Squares Method. Available online: <https://www.geotomosoft.com/index.php> (accessed on 30 October 2021).
48. Russell, S.; Norvig, P. Artificial Intelligence: A Modern Approach. 2002. Available online: <https://storage.googleapis.com/pub-tools-public-publication-data/pdf/27702.pdf> (accessed on 30 October 2021).
49. Rojas, R. *Neural Networks: A Systematic Introduction*; Springer Science & Business Media: Berlin/Heidelberg, Germany, 2013.
50. Nilsson, N.J. *Principles of Artificial Intelligence*; Morgan Kaufmann: Burlington, MA, USA, 2014.
51. LeCun, Y.; Bengio, Y.; Hinton, G. Deep learning. *Nature* **2015**, *521*, 436–444. [[CrossRef](#)] [[PubMed](#)]
52. Goodfellow, I.; Bengio, Y.; Courville, A. *Deep Learning*; MIT Press: Cambridge, MA, USA, 2016.
53. Kingma, D.P.; Ba, J.L. Adam: A Method for Stochastic Optimization. In Proceedings of the International Conference on Learning Representations, San Diego, CA, USA, 7–9 May 2015; pp. 1–13.
54. Heusel, M.; Ramsauer, H.; Unterthiner, T.; Nessler, B.; Hochreiter, S. GANs Trained by a Two Time Scale Update Rule Converge to a Local Nash Equilibrium. *Adv. Neural Inf. Processing Syst.* **2017**, *30*, 1–12.

## Article

# The Use of Machine Learning and Satellite Imagery to Detect Roman Fortified Sites: The Case Study of Blad Talh (Tunisia Section)

Nabil Bachagha <sup>1,\*</sup>, Abdelrazek Elnashar <sup>2</sup>, Moussa Tababi <sup>3</sup>, Fatma Souei <sup>4</sup> and Wenbin Xu <sup>1</sup><sup>1</sup> The School of Geo-Science and Info-Physics, Central South University, Changsha 410006, China<sup>2</sup> Department of Natural Resources, Faculty of African Postgraduate Studies, Cairo University, Giza 12613, Egypt<sup>3</sup> Faculty of Letters and Humanities of Sousse, University of Sousse, FLSHS-LR, Sousse 13ES11, Tunisia<sup>4</sup> Department of Computer Science, Hunan University, Changsha 410082, China

\* Correspondence: bachaghanabil@csu.edu.cn

**Abstract:** This study focuses on an ad hoc machine-learning method for locating archaeological sites in arid environments. Pleiades (PIB) were uploaded to the cloud asset of the Google Earth Engine (GEE) environment because they are not yet available on the platform. The average of the SAR data was combined with the PIB image in the selected study area called Blad Talh at Gafsa, which is located in southern Tunisia. This pre-desert region has long been investigated as an important area of Roman civilization (106 BCE). The results show an accurate probability map with an overall accuracy and Kappa coefficient of 0.93 and 0.91, respectively, when validated with field survey data. The results of this research demonstrate, from the perspective of archaeologists, the capability of satellite data and machine learning to discover buried archaeological sites. This work shows that the area presents more archaeological sites, which has major implications for understanding the archaeological significance of the region. Remote sensing combined with machine learning algorithms provides an effective way to augment archaeological surveys and detect new cultural deposits.

**Keywords:** archaeological; machine learning; Google Earth Engine; remote sensing; fortified sites

**Citation:** Bachagha, N.; Elnashar, A.; Tababi, M.; Souei, F.; Xu, W. The Use of Machine Learning and Satellite Imagery to Detect Roman Fortified Sites: The Case Study of Blad Talh (Tunisia Section). *Appl. Sci.* **2023**, *13*, 2613. <https://doi.org/10.3390/app13042613>

Academic Editor: Tung-Ching Su

Received: 20 January 2023

Revised: 10 February 2023

Accepted: 12 February 2023

Published: 17 February 2023



**Copyright:** © 2023 by the authors. Licensee MDPI, Basel, Switzerland. This article is an open access article distributed under the terms and conditions of the Creative Commons Attribution (CC BY) license (<https://creativecommons.org/licenses/by/4.0/>).

## 1. Introduction

Similar to most research-driven fields, archaeology fundamentally depends on the following two precious and scarce resources: time and money [1]. Archaeologists often travel long distances to reach areas of interest and devote a considerable amount of time to excavations and surveys. Additionally, the discovery of archaeological sites is among the most time-consuming and labour-intensive activities. Archaeologists often use advanced technologies to search for less expensive and faster methodologies for archaeological research. Southern Tunisia is a vast region with difficult access to the investigation area and limited opportunities for in-person data collection. Consequently, land managers spend precious and dwindling resources conducting expensive surveys that result in very few representative samples. One way to address this problem is to develop survey strategies that focus on archaeological potential. Satellite image analysis is a relatively low-cost method with great potential for addressing these needs. The application of remote sensing technology is an effective method for producing relatively complete records of archaeological settlement patterns and human activity at the landscape scale. The literature concerning archaeological remote sensing (RS) has shown that multispectral satellite sensors and airborne LiDAR are particularly useful for addressing survey coverage and positioning issues [2–7]. In many regions worldwide, RS has been used to detect and map archaeological proxy indicators [8–12] by leveraging multisource imagery and spatial pattern analyses. RS technologies enable the discovery of new sites and maps

of ancient remnants and can be used to assist with the digital reconstruction of ancient monuments and their environmental backgrounds. For example, in Mediterranean regions, such as Greece and Croatia, several studies have demonstrated excellent performance using a variety of passive and active remote sensing data (including multispectral imagery, thermal images, and UAV-based LiDAR data) to identify ancient Roman remains [13–17]. Fonte et al. [18] evaluated and debated the use of digital modelling tools in northwestern Iberia to identify and define Roman roads through GIS-based spatial analyses.

In recent years, RS-based progressive archaeological studies have steadily integrated machine-learning algorithms that enable automated feature finding [19]. Most applications of these methods have focused on small-scale feature detection using LiDAR [20–22] or WorldView satellite data [8,23,24]. In the east, Menze and Ur [25] applied a random forest (RF) classifier to a multitemporal collection of ASTER imagery to classify probable anthrosols. In the Cholistan Desert, Hector et al. [19] applied an RF classifier that integrates a multisensor, multitemporal machine learning approach to detecting archaeological mounds, and Abdulmalik et al. [26,27] used an artificial neural network model combined with a geographic information system (GIS) and remote sensing for surface water detection. Other studies have used multiple types of information to identify archaeological remains or threats to archaeological heritage, such as urban sprawl and archaeological looting [28–30]. Combined with machine learning algorithms, remote sensing provides an effective way to expand investigation areas and detect new cultural deposits [31–34]. In particular, the application of this technology allows researchers to (1) investigate remote areas that are not easy to access due to harsh geography and (2) survey vast and complex environments (characterised, for example, by otherwise challenging topography). Platforms, such as Google Earth Engine (GEE) [35], provide a scalable, cloud-based, geospatial retrieval and processing platform, particularly in remote areas with little or almost no ground information. Google Earth Engine is a cloud-based platform that makes it simple to access high-performance computing resources for covering geospatial datasets. Once an algorithm is developed on GEE, users can produce regular data products or deploy interactive applications powered by Google Earth Engine resources. Archaeologists have only recently begun to search for more complex models, drawing on innovative analysis of spatial and statistical computing and machine learning methods [36,37]. To date, these studies are increasing when dealing with the detection of archaeological sites based on high-resolution satellite or drone imagery and in pottery classification [38–40]. Several studies have applied different methods for the identification of buried structures [5,41]. For instance, in arid or desert environments, satellite remote data provides very reliable results that can be used to analyse archaeological sites and their environments. According to previous research, there are more Roman civilisation sites in this area [8], but only a few have been uncovered by remote sensing methods and identified the major distinguishing features of Roman settlements, such as villa and tower walls. In this context, the discovery of archaeological features using machine learning classification algorithms has emerged as one of the most important topics regarding remote sensing; it is an important method to better understand and reconstruct ancient landscapes. Thus far, these topics have mainly been studied by experts, sometimes with the help of automated tools, which results in a very costly and time-consuming process. Therefore, in recent years, many automation methods combining satellite image processing with machine learning models have been developed [19,42–45].

Due to the difficult geography, the investigation of ancient sites in this region is not easy; therefore, machine learning via satellite can play an important role in the detection and documentation of archaeological sites. The aim of this study is to evaluate the potential offered by the combined use of remote sensing data and machine learning to discover fortified sites in arid areas. An innovative aspect of our approach is the combination of very high spatial resolution satellite (PB1) technology with SAR data for better detection and to help obtain enhanced results.

## 2. Materials and Methods

### 2.1. Study Area

The study area is positioned in Blad Talh (see Figure 1). The weather is hot, and the average temperature is 19.6 °C; the location receives less than 100 mm of precipitation annually [46,47]. The climate is characterised by extremely irregular rainfall that varies across seasons and within the same season. The alternation of rainy and dry years occurs without a defined pattern, and periods of prolonged drought often occur. The location of Blad Talh (between 34°26′8.18″ N and 34°21′36.52″ N and between 9°20′3.93″ E and 9°30′56.12″ E) is shown in Figure 1. It is formed by a series of high plains that are separated by mountains and gradually descend towards the south. Blad Talh has a maximum height of 1165 metres and is characterised by a unique morphology. Blad Talh has been the subject of several studies, mostly geological in nature, that assessed the tectonic and structural formation of two mountain ranges, the Orbita-Bouhedma and Chemsî-Belkhir. Despite its geographical position, located less than 40 km from the Mediterranean and more than 100 km north of the Sahara, Blad Talh is part of pre-Saharan Tunisia, bordered to the north by the Orbita-Bouhedma link, and is classified in the arid bioclimatic stage. This region played an important historical role in the Roman era and was part of the sensitive defence system (Limes) located along the desert border, as attested by the several forts that provided protection [8,46–49]. Many sites that appear to be military structures—forts or towers of various sizes—have been identified at these locations based on their layouts and the methods used to construct them. The study area, Blad Talh, was a region of great importance in Roman times. In a report by Toussaint on the campaign of 1902–1903 [50], we found that the fortification of KSAR GROUECH was especially important. The general assessment of this report leads to the conclusion that the Roman ruins in the region of Blad Talh are very numerous in the plains and much rarer and even less important in the mountainous regions.

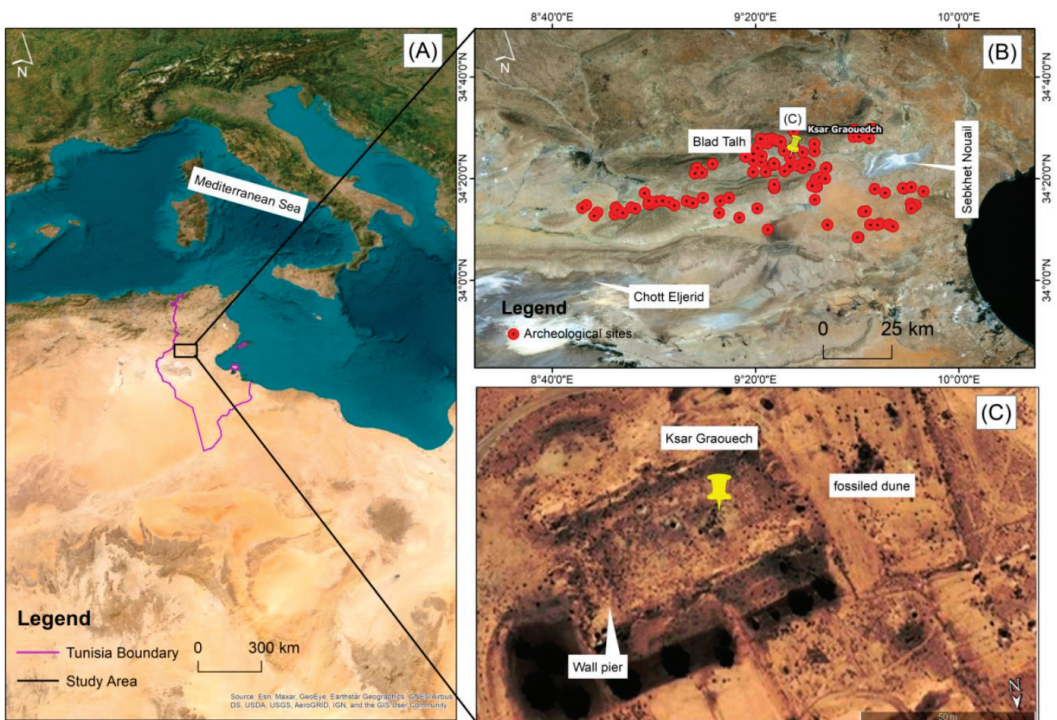


**Figure 1.** (A) Study area location in Tunisia (North Africa); (B) Archaeological sites in the Roman Fort area; (C) Fort of KSAR GRAOUECH surrounding wall and remains.

### 2.2. Methodology

The study describes the process of archaeological site detection and the development of an integrated approach that includes remote sensing, a geographic information system, and random forest to achieve these objectives. First, we selected Blad Talh for this research because of the authenticated archaeological remains and the opportunity to gather survey information for this project in November 2021. In total, 101 known archaeological sites are located in Sebkheth Nouail (Figure 1B). Based on a field survey of the entire study area, the archaeological sites in this area were classified. After the field sample collection was carried out by GNSS, satellite imagery was used to locate the archaeological sites at each selected location using ArcGIS based on the actual locations identified by the GNSS instrument. The second step is to use very high resolution (VHR) data to delineate and map study area sites, as well as Sentinel-1 data, which is used as input to help achieve better results. For geometric corrections, these images were imported into the ArcGIS 10.4 package using WGS 84 and UTM zone 32. In the third step, a random forest was applied using a combination of VHR and SAR data in this study, while employing Google Earth Engine as a platform to decrease the computational time and avoid any other barriers. These sensors were a crucial factor in ensuring that the features that would generate values analogous to those of spots in one source were distinguished from the other features. The final step was survey validation and determining archaeological site significance using remote sensing-based archaeological surveys. Remote sensing, machine learning, and GNSS allow us to identify unknown sites and provide new directions for future archaeological research in our study area in the ancient Roman period. The overall methodology is presented in Figure 2, while the specifics of each major section are given in the subsequent sections.

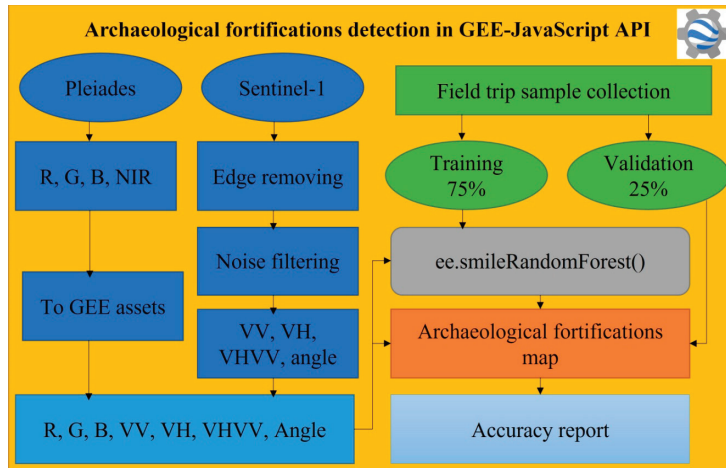


Figure 2. Framework approach.

### 2.3. Field Investigation Sample Collection

We selected Blad Talh for this research because of the authenticated archaeological remains and the opportunity to gather survey information for this project. The database recaptured from the historic record of the region allowed an overview of the literature review of the Roman period. The GIS integration of the results of these different steps was critical to planning a systematic field survey focused on specific areas of interest, for which the primary results are presented. In November 2021, the search team arrived at the study area of interest. A number of ceramic African sigils were found at these sites. Along these roads, we have classified these sites of interest as being Roman fortified structures based on the ancient remains observed at these sites. By coordinating our findings with GIS, remote sensing, and machine learning, the importance of these new fortifications allowed

speculation regarding their ancient conditions. By confirming our results with remote sensing images and machine learning, we aimed to study the spatial distributions of the archaeological remains and reconstruct the Roman settlement in the region.

## 2.4. Data Preprocessing

### 2.4.1. Pleiades

These images were obtained from the Pleiades sensor (P1B) in a strip of the Blad Talh region with the simultaneous acquisition of panchromatic and multispectral information in the Universal Transverse Mercator (UTM) planar projection, Zone 32 N, and WGS 84 datum on 16 July 2021. Of course, the two sets of bands had two different geometric resolutions (Table 1). While the multispectral bands had a ground resolution of 2.14 m, we used 2.14 \* 2.14 m/px. The acquisition in the multispectral mode was subdivided into the following four bands of the spectrum: NIR, red, green, and blue. In the first stage of the analysis, P1B images were used to study the archaeological landscape [51] and highlight the most important areas where the cartographic features were determined (boundaries, forts, sites, etc.).

**Table 1.** Pleiades data from Blad Talh acquired on 16 July 2021.

Band Name	Wavelength (nm)	Spatial Resolution (m)
Blue	430–550	2.14
Green	500–620	2.14
Red	590–710	2.14
Near-infrared	740–940	2.14

### 2.4.2. Sentinel-1

Sentinel-1 (S1) in the band C imagery contains a 12- or 6-day revisit cycle depending on the availability of images 1A and 1B with 10 m spatial resolution. The analysis presented here selected the interferometric wide swath mode, which is the main operational mode and produces data in single (HH or VV) or double (HH + HV or VV + VH) polarisation in both ascending and descending modes. Each scene available at GEE was preprocessed using the Sentinel-1 Toolbox to (1) remove low-intensity noise and invalid data from scene edges and (2) remove thermal noise [19]. The edge of S1 was omitted using the ‘connected components’ method in GEE, which hides sets of contiguous pixels processed with values less than  $-25$  dB in the VV polarisation [52,53]. The VV and VH noises were filtered using the refined Lee filter [54]. We collected S1 data on 13 and 18 July 2021. In this study, the mean of both images was combined with the Pleiades image. In addition, Sentinel-1 data helped obtain better results. SAR is able to reflect the soil’s roughness, texture, and the different physical conditions of the ground. Another benefit of using SAR is that it has a certain amount of soil penetration in dry sand, which makes it particularly suitable for this specific area.

### 2.4.3. Processing Environment

The Google Earth Engine (GEE) platform is currently a free answer to the matter of restricted access to processing power [19,35]. GEE is a cloud-based platform that enables a planetary-scale analysis of petabytes of freely obtainable satellite imagery. Combining this large amount of information with the parallel computing strength of Google’s infrastructure facilitates the rapid and easy evaluation of satellite images. GEE parallelises and executes code developed in JavaScript or Python, exploiting Google’s cloud computing infrastructure and allowing work with intensive processes at new scales. This study used GEE for the following three reasons: (1) it is a free platform that has many built-in functions for geospatial analysis and provides quick results without downloading datasets to a local storage system; (2) it has been widely used in several environmental studies [55–57]; and (3) it uses one processing environment and may reduce the uncertainties introduced by various techniques, such as temporal aggregation, resampling (e.g., downscaling and

upsampling), and data reprojection. Notably, the final results from the GEE could be used to create maps (raster.tif) and tables (table.csv) in Google Drive for further processing in the Google Collaboratory (Colab) cloud service [58]. Pleiades bands (blue, green, red, and NIR) were uploaded to the cloud asset of the GEE environment because they are not yet available in the Earth Engine. Thus, the overall framework of the research can be applied to other regions to achieve related aims.

#### 2.4.4. Random Forest Classifier and Accuracy Report

Several artificial intelligence models can be used to process geospatial data when searching for sites in different environments [34,59–62]. The present study aims to detect and map fortified archaeological sites using an integrated method composed of RS data, GIS, field surveys, and a random forest algorithm. The steps of this model followed to classify archaeological sites included categorising the image composite, collecting training data, training the classifier model, and validating the classifier with a separated dataset. We use a selection of 101 archaeological sites linked in Blad Talh’s investigation on pre-desert zones as our training ( $n = 76$ ) and confirmation ( $n = 25$ ) sets. Notwithstanding the existence of quality problems in Blad Talh’s data, we sort out those sites that might be evidently specified and precisely situated in the high-resolution imagery obtainable in GEE. These matched up with large and well-preserved sites. Polygons were drawn in GEE to outline the areas of the designated sites from which pixel values in the image composite could be extracted for algorithm training. The random forest classification algorithm was applied in this study [56,63,64]. An RF classifier was chosen for the GEE machine-learning implementation. The RF establishes a number of 128 trees on preliminary training samples, but it takes every split in a tree into consideration. For instance, a new subset of predictors is considered randomly in every split when splitting nodes. In addition, the average of the resulting trees helps to evade overfitting and is therefore more stable and reliable than the other decision tree-based classifiers [63,65]. Moreover, RF classifiers can handle a small number of training samples, and it is possible to get the number of votes for each class. These are two advantages that are particularly useful for RS-based archaeology with limited land-use and cover information. In the current GEE algorithm, the RF is combined with trees, which is considered a sufficient value to gain perfect results without unnecessarily increasing the computational cost. The probability mode of the RF was set to evaluate, filter, and refine the results to ameliorate the algorithm’s detection potential.

Usually, 75% of the samples are used for the training tree, while the remaining 25% are used for confirmation [63,65]. Herein, the machine-learning process went through three iterations. The original iteration of the algorithm generated pleasant results in that it had the ability to explicitly categorise known sites used as training data and many potential sites by high RF probability values. However, two additional iterations were necessary to adjust the pixels to higher percentages that did not correspond to archaeological sites. RF classifier analysis is a probability domain in bitmap format, where each value records the probability that a given pixel is a “vulnerable site.” The RF probability limit for the site values was determined after careful examination of the test data on high-resolution images, which produced a raster map of the clusters (“fortified sites”). A higher threshold resulted in better identification of large, clear sites, but many small pixel clusters corresponding to the small sites covered were lost. Confusion metrics were used to calculate RF accuracy, including the overall accuracy and kappa coefficient. Several researchers demonstrated the perfect application of the GEE platform for training and applied an RF classifier due to its high performance [19,66].

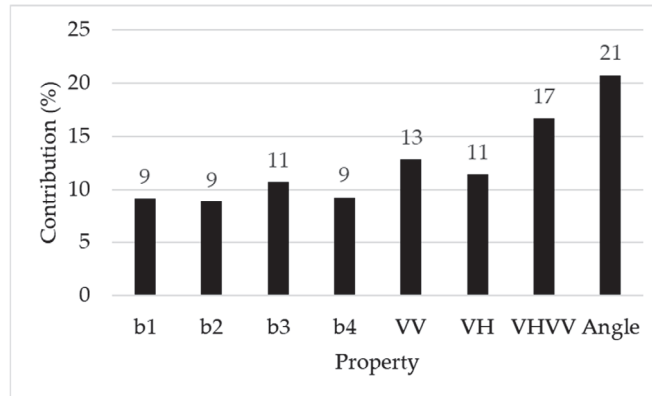
### 3. Results

Using the proposed methodology, we succeeded in detecting fortified sites that were previously unknown in Blad Talh. The automated detection of fortified sites exhibited high accuracy, equal to that of human detection. The results show that machine learning performed with high accuracy (see Table 2).

**Table 2.** Classification results of the study area.

Type	Overall Accuracy	Kappa Coefficient
Validation	0.93	0.91

The image combines SAR bands (a single VV and VH and a dual VH–VV band) and P1B bands (b1–b4) (as shown in Figure 3). The high-quality P1B and Sentinel-1 bands are not affected by specific environmental or vision conditions.

**Figure 3.** Feature importance in the classification model.

To the best of our understanding, as of mid-2021, the P1B image received on 16 July 2021 was the most current VHR optical satellite image covering Blad Talh that was accessible online through the GEE. The GEE and machine learning have proven to be applicable instruments for automatically detecting archaeological sites in satellite images. The GEE, machine learning, and remote sensing were highly effective at the site scale and identified pixels of archaeological remains. Furthermore, pixels of fortified structures were successfully detected in Blad Talh, confirming the ability of the GEE to quickly run an analysis on a substantial scale. The discovery and distribution of archaeological sites extended towards the southern part of the Blad Talh area and the surrounding pre-desert towards the east, which was a region that was relatively unreachable in past investigations. Predictably, the allocation of the fortified sites detected by the algorithm was concentrated in the Blad Talh area. Sentinel-1 texture differences between layers were accentuated in the area (see Figure 3).

The algorithm's ability to detect fortified archaeological sites is likely due to polarisation bands and the capacity of the SAR C-band to penetrate soil. Because of vegetation and sand cover, the RF potential produced only some well-illustrated square shapes. The majority of the newly proposed fortified sites presented segmented square shapes or amorphous groups of pixels. It is quite possible that in addition to these five detection sites, there are also remains of sand-covered archaeological sites with low RF probability values. Notably, when high-resolution visible images were used, the algorithm still assisted in identifying small pixels or backscattering. SAR alone showed no significant change in land cover. As a result, SAR alone cannot give enough information to identify archaeological sites. Also, the Pleiades images are not capable of segregating the spectral structures of the sites on their own using an RF classifier. Furthermore, our algorithm was designed to integrate Sentinel-1 and PB1 images for better archaeological discovery, an approach that showed accurate results (see Figure 4). Comparing the results between high-resolution imagery PB1 without SAR images and the virtual absence of sites, their combination for archaeological detection of the known fortified site was used as a validation set (see Figure 4). When possible, the new detection was matched to previous research on past archaeological sites [8,47,67]. The



archaeological sites relative to the existence of sand dunes suggested that many more sites can be covered or located underground in the pre-desert, and thus, the aeolian sediments in southern Tunisia may have played an important role in both the field records of the area and the discernibility of the archaeological ruins. Regions with a large number of sites were located in open mudflats that were distributed throughout the area, while many sites were still relatively covered underground. Five newly detected fortified sites were identified (see Figure 5). The distribution of the archaeological sites extended towards the southern part of the Blad Talh area and the surrounding pre-desert towards the east, which was a region that was relatively unreachable in past investigations. The resulting cluster of high-RF probability pixels showing fortified sites was used to rebuild the regions. Image interpretation was performed using P1B, SAR data, and machine learning. The blend of these data secured enough environmental variability and time to estimate and determine the potential extent of the fortified sites that the algorithm specified. Because of the sand cover, the RF probability yielded only a few well-defined square shapes. Most of the newly proposed sites present fragmentary square shapes and elongated bands of pixels. It is quite possible that in addition to these discovered sites, there are also the remains of archaeological sites covered by sand or shrub vegetation with low RF probability values. It is worth emphasizing that the algorithm helped to identify small groups of site pixels.

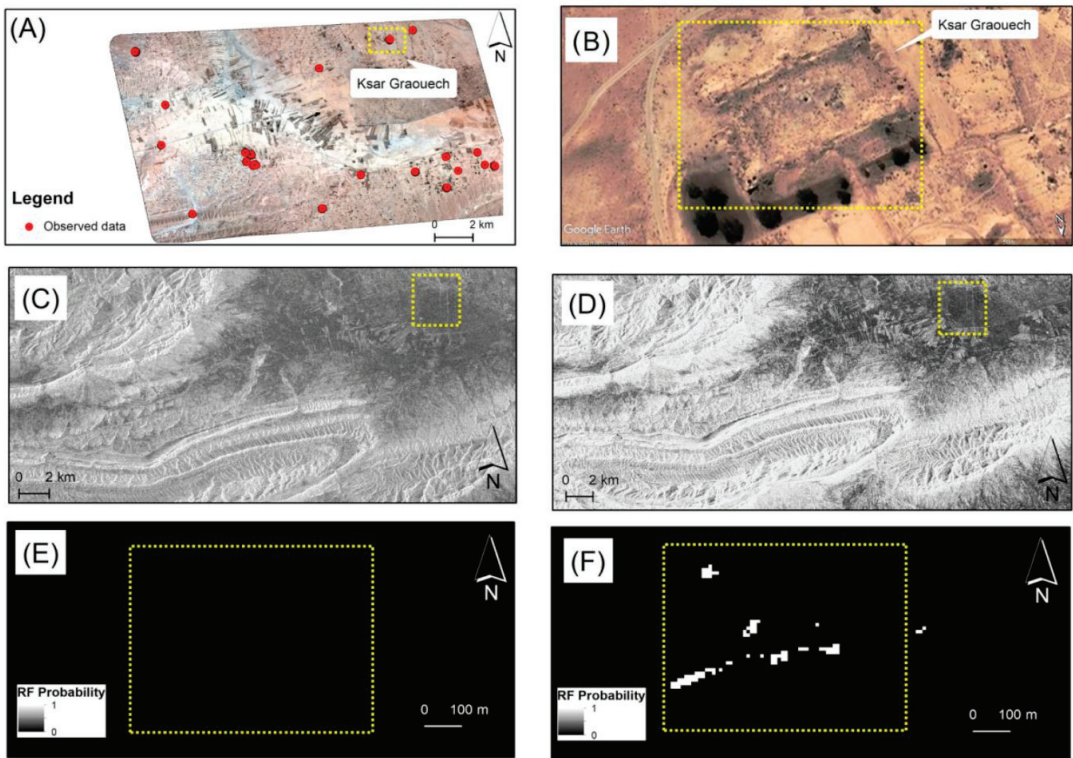


**Figure 4.** (A) The study area, showing the distribution of sites. (B) A Google Earth base map locating a well-preserved fort. (C) Dual Sentinel-1 band [VV, VH] in ascending mode. (D) Single Sentinel-1 band [VV] in ascending mode. Results of the RF classifier: (E) Visible high-resolution PB1 imagery without SAR images compared to the virtual absence of sites. (F) An example of SAR images combined with PB1 that detected a known fortified site used as a validation set; note that the white dots scattered through the region indicate high-RF probability sites.

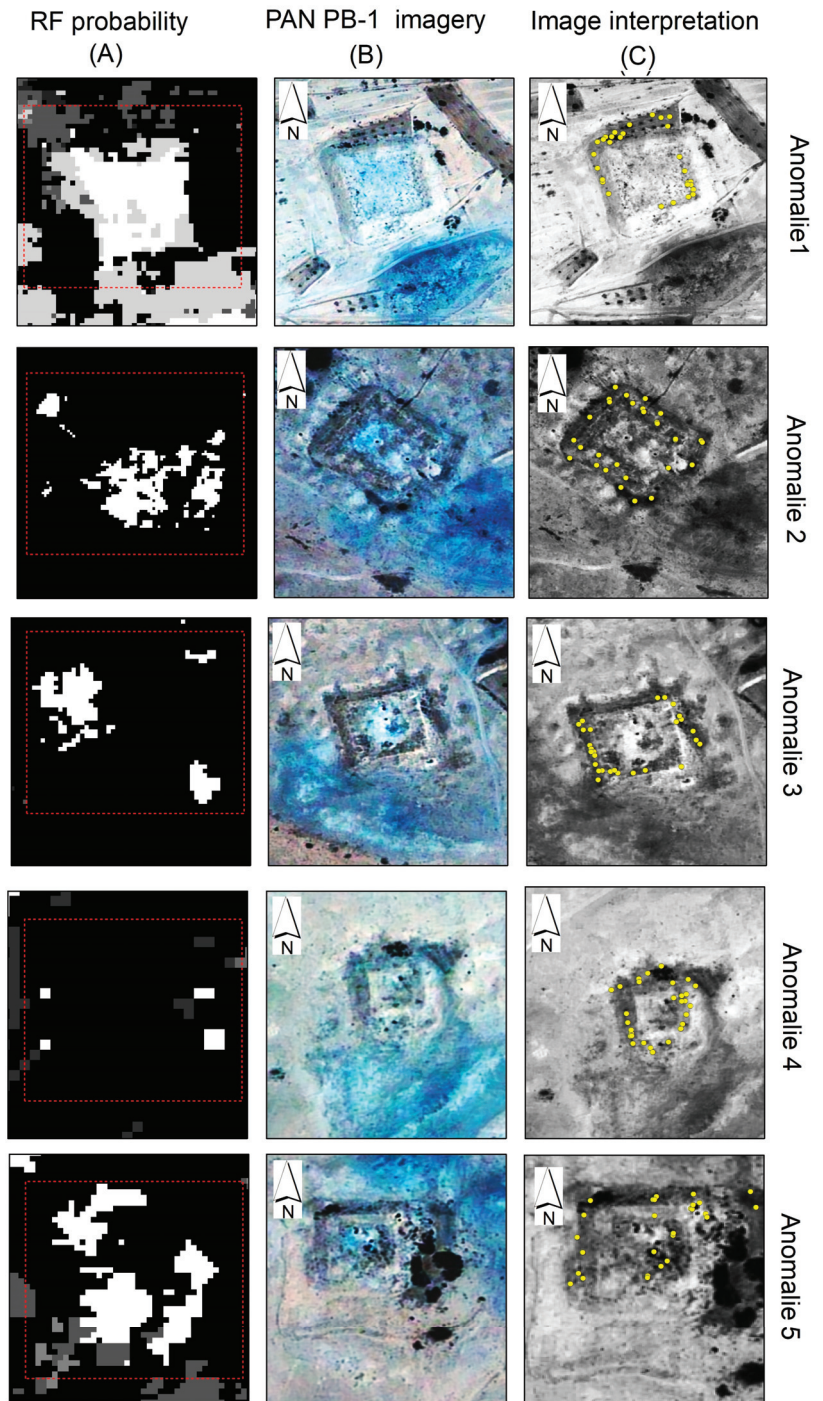


**Figure 5.** RF probability results. (A) Illustration of fortified detection sites. (B) Clustering of high-probability pixels in the area showing the detection structures of fortified sites. (C) Pan sharpened Pleiades imagery. Image was interpreted as signifying the existence of a fort hidden underground.

#### 4. Discussion

The RF method, which has been used in the classification of remote sensing data since the early 2000s, was chosen as the classification algorithmic rule for this study due to its simplicity of implementation, robustness, and possible predictability [63,68,69]. The challenge we faced was the discovery of fortified sites. Our objective was to develop a straightforward yet efficient methodology that combined remote sensing techniques and automated archaeological remains discovery, as well as to evaluate the potential offered by the combined use of remote sensing data and machine learning to discover fortified sites in arid areas. Using a substantive approach, we confirmed an advantage similar to that of other applications of machine learning techniques, and we show that the RF potential field-detected sites may be considered ancient settlements. In this research, given the high likelihood of improvement in the classification accuracy, we assessed the RF's performance in a wider context (different archaeological features or sites). As shown in the results section, the performance of the RF classifier is highly satisfactory, with a kappa coefficient of 0.91 and a precision and overall accuracy of 0.93 in the "fortified site group." The RF potential area highlights five unknown locations shown on historical maps. The sites are partly hidden by sand, and the RF potential only shows different parts of the structures' fortified sites, which was verified by a field survey. The discovery of these sites is very important because it documents the existence of ancient Roman fortifications. Based on previous studies, there are more sites of Roman civilisation in this area [8,47], and only some small sites have been uncovered by remote sensing methods. Currently, new sites could be included with those previously identified and dated by Bachagha et al. [8,47,67]. To try to understand the changes in the settlement distribution over time, research in southern Tunisia documented all sites encountered, including those of the Roman era. Considering that most of the previously reported sites were settlements attributed to periods of Roman civilisation, there is a high possibility that most of the newly discovered sites were also occupied during the same period. Fortified structures such as fortresses and defensive works are fairly common features of the archaeological landscape in southern Tunisia. Such features have previously been uncovered in the city of Gafsa. In this study, we were able to locate five fortified sites situated south of the Blad Talh area. The fortified sites were built on approximately level ground in a nearly square form that is covered by sand dunes. The layout showed visible signs of erosion on all sides, and loot pits were visible, especially on the south side. Based on our findings in the literature, we propose a suitable reconstruction of the ancient settlement in Gafsa, indicating that the fortifications in the locale were a defence project planned to defend, protect, and control the Limes [8,70–74]. We found fortified sites located in the same area and close to each other, in contrast to previous research [8]. The fortified sites were separated by a distance of approximately 2.5 km. From the machine learning and PIB data of the study area, a red-dashed line rectangle can be seen in Figure 5. Using machine learning and PIB data surveying, we demonstrate the detection of hidden fortified sites in Gafsa, which is well-situated across the frontier of the Roman or Byzantine era in southern Tunisia.

##### *Surveys: Validation and Archaeological Site Significance*

Building on recent advances in digital image analysis and feature detection, we developed an RF algorithm that allows the automated detection of these types of enclosures in Pleiades images with high resolution and Sentinel-1 for better archaeological detection. We also used SAR images to increase the accuracy of classification, which provided good results. In addition, we only used the Google Earth Engine for the view, so we cannot use it for building a machine learning detection model. We successfully used the RF model to detect new sites in satellite imagery. The model detected these sites, which we verified and confirmed in the field. We built the training dataset using both Pleiades and Sentinel-1 images in the Google Earth Engine. Of course, the identification of any object or location as archaeological remains based on images requires confirmation from the ground. The discovered sites described above were confirmed in the area of Blad Talh in southern

Tunisia by machine learning, remote sensing data, and field investigation. Other than the surrounding wall and the ruins of the fortified sites, no other archaeological ruins were seen above ground. Almost all the visual features in the analysed RF results were determined to be micro-topographical results of archaeological importance. As a result, our approach reveals a different layout of archaeological sites, and the algorithms identified structures in the area very well. In November 2021, the exploration team arrived at sites approximately 10 km north of the suspected location of the ancient Roman fortification, KSAR GRAOUECH (a square-shaped mark). Each side of the suspected location was measured to be around 50 m long. These anomalies have no intact walls, but the remains of some wall piers were investigated to identify anomalies. Shards of ancient ceramics were scattered among the walls, and their environs date back to the Roman period, as shown in Figure 6G,I,N,L. Buried walls at these five fortified sites were also unearthed, representing the appearance of concealed remains, as shown in Figure 6C,E,H,J,M. The field investigation conducted in this region reveals the existence of a farm dating back between the Roman Empire and Byzantine times based on the discovery of tiles and shards of ancient ceramics from the Roman period. These fortified sites are situated between Capsa (Gafsa) and the coastal towns of Iunci and Lariscus. Controlling one of the passes to the north would have been of obvious strategic importance during the Roman era, a consideration that strongly supports their inclusion in the list of official fortifications of that period. In addition, these sites have common topographical and archaeological features, and their dimensions are relatively similar to each other. According to Trouset [74], these fortified sites are widely spread in the rear Limes area and are located on the immediate edge of a Roman road or in a control location of a passage; some have been identified as military works that are a part of the defensive system. In the report by Rebuffat et al. [75], these were probably fortified farms that adopted a plan inspired by the military project. The parallels between military architecture and these fortified sites, namely Mattingly Qsur, are very evident in the adoption of the rectangular form with towers projecting from two or four facades [76]. The results of studies investigating this type of site in Fazzan and Cyrenaica in eastern and western Libya, respectively, confirm that the peak occupation of fortified sites occurred after the end of the third century and continued in some regions in later times. More specifically, the majority were occupied between the 4th and 6th centuries (350–540 AD) [77].

Indeed, the general landscape of the Blad Talh was a highly important part of the ancient Roman period. As a result, based on our fortified sites and the literature, we firmly conclude that Blad Talh has played a critical historical role in migration between ancient cities located in current-day north and south Tunisia, as attested by the caravan roads. It was also a part of the sensitive defence system (Limes) located along the desert border, as attested by the several forts that protected the area (Figure 7).

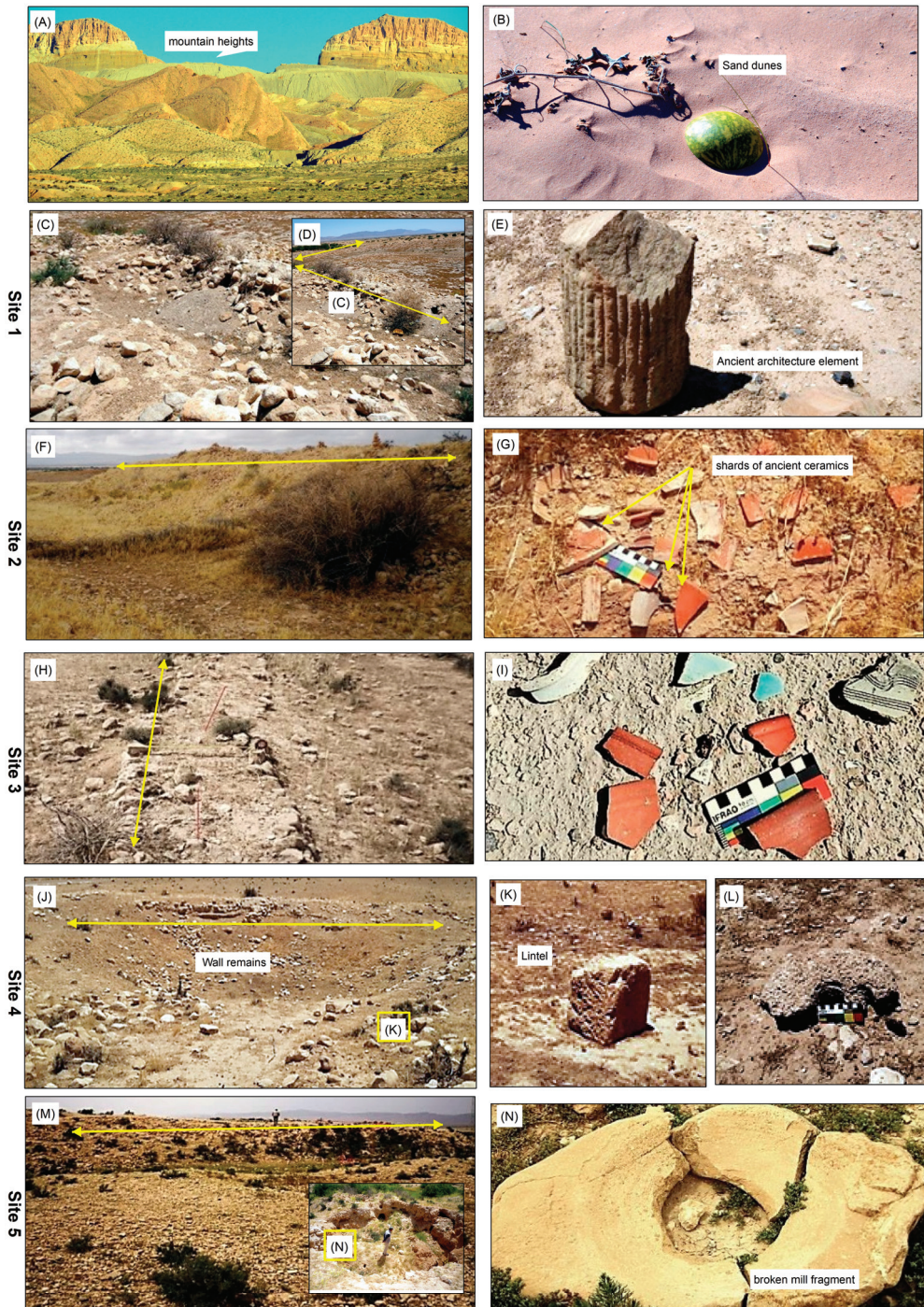


**Figure 6.** Magnified views of anomalies 1 to 5. (A,B) Landscape of the study area. (G,I,N,L) Shards of ancient ceramics. (E) Ancient Architecture element (K) Lintel photographed at the entrance to a fortress. (C,D,F,H,J,M) Field photos of wall remains.

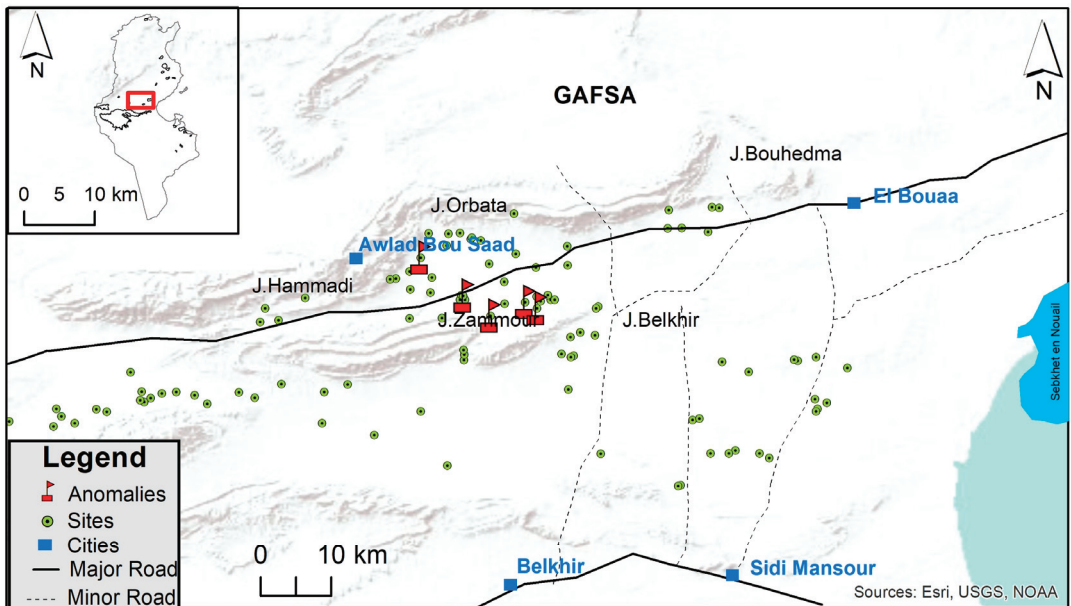


**Figure 7.** Comprehensive archaeological map of the Blad Talh landscape in the ancient Roman period: localities and ancient road networks. Modified from [71].

## 5. Conclusions

In summary, we present an integrated workflow that combines SAR images and optical Pleiades imagery with basic spatial analysis in the Google Earth Engine for automatically detecting fortified sites. The random forest-based approach demonstrates that it is a useful tool for overcoming problems with data size and structure. Our research illustrates the applicability of this detection technique to fortifications and demonstrates that it is possible to automate fortification discoveries for the first time in Tunisia. It is possible to summarise insights and knowledge directly from the data, and the algorithm is able to highlight relationships between archaeological sites. The machine-learning algorithm we use is capable of identifying all the currently known sites in the study area and the accurate locations of new fortified sites. The approach provides outputs that are significantly superior to those obtained with a single-source RS technique. RS-based applications in arid and semi-arid regions elsewhere can benefit from the integration of globally available Pleiades and Sentinel data into an accessible, flexible, and repeatable GEE environment to perform and evaluate machine learning workflows. Even though the approach shows accurate results, the limited availability of VHR data and the expense to obtain the data are considered a limitation of this study that can be improved in the future. Archaeological data, along with landscape analysis and mapping items affecting site visibility, indicates that these are only a few of the fortified sites in the region, many of which may be covered by sand in the surveyed area. We discovered fortified sites hidden by thick vegetation and confirmed these sites using field investigation, remote sensing, and machine learning. The outcome of the work presented here provides advances in the technology and archaeology domains. Technologically, using these methods, various derived models are used to evaluate their abilities in investigating the micro-topography of a site of archaeological importance under a sand dune. The results viewed from an archaeological perspective are interesting. The machine learning-based method enabled us to detect five fortified sites for which only some data was obtainable from past records and shed new light on the fortified KSAR GROUECH structure dating back to the Byzantine period (6th century), for which only the presence of a fort was well-known. The findings are validated by on-site

processing, demonstrating that the automatic procedure can identify and extract the major distinctive characteristics of Roman settlements, such as villas and tower walls. Notably, the exploration elaborated in this research is promising in terms of technological invention. By providing for previous quantitative examinations in this region, our exploration raises awareness of the need to use quantitative styles to address more pressing questions, similar to those about the protection and preservation of threatened archaeological sites. As a result, one of the benefits of this research is that it demonstrates, from the perspective of archaeologists, the capability of satellite data and machine learning to discover buried archaeological sites. While this study focuses on archaeological sites in southern Tunisia, the proposed approach is effective in terms of time and cost, particularly in locations where data availability is scarce. Validation of this approach was proved using the nature and characteristics of the study area, and we expect that the classification accuracy of our approach would be further improved by using a convolutional neural network (CNN) and images obtained by the Google Earth Engine.

**Author Contributions:** Conceptualisation: N.B., W.X. and A.E.; methodology, A.E. and N.B.; software, N.B. and A.E.; validation, N.B., W.X. and A.E.; formal analysis, N.B., W.X. and A.E.; investigation, N.B., M.T. and A.E.; resources, W.X., N.B., and M.T.; data curation, N.B., M.T., A.E., F.S.; writing—original draft preparation, N.B., W.X., A.E., M.T., W.X. and F.S.; writing and supervision, W.X. All authors have read and agreed to the published version of the manuscript.

**Funding:** This work was supported by the National Natural Science Foundation of China (No. 42174023).

**Institutional Review Board Statement:** Not applicable.

**Informed Consent Statement:** Not applicable.

**Data Availability Statement:** Sentinel-1 data are available via the European Space Agency’s Copernicus Open Access Hub <https://scihub.copernicus.eu/> (accessed on 13 July 2021).

**Conflicts of Interest:** The authors have no conflict of interest to declare.

## References

- Giardino, M.; Haley, B.S. Airborne Remote Sensing and Geospatial Analysis. In *Remote Sensing in Archaeology: An Explicitly North American Perspective*; University of Alabama Press: Tuscaloosa, AL, USA, 2006; pp. 47–77.
- Chase, A.F.; Chase, D.Z.; Fisher, C.T.; Leisz, S.J.; Weishampel, J.F. Geospatial revolution and remote sensing LiDAR in Mesoamerican archaeology. *Proc. Natl. Acad. Sci. USA* **2012**, *109*, 12916–12921. [[CrossRef](#)] [[PubMed](#)]
- Lasaponara, R.; Masini, N. Image Enhancement, Feature Extraction and Geospatial Analysis in an Archaeological Perspective. In *Satellite Remote Sensing*; Springer: Berlin/Heidelberg, Germany, 2012; pp. 17–63.
- Leisz, S.J. An Overview of the Application of Remote Sensing to Archaeology during the Twentieth Century. In *Mapping Archaeological Landscapes from Space*; Springer: New York, NY, USA, 2013; pp. 11–19.
- Luo, L.; Wang, X.; Guo, H.; Lasaponara, R.; Zong, X.; Masini, N.; Wang, G.; Shi, P.; Khatteli, H.; Chen, F.; et al. Airborne and spaceborne remote sensing for archaeological and cultural heritage applications: A review of the century (1907–2017). *Remote Sens. Environ.* **2019**, *232*, 111280. [[CrossRef](#)]
- Verhoeven, G.J. Are we there yet? A review and assessment of archaeological passive airborne optical imaging approaches in the light of landscape archaeology. *Geosciences* **2017**, *7*, 86. [[CrossRef](#)]
- Verschoof-van der Vaart, W.B.; Lambers, K. Applying automated object detection in archaeological practice: A case study from the southern Netherlands. *Archaeol. Prospect.* **2022**, *29*, 15–31. [[CrossRef](#)]
- Bachagha, N.; Wang, X.; Luo, L.; Li, L.; Khatteli, H.; Lasaponara, R. Remote sensing and GIS techniques for reconstructing the military fort system on the Roman boundary (Tunisian section) and identifying archaeological sites. *Remote Sens. Environ.* **2020**, *236*, 111418. [[CrossRef](#)]
- Beck, A.; Philip, G.; Abdulkarim, M.; Donoghue, D. Evaluation of Corona and Ikonos high resolution satellite imagery for archaeological prospection in western Syria. *Antiquity* **2007**, *81*, 161–175. [[CrossRef](#)]
- Orengo, H.; Krahtopoulou, A.; Garcia-Molsosa, A.; Palaiochoritis, K.; Stamati, A. Photogrammetric re-discovery of the hidden long-term landscapes of western Thessaly, central Greece. *J. Archaeol. Sci.* **2015**, *64*, 100–109. [[CrossRef](#)]
- Parcak, S. Satellite remote sensing methods for monitoring archaeological tells in the Middle East. *J. Field Archaeol.* **2007**, *32*, 65–81. [[CrossRef](#)]
- Masini, N.; Lasaponara, R. Sensing the Past from Space: Approaches to Site Detection. In *Sensing the Past*; Springer: Berlin/Heidelberg, Germany, 2017; pp. 23–60.

13. Barceló, J.A.; De Almeida, V. Functional analysis from visual and non-visual data. an artificial intelligence approach. *Mediterr. Archaeol. Archaeom.* **2012**, *12*, 273–321.
14. Hatzopoulos, J.N.; Stefanakis, D.; Georgopoulos, A.; Tapinaki, S.; Pantelis, V.; Liritzis, I. Use of Various Surveying Technologies to 3d Digital Mapping and Modelling of Cultural Heritage Structures for Maintenance and Restoration Purposes: The Tholos in Delphi, Greece. *Mediterr. Archaeol. Archaeom.* **2017**, *17*, 311–336.
15. Kaimaris, D. Ancient theaters in Greece and the contribution of geoinformatics to their macroscopic constructional features. *Sci. Cult.* **2018**, *4*, 9–25.
16. Kaimaris, D. Utilization of Different Sensors in Uav for The Detection and Optimal Visual Observation of the Marks over Buried Ancient Remains. *Sci. Cult.* **2022**, *8*, 129–146.
17. Popović, S.; Bulić, D.; Matijašić, R.; Gerometta, K.; Boschian, G. Roman Land Division in Istria, Croatia: Historiography, Lidar, Structural Survey and Excavations. *Mediterr. Archaeol. Archaeom.* **2021**, *21*, 165–178.
18. Fonte, J.; Parcero-Oubiña, C.; Costa-García, J. A GIS-Based Analysis of the Rationale behind Roman Roads. In *The Case of the So-Called via XVII (NW Iberian Peninsula)*; Mediterranean Archaeology and Archaeometry: Mytilene, Greece, 2017; Volume 17, pp. 163–189.
19. Orengo, H.A.; Conesa, F.C.; Garcia-Molsosa, A.; Lobo, A.; Green, A.S.; Madella, M.; Petrie, C.A. Automated detection of archaeological mounds using machine-learning classification of multisensor and multitemporal satellite data. *Proc. Natl. Acad. Sci. USA* **2020**, *117*, 18240–18250. [[CrossRef](#)] [[PubMed](#)]
20. Guyot, A.; Hubert-Moy, L.; Lorho, T. Detecting Neolithic burial mounds from LiDAR-derived elevation data using a multi-scale approach and machine learning techniques. *Remote Sens.* **2018**, *10*, 225. [[CrossRef](#)]
21. Martins, K.; Blenkinsopp, C.E.; Power, H.E.; Bruder, B.; Puleo, J.A.; Bergsma, E.W.J. High-resolution monitoring of wave transformation in the surf zone using a LiDAR scanner array. *Coast. Eng.* **2017**, *128*, 37–43. [[CrossRef](#)]
22. Evans, D.; Fletcher, R. The landscape of Angkor Wat redefined. *Antiquity* **2015**, *89*, 1402–1419. [[CrossRef](#)]
23. Biagetti, S.; Merlo, S.; Adam, E.; Lobo, A.; Conesa, F.C.; Knight, J.; Bekrani, H.; Crema, E.R.; Alcaina-Mateos, J.; Madella, M. High and medium resolution satellite imagery to evaluate late Holocene human–environment interactions in arid lands: A case study from the Central Sahara. *Remote Sens.* **2017**, *9*, 351. [[CrossRef](#)]
24. Thabeng, O.L.; Merlo, S.; Adam, E. High-resolution remote sensing and advanced classification techniques for the prospection of archaeological sites’ markers: The case of dung deposits in the Shashi-Limpopo Confluence area (southern Africa). *J. Archaeol. Sci.* **2019**, *102*, 48–60. [[CrossRef](#)]
25. Cigna, F.; Tapete, D.; Lasaponara, R.; Masini, N. Amplitude change detection with ENVISAT ASAR to image the cultural landscape of the Nasca region, Peru. *Archaeol. Prospect.* **2013**, *20*, 117–131. [[CrossRef](#)]
26. Assaf, A.T.; Sayl, K.N.; Adham, A. Surface Water Detection Method for Water Resources Management. *J. Phys. Conf. Ser.* **2021**, *1973*, 012149. [[CrossRef](#)]
27. Muneer, A.S.; Sayl, K.N.; Kamal, A.H. Modeling of spatially distributed infiltration in the Iraqi Western Desert. *Appl. Geomat.* **2021**, *13*, 467–479. [[CrossRef](#)]
28. Agapiou, A.; Lysandrou, V.; Hadjimitsis, D.G. Optical remote sensing potentials for looting detection. *Geosciences* **2017**, *7*, 98. [[CrossRef](#)]
29. Cigna, F.; Tapete, D. Tracking human-induced landscape disturbance at the nasca lines UNESCO world heritage site in Peru with COSMO-SkyMed InSAR. *Remote Sens.* **2018**, *10*, 572. [[CrossRef](#)]
30. Tapete, D.; Cigna, F.; Donoghue, D. ‘Looting marks’ in space-borne SAR imagery: Measuring rates of archaeological looting in Apamea (Syria) with TerraSAR-X Staring Spotlight. *Remote Sens. Environ.* **2016**, *178*, 42–58. [[CrossRef](#)]
31. Bennett, R.; Cowley, D.; De Laet, V. The data explosion: Tackling the taboo of automatic feature recognition in airborne survey data. *Antiquity* **2014**, *88*, 896–905. [[CrossRef](#)]
32. Davis, D.S. Object-based image analysis: A review of developments and future directions of automated feature detection in landscape archaeology. *Archaeol. Prospect.* **2019**, *26*, 155–163. [[CrossRef](#)]
33. LiDAR, A.M.D.U. Object-Based Image Analysis in Beaufort County, SC. *Southeast. Archaeol.* **2019**, *38*, 23–37.
34. Trier, D.; Cowley, D.; Waldeland, A.U. Using deep neural networks on airborne laser scanning data: Results from a case study of semi-automatic mapping of archaeological topography on Arran, Scotland. *Archaeol. Prospect.* **2019**, *26*, 165–175. [[CrossRef](#)]
35. Gorelick, N.; Hancher, M.; Dixon, M.; Ilyushchenko, S.; Thau, D.; Moore, R. Google Earth Engine: Planetary-scale geospatial analysis for everyone. *Remote Sens. Environ.* **2017**, *202*, 18–27. [[CrossRef](#)]
36. Gualandi, M.L.; Gattiglia, G.; Anichini, F. An open system for collection and automatic recognition of pottery through neural network algorithms. *Heritage* **2021**, *4*, 140–159. [[CrossRef](#)]
37. Sayl, K.N.; Sulaiman, S.O.; Kamel, A.H.; Muhammad, N.S.; Abdullah, J.; Al-Ansari, N. Minimizing the impacts of desertification in an arid region: A case study of the west desert of Iraq. *Adv. Civ. Eng.* **2021**, *2021*, 5580286. [[CrossRef](#)]
38. Caspari, G.; Crespo, P. Convolutional neural networks for archaeological site detection—Finding “princely” tombs. *J. Archaeol. Sci.* **2019**, *110*, 104998. [[CrossRef](#)]
39. Chen, L.; Priebe, C.E.; Sussman, D.L.; Comer, D.C.; Megarry, W.P.; Tilton, J.C. Enhanced archaeological predictive modelling in space archaeology. *arXiv* **2013**, arXiv:1301.2738.
40. Garcia-Molsosa, A.; Orengo, H.A.; Lawrence, D.; Philip, G.; Hopper, K.; Petrie, C.A. Potential of deep learning segmentation for the extraction of archaeological features from historical map series. *Archaeol. Prospect.* **2021**, *28*, 187–199. [[CrossRef](#)] [[PubMed](#)]



41. Lasaponara, R.; Masini, N. Identification of archaeological buried remains based on the normalized difference vegetation index (NDVI) from Quickbird satellite data. *IEEE Geosci. Remote Sens. Lett.* **2006**, *3*, 325–328. [CrossRef]
42. Duporge, I.; Isupova, O.; Reece, S.; Macdonald, D.W.; Wang, T. Using very-high-resolution satellite imagery and deep learning to detect and count African elephants in heterogeneous landscapes. *Remote Sens. Ecol. Conserv.* **2021**, *7*, 369–381. [CrossRef]
43. Fiorucci, M.; Khoroshiltseva, M.; Pontil, M.; Traviglia, A.; Del Bue, A.; James, S. Machine learning for cultural heritage: A survey. *Pattern Recognit. Lett.* **2020**, *133*, 102–108. [CrossRef]
44. Yaworsky, P.M.; Vernon, K.B.; Spangler, J.D.; Brewer, S.C.; Coddling, B.F. Advancing predictive modeling in archaeology: An evaluation of regression and machine learning methods on the Grand Staircase-Escalante National Monument. *PLoS ONE* **2020**, *15*, e0239424. [CrossRef]
45. Akinosho, T.D.; Oyedele, L.O.; Bilal, M.; Ajayi, A.O.; Delgado, M.D.; Akinade, O.O.; Ahmed, A.A. Deep learning in the construction industry: A review of present status and future innovations. *J. Build. Eng.* **2020**, *32*, 101827. [CrossRef]
46. Khanoussi, M. Note sur la date de promotion de Capsa (Gafsa, en Tunisie) au rang de colonie romaine (Note d'information). *Comptes Rendus Séances L'Académie Inscr. Belles-Lett.* **2010**, *154*, 1009–1020. [CrossRef]
47. Bachagha, N.; Xu, W.; Luo, X.; Masini, N.; Brahmi, M.; Wang, X.; Souei, F.; Lasaponara, R. On the Discovery of a Roman Fortified Site in Gafsa, Southern Tunisia, Based on High-Resolution X-Band Satellite Radar Data. *Remote Sens.* **2022**, *14*, 2128. [CrossRef]
48. Tissot, C. Géographie comparée de la province romaine d'Afrique, 261. *Paris* **1884**, *8*, 160.
49. Euzennat, M. Quatre années de recherches sur la frontière romaine en Tunisie méridionale. *Comptes Rendus Séances L'Académie Inscr. Belles-Lett.* **1972**, *116*, 7–27. [CrossRef]
50. Toussaint, P.-M.; Guéneau, L.L.J. Résumé des Reconnaissances Archéologiques Exécutées par les Officiers des Brigades Topographiques d'Algérie et de Tunisie Pendant la Campagne 1903-1904», in BCTH. pp. 223–241. Available online: [https://scholar.google.com/scholar?hl=en&as\\_sdt=0%2C5&q=PM+Toussaint%2C+LLJ+Gu%C3%A9neau++1904&btnG=](https://scholar.google.com/scholar?hl=en&as_sdt=0%2C5&q=PM+Toussaint%2C+LLJ+Gu%C3%A9neau++1904&btnG=) (accessed on 19 January 2023).
51. Stewart, C.; Oren, E.D.; Cohen-Sasson, E. Satellite remote sensing analysis of the Qasrawet archaeological site in North Sinai. *Remote Sens.* **2018**, *10*, 1090. [CrossRef]
52. D'Andrimont, R.; Lemoine, G.; van der Velde, M. Targeted grassland monitoring at parcel level using sentinels, street-level images and field observations. *Remote Sens.* **2018**, *10*, 1300. [CrossRef]
53. D'Andrimont, R.; Verhegghen, A.; Lemoine, G.; Kempeneers, P.; Meroni, M.; van der Velde, M. From parcel to continental scale—A first European crop type map based on Sentinel-1 and LUCAS Copernicus in-situ observations. *Remote Sens. Environ.* **2021**, *266*, 112708. [CrossRef]
54. Lee, J.-S. Refined filtering of image noise using local statistics. *Comput. Graph. Image Process.* **1981**, *15*, 380–389. [CrossRef]
55. Elnashar, A.; Zeng, H.; Wu, B.; Fenta, A.A.; Nabil, M.; Duerler, R. Soil erosion assessment in the Blue Nile Basin driven by a novel RUSLE-GEE framework. *Sci. Total Environ.* **2021**, *793*, 148466. [CrossRef]
56. Zeng, H.; Elnashar, A.; Wu, B.; Zhang, M.; Zhu, W.; Tian, F.; Ma, Z. A framework for separating natural and anthropogenic contributions to evapotranspiration of human-managed land covers in watersheds based on machine learning. *Sci. Total Environ.* **2022**, *823*, 153726. [CrossRef]
57. Elnashar, A.; Zeng, H.; Wu, B.; Gebremicael, T.G.; Marie, K. Assessment of environmentally sensitive areas to desertification in the Blue Nile Basin driven by the MEDALUS-GEE framework. *Sci. Total Environ.* **2022**, *815*, 152925. [CrossRef] [PubMed]
58. Carneiro, T.; Da Nobrega, R.V.M.; Nepomuceno, T.; Bian, G.-B.; De Albuquerque, V.H.C.; Filho, P.P.R. Performance analysis of google colab as a tool for accelerating deep learning applications. *IEEE Access* **2018**, *6*, 61677–61685. [CrossRef]
59. Guyot, A.; Lennon, M.; Lorho, T.; Hubert-Moy, L. Combined detection and segmentation of archeological structures from LiDAR data using a deep learning approach. *J. Comput. Appl. Archaeol.* **2021**, *4*, 1. [CrossRef]
60. Kamel, A.H.; Afan, H.A.; Sherif, M.; Ahmed, A.N.; El-Shafie, A. RBFNN versus GRNN modeling approach for sub-surface evaporation rate prediction in arid region. *Sustain. Comput. Inform. Syst.* **2021**, *30*, 100514. [CrossRef]
61. Soroush, M.; Mehrtash, A.; Khazraee, E.; Ur, J.A. Deep learning in archaeological remote sensing: Automated qanat detection in the Kurdistan region of Iraq. *Remote Sens.* **2020**, *12*, 500. [CrossRef]
62. Yang, S.; Luo, L.; Li, Q.; Chen, Y.; Wu, L.; Wang, X. Auto-identification of linear archaeological traces of the Great Wall in northwest China using improved DeepLabv3+ from very high-resolution aerial imagery. *Int. J. Appl. Earth Obs. Geoinf.* **2022**, *113*, 102995. [CrossRef]
63. Breiman, L. Random forests. *Mach. Learn.* **2001**, *45*, 5–32. [CrossRef]
64. Kheir, A.M.; Ammar, K.A.; Amer, A.; Ali, M.G.; Ding, Z.; Elnashar, A. Machine learning-based cloud computing improved wheat yield simulation in arid regions. *Comput. Electron. Agric.* **2022**, *203*, 107457. [CrossRef]
65. Breiman, L. Bagging predictors. *Mach. Learn.* **1996**, *24*, 123–140. [CrossRef]
66. Tuvdendorj, B.; Zeng, H.; Wu, B.; Elnashar, A.; Zhang, M.; Tian, F.; Nabil, M.; Nanzad, L.; Bulkhbai, A.; Natsagdorj, N. Performance and the Optimal Integration of Sentinel-1/2 Time-Series Features for Crop Classification in Northern Mongolia. *Remote Sens.* **2022**, *14*, 1830. [CrossRef]
67. Bachagha, N.; Luo, L.; Wang, X.; Masini, N.; Moussa, T.; Khatteli, H.; Lasaponara, R. Mapping the Roman water supply system of the Wadi el Melah Valley in Gafsa, Tunisia, using remote sensing. *Sustainability* **2020**, *12*, 567. [CrossRef]

68. Gislason, P.O.; Benediktsson, J.A.; Sveinsson, J.R. Random Forest Classification of Multisource Remote Sensing and Geographic Data. In Proceedings of the IGARSS 2004. 2004 IEEE International Geoscience and Remote Sensing Symposium, Anchorage, AK, USA, 20–24 September 2004; IEEE: Piscataway, NJ, USA, 2004.
69. Feng, Q.; Liu, J.; Gong, J. UAV remote sensing for urban vegetation mapping using random forest and texture analysis. *Remote Sens.* **2015**, *7*, 1074–1094. [[CrossRef](#)]
70. Moussa, T. Essai D'identification d'un Oronyme de l'Antiquité Tardive: L'Agalumnus de la Johannide. In *Africa et in Moesia: Borders of the Roman World Sharing Heritage of North Africa and the Lower Danube*; Bucharest University Press and National Commission of Romania for UNESCO: Paris, France, 2021; pp. 107–116.
71. Moussa, T. Bled Talh (Sudtunisien) dans l'Antiquité: l'occupation du Sol. In *Thèse de Doctorat en Histoire Ancienne. (Dir. Abellatif Mrabet)*; FLSH: Sousse, Tunisie, 2020; 365p.
72. Pringle, D. The Defence of Byzantine Africa, from Justinian to the Arab Conquest. In *An Account of the Military History and Archaeology of the African Provinces the Sixth and Seventh Centuries*; International Series; BAR: Oxford, UK, 1981; p. 99.
73. Mrabet, A. Identité de la Tripolitaine Occidentale: De Quelques Signalements Archéologiques. In *Provinces et Identités Provinciales Dans l'Afrique Romaine*; Tables rondes du CRAHM: Caen, France, 2011; pp. 221–237.
74. Troussset, P. *Recherches sur le Limes Tripolitanus du Chott El-Djérid à la Frontière Tuniso-Libyenne*; CNRS: Paris, France, 1974; p. 135.
75. Rebuffat, C.F.R. Les Fermiers du désert Dans L'Africaromana V. In Proceedings of the Attidel V Convegno di Studio, Sassari, Italy, 11–13 December 1988; pp. 35–43.
76. Mattingly, D.J.; Sterry, M.; Leitch, V. Fortified Farms and Defended Villages of Late Roman and Late Antique Africa. 2013. Available online: [https://scholar.google.com/scholar?hl=en&as\\_sdt=0%2C5&q=77.Emrage%2C+A.S.+Roman+Fortified+Farms+%28qsur%29+and+Military+Sites+in+the+Region+of+the+Wadi+Al-Kuf%2C+Cyrenaica+%28Eastern+Libya%29.+Ph.D.+Dissertation%2C+University+of+Leicester%2C+Leicester%2C+UK%2C+2015.&btnG=](https://scholar.google.com/scholar?hl=en&as_sdt=0%2C5&q=77.Emrage%2C+A.S.+Roman+Fortified+Farms+%28qsur%29+and+Military+Sites+in+the+Region+of+the+Wadi+Al-Kuf%2C+Cyrenaica+%28Eastern+Libya%29.+Ph.D.+Dissertation%2C+University+of+Leicester%2C+Leicester%2C+UK%2C+2015.&btnG=) (accessed on 19 January 2023).
77. Emrage, A.S. Roman Fortified Farms (qsur) and Military Sites in the Region of the Wadi Al-Kuf, Cyrenaica (Eastern Libya). Ph.D. Dissertation, University of Leicester, Leicester, UK, 2015.

**Disclaimer/Publisher's Note:** The statements, opinions and data contained in all publications are solely those of the individual author(s) and contributor(s) and not of MDPI and/or the editor(s). MDPI and/or the editor(s) disclaim responsibility for any injury to people or property resulting from any ideas, methods, instructions or products referred to in the content.



## Article

# A Simulation Method of Two-Dimensional Sea-Surface Current Field for Trajectory Crossing Spaceborne SAR

Yan Li <sup>1,2,3</sup>, Jinsong Chong <sup>1,2,3,\*</sup> and Zongze Li <sup>1,2,3</sup>

<sup>1</sup> National Key Lab of Microwave Imaging Technology, Beijing 100190, China; liyan1603@mails.ucas.ac.cn (Y.L.); lizongze20@mails.ucas.ac.cn (Z.L.)

<sup>2</sup> Aerospace Information Research Institute, Chinese Academy of Sciences, Beijing 100190, China

<sup>3</sup> School of Electronics, Electrical and Communication Engineering, University of Chinese Academy of Sciences, Beijing 100049, China

\* Correspondence: lily@mail.ie.ac.cn; Tel.: +86-10-5888-7125

**Abstract:** The trajectory-crossing method is an important and effective method for spaceborne SAR (synthetic aperture radar) to detect a two-dimensional current field. However, in practical applications, there are few spaceborne SAR data that meet the requirements of close acquisition time and overlapping trajectories, which makes it difficult to comprehensively analyze the impact of different systems and environmental parameters on current measurement results from real data processing. With the proposal of a SAR constellation plan in the future, the data resources will be constantly enriched, and the trajectory-crossing method will be widely used. It is, thus, necessary to lay some theoretical foundation at present. A two-dimensional sea-surface-current-field simulation method for trajectory crossing spaceborne SAR is proposed in this paper. Based on the principles of the trajectory-crossing method, the proposed method can realize the simulation of two-dimensional sea-surface-current field under given spaceborne SAR system and environmental parameters. In this paper, the simulation process of this method is given, and the simulation experiment is performed. Compared with the current measurement results of SAR data, the simulation experiment shows that the current velocity error is less than 0.03 m/s and the direction error is less than 10 degrees, which proves the reliability of the proposed simulation method. The proposed method lays a foundation for analyzing the influence of various parameters in the application of the trajectory-crossing method.

**Keywords:** synthetic aperture radar; trajectory-crossing method; sea-surface current; simulation analysis

**Citation:** Li, Y.; Chong, J.; Li, Z. A Simulation Method of Two-Dimensional Sea-Surface Current Field for Trajectory Crossing Spaceborne SAR. *Appl. Sci.* **2022**, *12*, 5900. <https://doi.org/10.3390/app12125900>

Academic Editor: Tung-Ching Su

Received: 17 February 2022

Accepted: 7 June 2022

Published: 9 June 2022

**Publisher's Note:** MDPI stays neutral with regard to jurisdictional claims in published maps and institutional affiliations.



**Copyright:** © 2022 by the authors. Licensee MDPI, Basel, Switzerland. This article is an open access article distributed under the terms and conditions of the Creative Commons Attribution (CC BY) license (<https://creativecommons.org/licenses/by/4.0/>).

## 1. Introduction

As an important ocean dynamic parameter, the sea-surface-current field has a profound impact on climate change, ocean engineering, fishery resources, energy, offshore target detection and so on [1,2]. Therefore, monitoring of ocean currents is becoming crucial. Spaceborne synthetic aperture radar (SAR) has the ability to observe the earth all day, in all weather and at high-resolution, which makes it an important remote-sensing tool that can retrieve the sea-surface-current field.

Currently, along-track interferometry (ATI) [3] and Doppler centroid analysis (DCA) [4] are the two main techniques for spaceborne SAR to detect ocean current fields; however, they can only retrieve the range velocity component of the current, i.e., they cannot directly obtain the current vector—that is, the two-dimensional current field. Generally, two sets of SAR data with crossed trajectories can be used to synthesize the velocity components in two different directions on the overlapping sea-surface area to thus obtain the current vector. This is an important two-dimensional current field detection method, which is denoted as a trajectory-crossing method in this paper.

However, due to the requirement that the overlapping area needs to cover the research scope and as the data acquisition time is close, there are fewer real spaceborne SAR data to meet this feature. The current measurement ability of the trajectory-crossing method is only

verified in some airborne [5] and spaceborne [6] SAR data processing, and there is a lack of further research for the impact of different system and environmental parameters on the current measurement effect. Therefore, simulation is an effective research method. At present, to the best of knowledge, there is no specific simulation method for the trajectory crossing current measurement process.

Due to the complexity of sea-surface electromagnetic scattering, the simulation of sea-surface SAR data usually does not start from the original echo but mainly considers the modeling using wave spectrum and modulation transfer function. In 2000, Romeiser and Thompson [7] proposed a sea-surface Doppler spectrum model based on the improved combined sea-surface model, in which the wave–current interaction and the modulation transmission process of sea-surface backscattering were considered [8,9]. Then, the model was integrated into SAR ocean imaging model and widely used in sea-surface current measurement and simulation [10–12]. Therefore, this model provides a possibility for the simulation of two-dimensional sea-surface-current field for trajectory crossing spaceborne SAR.

Based on the principle of the sea-surface SAR imaging process and trajectory-crossing method, a two-dimensional current field simulation method is proposed in this paper. In the second part, the specific process of the proposed simulation method is given. In the third part, the simulation experiment and verification are conducted. Finally, the above is summarized.

## 2. Simulation Method of Two-Dimensional Sea-Surface Current Field for Trajectory Crossing Spaceborne SAR

The trajectory-crossing method needs to use two sets of spaceborne SAR data with overlapping areas, usually from ascending and descending passes, respectively, and their acquisition time should be close. Geometric relationships of different velocity components of sea-surface motion over overlapping area are shown in Figure 1, where the blue and red thick arrows indicate the flight direction of the ascending and descending satellite, respectively. The sea-surface imaging range is  $S$  and  $G$ , bounded by blue and red dashed lines, respectively. The middle is the overlapping area of  $S$  and  $G$ , where  $V_{tot}$  and  $D_{tot}$  represent the magnitude and direction of current velocity, respectively. Sea-surface movement produces projection components in four directions, where  $V_S$  and  $V_G$  represent horizontal radial velocity components along beams far from the ascending and descending satellites.  $V_V$  and  $V_U$  represent surface velocity components along the north–south and east–west directions, respectively. In addition,  $\alpha$  represents the intersection angle between the direction of the beam center line and the east–west direction on the horizontal plane.

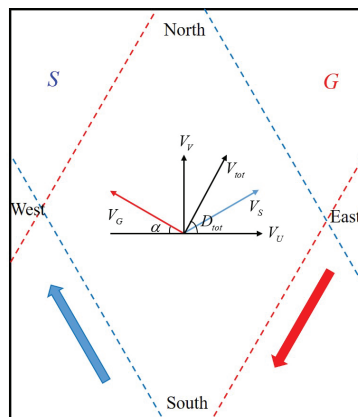


**Figure 1.** Schematic diagram of the geometric relationship between the sea-surface velocity and its components in the trajectory-crossing method.

The simulation method proposed in this paper is mainly divided into three parts: radial velocity simulation, wave velocity simulation and current vector simulation. The flow chart is shown in Figure 2. The first step is to calculate the radial velocity using the SAR ocean imaging model, the second step is to calculate the wave motion component, and the third step is to calculate the two-dimensional current field combined with the trajectory-crossing method. The radar parameters include the signal frequency, look direction of the beam and incident angle. Platform parameters include the satellite orbit height and flight speed.

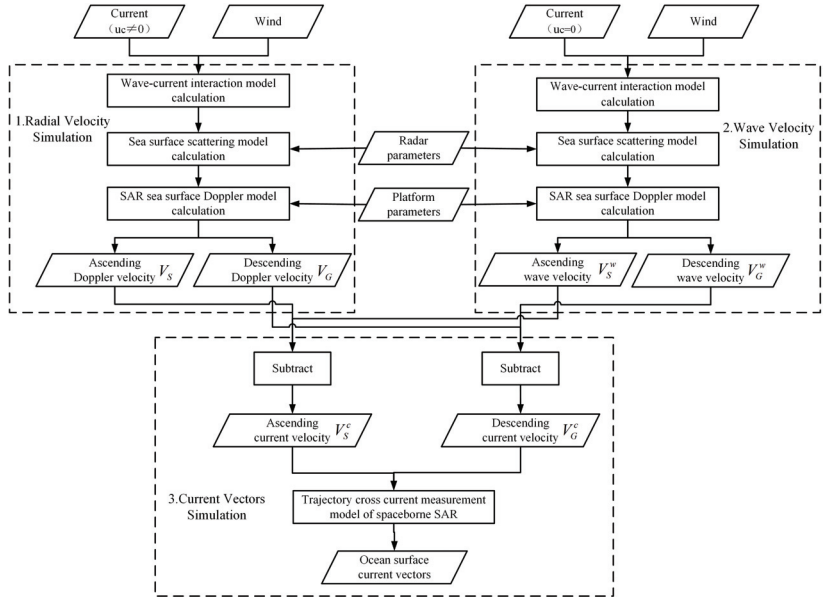


**Figure 2.** Flow chart of two-dimensional sea-surface-current-field simulation for trajectory crossing spaceborne SAR.

Based on the SAR ocean imaging model [7–9] proposed by Romeiser, University of Hamburg, Germany, the sea-surface horizontal radial velocity components along the spaceborne SAR beam look in directions with the ascending and descending passes simulated. The model supports simulation in the frequency range of 0.4 to 35 GHz. The main processes include the calculation of the wave–current interaction model, sea-surface scattering model and sea-surface SAR Doppler model.

Wave–current interaction is a physical process that must be considered in the real sea motion environment. We need to first give the sea-surface-current field and wind field parameters and then solve the action spectrum balance equation and calculate the modulated wave spectrum according to the weak hydrodynamic interaction theory. The action spectrum balance equation to be solved is [9,13,14]

$$\frac{\partial N(x, k, t)}{\partial t} + [c_g(k) + U(x, t)] \frac{\partial N(x, k, t)}{\partial x} - k \frac{\partial U(x, t)}{\partial x} \frac{\partial N(x, k, t)}{\partial k} = Q(x, k, t) \quad (1)$$

where  $t$  represents time,  $x = (x, y)$  represents the sea-surface spatial position,  $k = (k_x, k_y)$  represents the wave number, and  $k_x$  and  $k_y$  represent the wave numbers in the X and Y directions, respectively.  $N$  represents the action spectral density of sea-surface micro scale wave,  $U$  represents the surface current field, and  $C_g$  represents the modulated wave group velocity. These variables about ocean waves are related to the conditions of sea-surface wind field.  $Q$  represents the source function:

$$Q(\mathbf{x}, \mathbf{k}, t) = \mu(\mathbf{k})N(\mathbf{x}, \mathbf{k}, t) \left(1 - \frac{N(\mathbf{x}, \mathbf{k}, t)}{N_0(\mathbf{k})}\right) \tag{2}$$

where  $N_0$  represents the action spectral density in the sea-surface equilibrium state, and  $\mu$  represents the relaxation rate.

The relationship between the wave spectrum and action spectral density is [15]

$$N(\mathbf{x}, \mathbf{k}, t) = \frac{\rho\omega_0(\mathbf{k})}{k}\psi(\mathbf{x}, \mathbf{k}, t) \tag{3}$$

where  $\psi$  represents the modulated wave spectrum. The natural angular frequency  $\omega_0(\mathbf{k}) = \sqrt{gk + (\tau_s/\rho)k^3}$ ,  $g$  is the gravitational acceleration,  $\rho$  is the seawater density, and  $\tau_s$  is the seawater surface tension.

The sea-surface scattering model is based on the improved combined sea-surface model [8,9] proposed by Romeiser and Alpers, which considers the modulation effect of large-scale wave on small-scale Bragg waves. The normalized scattering coefficient can be calculated by taking the modulated wave spectrum and the given radar parameters as the input of the scattering model [8,16]

$$\begin{aligned} \langle \sigma \rangle &= \sigma^{(0)} + \langle \sigma^{(2)} \rangle \\ &= \sigma|_{s=0} + \iint \left( \left. \frac{\partial^2 \overset{\wedge}{\sigma}}{\partial s_p \partial s_p} \right|_{s=0} + \left. \frac{\partial^2 \overset{\vee}{\sigma}}{\partial s_p \partial s_p} \right|_{s=0} \right) \cdot k_p^2 \psi(\mathbf{k}) d^2 \mathbf{k} \\ &\quad + \iint \left( \left. \frac{\partial^2 \overset{\wedge}{\sigma}}{\partial s_n \partial s_n} \right|_{s=0} + \left. \frac{\partial^2 \overset{\vee}{\sigma}}{\partial s_n \partial s_n} \right|_{s=0} \right) \cdot k_n^2 \psi(\mathbf{k}) d^2 \mathbf{k} \\ &\quad + \iint \left( \left. \frac{\partial^2 \overset{\wedge}{\sigma}}{\partial s_p \partial s_n} \right|_{s=0} + \left. \frac{\partial^2 \overset{\vee}{\sigma}}{\partial s_p \partial s_n} \right|_{s=0} \right) \cdot k_p k_n \psi(\mathbf{k}) d^2 \mathbf{k} \end{aligned} \tag{4}$$

where the symbol  $\langle \cdot \rangle$  represents the statistical average;  $\sigma^{(0)}$  represents the normalized backscattering coefficient when the sea-surface slope is zero;  $\langle \sigma^{(2)} \rangle$  is the sum of second-order Bragg scattering caused by sea-surface slope;  $\mathbf{s} = (s_p, s_n)$  represents the sea-surface slope vector;  $k_p$  and  $k_n$ , respectively, represent the Bragg wave number components parallel and perpendicular to the radar look direction;  $\psi(\mathbf{k})$  represents the wave number spectrum;  $\wedge$  and  $\vee$  denote the Fourier transform and its conjugate of  $\sigma$  to wave number  $\mathbf{k}$ ; and  $\wedge \vee$  and  $\vee \wedge$  denote the Fourier transform and its conjugate of  $\sigma$  to combined wave number  $k_1 - k_2$ .

The Doppler spectrum and variance can be calculated using the double Gaussian Doppler spectrum model [7] proposed by Romeiser and Thompson, which divides the sea-surface echo into the superposition of the Bragg wave Doppler spectrum far from and towards the radar. Each Doppler spectrum component is defined as a Gaussian shape and expressed as

$$\begin{aligned} S(f_D) &= \frac{\langle \sigma_+ \rangle}{\sqrt{2\pi\gamma_{D+}^2}} e^{-(f_D - \langle f_{D+} \rangle_\sigma)^2 / \gamma_{D+}^2} \\ &\quad + \frac{\langle \sigma_- \rangle}{\sqrt{2\pi\gamma_{D-}^2}} e^{-(f_D - \langle f_{D-} \rangle_\sigma)^2 / \gamma_{D-}^2} \end{aligned} \tag{5}$$

where  $\pm$  represents the Bragg wave components away from and towards the radar, respectively;  $\langle f_{D\pm} \rangle_\sigma$  is the Doppler center weighted by the normalized backscattering coefficient; and  $\gamma_{D\pm}$  is the variance of Doppler spectrum. The specific calculation formulas of  $\langle f_{D\pm} \rangle_\sigma$  and  $\gamma_{D\pm}$  can be found in [7]. Then, the horizontal Doppler velocity  $V_{dop}$  along the beam radial direction can be expressed as

$$V_{dop} = \frac{\pi \cdot \langle f_{D\pm} \rangle_{\sigma}}{k_e \sin \theta} \tag{6}$$

where  $k_e$  is the wave number of the electromagnetic waves, and  $\theta$  is the incident angle. Therefore, the radial horizontal sea-surface Doppler velocity along the ascending and descending satellite beam represented by  $V_S$  and  $V_G$  in Figure 2 is calculated successively by the above process.

The radial velocity is actually the Doppler velocity that reflects the average motion state of scatterers in the sea-surface resolution unit. In the range of medium incident angles, the radial Doppler velocity  $u_r$  includes not only the current velocity but also the component of the sea-surface wave motion [17].

$$u_r = u_c + u_o + u_b \tag{7}$$

where  $u_c$  is the current velocity,  $u_o$  is the large-scale wave orbital velocity, and  $u_b$  is the net Bragg wave phase velocity.

At present, the related wave motion model is not perfect, and thus it is difficult to extract the current velocity component by directly calculating the accurate wave velocity [10]. The authors in [18] stated that when there is no current field, the sea-surface velocity obtained by using the SAR ocean imaging model comes from the wave motion. Therefore, in the second step, the input current field velocity is set to zero, combined with the same wind field, and through the calculation process similar to the radial velocity, the wave motion velocities in the ascending and descending beam direction are obtained, which are  $V_S^w$  and  $V_G^w$ , respectively. Since the influence of large-scale waves is considered in the previously used wave spectrum and scattering model, the simulated wave velocities include the sum of the last two velocity components of Equation (7).

By making a difference between the radial Doppler velocity and the wave velocity, the current velocity components  $V_S^c$  and  $V_G^c$  in the ascending and descending beam direction can be obtained:

$$V_S^c = V_S - V_S^w \tag{8}$$

$$V_G^c = V_G - V_G^w \tag{9}$$

Then, combined with the trajectory crossing current measurement geometric model in Figure 1, the east–west velocity component  $V_U$  and north–south velocity component  $V_V$  of the sea-surface current can be calculated:

$$V_U = \frac{V_S^c - V_G^c}{2 \cos \alpha} \tag{10}$$

$$V_V = \frac{V_S^c + V_G^c}{2 \sin \alpha} \tag{11}$$

Finally, the magnitude and direction of the current vector are, respectively, expressed as:

$$V_{tot} = \sqrt{V_U^2 + V_V^2} = \frac{\sqrt{V_S^2 + V_G^2 - 2V_S V_G \cos(2\alpha)}}{\sin(2\alpha)} \tag{12}$$

$$D_{tot} = \arctan\left(\frac{V_V}{V_U}\right) = \arctan\left(\frac{V_S + V_G}{(V_S - V_G) \tan \alpha}\right) \tag{13}$$

### 3. Simulation Experiment and Verification

In this section, a simulation experiment was conducted based on the spaceborne SAR system and sea environment parameters. The effectiveness of the simulation method was verified by comparing the simulation results with the measurement results using SAR data. First, the spaceborne SAR data, system parameters and input sea environment data involved in the experiment are introduced. The geographical location of the spaceborne



SAR data used in this paper is shown in Figure 3. This is the Mozambique strait between southeast Africa and Madagascar, where the sea surface is affected by the warm current of Mozambique, and the motion state is relatively stable. The red box indicates the stripmap SAR data range of ESA sentinel-1 satellite’s ascending pass, the acquisition time is 8 October 2019, 15:35 UTC (orbit number: 018385), the black box indicates the stripmap SAR data range of China Gaofen-3 (GF-3) satellite’s descending pass, and the acquisition time is 9 October 2019, 02:43 UTC (orbit number: 016651). Although these two SAR data were not acquired at the same time, the time interval is short, the current motion status is basically unchanged here, and these two SAR images overlap partially in this sea area, which meets the requirements of the trajectory-crossing method.

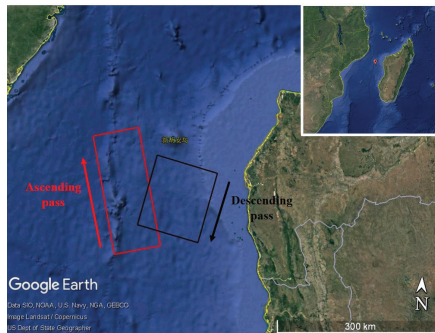


Figure 3. Spatial geographic location of the actual SAR data.

Figure 4 shows the SAR amplitude image of Sentinel-1 satellite and the horizontal radial Doppler velocity image of its secondary product. The dimmer brightness in the lower left corner of Figure 4a is due to the lower wind speed and the weaker echo energy due to the oil spill on the sea, which also results in errors in the Doppler velocity, as shown in the corresponding position in Figure 4b. The absolute values are small in the lower right part of the Doppler velocity map, and the overall velocity includes the influence of sea-surface wind and wave motion, which needs to be further removed.

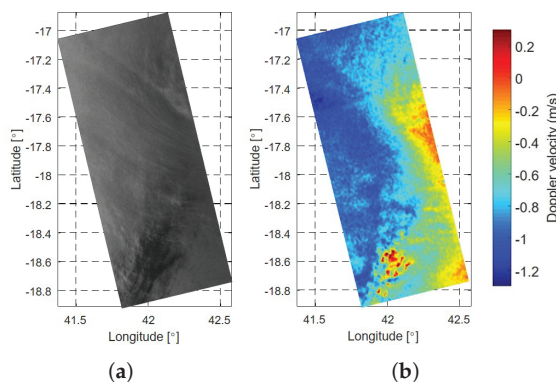
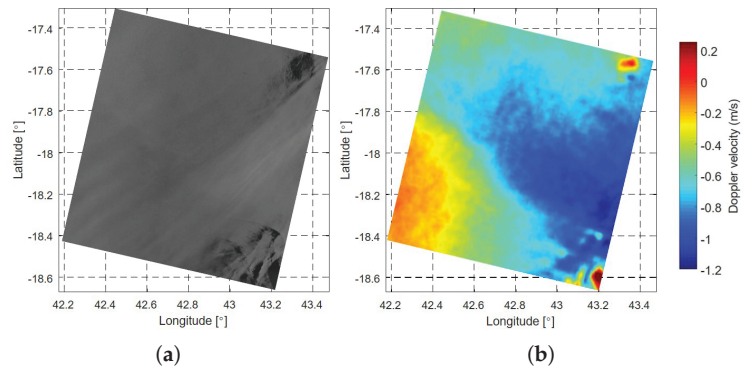


Figure 4. Sentinel-1 SAR (a) amplitude image and (b) radial Doppler velocity.

Figure 5 shows the SAR amplitude image of the GF-3 satellite and the Doppler velocity estimated from the single look complex (SLC) data. The dark part of the right corner of Figure 5a is obviously affected by the sea oil film, which reduces the signal-to-noise ratio of the image. The Doppler velocity of Figure 5b is estimated from the Doppler processing in reference [19]. It can be seen that the absolute value in the lower left corner of the image is

small, in addition to the anomaly in the oil film position, and the overall velocity overlaps with the influence of the wind and wave motion.



**Figure 5.** GF-3 SAR (a) amplitude image and (b) radial Doppler velocity.

Although the overlap range of the above SAR data is small, it has clear velocity characteristics, which is conducive to the validation of simulation method. Therefore, a simulation experiment was performed in this sea area. The input system parameters are consistent with the real SAR data parameters, representing the ascending Sentinel-1 satellite and the descending GF-3 satellite, respectively, as shown in Table 1. It should be noted that, at present, there are few ascending and descending data from a single satellite that can meet the requirements of irradiating the same sea area at a short time, and it is difficult to obtain them directly. In future applications, two or more satellites must cooperate to obtain the ascending and descending passes data of the same space-time sea area for current measurement. Therefore, the following dual satellite SAR data processing and system simulation are of practical significance.

**Table 1.** Simulation parameters.

Parameters	Sentinel-1 (Ascending)	GF-3 (Descending)	Units
Radar Frequency	5.4	5.4	GHz
Incident Angle	26.3	35	deg
Beam Direction	15	165	deg
Platform Speed	7590	7568	m/s
Orbit Altitude	707	713	km

The hybrid coordinate ocean model (HYCOM) reanalysis current field data and the European centre for medium-range weather forecasts (ECMWF) wind field data are obtained for the simulation input, respectively, as shown in Figure 6. The HYCOM model reanalysis data, which combines satellite altimeter data with temperature and salt data obtained by a buoy, is widely used in ocean current research [20–22]. The date selected for the HYCOM data is the same as Sentinel-1 SAR data acquisition date with spatial resolution of 1/12 degree. Wind field data at the same time and place were obtained from the ECMWF website with spatial resolution of 1/4 degree, and interpolated to ensure the same number of data points as the input current field. From the input data, it is known that the velocity in the overlapping area is small, and the sea-surface wind speed is mainly in the range of 2–7 m/s, which belongs to the moderate wind speed.

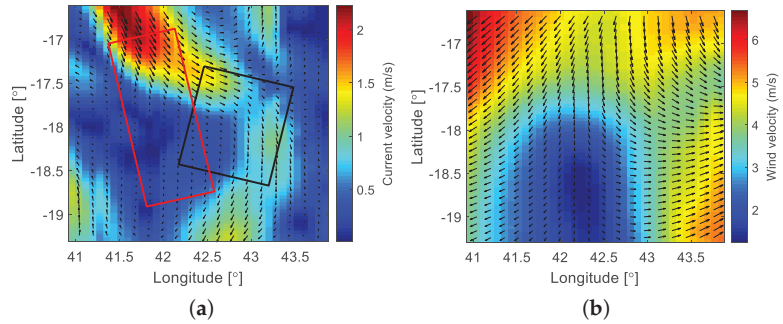


**Figure 6.** Simulation input sea-surface environment data. (a) current field and (b) wind field.

The given current and wind data are input into the SAR ocean imaging model to calculate the radial Doppler velocity  $V_S$  under the parameters of ascending Sentinel-1 satellite and the radial Doppler velocity  $V_G$  under the parameters of descending GF-3 satellite, as shown in Figure 7a,b, respectively. It can be seen that, due to the same orbital inclination of these two satellites, the distribution of the relative value of the velocity in the look direction of the two beams is approximately symmetrical; however, the absolute value is different due to the influence of wind and wave motion. Figure 7c,d shows the wave velocity when the current field is set to zero under the same wind field conditions, in which the absolute value of the velocity changes due to the change of the relationship between wind direction and beam look direction. When the wind direction is perpendicular to the beam look direction, the wave velocity is zero, which is consistent with the research conclusion in the literature [11].

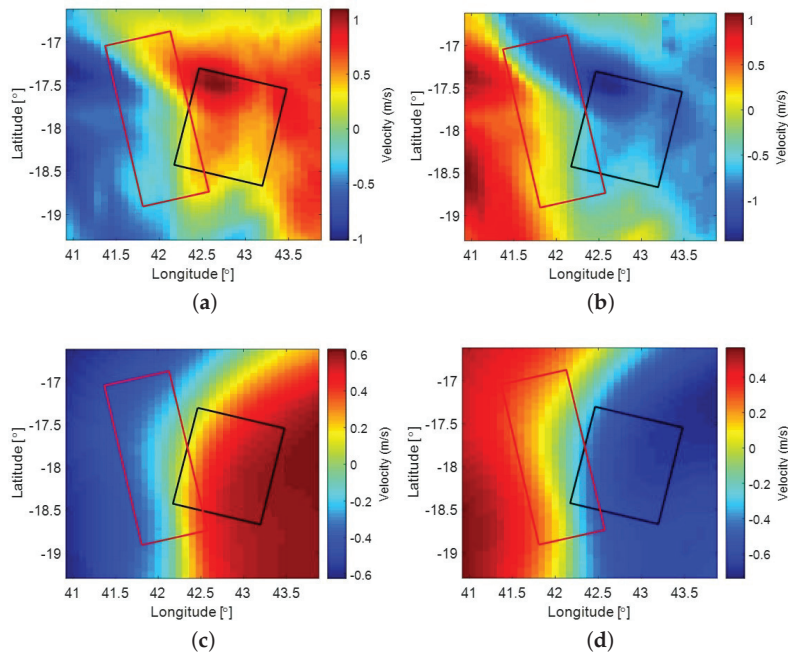


**Figure 7.** (a) Sea-surface radial velocity along the ascending beam. (b) Sea-surface radial velocity along the descending beam. (c) Wave velocity along the ascending beam. (d) Wave velocity along the descending beam.

According to the flow chart in Figure 2, the corresponding sea-surface radial velocity and wave velocity of ascending and descending passes in Figure 8 are subtracted, and the current vectors are calculated using the trajectory-crossing method. The simulated two-dimensional current field is shown in Figure 8. Comparing with the input current field given in Figure 6a, we found that they were in good agreement. Note that, as for the computational demand, the calculation process of this method takes only a few minutes, the calculation amount of wave spectrum is the largest. The calculation times will be different according to the amount of input current and wind data.

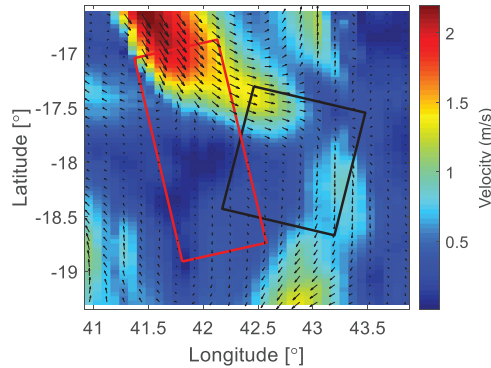


Figure 8. Simulation results of two-dimensional current field.

To quantitatively validate the experimental results, we selected eight geographic locations in the overlap area (Figure 9) and compare the simulation results with the SAR data measurement results, as shown in Table 2. As the size of the simulated current field resolution unit is about 8 km and that estimated from Sentinel-1 and GF-3 SAR data is about 1 km, the  $8 \times 8$  Doppler velocities around the corresponding eight latitude and longitude positions in Figures 4b and 5b are averaged. After subtracting the simulated wave velocity in Figure 7 from the average data, the two-dimensional current field results of the SAR data are calculated in combination with Equations (8)–(13). It can be seen that the corresponding current velocity and direction are close. However, because the current and wind data input by the simulation will be different from the instantaneous environment in the real SAR data, there will also be discrepancies between the data in Table 2.

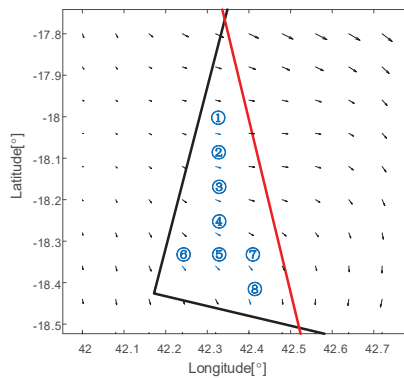


Figure 9. Location points in the current field as verification.

**Table 2.** Comparison between the simulated and measured current data.

Location Point	Coordinate	Simulated Data		Measured Data	
		Velocity	Direction	Velocity	Direction
1	(42.32–18.04)	0.260 m/s	−9.66°	0.250 m/s	−16.74°
2	(42.32–18.12)	0.293 m/s	−12.68°	0.261 m/s	−17.59°
3	(42.32–18.20)	0.322 m/s	−19.78°	0.299 m/s	−24.05°
4	(42.32–18.28)	0.312 m/s	−33.06°	0.275 m/s	−37.45°
5	(42.32–18.36)	0.317 m/s	−42.84°	0.294 m/s	−47.56°
6	(42.24–18.36)	0.295 m/s	−55.31°	0.263 m/s	−58.59°
7	(42.40–18.36)	0.285 m/s	−47.69°	0.256 m/s	−59.21°
8	(42.40–18.44)	0.297 m/s	−72.36°	0.268 m/s	−80.77°

The statistical analysis of the experimental data is shown in Figure 10. Figure 10a shows a scatterplot of the velocity of the simulated current field compared with that of the measured current field from SAR data, with a correlation coefficient greater than 0.9 and a root mean square error (RMSE) of 0.028 m/s. Figure 10b shows the scatterplot comparing the direction of the simulated current compared with that of the measurement data. The correlation coefficient is greater than 0.98 and the root mean square error (RMSE) is 6.05 degrees. It can be seen that the simulated current field is in good agreement with the measured current of SAR data.

We also notice that there is a visible deviation between these two data, which will not only come from the difference of input data but also be limited by the model. For example, the wave spectrum is different from the real sea-surface state. Nevertheless, we believe that the simulation results are consistent with the measurement results. Therefore, the proposed method in this paper can effectively simulate the two-dimensional sea-surface-current field in the given spaceborne SAR system and marine environment parameters. The results also show that the proposed simulation method is conducive to the parameter analysis process of the trajectory-crossing method in the application of current measurement in the future.

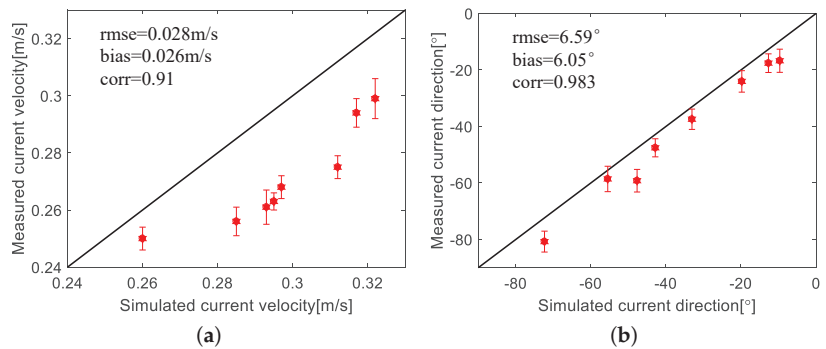


**Figure 10.** Statistical comparison between the simulated current field and SAR data measured current field. (a) Velocity and (b) direction.

#### 4. Conclusions

With the continuous enrichment of spaceborne SAR data in the future, the trajectory-crossing method to measure the two-dimensional current field on the sea surface will be widely used. However, at present, it is difficult to comprehensively analyze the influence of system and environmental parameters on the current measurement effect from the real SAR data. In this paper, a simulation method of two-dimensional sea-surface-current field for trajectory crossing spaceborne SAR is proposed, which can realize two-dimensional current field simulation under the given spaceborne SAR system and environmental pa-

rameters. In the simulation process, the wave–current interaction and the influence of sea-surface backscattering on the SAR Doppler centroid frequency are considered, and the influence of the wave motion on the current measurement results is removed.

The simulation experiment selected the real spaceborne SAR system and sea-surface environment parameters, and the results are in good agreement with the SAR data processing results, which shows the effectiveness of the simulation method in this paper. Therefore, the proposed method is conducive to the parameter analysis process of the trajectory-crossing method in the application of current measurement. However, because the influence of the wave-breaking scattering mechanism under high wind speed and sea conditions was not considered, the simulation method in this paper is not suitable for two-dimensional current field simulation in extreme marine environments. In future work, more scattering mechanisms will be considered to improve the scope of application and promote the development of application research for two-dimensional sea-surface-current field measurements.

**Author Contributions:** Conceptualization, Y.L. and J.C.; Methodology, Y.L.; Software, Y.L. and Z.L.; Validation, Y.L. and Z.L.; Formal analysis, Y.L., J.C. and Z.L.; Investigation, Y.L.; Writing—original draft preparation, Y.L.; Writing—review and editing, J.C. and Y.L.; Supervision, J.C. All authors have read and agreed to the published version of the manuscript.

**Funding:** This research received no external funding.

**Institutional Review Board Statement:** Not applicable.

**Informed Consent Statement:** Not applicable.

**Data Availability Statement:** Not applicable.

**Conflicts of Interest:** The authors declare no conflict of interest.

## References

1. Fischer, J.; Fleming, N.C. *Operational Oceanography: Data Requirements Survey*; Southampton Oceanography Centre: Southampton, UK, 1999.
2. Xu, Z.; Zhang, H.; Wang, Y.; Wang, X.; Xue, S.; Liu, W. Dynamic detection of offshore wind turbines by spatial machine learning from spaceborne synthetic aperture radar imagery. *J. King Saud Univ. Comput. Inf. Sci.* **2022**, *34*, 1674–1686. [[CrossRef](#)]
3. Goldstein, R.M.; Zebker, H. Interferometric radar measurement of ocean surface currents. *Nature* **1987**, *328*, 707–709. [[CrossRef](#)]
4. Chapron, B.; Collard, F.; Arduin, F. Direct measurements of ocean surface velocity from space: Interpretation and validation. *J. Geophys. Res. Oceans* **2005**, *110*, C07008. [[CrossRef](#)]
5. Kim, D.-J.; Moon, W.M.; Moller, D.; Imel, D.A. Measurements of ocean surface waves and currents using L- and C-band along-track interferometric SAR. *IEEE Trans. Geosci. Remote Sens.* **2003**, *41*, 2821–2832.
6. Fernández-Prieto, D.; Sabia, R. *Remote Sensing Advances for Earth System Science*; Springer: Berlin/Heidelberg, Germany, 2013.
7. Romeiser, R.; Thompson, D.R. Numerical Study on the Along-Track Interferometric Radar Imaging Mechanism of Oceanic Surface Currents. *IEEE Trans. Geosci. Remote Sens.* **2000**, *38*, 446–458. [[CrossRef](#)]
8. Romeiser, R.; Alpers, W.; Wismann, V. An improved composite surface model for the radar backscattering cross section of the ocean surface 1. Theory of the model and optimization/validation by scatterometer data. *J. Geophys. Res. Oceans* **1997**, *102*, 25237–25250. [[CrossRef](#)]
9. Romeiser, R.; Alpers, W. An improved composite surface model for the radar backscattering cross section of the ocean surface 2. Model response to surface roughness variations and the radar imaging of underwater bottom topography. *J. Geophys. Res. Oceans* **1997**, *102*, 25251–25267. [[CrossRef](#)]
10. Yu, X.Z.; Chong, J.S.; Hong, W. An Iterative Method for Ocean Surface Current Retrieval by Along-track Interferometric SAR. *J. Electron. Inf. Technol.* **2012**, *34*, 2660–2665. [[CrossRef](#)]
11. Elyouncha, A.; Eriksson, L.; Romeiser, R.; Ulander, L. Empirical Relationship Between the Doppler Centroid Derived from X-Band Spaceborne InSAR Data and Wind Vectors. *IEEE Trans. Geosci. Remote Sens.* **2021**, *60*, 4201120. [[CrossRef](#)]
12. Wang, W.Y.; Xie, C.H.; Yuan, X.Z.; He, Z.H.; Ding, Z.G. Performance Analysis of Sea Surface Current Measurement by GF-3 Satellite ATI Mode. *Spacecr. Eng.* **2017**, *26*, 132–139.
13. Longuet-Higgins, M.S.; Stewart, R.W. Radiation stresses in water waves; a physical discussion, with applications. *Deep-Sea Res. Oceanogr. Abstr.* **1964**, *11*, 529–562. [[CrossRef](#)]
14. Whitham, G.B. Non-Linear Dispersive Waves. *Proc. R. Soc. Lond. Ser. A Math. Phys. Sci.* **1965**, *283*, 238–261.
15. Whitham, G.B. A general approach to linear and non-linear dispersive waves using a Lagrangian. *J. Fluid Mech.* **1965**, *22*, 273–283.

16. Yu, Y.; Wang, X.Q.; Zhu, M.H.; Xiao, J. Three-Scale Radar Backscattering Model of the Ocean Surface Based on Second-Order Scattering. *Acta Electron. Sin.* **2008**, *36*, 1771–1775. [[CrossRef](#)]
17. Mollerl, D.; Wernerl, C.; Frasier, S. Feasibility Study and System Design for a Spaceborne Along-track Interferometer/Scatterometer. 1998. Available online: <http://hdl.handle.net/2014/20694> (accessed on 6 June 2021).
18. Farquharson, G.; Aslebagh, S.; Romeiser, R. Estimating Nearshore Ocean Currents from Airborne ATI-SAR. In Proceedings of European Conference on Synthetic Aperture Radar, Hamburg, Germany, 6–9 June 2016; pp. 1–5.
19. Hou, F.C.; Meng, J.M.; Zhang, X.; Sun, L.N. Using the Doppler Shift Method to Retrieve the ASAR Sea Surface Velocity. *Adv. Mar. Sci.* **2019**, *37*, 118–127.
20. Backeberg, B.C.; Bertino, L.; Johannessen, J.A. Evaluating two numerical advection schemes in HYCOM for eddy-resolving modelling of the Agulhas Current. *Ocean. Sci.* **2009**, *5*, 173–190. [[CrossRef](#)]
21. Seo, S.; Park, Y.-G.; Park, J.-H.; Lee, H.J.; Hirose, N.J.O.; Research, P. The Tsushima Warm Current from a high resolution ocean prediction model, HYCOM. *Ocean. Polar Res.* **2013**, *35*, 135–146. [[CrossRef](#)]
22. Wang, M.; Liu, Z.; Zhu, X.; Yan, X.; Zhang, Z.; Zhao, R. Origin and formation of the Ryukyu Current revealed by HYCOM reanalysis. *Acta Oceanol. Sin.* **2019**, *38*, 1–10. [[CrossRef](#)]

## Article

# Field Radiometric Calibration of a Micro-Spectrometer Based on Remote Sensing of Plateau Inland Water Colors

Jiarui Shi <sup>1,2</sup>, Qian Shen <sup>1,2,\*</sup>, Yue Yao <sup>1,2</sup>, Fangfang Zhang <sup>1,2</sup>, Junsheng Li <sup>1,2</sup> and Libing Wang <sup>1,2</sup>

<sup>1</sup> Big Earth Data Reveals Imbalance in Progress towards the Environmental SDG Indicators in China, Beijing 100094, China

<sup>2</sup> Key Laboratory of Digital Earth Science, Aerospace Information Research Institute, Chinese Academy of Sciences, Beijing 100094, China

\* Correspondence: shenqian@radi.ac.cn

**Abstract:** Remote sensing reflectance ( $R_{rs}$ ), which is currently measured mainly using the above-water approach, is the most crucial parameter in the remote sensing inversion of plateau inland water colors. It is very difficult to measure the  $R_{rs}$  of plateau inland unmanned areas; thus, we provide a measurement solution using a micro-spectrometer. Currently, commercial micro-spectrometers are not factory calibrated for radiation, and thus, a radiometric calibration of the micro-spectrometer is an essential step. This article uses an Ocean Optics micro-spectrometer (STS-VIS) and a traditional water spectrometer (Trios) to simultaneously measure the irradiance and radiance of diffuse reflectance plates with different reflectance values for field calibration. The results show the following: (1) different fiber types have different calibration coefficients, and the integration time is determined according to the diameter of the fiber and the type of fiber, and (2) by comparing the simultaneous measurement results of STS-VIS with Trios, the mean absolute percentage difference (MAPD) of both reached 18.64% and 5.11% for Qinghai Lake and Golmud River, respectively, which are accurate  $R_{rs}$  measurements of water bodies. The  $R_{rs}$  of the Hoh Xil and Qarhan Salt Lake water bodies in unmanned areas of China was measured, and this was the first collection of in situ spectral information with a micro-spectrometer. This article shows that the micro-spectrometer can perform the in situ measurement of water  $R_{rs}$  in unmanned inland areas. With this breakthrough in the radiometric performance of the micro-spectrometer, we are able to obtain more accurate remote sensing reflectance results of unmanned water bodies.

**Keywords:** field radiometric calibration; micro-spectrometer; remote sensing reflectance; plateau inland waters

**Citation:** Shi, J.; Shen, Q.; Yao, Y.; Zhang, F.; Li, J.; Wang, L. Field Radiometric Calibration of a Micro-Spectrometer Based on Remote Sensing of Plateau Inland Water Colors. *Appl. Sci.* **2023**, *13*, 2117. <https://doi.org/10.3390/app13042117>

Academic Editor: Tung-Ching Su

Received: 15 November 2022

Revised: 3 February 2023

Accepted: 4 February 2023

Published: 7 February 2023



**Copyright:** © 2023 by the authors. Licensee MDPI, Basel, Switzerland. This article is an open access article distributed under the terms and conditions of the Creative Commons Attribution (CC BY) license (<https://creativecommons.org/licenses/by/4.0/>).

## 1. Introduction

Remote sensing reflectance ( $sr^{-1}$ ) of water bodies is an important apparent optical quantity that can be detected in water color remote sensing and is one of the important parameters to quantify the spectral information of water bodies [1]. The field measurement of water remote sensing reflectance is a key step in the remote sensing of water color, and is widely used in the research and commercialization of satellite authenticity verification, water quality parameter inversion [2], cyanobacterial bloom [3] and black-odor water body identification [4]. The remote sensing of water color can be divided into the remote sensing of marine water bodies and the remote sensing of inland water bodies, with the remote sensing of marine water bodies being utilized to mainly observe the surface chlorophyll-a (Chl-a) concentration [5], suspended particular matter (SPM) concentration [6] and colored dissolved organic matter (CDOM) [7]. The remote sensing of inland water bodies has been used to estimate, in addition to the parameters mentioned above, total phosphorus (TP), total nitrogen (TN), the trophic state index (TSI) and, more recently, dissolved organic carbon in an eutrophic lake [8] and methane emissions in a lake [9].



Current spectrometers dedicated to  $Rrs$  based on water bodies include the Analytical Spectral Devices (ASD) series from Malvern Panalytical in the UK [10], the Profiling Reflectance Radiometer (PRR) series from Biospherical in the USA [11], the PAMSES series from Trios in Germany [12] and the Satlantic series from a subsidiary of SeaBird in the USA [13]. Measuring the  $Rrs$  is an essential step in both marine remote sensing and inland water remote sensing. In oceanic remote sensing, the spectrometer is mainly carried on board a research vessel for walk-around measurements, and the same method is applied in inland lakes. There is a great deal of preparation before the measurement is carried out: firstly, the spectrometer is charged; secondly, the instruments are inventoried for transport; and finally, the spectrometer is deployed on board the research vessel. All of the above spectrometers can be utilized for the measurement of parameters in water bodies. However, they all are of a large size and weight and require a power supply, and thus, we cannot bring the spectrometer to lakes or rivers in unmanned areas such as the Tibetan Plateau. Therefore, there has been a gap in our knowledge on the water spectra of lakes or rivers in unmanned areas of the Tibetan Plateau. Furthermore, in inland water environments there are often unpopulated waters and waters that cannot be measured by using large vessels, and the above-mentioned water body  $Rrs$  cannot be measured. Micro-spectrometers have the advantage of being small in size [14], and instead of spectrometers, they have been carried on board unmanned aerial vehicles or unmanned ships for  $Rrs$  measurements to solve these problems. Nowadays, scholars often use imaging spectrometers for spectrometric measurements via unmanned aerial vehicles, and there are empirical linear-based [15] and look-up table methods [16] for radiometric calibrations of imaging spectrometers. The main applications are in vegetation and crop studies [17], and scholars have also used them to perform techniques for estimating water quality parameters [18,19]. However, imaging spectrometers tend to have a low signal-to-noise ratio for measuring the remote sensing spectra of water bodies. However, none of the current commercial micro-spectrometers are radiometrically calibrated; thus, we need to carry out a radiometric calibration of the micro-spectrometer.

The radiometric calibration of the micro-spectrometer can be performed by using a high-precision spectrometer and a micro-spectrometer to simultaneously measure high-precision stable irradiance and irradiance sources and to solve for the conversion relationship between the digital number (DN) recorded by the micro-spectrometer and the radiance and irradiance values received by the micro-spectrometer. The main radiometric calibration methods used thus far for remote sensing sensors are laboratory integrating sphere calibration [20–22], on-station calibration [23], diffuse reflectance plate calibration [24,25], etc. Laboratory integrating sphere calibration is mainly a high-precision test of parameters, such as the remote sensor electronic gain and bias, central wavelength and bandwidth of each channel, signal-to-noise ratio, spatial resolution and spectral response function using relevant laboratory equipment, which is traceable with a low-temperature absolute radiometer or a standard blackbody uniform radiation quantification standard. On-station calibrations use a calibration system mounted on a satellite platform to periodically monitor changes in the radiation response of the satellite during its orbital operation. Diffuse reflectance plate calibration uses a diffuse reflectance plate and a spectrometer probe for simultaneous fixed-point continuous observation. Concerning the radiometric calibration methods for remote sensing sensors, only laboratory integrating sphere calibration and field diffuse reflectance plate calibration methods can meet the requirements for the radiometric calibration of micro-spectrometers. The field diffuse reflector calibration method is simple and easy to operate, whereas the laboratory integrating sphere calibration requires a lot of time and money, and our group does not meet the conditions for conducting laboratory integrating sphere calibration. Therefore, the field diffuse reflector calibration method is chosen for the radiation calibration of the micro-spectrometer.

The main purpose of this article is a preliminary evaluation of the feasibility and accuracy of micro-spectrometer measurements of the  $Rrs$  of plateau inland water colors. Specifically: (1) we calculated the micro-spectrometer radiometric calibration coefficients

using different fiber types; (2) we quantified the accuracy of measuring the  $R_{rs}$  of clear and turbid waters in plateau inland water bodies and (3) we provided a case study of the application of the micro-spectrometer to  $R_{rs}$  of plateau inland water bodies in unmanned areas.

## 2. Data and Methods

### 2.1. Equipment and Methods

The equipment used in the micro-spectrometer radiometric calibration is shown in Figure 1 and includes the following: the micro-spectrometer (STS-VIS, Ocean Optics company, Orlando, FL, USA), an optical fiber, a cosine receiver, a spectrometer (Trios, TriOS Mess, Rastede, Germany), a diffuse reflectance plate with different reflectance values and a target cloth, a micro-spectrometer linked to the optical fiber to measure radiance and a micro-spectrometer linked to the optical fiber and cosine receiver to measure irradiance. The diffuse reflectance plate and the target cloth provide stable and varying values of irradiance and radiance. The measured spectral ranges and spectral resolution of Trios and STS-VIS are shown in Table 1. The Trios can measure spectra from 200 nm up to 1100 nm with a spectral resolution of 3.3 nm, whereas the STS-VIS can measure spectra from 350 to 810 nm with a spectral resolution of 2.2 nm. There are three common methods of field measurements of remotely-sensed reflectance ratios in water bodies: the in-water approach [26], the above-water approach [27] and the skylight-blocked approach [28]. The in-water approach generally uses more expensive instruments, which are complex to operate and deploy, and are subject to a certain amount of self-shadowing and uncertainty in the data results. This method can generally only be used in water depths greater than 10 m, and thus, this method is very widely used in pelagic Class I waters, but rarely in inland waters. The skylight-blocked approach uses a mask to directly block the sky light from the field of view of the observation sensor, thus enabling the direct measurement of the off-water irradiance of a water body. This method avoids the geometrical errors in observation caused by the complexity of the field and the uncertainties associated with the skylight rejection method. However, it requires a continuous power supply, and therefore, cannot measure water spectra in the unmanned areas of the Tibetan Plateau. The above-water method has the advantages of a simple field operation and the low cost of field experiments, and is currently the most commonly used measurement method in the study of the spectral properties of water bodies; however, it is affected by water and weather conditions. The details of this method of measurement can be found in Figure A1 in Appendix A. The main zenith angle conditions met by the instrument are that the downward irradiance sensor should point vertically towards the sky, the radiance sensor for measuring sky light should be equal to  $50^\circ$  and the radiance sensor for measuring sky light should be equal to  $140^\circ$ . The main azimuth angle conditions met by the instrument are that the angle between the left and right sunlight should be equal to  $45^\circ$ . This helps avoid sun glint. This method is the easiest water body measurement method to implement in unmanned lakes on a plateau; therefore, the above-water method was selected for this paper to carry out spectral measurements of water bodies in unmanned areas on the Tibetan Plateau, and the formula for measuring  $R_{rs}$  is as follows (Equation (1)):

$$R_{rs}(\lambda) = \frac{L_w(\lambda)}{E_d(\lambda)} = \frac{L_u(\lambda) - r_{sky}(\lambda)L_{sky}(\lambda)}{E_d(\lambda)} \quad (1)$$

$R_{rs}$  is equal to the ratio of the off-water radiance to the downward irradiance, and in the above formula,  $L_u(\lambda)$  is the total off-water radiance,  $r_{sky}(\lambda)$  can be derived from the look-up table [29],  $L_{sky}(\lambda)$  is the skylight radiance and  $E_d(\lambda)$  is the downward irradiance. They are measured simultaneously using a micro-spectrometer, using (a)-1 for sky radiance, (a)-2 for total off-water radiance and (a)-3 for downward irradiance, so as to avoid the effects of weather variations.



**Figure 1.** (a) Ocean Optics micro-spectrometers (STS-VIS); (a)-1 sensor for measuring sky radiance; (a)-2 sensor for measuring water radiance; (a)-3 sensor for measuring downward irradiance. (b) Ocean Optics and Hygirel fiber. (c) Cosine Correctors. (d) Trios. (e) Diffuse reflectance plates and target cloth (99%, 95%, 30%, 20%, 5%, and 2%).

**Table 1.** Parameter table of Trios and STS-VIS.

	Trios	STS-VIS
Wavelength (nm)	200–1100	350–810
Optical Resolution (nm)	3.3 nm	2.2 nm

The procedure for field calibration is to use the Trios sensors and micro-spectrometer to simultaneously measure diffuse reflectors with different reflectance values against a target cloth, and to obtain the simultaneously measured Trios radiance, irradiance and micro-spectra with their corresponding DN values. The formula for field-calibrated radiance is presented in Equation (2) and for field-calibrated irradiance in Equation (3).

$$L_{Trios} = gain \times DN_{STS-VIS} + offset \tag{2}$$

$$Ed_{Trios} = gain \times \widetilde{DN}_{STS-VIS} + offset \tag{3}$$

In Formula (2) above,  $L_{Trios}$  is the radiance of the different diffuse reflection plates measured by Trios, and  $DN_{STS-VIS}$  is the DN of the different diffuse reflection plates measured by the micro-spectrometer.  $Ed_{Trios}$  in Formula (3) is the irradiance of the different diffuse reflectors measured by Trios and  $\widetilde{DN}_{STS-VIS}$  is the the DN of the different diffuse reflection plates measured by the micro-spectrometer.

We used the micro-spectrometer to obtain the  $Rrs$  of plateau lakes as follows: firstly, the DN values obtained with the micro-spectrometers (a)-1, (a)-2 and (a)-3 are converted into radiance and irradiance according to Formulas (2) and (3), and then the  $Rrs$  of the micro-spectrometer is calculated according to Formula (1).

The micro-spectrometer needs to be physically connected to the micro-computer in the unmanned ship using a USB cable; additionally, we also need to use professional software to identify the sensor, and only after the identification is passed can the data

acquisition parameters be set. The main parameters to be set are integration time, multiple scan averaging, sliding average width and other parameters. It is also necessary to set the address where the spectrum file is to be saved. Once the settings are complete, the micro-spectrometer can be used for water spectrum acquisition.

2.2. Data Processing and Evaluation Metrics

We used the Oceanview 6.0 software for hardware control and we needed to set the integration time before collection. The integration times of the micro-spectrometer for measuring radiance and measuring irradiance are described in detail in Section 3.1. The micro-spectrometer and Trios both measure different floating-point wavelength data; therefore, we needed to resample the Trios and STS-VIS spectrometer data to the same integer wavelength for field radiation calibration. The cubic spline interpolation method has a small error (we have also compared the results of the other three resampling methods plotted in Figure A2 Appendix A). Thus, we used this method and obtained a result that is very small, as shown in Figure 2.

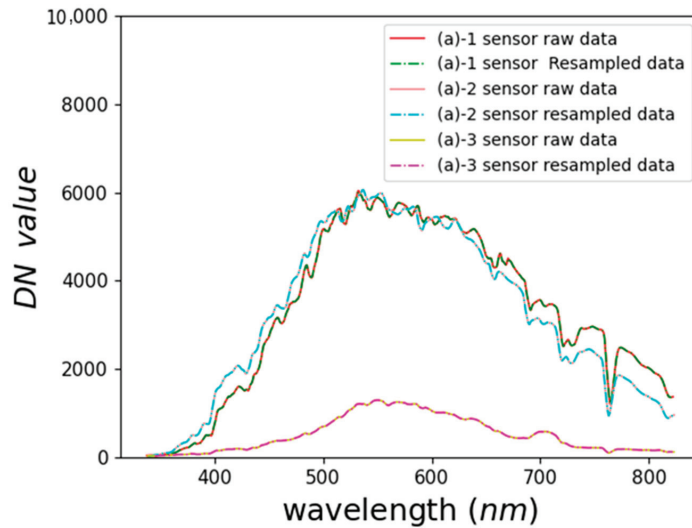


Figure 2. Comparison of raw and resampled data.

The following statistics were used to evaluate the spectral results, including the correlation coefficient ( $r$ ), bias and mean absolute percentage difference (MAPD).

$$r = \frac{\sum_{i=1}^n (S_{i,1} - \bar{S}_1)(S_{i,2} - \bar{S}_2)}{\sqrt{\sum_{i=1}^n (S_{i,1} - \bar{S}_1)^2 + \sum_{i=1}^n (S_{i,2} - \bar{S}_2)^2}} \tag{4}$$

$$\text{bias} = (S_{i,1} - S_{i,2}) / S_{i,2} \times 100\% \tag{5}$$

$$\text{MAPD} = \frac{1}{N} \sum_{i=1}^N |(S_{i,1} - S_{i,2}) / S_{i,2}| \times 100\% \tag{6}$$

where  $S_{i,1}$  and  $S_{i,2}$  denote the DN values corresponding to the measured diffuse reflectance plates, the gain and offset observed under different conditions and the  $Rrs$  measure with the Trios and micro-spectrometer.

In this article, we compare the effects of different fibers on the gain and offset, which is followed by a quantitative analysis to measure the spectra of different diffuse reflectors

with clear water and turbid water, and finally, we perform a first application demonstration in an unmanned area.

### 3. Results

We first determined the important acquisition parameter integration times for the micro-spectrometer under sunny conditions, then compared the gain and offset of two fiber types using a Hygirel fiber-optic micro-spectrometer (detailed parameters of the two types of micro-spectrometers are given in Section 3.2) and Trios under sunny conditions, and finally, we evaluated the simultaneous measurements of 95% and 20% for the diffuse reflectance plates, and 5% and 2% for the target cloth.

#### 3.1. Effect of Integration Time on Spectral Acquisition of Water

We all know that when a spectrometer performs electro-optical conversion it is mainly influenced by three main parameters [30]: the integration time, aperture and temperature of the micro-spectrometer. The longer the integration time, the more energy is collected by the micro-spectrometer; the larger the aperture, the more energy is collected by the micro-spectrometer; the temperature of the micro-spectrometer creates thermal noise; and different temperatures bring about different thermal noises. When measuring in the field, we pre-warmed the micro-spectrometer for 60 min to keep it below normal operating temperature to avoid the effects of thermal noise caused by temperature. For dealing with the effects of the aperture, micro-spectrometers are often used with a fixed fiber; thus, we use a fixed fiber diameter to control the effect of the aperture on the spectrum.

The signal-to-noise ratio (SNR) of a spectrometer is a very important metric when using micro-spectrometers for the spectral acquisition of water bodies. The current international water color satellites MODIS Terra/Aqua (spatial resolution: 250 m and 500 m), MERIS Envisat (spatial resolution: 300 m), VIIRS (spatial resolution: 750 m) and Sentinel-3A/B (spatial resolution: 300 m) all have SNRs greater than 1000 for measurements that occur in the ocean [31]; measurements in inland lakes mainly use Landsat OLI (spatial resolution: 30 m) HJ-1 (spatial resolution: 30 m), etc., all of which have SNRs greater than 100 [32]. The use of Landsat as a data source for lake water observations on the Qinghai–Tibet Plateau requires that the signal-to-noise ratio of the micro-spectrometer be greater than 100 for application in field measurements.

We believe that in the electro-optical conversion of a micro-spectrometer, the noise of the micro-spectrometer is caused by the dark current; thus, we calculated the SNRs as the total signal ratio over the dark current signal (Equation (7)). The SNRs are the ratio of the useful signal to the noisy signal in the total signal. The higher the signal-to-noise ratio, the better.

$$SNRs = \frac{L_{total}}{L_{darkcurrent}} \quad (7)$$

We first measured the dark current at different integration times after warming up the micro-spectrometer for 60 min (Figure 3a) and found that the dark current increased in a logarithmic fashion with integration time. The micro-spectrometer is considered to operate at a stable maximum temperature after 60 min of operation. As we used a reference plate with a maximum reflectance of 95% for field calibrations, but the DN range of the micro-spectrometer is 0–65,535, we first needed to ensure that we did not exceed the DN limit when collecting 95% of the reference plat and that our integration time was not too long, as the state of the water body changes rapidly. We should ideally be able to measure a water body spectrum within 2 s, but in a full water body spectrum measurement, the effects of waves, boat wake, etc., need to be taken into account. We generally took several measurements to average the water body spectra for field measurements.

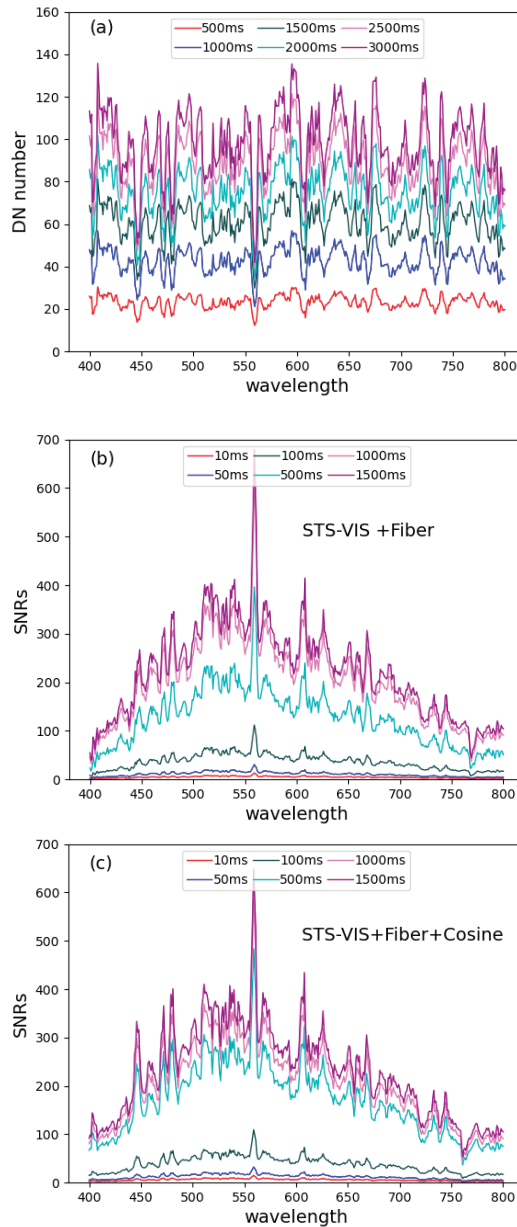


**Figure 3.** Dark current diagram for different integration times (a), SNR diagram for radiance measurement of DN values (b), SNR diagram for irradiance measurement of DN values (c).

Two schemes were used to measure 95% of the reference plate, the first using a micro-spectrometer and optical fiber to measure the DN values corresponding to radiance, and the second using a micro-spectrometer, optical fiber and cosine receiver to measure the DN values corresponding to irradiance. The SNR plot of the DN values corresponding to radiance (Figure 3b) shows that the integration time exceeds the SNRs ~100:1 at 500 ms, but that there are higher SNRs at 1000 ms and 1500 ms; therefore, we chose 1000 ms as the integration time for the DN values of radiance. The SNR diagram for the irradiance

corresponding to the DN value (Figure 3c) shows that the integration time exceeds the SNRs ~100:1 at 500 ms, and has similar SNRs at 500 ms, 1000 ms and 1500 ms; thus, we chose 500 ms as the integration time for the DN value of the irradiance.

3.2. Comparison of Gain and Offset Via Two Fiber Types

We performed field radiometric calibrations using different fiber types (Table 2). The two different fibers are from Ocean Optics (OC) and Hygirel (HY). The OC fiber is manufactured by Ocean Optics and has a spectral range of 200–1000 nm, and its core diameter is 600 μm and its length is 2 m; HY is manufactured by HAIJILEKEJI and has a spectral range of 200–1100 nm, and its core diameter is 1000 μm and its length is 2 m. Figure 4 shows the results of the field radiometric calibration coefficients gain and offset, which we evaluated using *r* for least squares regression coefficient accuracy. We found that (a)-1, (a)-2 and (a)-3 have a large variation in gain coefficients across fiber types, but there is a linear relationship, with *r* reaching 0.99 for Ocean Optics’ gain and Hygirel’s gain. The gain data are again noticeably jittery at 760 nm, which we attribute to the different integration times measured by Trios and STS-VIS at the time of measurement and to the variation in atmospheric gases. We post-processed the gain data by means of smoothing in subsequent processing. We also found for (a)-1, (a)-2 and (a)-3 that the offset coefficients vary considerably across fiber types and do not have any linear relationship, with *r* reaching 0.99 for offset obtained on sunny days. We found that the overall offset coefficient of HY is much larger than that of OC, which we believe is due to the different core diameters of the two fibers and the different amounts of sunlight energy entering the micro-spectrometer at the same integration time for HY and OC.

Table 2. Parameter table of different fiber types.

	Ocean Optics (OC)	Hygirel (HY)
Wavelength (nm)	200–1100	200–1100
Core Diameter (μm)	600	1000
Length (m)	2	2

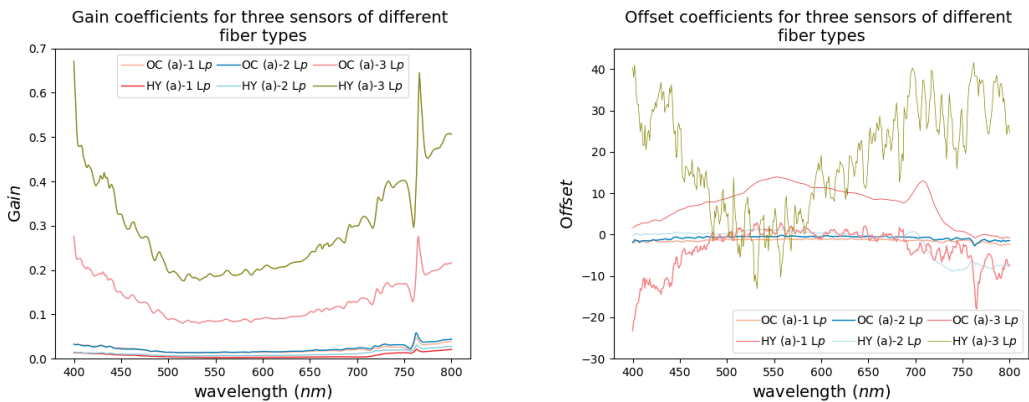


Figure 4. Graphs of gain and offset of micro-spectrometer connection with different fiber types.

We found that for a fixed integration time and different fiber types, there are different field radiometric calibration coefficients for gain and offset. We have made the gain and offset for sunny days for Ocean Optics and Hygirel fiber types publicly available for use so that a field radiometric calibration can be performed before use if a more accurate *Rrs* is required. Different fiber types mainly affect the calibration coefficients of gain and offset, and the field radiometric calibration coefficients of gain and offset for different

fiber types can be found at [https://github.com/765302995/FRC\\_Micro-spec](https://github.com/765302995/FRC_Micro-spec) (accessed on 15 November 2022).

### 3.3. Comparison of Radiance/Irradiance Measured in Four Diffuse Reflector/Target Cloths

When measuring four different reference plates using Trios and STS-VIS, we used the vertical measurement method because the reference plates are diffuse light sources. The results of the simultaneous measurements of the diffuse reflectance plate/target cloth using the micro-spectrometer and Trios under sunny conditions are shown in Figure 5. It can be seen that the micro-spectrometer and Trios have a large error at 760 nm in the oxygen absorption. In 95% of the diffuse reflectance plate results, the bias error of  $R_{rs}$  measured by the micro-spectrometer and Trios ranged from 0.5 to 1.6%; in 20% of the diffuse reflectance plate results, the bias error of  $R_{rs}$  measured by the micro-spectrometer and Trios ranged from  $-4.15$  to  $-7.44\%$ ; in 5% of the target cloth results, the bias error of  $R_{rs}$  measured by the micro-spectrometer and Trios ranged from  $-1.87$  to  $-12.63\%$ ; and in 2% of the target cloth results, the bias error of  $R_{rs}$  measured by the micro-spectrometer and Trios ranged from  $-22.9$  to  $-47.41\%$ . The lower the reflectance, the poorer the signal-to-noise ratio of the micro-spectrometer and, therefore, the greater the error in the measured reflectance.

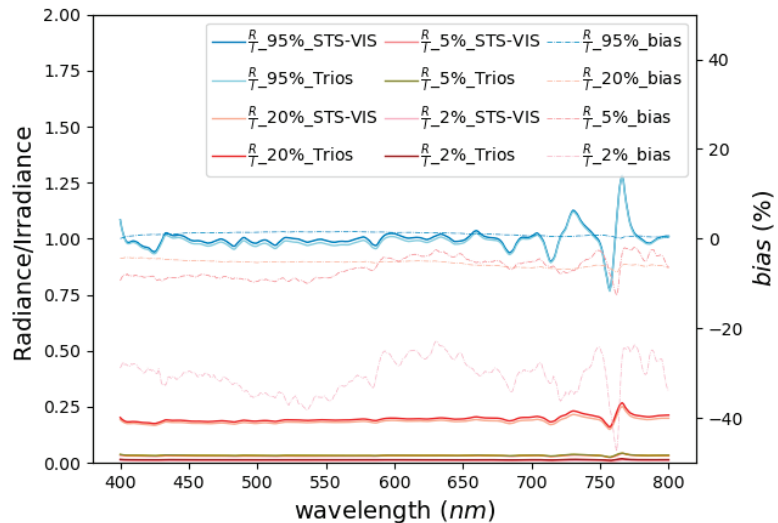


**Figure 5.** Diffuse reflectance plate results with bias plots for 95%, 20%, 5% and 2% measurements using Trios and micro-spectrometer.

## 4. Discussion

The  $R_{rs}$  accuracy and availability of micro-spectrometer measurements are evaluated here. We firstly evaluate the simultaneous measurements from Qinghai Lake and Golmud River waters using the micro-spectrometer and Trios, and finally, we carry the calibrated micro-spectrometer in the unmanned boat to perform the first measurement of the water body in plateau unmanned lakes.

The water body has a clear bidirectional reflectance distribution, so when we measure the water body, the measurement angle needs to meet the zenith angle of the sun at  $40^\circ$  and the solar azimuth angle at  $135^\circ$  or  $45^\circ$  to eliminate the influence of sun glint. We use the above-water approach to measure water bodies from the same angles as described above.

### 4.1. Comparison of $R_{rs}$ Measured in Two Plateau Inland Water Body Types

We carried out and compared  $R_{rs}$  measurements by using the micro-spectrometer and Trios on Qinghai Lake and in the Golmud city River, and the comparison results are shown



in Figure 6: there is an overestimation of  $Rrs$  when measured using the micro-spectrometer in Qinghai Lake (Figure 6a), where the  $r$  of  $Rrs$  measured by the micro-spectrometer and Trios is 0.99; the MAPD reaches 18.64%; and the bias is at 400–450 nm, 590–610 nm and 700–750 nm, all which exceeded 20%. We can see from the in situ photo (a) that this inland lake of the Qinghai–Tibet Plateau is a clean type. The cleaner the water body, the lower the reflectivity of the water body and the lower the SNR of the micro-spectrometer, meaning that the MPAD is larger. However, we can see by the shape of the water body spectrum that we obtained a complete measurement of the spectral shape of the clean water body. There is an underestimation of  $Rrs$  in the Golmud River when measured with the micro-spectrometer (Figure 6b); the micro-spectrometer and Trios reached an  $r$  of 0.99 for  $Rrs$ , an MAPD of 5.11% and a bias of over 10% at 700–750 nm. We can see from the in situ photo (b) that this inland river of the Qinghai–Tibet Plateau has a turbid type. The more turbid the water body, the higher the reflectance of the water body, and the higher the SNR of the micro-spectrometer. We can see by the shape of the water body spectrum that we obtained a complete measurement of the spectral shape of the clean water body. For the turbid water body, not only is the water body shape the same, but the value of the water body spectrum is also very similar; thus, the water body spectrum measured by the micro-spectrometer can be used for quantitative water body parameter research.

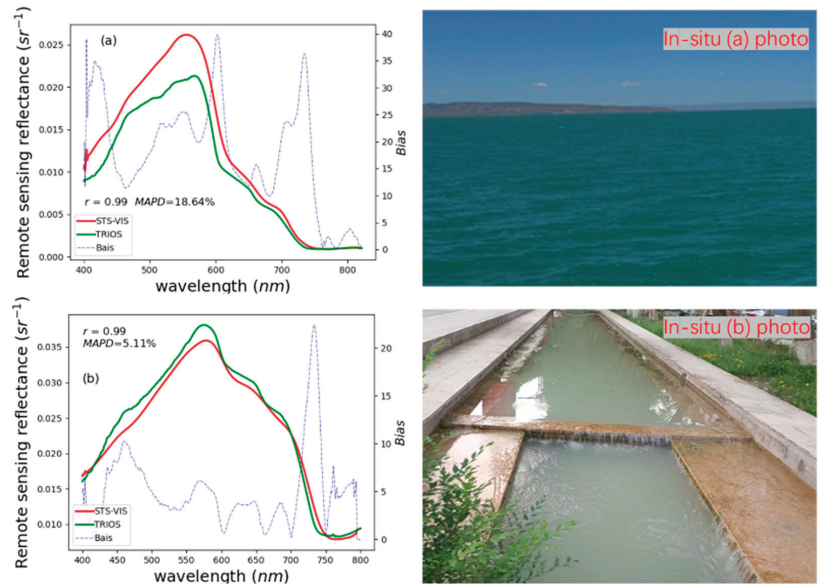


**Figure 6.** Micro-spectrometer measurements of clear water and turbid water  $Rrs$  and bias, and in situ photos of (a) spectrum of Qinghai Lake, (b) spectrum of Golmud city River.

#### 4.2. Unmanned Area Applications

In field experiments that are carried out in plateau inland waters, many lakes and rivers are in unmanned areas and, therefore, cannot be measured with spectrometers such as Trios. Instead, we can use micro-spectrometers to measure the spectra of unmanned water bodies. The calibrated micro-spectrometer is carried on unmanned boats for the measurements. We designed the route according to the GPS of the unmanned boat and in accordance with the experiment time to ensure that the three probes of the micro-spectrometer met the solar zenith angle of  $40^\circ$  and the solar azimuth angle of  $135^\circ$ , or met the  $45^\circ$  water measurement angle requirements. When the unmanned boat arrives at the predetermined point, the unmanned boat will stop and sway according to the water waves; thus, we arrived at the point moving slowly in order to obtain the measurement of the point walking water

body spectrum. Here, the water spectra of the Qarhan Salt Lake (DBX,NHBX) and the Hoh Xil Salt Lake (KKXL) were measured, as shown in Figure 7. From the in situ photos, it can be seen that DBX3 is the most turbid, with the highest water reflectance at 590 nm at  $0.055 \text{ sr}^{-1}$ , and at 500–700 nm exceeding  $0.03 \text{ sr}^{-1}$ , resulting in a heavy greyish-brown color. DBX8 is also more turbid, with the highest water reflectance at 600 nm at  $0.039 \text{ sr}^{-1}$ , and 550–720 nm. The reflectance of DBX6 reached the highest value at 600 nm at  $0.02 \text{ sr}^{-1}$ , and had a grey-green color; the reflectance of KKXL1 and KKXL2 reached the highest value at 580 nm, and the reflectance was more stable at 400–580 nm, and thus, the color of the water body was blue.

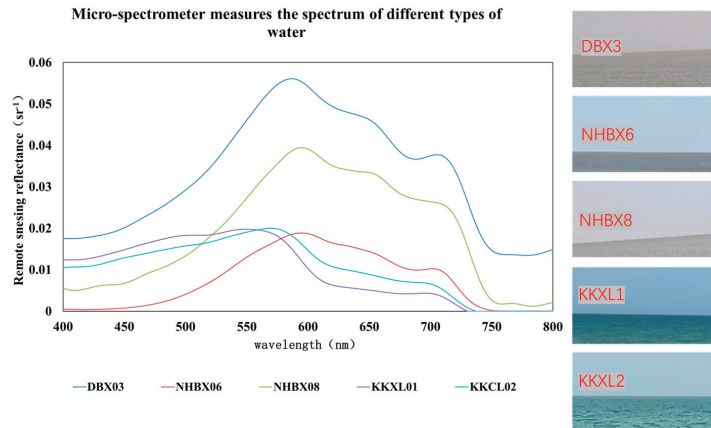


**Figure 7.** Micro-spectrometer measurements of unmanned areas of Qarhan and Hoh Xil Salt Lake Rrs and in situ photos.

## 5. Conclusions

Radiation calibration is needed to carry out irradiance and radiance measurements with micro-spectrometers. This work introduces the method of field radiation calibration for micro-spectrometers, analyzes the effect of different types of connected fibers on the radiation calibration, and analyzes the performance of micro-spectrometers in measuring Rrs in inland waters. The main findings are as follows: (1) Different fiber types mainly affect the calibration coefficients of gain and offset, and the field radiometric calibration coefficients of gain and offset for different fiber types can be found at [https://github.com/765302995/FRC\\_Micro-spec](https://github.com/765302995/FRC_Micro-spec) (accessed on 15 November 2022). (2) The MAPD of the micro-spectrometer reached 18.64% and 5.11% for clear water and turbid water, respectively, and the water body Rrs values of unmanned plateau lakes were obtained for the first time using the micro-spectrometer. This article shows that the micro-spectrometer can meet the requirements for field measurements of Rrs of water bodies in inland unmanned areas, and with this breakthrough in the radiation performance of the micro-spectrometer, we can obtain more accurate Rrs measurements of water bodies in unmanned areas.

**Author Contributions:** Conceptualization J.S. and Q.S.; project administration, Y.Y. and J.L.; writing—original draft preparation, J.S.; writing—review and editing, Q.S.; validation, L.W. and F.Z.; supervision, Q.S.; methodology, J.S. All authors have read and agreed to the published version of the manuscript.

**Funding:** This work was supported in part by the National Key Research and Development Program of China under grant number 2021YFB3901101.

**Institutional Review Board Statement:** Not applicable.

**Informed Consent Statement:** Not applicable.

**Data Availability Statement:** Not applicable.

**Acknowledgments:** The authors would like to thank Qian Shen from the Key Laboratory of Digital Earth Science, Aerospace Information Research Institute, Chinese Academy of Sciences for help with writing. We are also thankful to all anonymous reviewers for their constructive comments provided on the study. Thanks to Ge Yongquan and Gao Hangyu from Shenyang Jianzhu University for their help in obtaining the data.

**Conflicts of Interest:** The authors declare no conflict of interest.

**Appendix A**

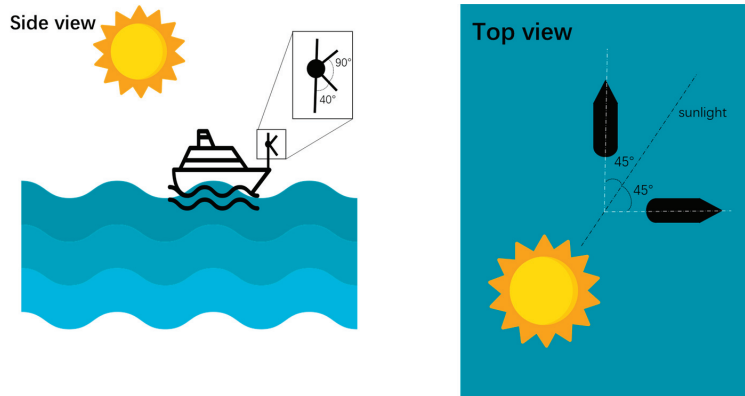


**Figure A1.** Conceptual view of the unmanned ship carrying a micro-spectrometer to collect water body spectrum; the side view details the angle of measurement of the zenith angle of the three sensors followed for spectrum collection and the top view details the angle of measurement of the azimuth of the three sensors for spectrum collection.

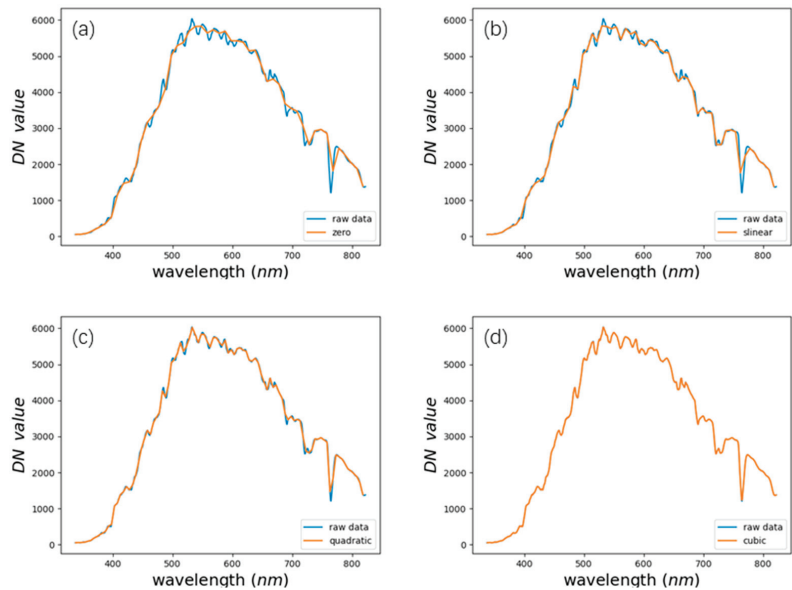


**Figure A2.** Comparison figure of different spectral resampling methods, (a) zero spline interpolation; (b) linear spline interpolation; (c) quadratic spline interpolation; (d) cubic spline interpolation.

## References

1. Antoine, D.; IOCCG. *Ocean-Colour Observations from a Geostationary Orbit*; International Ocean Colour Coordinating Group (IOCCG): Dartmouth, NS, Canada, 2012.
2. Chawla, I.; Karthikeyan, L.; Mishra, A.K. A Review of Remote Sensing Applications for Water Security: Quantity, Quality, and Extremes. *J. Hydrol.* **2020**, *585*, 124826. [CrossRef]
3. Hou, X.; Feng, L.; Dai, Y.; Hu, C.; Gibson, L.; Tang, J.; Lee, Z.; Wang, Y.; Cai, X.; Liu, J.; et al. Global Mapping Reveals Increase in Lacustrine Algal Blooms over the Past Decade. *Nat. Geosci.* **2022**, *15*, 130–134. [CrossRef]
4. Shen, Q.; Yao, Y.; Li, J.; Zhang, F.; Wang, S.; Wu, Y.; Ye, H.; Zhang, B. A CIE Color Purity Algorithm to Detect Black and Odorous Water in Urban Rivers Using High-Resolution Multispectral Remote Sensing Images. *IEEE Trans. Geosci. Remote Sens.* **2019**, *57*, 6577–6590. [CrossRef]
5. O'Reilly, J.; Maritorena, S.; Mitchell, B.; Siegel, D.; Carder, K.; Garver, S.; Kahru, M.; McClain, C. Ocean Color Chlorophyll Algorithms for SEAWIFS. *J. Geophys. Res.* **1998**, *103*, 24937–24953. [CrossRef]
6. Ni, Z.; Wang, S.; Wang, Y. Characteristics of Bioavailable Organic Phosphorus in Sediment and Its Contribution to Lake Eutrophication in China. *Environ. Pollut.* **2016**, *219*, 537–544. [CrossRef]
7. Chen, Z.; Hu, C.; Comny, R.N.; Muller-Karger, F.; Swarzenski, P. Colored Dissolved Organic Matter in Tampa Bay, Florida. *Mar. Chem.* **2007**, *104*, 98–109. [CrossRef]
8. Liu, D.; Yu, S.; Xiao, Q.; Qi, T.; Duan, H. Satellite Estimation of Dissolved Organic Carbon in Eutrophic Lake Taihu, China. *Remote Sens. Environ.* **2021**, *264*, 112572. [CrossRef]
9. Federico, B.; Marco, C.; Jixi, G.; Robert, H.; Massimo, M.; Yanming, R.; Patrizia, S.; Luigi, T. Remote Sensing Methodology for the Estimation of Methane Emissions from Chinese Lakes. In Proceedings of the 2008 International Workshop on Earth Observation and Remote Sensing Applications, Beijing, China, 30 June–2 July 2008; IEEE: Piscataway, NJ, USA, 2018; pp. 1–6.
10. The Analytical Spectral Devices, FieldSpec. Available online: <https://www.malvernpanalytical.com/en/products/product-range/asd-range/fieldspec-range> (accessed on 9 August 2022).
11. High-Resolution Profiling Reflectance Radiometer (PRR). Available online: [http://www.biospherical.com/index.php?option=com\\_content&view=article&id=51&Itemid=67](http://www.biospherical.com/index.php?option=com_content&view=article&id=51&Itemid=67) (accessed on 9 August 2022).
12. GmbH, T. RAMSES. Available online: <https://www.trios.de/en/ramses.html> (accessed on 9 August 2022).
13. Hyperspectral Surface Acquisition System Sea-Bird Scientific. Available online: <https://www.seabird.com/hyperspectral-surface-acquisition-system/product?id=54627923900&callback=qs> (accessed on 9 August 2022).
14. Yang, Z.; Albrow-Owen, T.; Cai, W.; Hasan, T. Miniaturization of Optical Spectrometers. *Science* **2021**, *371*, 0722. [CrossRef]
15. Zarzar, C.M.; Dash, P.; Dyer, J.L.; Moorhead, R.; Hathcock, L. Development of a Simplified Radiometric Calibration Framework for Water-Based and Rapid Deployment Unmanned Aerial System (UAS) Operations. *Drones* **2020**, *4*, 17. [CrossRef]
16. Cao, H.; Gu, X.; Wei, X.; Yu, T.; Zhang, H. Lookup Table Approach for Radiometric Calibration of Miniaturized Multispectral Camera Mounted on an Unmanned Aerial Vehicle. *Remote Sens.* **2020**, *12*, 4012. [CrossRef]
17. Shi, G.; Du, X.; Du, M.; Li, Q.; Tian, X.; Ren, Y.; Zhang, Y.; Wang, H. Cotton Yield Estimation Using the Remotely Sensed Cotton Boll Index from UAV Images. *Drones* **2022**, *6*, 254. [CrossRef]
18. Gege, P.; Dekker, A.G. Spectral and Radiometric Measurement Requirements for Inland, Coastal and Reef Waters. *Remote Sens.* **2020**, *12*, 2247. [CrossRef]
19. Cao, Z.; Ma, R.; Liu, J.; Ding, J. Improved Radiometric and Spatial Capabilities of the Coastal Zone Imager Onboard Chinese HY-1C Satellite for Inland Lakes. *IEEE Geosci. Remote Sens. Lett.* **2021**, *18*, 193–197. [CrossRef]
20. Leroy, M.; Henry, P.; Guenther, B.; McLean, J. Comparison of CNES Spherical and NASA Hemispherical Large Aperture Integration Sources: II. Using the SPOT-2 Satellite Instruments. *Remote Sens. Environ.* **1990**, *31*, 97–104. [CrossRef]
21. Shi, J.; Li, M.; Hu, Y.; Wang, X.; Xu, H.; Chi, G.; Hong, J. Laboratory Calibration of an Ultraviolet–Visible Imaging Spectropolarimeter. *Remote Sens.* **2022**, *14*, 3898. [CrossRef]
22. Sun, Y.C.; Huang, C.; Xia, G.; Jin, S.Q.; Lu, H.B. Accurate Wavelength Calibration Method for Compact CCD Spectrometer. *J. Opt. Soc. Am. A Opt. Image Sci. Vis.* **2017**, *34*, 498–505. [CrossRef]
23. Xiong, X.; Erives, H.; Xiong, S.; Xie, X.; Esposito, J.; Sun, J. Performance of Terra MODIS Solar Diffuser and Solar Diffuser Stability Monitor. In Proceedings of the Optics and Photonics 2005, San Diego, CA, USA, 31 July–4 August 2005; pp. 58820S.1–58820S.10.
24. Xiong, X.; Barnes, W. An Overview of MODIS Radiometric Calibration and Characterization. *Adv. Atmos. Sci.* **2006**, *23*, 69–79. [CrossRef]
25. Adão, T.; Hruška, J.; Pádua, L.; Bessa, J.; Peres, E.; Morais, R.; Sousa, J.J. Hyperspectral Imaging: A Review on UAV-Based Sensors, Data Processing and Applications for Agriculture and Forestry. *Remote Sens.* **2017**, *9*, 1110. [CrossRef]
26. Smith, R.C.; Booth, C.R.; Star, J.L. Oceanographic Biooptical Profiling System. *Appl. Opt.* **1984**, *23*, 2791–2797. [CrossRef]
27. Mueller, J.L. Above-Water Radiance and Remote Sensing Reflectance Measurement and Analysis Protocols. In *Ocean Optics Protocols for Satellite Ocean Color Sensor Validation Revision 3*; NASA Goddard Space Flight Center: Greenbelt, MD, USA, 2000; Volume 2, pp. 171–181.
28. Lee, Z.; Pahlevan, N.; Ahn, Y.-H.; Greb, S.; O'Donnell, D. Robust Approach to Directly Measuring Water-Leaving Radiance in the Field. *Appl. Opt.* **2013**, *52*, 1693–1701. [CrossRef]
29. Mobley, C.D. Estimation of the Remote-Sensing Reflectance from above-Surface Measurements. *Appl. Opt.* **1999**, *38*, 7442–7455. [CrossRef]

30. Huang, C.; Zhang, L.; Fang, J.; Tong, Q. A Radiometric Calibration Model for the Field Imaging Spectrometer System. *IEEE Trans. Geosci. Remote Sens.* **2013**, *51*, 2465–2475. [[CrossRef](#)]
31. Hu, C.; Feng, L.; Lee, Z.; Davis, C.O.; Mannino, A.; McClain, C.R.; Franz, B.A. Dynamic Range and Sensitivity Requirements of Satellite Ocean Color Sensors: Learning from the Past. *Appl. Opt.* **2012**, *51*, 6045–6062. [[CrossRef](#)]
32. Cao, Z.; Ma, R.; Duan, H.; Xue, K. Effects of Broad Bandwidth on the Remote Sensing of Inland Waters: Implications for High Spatial Resolution Satellite Data Applications. *ISPRS J. Photogramm. Remote Sens.* **2019**, *153*, 110–122. [[CrossRef](#)]

**Disclaimer/Publisher’s Note:** The statements, opinions and data contained in all publications are solely those of the individual author(s) and contributor(s) and not of MDPI and/or the editor(s). MDPI and/or the editor(s) disclaim responsibility for any injury to people or property resulting from any ideas, methods, instructions or products referred to in the content.

Review

# Geographic Scene Understanding of High-Spatial-Resolution Remote Sensing Images: Methodological Trends and Current Challenges

Peng Ye <sup>1,2,3,4</sup>, Guowei Liu <sup>2,\*</sup> and Yi Huang <sup>5,6</sup>

<sup>1</sup> Urban Planning and Development Institute, Yangzhou University, Yangzhou 225127, China; 007839@yzu.edu.cn

<sup>2</sup> College of Architectural Science and Engineering, Yangzhou University, Yangzhou 225127, China

<sup>3</sup> Key Lab of Virtual Geographic Environment, Ministry of Education, Nanjing Normal University, Nanjing 210023, China

<sup>4</sup> Jiangsu Center for Collaborative Innovation in Geographical Information Resource Development and Application, Nanjing 210023, China

<sup>5</sup> Smart Health Big Data Analysis and Location Services Engineering Lab of Jiangsu Province, Nanjing University of Posts and Telecommunications, Nanjing 210023, China; huangyi@njupt.edu.cn

<sup>6</sup> School of Geographic and Biologic Information, Nanjing University of Posts and Telecommunications, Nanjing 210023, China

\* Correspondence: arguoweiliu@yzu.edu.cn; Tel.: +86-155-2142-2026

**Abstract:** As one of the primary means of Earth observation, high-spatial-resolution remote sensing images can describe the geometry, texture and structure of objects in detail. It has become a research hotspot to recognize the semantic information of objects, analyze the semantic relationship between objects and then understand the more abstract geographic scenes in high-spatial-resolution remote sensing images. Based on the basic connotation of geographic scene understanding of high-spatial-resolution remote sensing images, this paper firstly summarizes the keystones in geographic scene understanding, such as various semantic hierarchies, complex spatial structures and limited labeled samples. Then, the achievements in the processing strategies and techniques of geographic scene understanding in recent years are reviewed from three layers: visual semantics, object semantics and concept semantics. On this basis, the new challenges in the research of geographic scene understanding of high-spatial-resolution remote sensing images are analyzed, and future research prospects have been proposed.

**Keywords:** geographic scene; high-spatial-resolution remote sensing image; scene understanding; semantic hierarchy of geographic scene; remote sensing image processing

**Citation:** Ye, P.; Liu, G.; Huang, Y. Geographic Scene Understanding of High-Spatial-Resolution Remote Sensing Images: Methodological Trends and Current Challenges. *Appl. Sci.* **2022**, *12*, 6000. <https://doi.org/10.3390/app12126000>

Academic Editor: Amerigo Capria

Received: 5 May 2022

Accepted: 8 June 2022

Published: 13 June 2022

**Publisher's Note:** MDPI stays neutral with regard to jurisdictional claims in published maps and institutional affiliations.



**Copyright:** © 2022 by the authors. Licensee MDPI, Basel, Switzerland. This article is an open access article distributed under the terms and conditions of the Creative Commons Attribution (CC BY) license (<https://creativecommons.org/licenses/by/4.0/>).

## 1. Introduction

Remote sensing, as a comprehensive modern surveying and mapping technology, plays an important role in Earth observation. In recent years, as a result of the rapid development of sensor technology, aerospace platform technology and data communication technology, as well as the vigorous promotion of relevant international organizations, the global observation capability of the space–air–ground integration has been greatly enhanced [1]. At present, a large number of high-spatial-resolution (HSR) remote sensing images with meters, or even sub-meters, can be obtained. In HSR remote sensing images, various realistic geographic scenes are clearly presented: for instance, artificial construction scenes such as urban residential areas, ports and airports; disaster scenes such as landslides, mudslides and earthquakes; and natural scenes such as forests and beaches [2]. This small-scale observation means that HSR remote sensing images can provide more complex surface structure information and more sophisticated texture and size information. Consequently,

it has been applied to urban planning, disaster management, environmental monitoring, military activities and many other fields [3,4].

As a collection of multiple objects and their surroundings in the real world, understanding the semantics of scenes is an important task in remote sensing image interpretation. Scene understanding is based on the perception of remote sensing image data, combined with visual analysis, image processing, pattern recognition and other technical means, to mine the characteristics and patterns in the image from different levels such as computational statistics, behavioral cognition and semantics, so as to realize the effective analysis, cognition and representation of the scene. However, due to the limitations of space imaging technology, HSR remote sensing images, although of higher spatial resolution, are relatively deficient in spectral information [5]. In HSR remote sensing images, the spectral heterogeneity of the same type of ground objects is enhanced, and the spectral diversity of different ground objects is reduced, which leads to the decline in statistical separability of different types of ground objects in the spectral domain [6]. Therefore, understanding the geographic scenes in the HSR remote sensing images includes the identification of both objects and the relationships between objects, as well as the analysis of themes categories with richer concepts and content implied in the geographic scene. Because of the complexity and intersection of these tasks, the research on geographic scene understanding of HSR remote sensing images still faces many challenges, mainly including the following three aspects:

- (1) In terms of the basic principles of geographic scene understanding, the machine will identify the objects or targets contained in the scene according to the similarity of image data. In contrast, humans analyze the semantic information of scene content through the category and spatial distribution of ground objects, and form high-level features through abstract concepts [7]. There is a semantic gap between the conceptual similarity of human understanding and the digital storage form similarity of machine identify. This makes it impossible to relate low-level visual features (such as color, shape, texture, etc.) to high-level semantic information directly.
- (2) In terms of the data characteristics of HSR remote sensing images, the improved spatial resolution makes the ground objects in the images have more fine texture features, more obvious geometric structure and clearer location layout. Correspondingly, it also aggravates the difficulty of data processing in intelligent image interpretation. In high resolution images, the spectral heterogeneity of similar objects is enhanced, and the spectral difference of different objects is reduced. This leads to a decrease in the statistical separability of different ground objects in the spectral domain [8]. A high resolution does not necessarily promote an improvement in interpretation accuracy.
- (3) In terms of the sophistication of geographic scenes, the structure and composition of the geographic scenes in the HSR remote sensing images are complex, highly variable and even messy. The types of geographic scenes with the same ground objects may be different. However, different types of ground objects also appear in similar geographic scenes [9]. Consequently, understanding the semantic information of the geographic scene and constructing the corresponding semantic feature description is crucial.

As an extension of remote sensing image interpretation, the complexity and comprehensiveness of geographic scene understanding based on HSR images is beyond the general processing task of remote sensing. Although significant progress has been made in the research of feature extraction, target detection, scene classification and other sub-tasks, these sub-tasks lack a unified framework to cross the “semantic gap” to understand the high-level semantics of the geographic scenes. Thus, it is necessary to integrate these sub-tasks according to the human cognitive model in understanding the geographic scenes of HSR remote sensing images. In recent years, many researchers who are engaged in computer vision have realized the importance of a “holistic understanding” of geographic scenes and put forward the research approaches of task integration and feature integration. However, there is no systematic research on the geographic scene of HSR remote sensing images as a comprehensive and complete field of intelligent information processing. This paper is focused on answering the following research questions:

- (1) What are the objectives of geographic scene understanding?
- (2) How are remote sensing approaches being used for geographic scene understanding?
- (3) What are the current gaps in HSR remote-sensing-based geographic scene understanding?

The rest of the paper is organized as follows: Section 2 describes the basic ideas of geographic scene understanding based on HSR remote sensing images; Section 3 presents the semantic understanding approaches of the visual layer; Section 4 presents the semantic understanding approaches of the object layer; Section 5 presents the semantic understanding approaches of the concept layer; and Section 6 discusses the open problems and challenges in the future. The paper closes with a conclusion in Section 7.

## 2. Basic Ideas

The concept of geographic scene understanding of remote sensing images includes two aspects, namely, “remote sensing image understanding” and the “geographic scene”. Remote sensing image understanding is a cognitive process to realize the objective things and their laws reflected by remote sensing images through observing, distinguishing, identifying and reasoning remote sensing images and interpreting the content of remote sensing images semantically. The geographic scene is a regional complex with a specific structure and function, which is composed of various natural and human factors in a certain region [10]. In remote sensing images, the geographic scene is a closed region composed of different ground objects. The geographic scene generally involves three aspects: (1) the constituent elements of the scene structure, (2) the relationship between these elements and (3) the function of the set of these elements. Therefore, the research object of geographic scene understanding of remote sensing images is the regional complex composed of ground objects with certain spatial distribution patterns. The research objective is to interpret the research object as a series of meaningful and understandable semantic information.

HSR remote sensing images can reflect the more detailed composition and spatial distribution of the ground objects, which is a microcosm of the real geographic scene. Owing to increased spatial resolution and unique imaging methods, geographic scenes in HSR remote sensing images have the following characteristics:

- (1) The categories of ground objects in the geographic scene are diverse. The same category of geographic scene can contain different ground objects, and different geographic scenes can also contain the same ground objects. Different objects also have different characteristics in terms of spectrum, texture and structure [11].
- (2) The categories of ground objects in the geographic scene have variability. The change in the categories of some ground objects in geographic scenes does not necessarily lead to a change in the whole semantic information of geographic scenes [12].
- (3) The spatial relationship between ground objects in geographic scenes is complex. Different distribution forms between ground objects lead to different semantic information of geographic scenes. Other relevant characteristics are shown in Figure 1.

The characteristics of HSR remote sensing images also make the following special features in understanding geographic scenes:

(1) The semantic information of geographic scenes in HSR remote sensing images is hierarchical. The content description of HSR remote sensing images has the hierarchical inclusion relation of “Pixel-Region-Target-Scene”. Different levels of image content reflect the semantic information with different levels of abstraction, which can be divided into the visual layer, object layer and concept layer (Figure 2). The visual layer is the description of pixel-level image content, including color, texture, shape and other original visual characteristics. The semantic information of the visual layer can be obtained directly from image processing without any external knowledge and experience [13]. The object layer is the description of region-level and target-level image content, including the individual features of objects and the local features of spatial relations among objects [14]. The semantic information of the object layer needs to be obtained through simple reasoning, and it is necessary to use external knowledge and experience to assist this reasoning. The concept layer is a description of the scene-level image content, including the abstract attributes of



the image. The semantic information of scene level involves the semantic features of scene representation or higher-level behavior or emotion analysis, and it needs to link image content with abstract concepts through complex reasoning and subjective judgment [15].

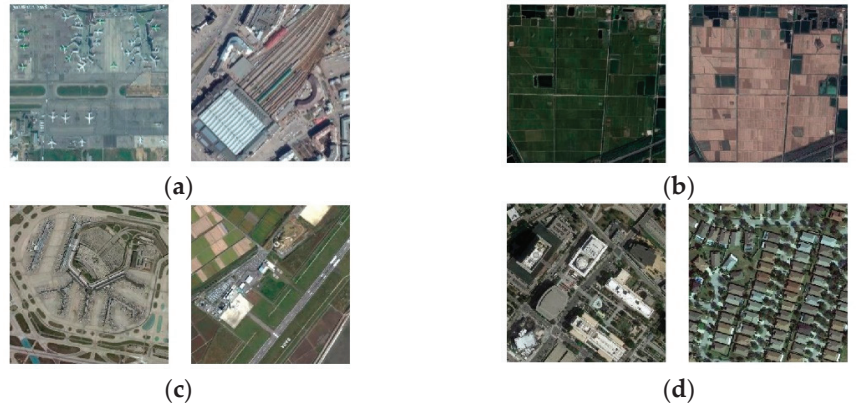


**Figure 1.** Image characteristics of geographic scenes in HSR remote sensing: (a) reflects the diversity of the ground objects in the geographic scene; (b) reflects the diversity of imaging conditions of HSR remote sensing images; (c) reflects the differences in the types of ground objects in the same category of geographic scenes; (d) reflects the similarity in the types of ground objects in different categories of geographic scenes.

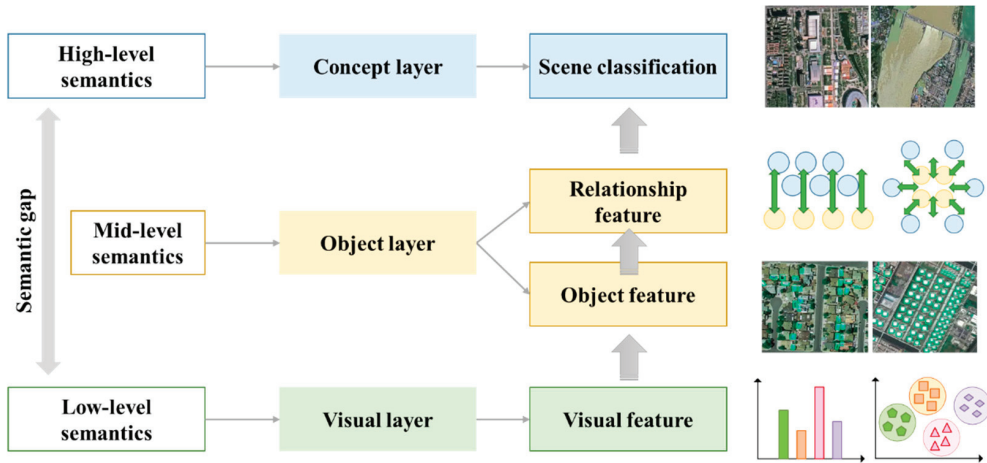


**Figure 2.** Semantic hierarchy model of three layers structure.

There is a dialectical relationship between the tasks of geographic scenes understanding at different semantic layers. The input of geographic scene understanding is the original HSR remote sensing images, and the output is semantic information of the geographic scene. In the tasks of geographic scene understanding, it is necessary to combine the semantic processing of the visual layer and object layer (feature extraction and target recognition) with the semantic reasoning of the concept layer (scene description and classification), the different tasks are interdependent on each other [16]. The cognition of visual and object layer semantics can form the inference of concept layer semantics, and the cognition of concept layer semantics can be used as knowledge to guide the extraction of visual and object layer semantics.

(2) Spatial structure characteristics play an important role in the geographic scene understanding of HSR remote sensing images. Because of the global and polysemy of the geographic scene, the geographic scene understanding is not a simple stacking of some local semantics [17]. In the same category of the geographic scene, the objects of the same type have similar individual characteristics and spatial distribution patterns. However, there are different structural features among different categories of geographic scenes. In Figure 3, these two geographic scenes of “residential area” and “industrial area” contain similar visual features and object types, which are composed of buildings, roads and vegetation. However, there are great differences in spatial structures between objects, which is a critical factor to distinguish the categories of geographic scenes. Therefore, the spatial structure characteristics of geographic scenes are relatively stable, and making full use of spatial information such as geometry, texture and context of HSR remote sensing images is an effective way to improve the understanding of geographic scenes [18,19].

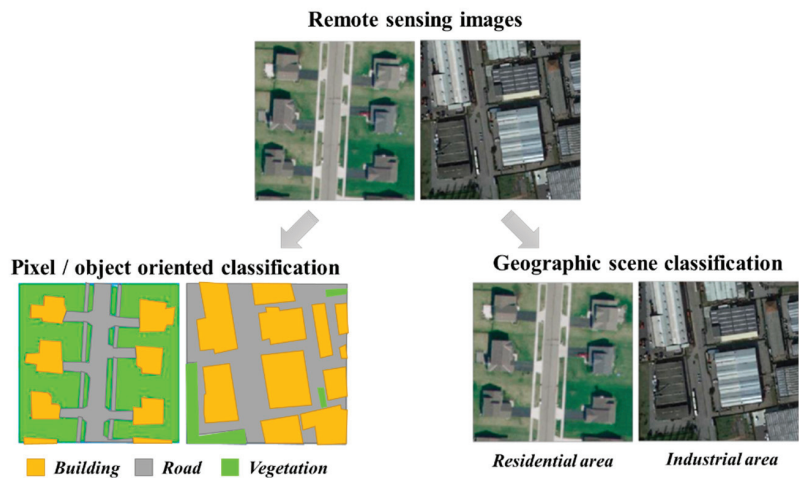


**Figure 3.** Understanding differences of geographic scenes at different semantic layers.

(3) The data characteristics of HSR remote sensing images have both opportunities and challenges for the geographic scene understanding. The amount of HSR remote sensing images increases significantly. As the spatial resolution increases, the area of the ground covered by each pixel decreases significantly. This makes the ground object details and spatial distribution of HSR remote sensing images clearer. Compared with medium–low-resolution remote sensing images, HSR remote sensing images can be interpreted at the scene level, where semantic information is more abstract. However, compared with natural images, the HSR remote sensing images used for geographic scene understanding are less accessible in terms of data availability, except for the differences in shooting distance, shooting angle and imaging sensors. Natural images can be easily and quickly obtained from the Internet, and a large amount of data has been given the relevant label information when uploaded to the Internet [20]. For example, the ImageNet dataset [21,22] contains more than 14 million labeled samples in 1000 categories. HSR remote sensing images are not freely available for political, military and security reasons. HSR remote sensing images often rely on professional interpretation or even field research to obtain the correct label, the available sample size is limited. For instance, the UC-Merced dataset contains only 21 categories, with a total of 2100 labeled samples. Currently, the HSR remote sensing image datasets commonly used for geographic scene understanding are shown in Table 1.

**Table 1.** Comparison of existing public datasets.

Datasets	Spatial Resolution (m)	Image Size	Number of Categories	Number of Samples per Category	Total Number of Samples	Year of Publication
UC-Merced [23]	0.3	256 × 256	21	100	2100	2010
WHU-RS19 [24]	0.5	600 × 600	12	50	950	2010
RSSCN7 [25]	-	400 × 400	7	400	2800	2015
RSC11 [26]	0.2	512 × 512	11	About 100	1232	2016
SIRI-WHU [27]	2	200 × 200	12	200	2400	2016
NWPU-RESISC45 [28]	0.2–30	256 × 256	45	700	31,500	2017
PatternNet [29]	0.062–4.693	256 × 256	38	800	-	2017
AID [30]	-	-	30	-	10,000	2017
EuroSAT [31]	-	64 × 64	10	2000–3000	27,000	2019

### 3. Semantic Understanding of Visual Layer

The semantic understanding of the visual layer of the geographic scene is the extraction of basic characteristics from remote sensing image data. The essence of geographic scene understanding is to establish the mapping relationship between low-level visual features and high-level scene semantics. Thus, extracting the visual features of HSR remote sensing images is the basis of the content description of geographic scenes, which includes local features and global features.

The global feature is the feature that can represent the whole image, and it has good invariance, simple calculation and intuitive representation. Common global features include color features, texture features and shape features. Among them, color features such as color sets, color moments, color correlation diagrams, color histograms [32] and color aggregation vectors [33–35] are insensitive to size and orientation and have good stability [36]. Texture features such as gray level co-occurrence matrix (GLCM) [37], the grayscale difference [38], autocorrelation function [39], gray-level run-length [40], local binary pattern (LBP) [41], etc., are characterized by local irregularity, but macroscopic regularity. Visual features cannot only describe the basic attributes of the image such as color, texture and shape, but also reflect the deep structure information of the image. In 2001, GIST was proposed by Aude Oliva et al. simulating human vision to roughly extract the image and its context information [42]. GIST can extract spectral information from the image globally as its representation without segmenting the image or detecting the target in advance. GIST is simple and easy to use. However, with the increasing complexity of image content and structure, such as the analysis granularity being too coarse to ignore the details of the objects in the scene, the result of image processing is far from the correct result. In general, the global features are sensitive to the actual imaging conditions, and the robustness and generalization ability are relatively poor.

The local feature can effectively resist various affine transformations and have some invariance. David Lowe has come up with a landmark local feature descriptor, the scale invariant feature transform (SIFT), which has good scale invariance and rotational invariance [43]. Thus, SIFT is one of the most widely used features in image processing. Bay et al. present an accelerated robust feature descriptor (SURF) inspired by SIFT [44]. While SURF is inferior to SIFT in scale scaling and rotational invariance, it is superior in blur and illumination variation and is several times faster than SIFT. With the advancement of research, the instability of color, light and gradient features in the process of recognition became an obstacle to image classification. The histograms of oriented gradients (HOG) feature proposed in 2005 continue the high recognition accuracy characteristic of the local feature; the gradient histogram method is used to effectively solve the problem of the low recognition rate of local scene contours due to the sensitivity of light and gradient features [45]. However, HOG features have high dimensions, low computational efficiency and great redundancy and do not consider the effect of scale transformation on classification results. The CENTRIST feature proposed by Wu et al. in 2010 solves this problem well [46]. Through the census transformation of the acquired pixels, these pixels are transformed into statistical histograms to form the CENTRIST feature to extract the object's local shape

structure. After the CENTRIST transformation, the image still retains the global and local structure information. Therefore, it can simulate the human visual system and describe the shape and texture of objects accurately.

Global features and local features have their own advantages and disadvantages. Different visual features are suitable for different tasks of geographic scene understanding. In HSR remote sensing image description, visual feature extraction should not only keep the invariance of features but should also fuse the spatial structure information of the features.

#### 4. Semantic Understanding of Object Layer

Object layer semantics mainly describe the logical concepts of scenes in images, usually based on a large number of visual layer descriptors. Compared with the visual layer, the object layer is closer to the human understanding of the geographic scene. For instance, in the process of geographic scene understanding, we rely more on the houses and roads in the images, rather than recognizing that there are small dense and regular highlighted areas, narrow and long gray-banded areas and so on in the image. Houses, roads, sky and grass, which conform to human cognition, constitute the object layer semantics of geographic scenes. In addition, object layer semantics can also be abstract local areas, such as visual words generated by feature detection algorithms. There is also a certain context structure between different objects, forming a corresponding spatial relationship. Thus, a geographic scene is a combination of a set of specific objects. According to the different semantic forms of objects, there are three types: target object semantics, local area semantics and spatial structure semantics.

##### 4.1. Target Object Semantics

The object layer semantics of the geographic scene are usually concentrated on the basic level of human cognition, which can be represented by many target objects (Figure 4). For the semantic understanding of the target object, it is necessary to use the target detection algorithm to clarify the types of each object. In the fields of computer vision and pattern recognition, many target detection algorithms have been developed, for instance: the threshold-based detection method [47], the template-based detection method [48], target detection based on Hough transform or Hough forest [49], target detection based on classifiers [50], etc. For the target detection of HSR remote sensing images, the method of target detection in the computer vision field is usually used for reference, and the research is carried out around the object of special interest, in particular, the artificial structures closely related to human activities, such as buildings [51], ports [52], airport runways [53], roads [54], warships [55] and so on. For artificial structures with obvious shape features, it is generally possible to directly use their unique shape features for detection, for instance, extracting straight lines to detect linear targets in images [56]. For complex targets, the corresponding models can be constructed; for instance, the “Building” target model can be constructed by texture, shape and SIFT features, and the “Port” target model can be constructed by combining the information of coastline, wharf and embankment [57].

For the target detection of HSR remote sensing images, it is more challenging to detect objects with large image sizes and various details. Target detection of HSR remote sensing images is studied from different perspectives. A multi-layer SVM classifier is used to exclude non-target regions to improve the speed of target detection in high-resolution remote sensing images [58]. The large remote sensing image is divided into smaller blocks, the salient and synopsis features of each block are extracted, and the target detection is realized by classification [59]. Target detection is also accomplished by first segmenting HSR remote sensing images and then merging regions related to the target based on knowledge [60]. In addition, the successful application of visual selective attention to the target location in large-format remote sensing images, and the results show that the visual attention mechanism can quickly focus on the place where the object to be detected appears in the complex large image. These methods are all beneficial explorations in the target detection of HSR remote sensing images [61].



**Figure 4.** Target detection schematic. (a) is the original remote sensing image; (b) reflects that the candidate locations of the targets are found in the image; (c) reflects the results of target identifications.

The existing target detection methods have strong pertinence and lack universal and robust target detection models and algorithms. The motion characteristics of the target to be detected (such as ship wake, submarine track), the use of the shadow of the target in the image, the removal of the visible cloud cover and so on need to improve the target detection model with pertinence. To realize the practicality of target detection, it is necessary to establish a target detection model and a fast algorithm for multi-source data fusion.

#### 4.2. Local Area Semantics

Remote sensing images can also be divided according to specific rules. By extracting the local image descriptor of each sub-block, the correspondence between the local descriptor and the local semantic concept is established, and the object layer semantics are extracted. Due to the differences of descriptors, feature extraction methods of the local area can be divided into three categories: visual dictionary, feature mapping and topic model.

##### 4.2.1. Visual Dictionary

The visual dictionary, also known as the visual codebook, maps feature data onto individual codewords to generate feature vectors with codebook length [62]. The construction of a visual dictionary is essentially a cluster problem, and the visual codewords correspond to the cluster center. In the task of geographic scene understanding, the visual dictionary connects the image visual features with the scene semantics.

Whether the design of a visual dictionary is effective mainly includes three aspects: resolution, compactness and universality. (1) The resolution of the visual dictionary is reflected in the similarity between visual words. The lower the similarity, the higher the resolution. (2) The compactness is reflected in the choice of codebook length, which corresponds to different classification accuracies. A high recognition rate can be achieved by selecting a suitable visual dictionary. (3) The universality mainly refers to whether the visual dictionary needs to be relearned if the data of new categories are added. Existing dictionary learning includes generative (unsupervised) and discriminative (supervised) approaches. Perronnin et al. design a universal visual dictionary and a category visual dictionary to compete for the description of image content. The universal visual dictionary is used to describe all image scene classes, and the category visual dictionary for a certain scene class can be obtained by adaptive learning from the universal visual dictionary [63]. If an image belongs to a given class, a category visual dictionary is more suitable for describing the image than a general visual dictionary. On the contrary, the general visual dictionary is more suitable to describe the image than the category visual dictionary. However, traditional visual dictionaries are prone to a lack of clear meaning or polysemy. To solve the above problems, Su et al. use semantic attributes to clarify semantic meaning and integrate semantic attributes into the visual dictionary to remove the ambiguity of visual words [64].

#### 4.2.2. Feature Mapping

After constructing the visual dictionary, it is necessary to encode and map the local features of the image, and to represent the semantic information of the image by transforming the local features into some organized form of visual words. In addition, there are some problems such as the low efficiency of dictionary generation, serious quantization errors and the lack of spatial information of visual words. Furthermore, the image semantic representation based on the visual dictionary is a linear representation, which only performs well in the case of the classifier with the nonlinear kernel, such as support vector machine (SVM). This will undoubtedly reduce its usefulness, making it difficult to apply to large-scale data set classifications. In recent years, a semantic representation based on feature mapping has attracted more attention. Feature mapping is used to quantize and code the visual features according to the visual words and generate the representation of the visual features in the visual dictionary.

Vector quantization (VQ) is simple and convenient, but its constraint conditions are too strict, resulting in the lack of information after visual feature quantization. To overcome this shortcoming, the sparse regularization approach can be used to loosen the constraints in the VQ, which translates into a sparse coding [65,66]. Sparse coding (SC) uses a sparse regularization method to reduce quantization errors and improve the uniqueness of feature coding. However, sparse coding is only a shallow learning model with a single hidden layer. The visual dictionary acquired by shallow learning lacks the selectivity of features, which will reduce the semantic resolution of image content. On the basis of SC, the local-constrained linear coding (LLC) is proposed [67]. The sparsity of feature coding cannot guarantee its locality, while the locality of feature coding can guarantee its sparsity. As a result, LLC is more efficient and has a better refactoring effect and local smooth sparsity [68].

#### 4.2.3. Probabilistic Topic Model

In order to improve the performance of image semantic expression, a visual language model is proposed [69], which is inspired by the probabilistic topic model (PTM) of natural language understanding. Based on the visual language model, an image can be divided into many blocks as visual words according to certain rules, and these visual words have certain grammatical rules and spatial dependencies, also called visual grammar. The semantic information is represented by the co-occurrence frequency and spatial dependence of local features in the image. Common PTMs include probabilistic Latent Semantic Analysis (pLSA) [70] and Latent Dirichlet Allocation (LDA) [71].

To ameliorate the robustness of the visual language model to the change of target scale, Wu et al. extended the original model to multi-scale, and proposed the scale-invariant visual language model (m-VLM) [72]. Jing et al. use LDA to realize the scene classification of optical remote sensing images and compare it with the bag of visual words (BOVW) model [73]. The results show that LDA can provide more concise and abundant semantic information for image representation. In the parameter training stage, the probability of a visual language model is estimated by counting the frequency of a visual word or visual word combinations in the image. This approach equates the visual words in the target area of the image with the visual words in the background area, thus ignoring the negative impact of background noise on the target semantic representation [74]. Therefore, if we can distinguish the visual words in the background and assign the weight according to their contribution to the target, we can enhance the resolution of the visual language model to image semantic representation.

#### 4.3. Spatial Structure Semantics

The different arrangements of the objects that comprise the geographic scene will make the geographic scene have a different spatial structure. Spatial structure information in HSR images is contained in spectral features and prior knowledge. For the understanding of spatial structure semantics, it is necessary to describe, model and extract them and obtain

a vector model representing the structural features of processing units (pixels, primitives and targets).

#### 4.3.1. Pixel-Neighborhood-Window-Based Method

Taking a pixel as the basic processing unit, a window is defined for each pixel (also called the central pixel) in the image, which describes the spatial distribution pattern of the pixel values in the window area. The spatial structure features of the pixels in the window area are used as the spatial structure features of the central pixel [75]. This method describes the spatial structure of pixel neighborhoods. It can make up for the lack of spectral information of the central pixel by using the information of neighboring pixels, but it is important and uncertain for the reasonable selection of window size [76].

Among the existing methods, two kinds of neighborhood structure patterns are common. One is the interactive mode between the central pixel and its neighbor pixels, which is a “one-to-multiple” relationship. This relationship is represented using methods such as random fields, local spatial autocorrelation statistics and data fields [77,78]. The other is the spatial structure relationship of multiple pixels in the neighborhood window. The method equates the center pixel with its neighbor pixel, and is a “multiple-to-multiple” relationship, which is represented using methods such as the gray level co-occurrence matrix, global spatial autocorrelation statistic and the spatial semi-variogram function [79,80].

#### 4.3.2. Object-Oriented Method

The basic unit of object-oriented processing is homogeneous objects (image blocks, homogeneous areas or patches) with certain semantic information in images [81]. The method needs to segment the image to obtain the objects to further describe the spatial structure of the objects in the images [82]. The advantage of this method is that it has more abundant spatial relationships for the objects themselves and is convenient for extracting spatial features [83,84]. The deficiency of this method lies in its serious dependence on the quality of image segmentation. In fact, inaccurate image segmentation results in error accumulation when understanding spatial structure semantics [85].

#### 4.3.3. Rule-Partition-Based Method

The rule-partition-based method is similar to grid division. Firstly, the image is divided into regular (generally square) image blocks. Then, each image block is used as the processing unit to describe the spatial structure features of each image block [86]. This method is especially suitable for the detection of the spatial structure semantics of complex objects such as residential areas and aircraft. It does not focus on the detailed structure of objects in the image block but only on the statistical properties of the overall structure [87,88]. The deficiency of this method lies in how to determine the suitable partition of image blocks, especially when it cannot locate the object boundary accurately [89].

#### 4.3.4. Global Organization Method Based on Local Structure

In this method, firstly, the local structural features, such as feature points, feature lines and feature surfaces, are obtained. Then, according to the spatial structure of the objects, the global structure model of the objects is constructed by using certain organization rules and mathematical models [90]. The process is mainly based on the geometric structure of the object itself, spatial relationship information and prior knowledge of the object structure [91]. For instance, when extracting building targets in HSR remote sensing images, we can make full use of the feature that the building roof is a rectangular structure. Firstly, local structure features such as corners, lines and ridges are extracted. Then, the method of perceptual organization is used to organize it into a complete roof contour of the building [92,93]. This method accords with the cognition rule of people to things, but it has a higher request for the construction of mathematical models and the realization of calculation methods [94].

## 5. Semantic Understanding of Concept Layer

The concept layer belongs to high-level abstract semantics. The concept layer semantics of the geographic scene is the comprehensive judgment and representation of concepts such as function and pattern. The main application of the remote sensing image processing method is scene classification. In general, high-level semantic information can be acquired based on low-level information analysis, and low-level information can be transferred to higher-level by modeling. Through layer-by-layer refinement, the final representation of the concept layer semantics is closer to the abstract thinking of human beings, and then the geographic scene semantics in the HSR remote sensing images have more practical significance. Therefore, the concept layer semantics of geographic scenes are derived from the visual layer semantics or the object layer semantics.

### 5.1. Visual Features Based Method

The concept layer semantics of the geographic scene can be directly described by low-level visual feature attributes. The scene classification algorithm based on visual features extracts the low-level visual features (such as color, shape and texture), then describes the features and designs the classifier to infer the semantic information of the geographic scene. According to the different sources of low-level feature extraction, scene classification based on low-level features includes two categories: global-feature-based methods and local-feature-based methods. The extraction methods of global features and local features in visual features are detailed in Section 3 (Table 2). Common classifiers used for visual features include maximum likelihood [95], minimum distance [96] and K-means clustering [97].

**Table 2.** Comparison of main methods in visual features.

Name	Type	Output	Advantage	Disadvantage	Applicable
GIST	Global	Spectral information	Low computational complexity and easy to use	Poor performance in complex scenes with dense targets	Simple natural scenes
SIFT	Local	Neighborhood histogram	Suitable for translation, rotation, scale transformation	Poor performance in complex scenes with overall layout	Natural scenes
HOG		Vector	Representation of contours and edges	Poor performance in scenes with unstable shape structure	Scenes with global structural stability
CENTRIST		Census transformed value	Highlight local characteristics and reflect position information	Poor performance in complex and volatile scenes	Scenes with clear layout and sparse target distribution

A single low-level visual feature is not suitable for the complicated task of geographic scene classification, and more methods of multi-feature fusion are applied. Feature fusion combines color, texture and other features into high-dimensional feature descriptors, and then uses a neural network to achieve feature dimension reduction [98]. In addition, on the basis of local features, the image is divided into local blocks, and the low-level visual features of each block are taken to establish the multi-feature fusion descriptors [99,100]. Nevertheless, the method based on local or global visual features and their fusion of visual features is not effective. The core problem is that the concept layer semantics need to infer from the low-level features to obtain the high-level semantic representation, while the visual-features-based method just lacks this semantic representation.

### 5.2. Object Semantics Based Method

In order to fully describe the complex characteristics of the geographic scene, the extraction method of concept layer semantics based on object semantics is widely used in geographic scene understanding of HSR remote sensing images. By extracting the local features in the geographic scene, the local features are mapped to the visual dictionary or parameter space to obtain more distinguishable object layer features. Then, these features



are input into the classifier to obtain the comprehensive description features of the whole geographic scene.

### 5.2.1. Target-Recognition-Based Method

Geographic scenes involve the interaction of many objects in complex semantic patterns. According to the experience of human visual perception, images containing similar objects may represent the same geographic scene. When defining the category of the geographic scene, different objects have different importances in the scene. This prior knowledge provides ideas for the classification of geographic scenes.

The method based on object recognition will identify the semantics of each object in the geographic scene and train the classifier for concept semantic understanding based on the semantic information of each object. Typical approaches include Object Bank [101], Latent Pyramidal Regions [102], Bag of Parts [103] and Latent Semantic Analysis [104] (Table 3). These approaches assume that a scene consists of a series of targets, and that by identifying and recognizing those targets with significant discrimination, the category of the scene can be inferred from the semantics of those targets [105]. In these approaches, the problem of semantic understanding of the concept layer is first transformed into the problem of target recognition, and then the geographic scene is represented by image blocks containing multiple targets. However, the errors caused by target recognition will further result in “error propagation”, which will affect the semantic understanding of the geographic scene.

**Table 3.** Comparison of main methods in target recognition.

Name	Advantage	Disadvantage	Applicable
Object Bank	Identifiable targets and natural scenes	High computational complexity and high feature dimension	Natural scenes with landmark targets
Latent Pyramidal Regions	Good performance for regions with specific structures	Focus on the shape structure of the scene, lack of deep semantic understanding	Scenes with complex background and crowded targets
Bag of Parts	Good performance for areas with boundaries or corners		
Latent Semantic Analysis	The synonym is characterized by dimensionality reduction, and the redundant data are used	Polysemous words have low discrimination and high computational complexity	Scenes with heterogeneous information and clear boundaries

### 5.2.2. Local Semantics Based Method

To avoid the process of object detection and recognition, the HSR remote sensing image can be divided according to rules and the local image descriptors of each sub-block can be extracted. The correspondence between local descriptors and local semantic concepts is established, and the scene classification is completed by using the probability distribution of local semantic concepts. There are two main algorithms based on local semantic concepts: the probabilistic topic-model-based method and the bag-of-visual-words-model-based method. Because the feature of spatial structure expresses the relationship between objects, it does not exist independently. Therefore, this feature is often used in conjunction with the bag of visual words model or the probabilistic topic model to enhance semantics.

#### (1) Bag of visual words model

The visual codebook is defined in advance, and the image content is described by the probability distribution of the appearance of the visual codewords. Then, the geographic scenes are classified according to the probability distribution. In the process of constructing the bag of visual words model, feature extraction, visual dictionary learning, feature mapping and whether to add spatial context information all have an impact on the classification results [106].

In the aspect of feature extraction, we consider the construction of multi-feature scenes in low-dimensional space under different perspectives and use feature complementarity to carry out feature fusion to solve the problem of dimension reduction from a multi-

perspective [107]. Existing visual dictionary learning includes generation (unsupervised) and discriminant (supervised) methods [108,109]. After visual dictionary learning, the image local descriptor is mapped to the visual dictionary. The modification of the mapping method can improve the representation of local semantics [110]. In addition, feature description can be incorporated into feature space partitioning to capture the high-order structure inherent in the scene [111]. This makes the local semantics have both local gradient information, local structure information [112] and global spatial information [113–115].

(2) Probabilistic topic model

The scene semantic content is first modeled by probability distribution based on the codewords. Then, the latent semantic topics in the images are learned by using the probability distribution model. In addition, the geographic scenes are classified according to the probability distribution of latent semantic topics.

Semantic topic modeling includes the generative probabilistic model and the discriminative probabilistic model. The generative probabilistic model of the geographic scene is constructed according to the joint probability distribution of the scene category in the feature space, using pLSA [116], LDA [117] and improved LDA (ts-LDA, css-LDA) to mine the latent semantic information of visual words [118]. Because various scenes contain different space-level structures, spatial information can undergo weighted fusion based on local semantic content. The discriminative probabilistic model is based on the conditional probability distribution of the category of the geographic scene in feature space, and its core task is to design kernel function. Wu demonstrates that a support vector machine based on a histogram intersection kernel (HIK) is more efficient than a radial basis function kernel for histogram-based data [119].

The generative probabilistic model and the discriminative probabilistic model have their respective advantages and complementary characteristics. The contradiction between computational complexity and model complexity is the biggest problem in the generative probabilistic model, but it is not a problem in the discriminative probabilistic model. The discriminative probabilistic model does not consider the connection between geographic scenes when modeling different categories of the scene, which belongs to independent modeling. In [120], these two probabilistic models are combined to complete the task of scene classification, and the classification effect is better than the single probabilistic model.

5.3. Feature-Learning-Based Method

Both the method based on visual features and object semantics rely mainly on artificial design in feature extraction, which is not only subjective, and it is not enough for more complex HSR remote sensing images. In recent years, feature learning, especially deep learning, has been introduced into the field of remote sensing for semantic understanding of geographic scenes due to its excellent performance in image classification [121]. The general flow of geographic scene classification based on feature learning is shown in Figure 5.

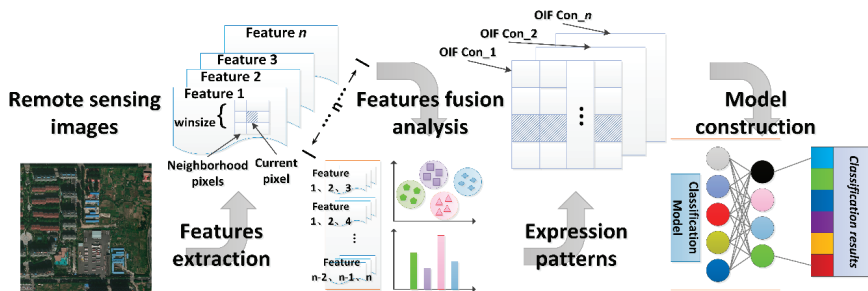
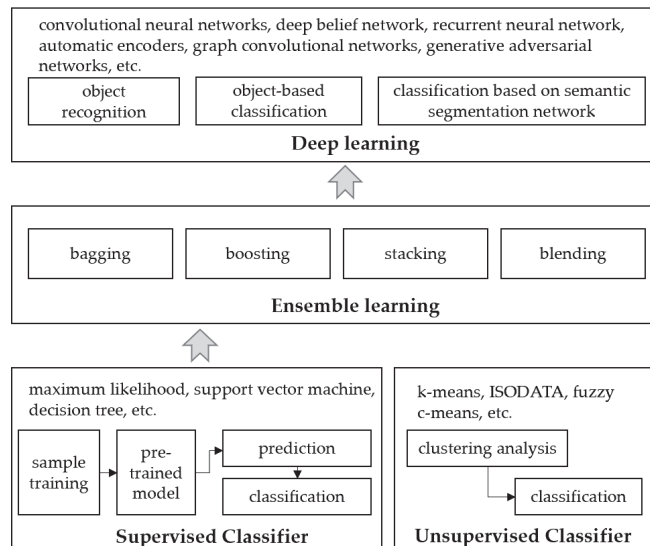


Figure 5. Geographic scene classification diagram.

Semantic understanding of the concept layer based on feature learning refers to the process of learning a potential scene classification feature through a series of mapping and transformation by using HSR remote sensing images as input of the model in machine learning tasks. Machine learning models can autonomously express and extract features from image data, abandoning the previous pattern of extracting features based on pre-designed rules [122,123]. Therefore, in the face of a complex surface environment, better classification results of geographic scenes can be obtained. At present, the commonly used machine learning models include sparse coding [124], neural network [125], support vector machine [126] and deep learning [127] (Figure 6). As a new intelligent method of pattern recognition in recent years, a deep learning network composed of multilaminar nonlinear mapping layers has become an especially important development direction in the field of remote sensing image processing [128]. Deep Learning is a deep structure neural network, which can extract the features of remote sensing images better than shallow structure models such as artificial neural networks and support vector machine models. Moreover, deep learning models can learn more abstract and distinguishable semantic features autonomously. The deep learning approach converts the semantic understanding of the concept layer into an end-to-end problem. On the one hand, the pre-trained deep learning network structure can be directly used to learn the global features in the visual layer of images to understand the semantics of the concept layer [129]. On the other hand, the deep learning network can also be used as a local feature extraction operator to jointly complete the semantic understanding of the concept layer with the help of feature code technology. Common deep learning models include convolutional neural networks (CNN) [130–132], deep belief network (DBN) [133], recurrent neural network (RNN) [134], automatic encoders [135], graph convolutional networks (GCN) [136], generative adversarial networks (GANs) [137,138] and so on. The deep learning method can be divided into three categories according to the supervision mode: (1) full supervision, (2) semi-supervised and (3) weak supervision.



**Figure 6.** Development of feature learning methods.

### 5.3.1. The Method Based on Fully Supervised Deep Learning

Nowadays, most geographic scene classifications of HSR remote sensing images based on deep learning can be classified as full supervision. The integration of multiple learning models is one of the ways to improve the learning effect. Zhu et al. [139] proposed an adaptive deep sparse semantic modeling (ADSSM), which combines the topic model with

CNN and effectively integrates sparse topic features and deep features at the semantic level. Cheng et al. [140] proposed a new loss function to train fused deep neural networks by combining deep learning with metric learning. Zhang et al. [141] combined CNN and CapsNet for scene classification. This approach combines the advantages of both networks while leveraging the powerful feature extraction capabilities of CNN and the excellent feature fusion and classification capabilities of CapsNet. He et al. [142] proposed a new skip-connected covariance network (SCCov) for remote sensing image scene classification. Sumbel et al. [143] presented the BigEarthNet, which is a new large-scale, multi-label Sentinel-2 benchmark archive. The experimental results obtained in the framework of scene classification problems show that a shallow CNN architecture trained on the BigEarthNet provides much higher accuracy compared to a state-of-the-art CNN model pre-trained on the ImageNet. Thus, the BigEarthNet opens up promising directions to advance operational remote sensing applications and research in massive Sentinel-2 image archives.

### 5.3.2. The Method Based on Semi-Supervised Deep Learning

Semi-supervised learning can make use of a large number of unlabeled samples, reducing the need for labeled samples, which, to some extent, solves the problem of insufficient labeled samples in the field of deep learning [144]. Han et al. [145] proposed a generic framework based on semi-supervised deep features from the perspective of expanding the scale of labeled samples. In this framework, multiple support vector machine (SVM) models are applied to the label recognition of easily confused category samples, which improves the label precision and the number of labeled samples, thus improving the generalization ability and classification precision of the network.

It is also an effective semi-supervised deep learning to construct a feature extraction model based on unsupervised learning in the feature learning stage, then train the classifier with labeled samples. Soto et al. [146] used a combination of labeled and unlabeled samples to train generative adversarial networks (GAN) and then used the trained classifiers for scene classification. At this point, the classifier has a large number of unlabeled samples of information, which is helpful to improve the final classification effect. Fan et al. [147] used the representative salient regions extracted from the image as unlabeled samples to train the feature extractor. Then, the extractor is used to extract the features of the samples to be classified. Finally, SVM is used to classify the extracted features.

### 5.3.3. The Method Based on Weak Supervised Deep Learning

In HSR remote sensing image scene classification tasks, weak supervision usually uses labeled samples similar to target samples to train scene classification models. This method divides the dataset into the source domain and target domain. The former is different from the latter but similar. The latter can obtain labels through various transfer learning and further be used for training scene classification models. Othman et al. [148] took the features extracted from labeled images as the source domain, and the features extracted from unlabeled images as the target domain. Then, apply them to network training and optimize the specified loss function to classify labeled and unlabeled data. Gong et al. [149] further improved deep structural metric learning (DSML) by proposing Diversity-Promoting-DSML (D-DSML), which reduces the parameter redundancy produced by DSML and improves the feature representation ability.

Some existing deep learning classification tools include OverFeat [150], DeCAF [151], Caffe [152], AlexNet and so on (Figure 7). However, in these models, learning millions of network parameters also requires millions of training data as input. In order to reduce the over-fitting problem, a smaller network structure can be constructed. However, the generalization ability of the network model trained by this method is limited, such as gradient enhancement convolutional neural network [153] and multi-perspective convolutional neural network [154]. Therefore, the unsupervised feature-learning method directly uses the network model trained on the data set of images as the feature extractor to extract the deep features of the image directly, or after the feature transformation is input into the clas-



**Table 4.** Comparison of main methods in geographic scene classification.

Method		Accuracy (%)	Other Indicators
Visual features-based method	Gabor texture [161]	76.91	-
	Color-HLS [161]	81.19	-
	NN-STSIM [162]	86	-
	Quaternion orientation difference [163]	85.48 ± 1.02	-
	MS-CLBP [164]	90.6 ± 1.4	-
Object-semantics-based method	BoVW [161]	76.81	-
	BoVW + SCK [161]	77.71	-
	SPM [161]	75.29	-
	SPCK ++ [165]	77.38	-
	HMFF [166]	92.38 ± 0.62	-
	CCM-BoVW [167]	86.64 ± 0.81	-
	Wavelet BoVW [168]	87.38 ± 1.27	-
	UFL [169]	81.67 ± 1.23	-
	COPD [170]	91.33 ± 1.11	-
	FV [171]	93.8	-
	VLAT [171]	94.3	-
	SG-UFL [172]	82.72 ± 1.18	-
	PSR [173]	89.1	-
	UFL-SC [174]	90.26 ± 1.51	-
	SAL-PLSA [175]	87.62	-
SAL-LDA [175]	88.33	-	
Feature-learning-based method	CaffeNet finetune [176]	95.48	-
	GoogleNet finetune [176]	97.1	-
	Multiview DL [177]	93.48 ± 0.82	84.35 (Sensitivity), 91.72 (Specificity)
	GBRCN [178]	94.53	-
	ADPM [179]	94.86	-
	HCSAE [180]	97.14 ± 1.19	-
	MARTA GANs [181]	94.86 ± 0.80	-
	Fusion by addition [182]	97.42 ± 1.79	-
	salM <sup>3</sup> LBP-CLM [183]	95.75 ± 0.80	-
	TEX-Nets [184]	97.72	-
	CCP-Net [185]	97.52 ± 0.97	-
	CNN (LOFs+GCFs) [186]	99.00 ± 0.35	-
	ARCNet-VGG16 [187]	99.12 ± 0.40	-
	D-CNN with VGG16 [188]	98.93 ± 0.10	-
	SAL-TS-Net [189]	98.90 ± 0.95	-
	Two-stream deep fusion [190]	98.02 ± 1.03	-
	PMS [191]	98.81	8.32 × 10 <sup>6</sup> (Number of neurons)
	SSF-AlexNet [192]	92.43 ± 0.46	-
VGG16+MSCP+MRA [193]	98.40 ± 0.34	-	
MCNN [194]	96.66 ± 0.90	-	
Bidirectional adaptive feature fusion [195]	95.48	-	

Although great progress has been made in geographic scene classification using deep learning algorithms, compared with the shallow algorithm, the classification effect has been improved obviously. However, the application of deep learning still faces many problems, such as the following:

- (1) In terms of training data, the success of a deep neural network is that it can fit large-scale samples without sacrificing generalization ability. In the field of geographic

scene understanding, it is difficult to construct a large-scale, high-quality and complete HSR remote sensing image dataset for training. Firstly, from the perspective of time, a training sample can only represent the sampling of a time section. However, the interpretations of objects are dynamic in different periods. This time heterogeneity puts forward higher requirements for the quality, scale and completeness of sample annotation [196]. Secondly, from the perspective of space, due to the differences in climate and light conditions, the distribution of ground objects in different geographic scenes has natural heterogeneity [197]. This spatial heterogeneity leads to the imbalance of sample categories in the supervised learning process, whether within the training set or between the training set and the test set, which leads to “over-fitting” or “under-fitting” problems.

- (2) In terms of learning mechanisms, supervised learning mainly relies on semantic support provided by manual annotation as the only learning signal for model training. If human labeling is regarded as prior knowledge, the machine has been limited in knowledge in the process of labeling [198]. However, for the huge amount of image data, the intrinsic information should be much more abundant than the semantic information provided by sparse labels. Therefore, over-reliance on a manual annotation will cause the risk of “inductive bias” in the trained model. Moreover, the computational cost is high, especially for small samples. Most of the deep learning models are trained on the established network structure and are then fine-tuned to obtain better network parameters. This training pattern is not suitable for ever-expanding datasets.

Although deep learning has a strong learning ability, compared with real artificial intelligence, it still lacks the ability of abstract knowledge representation, reasoning causality and logical relationship. Therefore, there is a long distance to understand the geographic scene automatically through feature learning.

## 6. Open Problems and Challenges

- (1) Integrated system engineering for geographic scene understanding

The research of HSR remote sensing images is often only used the visual information and a little semantic information, such as target detection, image classification, image segmentation, scene classification and so on. These researchers can often only detect a certain target contained in the image, or obtain the category labels of each pixel or the whole image, but they do not make full use of the features of the image. Thus, it is difficult to mine the attributes, characteristics and relationships among the objects in the image in detail. In this way, images are not fully understood at the semantic level and HSR remote sensing data are not fully utilized. The organic integration of single subtask or feature information of HSR remote sensing image processing can enhance the performance of understanding, and it is more suitable for people’s understanding mode of the geographic scene. The multi-class feature information and multi-subtasks are not completely independent, and the mutual influence and restriction factors should be considered comprehensively (Figure 8). Therefore, the construction of system engineering for geographic scene understanding can follow the following Formula (1):

$$Y = \{(feature_1 \oplus feature_2 \oplus \dots \oplus feature_n) \otimes (task_1 \oplus task_2 \oplus \dots \oplus task_n)\} \quad (1)$$

In the formula,  $Y$  is the system engineering for geographic scene understanding,  $\otimes$  and  $\oplus$  represent the different combinations of features and tasks.

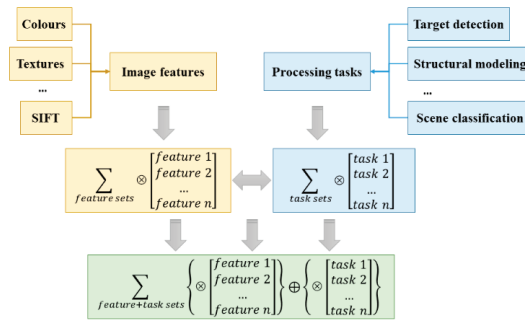


**Figure 8.** System engineering framework for geographic scene understanding based on HSR remote sensing image.

(2) Comprehensive semantic representation of the geographic scene in HSR remote sensing image

The purpose of geographic scene understanding based on HSR remote sensing image is to semantically explain the content at all layers in the geographic scene. It is necessary to construct a comprehensive semantic representation model of geographic scenes, and to standardize and integrate the various layers and types of semantic information obtained from the understanding of geographic scenes. The semantic parsing tree of a geographic scene can be constructed, and the tree structure of and/or a graph can be used to represent the semantic content of understanding. The semantic parsing tree of the geographic scene follows a unified semantic specification, which is generally divided into four levels “scene-object-part-pixel” (Figure 9). The “And” node represents the decomposition, such as “scene→object”, “object→part” and so on, which is followed the syntactic rules of “A→BCD”. Any geographic scene semantics can be represented by this parsing tree structure, and the semantic hierarchy of geographic scene is clearly divided, which has both semantic attributes and semantic relations between different levels.

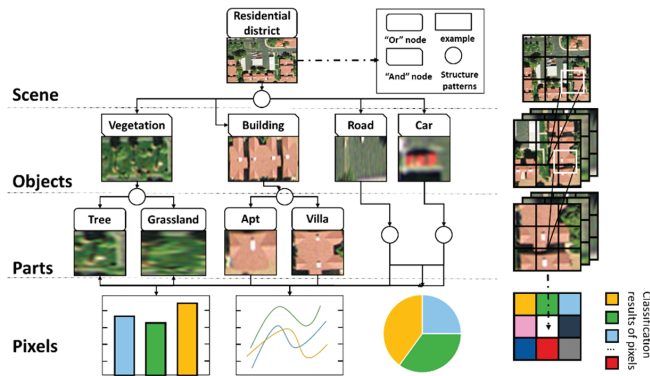


**Figure 9.** Hierarchical representation structure of the semantic of geographic scene.

(3) Adaptability for large-scale complex geographic scenes

With the massive growth of image data and the continuous subdivision of scene categories, the problem of geographic scene understanding is faced with unprecedented challenges both in image quantity and scene category. The understanding of real geographic scenes requires higher complexity and depth than scene classification, and the solution to this problem will have a profound impact on artificial intelligence technology. For the current semantic understanding approaches of geographic scenes, there are still the



following problems to be solved: (1) The semantic extraction ability of the visual layer is insufficient. Even considering multiple visual features, most of them are the simple superposition of different features. (2) The semantic modeling of object layer is redundant and lacks homogeneity in the description, which makes it difficult to take into account the computational efficiency and effect. (3) The semantic understanding of concept layer ignores spatial location information and globality. Whether it is visual-feature-based or object-semantic-based method, it is difficult to obtain an accurate global description of spatial location relationships and geographic scene characteristics at the same time. Thus, it is not conducive to an accurate understanding of the geographic scene.

(4) Fusion application of abundant multi-source data

In the big data era, the accessibility of various types of data has been broken through, creating conditions for the geographic scene understanding. On the one hand, the promotion of big data technology in the field of remote sensing has promoted the arrival of the era of remote sensing big data. Multi-source remote sensing data collaboration can integrate the advantages of various remote sensing observation methods and make up for the insufficient single sensor, which is one of the important research directions for the breakthrough of remote sensing image processing. On the other hand, the remote sensing image data record the natural environment of the surface, but the perception of changes in the social environment is scarce. The fusion of multi-source data is not only limited to HSR remote sensing data itself, but also needs to combine different types of data resources to make up for the deficiency of remote sensing monitoring. Social media data represented by Twitter, Facebook, Sina Weibo and Internet maps represented by GeoNames, GNIS, OpenStreetMap, etc., have become important sources of data for depicting the scenes of humanities and society. The fusion of HSR remote sensing images and multi-source data provides a new idea and method for geographic scene understanding.

## 7. Conclusions

Geographic scene understanding is one of the core tasks for middle and high-level cognition in remote sensing image processing tasks. Its complexity and comprehensiveness make it difficult to accurately understand the semantic information of geographic scenes. Based on the analysis of the basic concepts and core connotations of geographic scene understanding, this paper reviews the research status of geographic scene understanding from the tasks of different semantic layers in HSR remote sensing images. Geographic scene understanding decomposes the information of HSR remote sensing images into three semantic layers: based on the visual features of remote sensing images, the local objects, spatial structure and scene functions of the geographic scene are analyzed in a consistent cognitive system. This not only conforms to the logic and order of human cognition but also has significant interpretability of various semantic information. In terms of target detection, efficient and accurate feature representation and fusion of appropriate attention mechanisms are the core of extracting object category semantics. In terms of spatial structure description, pixel neighborhood window, object-oriented, rule partition and local structure are the main methods for extracting spatial structure semantics. In terms of scene classification, according to the semantic abstraction degree of extracted features, it mainly includes the visual feature classification method, object semantic classification method and feature learning classification method.

In future research, it is necessary to deeply study the intrinsic objective laws of various objects, textures, spaces and other information in geographic scene understanding, in order to reveal the relationship and influence mechanism between various features of images and different subtasks of image processing. The system engineering of geographic scene understanding is constructed from the global perspective, and the deep mechanism of human understanding of the geographic scene is explored. This is not only conducive to improving the adaptability of large-scale complex geographic scenes, but it also provides a universal cognitive structure for other HSR remote sensing images processing tasks such as image analysis and landscape investigation.

**Author Contributions:** Conceptualization, P.Y. and Y.H.; methodology, P.Y. and G.L.; validation, G.L.; formal analysis, P.Y.; investigation, P.Y. and G.L.; writing—original draft preparation, P.Y.; writing—review and editing, P.Y. and Y.H.; visualization, G.L.; supervision, G.L.; project administration, P.Y.; funding acquisition, P.Y. All authors have read and agreed to the published version of the manuscript.

**Funding:** This research was funded by the Open Foundation of Key Laboratory of Virtual Geographic Environment (Nanjing Normal University), the Ministry of Education (grant nos. 2021VGE01, and 2022VGE01), the Humanities and Social Sciences Foundation of Yangzhou University (grant no. xjj2021-08), the Open Foundation of Research Institute of Central Jiangsu Development, Yangzhou University (grant no. szfz202114) and the Open Foundation of Smart Health Big Data Analysis and Location Services Engineering Lab of Jiangsu Province (grant no. SHEL221 002).

**Institutional Review Board Statement:** Not applicable.

**Informed Consent Statement:** Not applicable.

**Data Availability Statement:** Not applicable.

**Acknowledgments:** The authors thank Xueying Zhang and Chunju Zhang for their critical reviews and constructive comments.

**Conflicts of Interest:** The authors declare no conflict of interest.

## References

- Li, D.; Zhang, L.; Xia, G. Automatic Analysis and Mining of Remote Sensing Big Data. *Acta Geod. Cartogr. Sin.* **2014**, *43*, 1211–1216.
- Dumitru, C.O.; Cui, S.; Schwarz, G.; Datcu, M. Information content of very-high-resolution sar images: Semantics, geospatial context, and ontologies. *IEEE J. Sel. Top. Appl. Earth Obs. Remote Sens.* **2014**, *8*, 1635–1650. [[CrossRef](#)]
- Zhang, Y.; Zheng, X.; Liu, G.; Sun, X.; Wang, H.; Fu, K. Semi-Supervised Manifold Learning Based Multigraph Fusion for High-Resolution Remote Sensing Image Classification. *IEEE Geosci. Remote Sens.* **2014**, *11*, 464–468. [[CrossRef](#)]
- Liu, Q.; Hang, R.; Song, H.; Li, Z. Learning multiscale deep features for high-resolution satellite image scene classification. *IEEE Trans. Geosci. Remote Sens.* **2018**, *56*, 117–126. [[CrossRef](#)]
- Gong, Z.; Zhong, P.; Yu, Y.; Hu, W. Diversified deep structural metric learning for land use classification in remote sensing images. In Proceedings of the 2017 IEEE International Geoscience and Remote Sensing Symposium (IGARSS), Fort Worth, TX, USA, 23–28 July 2017.
- Zhu, Q.; Zhong, Y.; Zhang, L. Scene classification based on the semantic-feature fusion fully sparse topic model for high spatial resolution remote sensing imagery. *Int. Arch. Photogramm. Remote Sens. Spat. Inf. Sci.* **2016**, *XLI-B7*, 451–457. [[CrossRef](#)]
- Biederman, I. Human image understanding: Recent research and theory. *Comput. Vis. Graph. Image Process.* **1985**, *31*, 400–401. [[CrossRef](#)]
- Tuia, D.; Ratle, F.; Pacifici, F.; Kanevski, M.; Emery, W.J. Active learning methods for remote sensing image classification. *IEEE Trans. Geosci. Remote Sens.* **2009**, *47*, 2218–2232. [[CrossRef](#)]
- Eakins, J. Automatic image content retrieval—Are we getting anywhere? In Proceedings of the Third International Conference on Electronic Library and Visual Information Research (ELVIRA3), Milton Keynes, UK, 10–12 May 1996.
- Lv, G.; Chen, M.; Yuan, L.; Zhou, L.; Wen, Y.; Wu, M.; Hu, B.; Yu, Z.; Yue, S.; Sheng, Y. Geographic scenario: A possible foundation for further development of virtual geographic environments. *Int. J. Digit. Earth* **2018**, *11*, 356–368.
- Zhong, Y.; Fei, F.; Zhang, L. Large patch convolutional neural networks for the scene classification of high spatial resolution imagery. *J. Appl. Remote Sens.* **2016**, *10*, 025006. [[CrossRef](#)]
- Lin, B.; Liu, Q.; Li, C.; Ye, Z.; Hui, M.; Jia, X. Using Bag of Visual Words and Spatial Pyramid Matching for Object Classification Along with Applications for RIS. *IEEE Trans. Geosci. Remote Sens.* **2022**, *60*, 1–14.
- Vyas, K.; Vora, Y.; Vastani, R. Bag-of-visual-words and spatial extensions for land-use classification. *Procedia Comput. Sci.* **2016**, *89*, 457–464. [[CrossRef](#)]
- Kasper, A.; Jäkel, R.; Dillmann, R. Using spatial relations of objects in real world scenes for scene structuring and scene understanding. In Proceedings of the 2011 15th International Conference on Advanced Robotics (ICAR), Tallinn, Estonia, 20–23 June 2011.
- Zhang, X.; Du, S. A Linear Dirichlet Mixture Model for decomposing scenes: Application to analyzing urban functional zonings. *Remote Sens. Environ.* **2015**, *169*, 37–49. [[CrossRef](#)]
- Gu, Y.; Wang, Y.; Li, Y. A Survey on Deep Learning-Driven Remote Sensing Image Scene Understanding: Scene Classification, Scene Retrieval and Scene-Guided Object Detection. *Appl. Sci.* **2019**, *9*, 2110. [[CrossRef](#)]
- Zhong, Y.; Wu, S.; Zhao, B. Scene Semantic Understanding Based on the Spatial Context Relations of Multiple Objects. *Remote Sens.* **2017**, *9*, 1030. [[CrossRef](#)]
- Qin, K.; Chen, Y.; Gan, S.; Feng, X.; Ren, W. Review on methods of spatial structural feature modeling of high resolution remote sensing images. *J. Image Graph.* **2013**, *18*, 1055–1064.

19. Hu, J. Multi-Level Feature Representation for Scene Classification with High Spatial Resolution Remote Sensing Images. Ph.D. Thesis, Wuhan University, Wuhan, China, 2019.
20. Long, Y.; Xia, G.; Li, S.; Yang, W.; Yang, M.; Zhu, X.; Zhang, L.; Li, D. On Creating Benchmark Dataset for Aerial Image Interpretation: Reviews, Guidances, and Million-AID. *IEEE J-STARS*. **2021**, *14*, 4205–4230. [[CrossRef](#)]
21. Deng, J.; Dong, W.; Socher, R.; Li, L.; Li, K.; Li, F. ImageNet: A large-scale hierarchical image database. In Proceedings of the 2009 IEEE Conference on Computer Vision and Pattern Recognition, Miami, FL, USA, 20–25 June 2009; pp. 248–255. [[CrossRef](#)]
22. Russakovsky, O.; Deng, J.; Su, H.; Krause, J.; Satheesh, S.; Ma, S.; Huang, Z.; Karpathy, A.; Khosla, A.; Bernstein, M.; et al. ImageNet Large Scale Visual Recognition Challenge. *Int. J. Comput. Vis.* **2015**, *115*, 211–252. [[CrossRef](#)]
23. Shahriari, M.; Bergevin, R. Land-use scene classification: A comparative study on bag of visual word framework. *Multimed. Tools Appl.* **2017**, *76*, 23059–23075. [[CrossRef](#)]
24. Xia, G.; Yang, W.; Delon, J.; Gousseau, Y.; Sun, H.; Maitre, H. Structural high-resolution satellite image indexing. In Proceedings of the ISPRS TC VII Symposium—100 Years ISPRS, Vienna, Austria, 5–7 July 2010; pp. 298–303.
25. Nilakshi, D.; Bhogeswar, B. A novel mutual information-based feature selection approach forefficient transfer learning in aerial scene classification. *Int. J. Remote sens.* **2021**, 2321–2325. [[CrossRef](#)]
26. Zhao, L.; Ping, T.; Huo, L. Feature significance-based multibag-of-visual-words model for remote sensing image scene classification. *J. Appl. Remote Sens.* **2016**, *10*, 035004. [[CrossRef](#)]
27. Zhao, B.; Zhong, Y.; Xia, G.; Zhang, L. Dirichlet-Derived Multiple Topic Scene Classification Model for High Spatial Resolution Remote Sensing Imagery. *IEEE Trans. Geosci. Remote Sens.* **2016**, *54*, 2108–2123. [[CrossRef](#)]
28. Cheng, G.; Han, J.; Lu, X. Remote sensing image scene classification: Benchmark and state of the art. *Proc. IEEE* **2017**, *105*, 1865–1883. [[CrossRef](#)]
29. Zhou, W.; Newsam, S.; Li, C.; Shao, Z. PatternNet: A benchmark dataset for performance evaluation of remote sensing image retrieval. *ISPRS J. Photogramm. Remote Sens.* **2017**, *145*, 197–209. [[CrossRef](#)]
30. Xia, G.; Hu, J.; Hu, F.; Shi, B.; Bai, X.; Zhong, Y.; Zhang, L.; Lu, X. AID: A Benchmark data Set for performance evaluation of aerial scene classification. *IEEE Trans. Geosci. Remote Sens.* **2017**, *55*, 3965–3981. [[CrossRef](#)]
31. Helber, P.; Bischke, B.; Dengel, A.; Borth, D. EuroSAT: A novel dataset and deep learning benchmark for land use and land cover classification. *IEEE J. Sel. Top. Appl. Earth Obs. Remote Sens.* **2019**, *12*, 2217–2226. [[CrossRef](#)]
32. Swain, M.J.; Ballard, D.H. Color indexing. *Int. J. Comput. Vis.* **1991**, *7*, 11–32. [[CrossRef](#)]
33. Forssén, P.E. Maximally Stable Colour Regions for Recognition and Matching. In Proceedings of the 2007 IEEE Conference on Computer Vision and Pattern Recognition, Minneapolis, MN, USA, 17–22 June 2007.
34. Sande, K.; Gevers, T.; Snoek, C. Evaluating color descriptors for object and scene recognition. *IEEE Trans. Pattern Anal. Mach. Intell.* **2010**, *32*, 1582–1596. [[CrossRef](#)]
35. Tao, D.; Jin, L.; Zhao, Y.; Li, X. Rank Preserving Sparse Learning for Kinect Based Scene Classification. *IEEE Trans. Cybern.* **2013**, *43*, 1406–1417. [[CrossRef](#)]
36. Banerji, S.; Sinha, A.; Liu, C. New image descriptors based on color, texture, shape, and wavelets for object and scene image classification. *Neurocomputing* **2013**, *117*, 173–185. [[CrossRef](#)]
37. Iqbal, N.; Mumtaz, R.; Shafi, U.; Zaidi, S.M.H. Gray level co-occurrence matrix (GLCM) texture based crop classification using low altitude remote sensing platforms. *PeerJ Comput. Sci.* **2021**, *7*, e536. [[CrossRef](#)]
38. Lv, H.; Liu, Y.; Xue, X.; Ma, T. Methods and Experiments of Background Subtraction and Grayscale Stretch for Remote Sensing Images. *Chin. J. Liq. Cryst. Disp.* **2012**, *27*, 235.
39. Li, Y.; Zhang, J.; Zhou, Y.; Niu, J.; Wang, L.; Meng, N.; Zheng, J. ISAR Imaging of Nonuniformly Rotating Targets with Low SNR Based on Coherently Integrated Nonuniform Trilinear Autocorrelation Function. *IEEE Geosci. Remote Sens. Lett.* **2020**, *99*, 1074–1078. [[CrossRef](#)]
40. Ru, C.; Li, Z.; Tang, R. A Hyperspectral Imaging Approach for Classifying Geographical Origins of *Rhizoma Atractylodis Macrocephalae* Using the Fusion of Spectrum-Image in VNIR and SWIR Ranges (VNIR-SWIR-FuSI). *Sensors* **2019**, *19*, 2045. [[CrossRef](#)] [[PubMed](#)]
41. Huang, L.; Chen, C.; Li, W.; Du, Q. Remote Sensing Image Scene Classification Using Multi-Scale Completed Local Binary Patterns and Fisher Vectors. *Remote Sens.* **2016**, *8*, 483. [[CrossRef](#)]
42. Oliva, A.; Torralba, A. Modeling the shape of the scene: A holistic representation of the spatial envelope. *Int. J. Comput. Vis.* **2011**, *42*, 145–175. [[CrossRef](#)]
43. Lowe, D. Distinctive image features from scale-invariant keypoints. *Int. J. Comput. Vis.* **2004**, *60*, 91–110. [[CrossRef](#)]
44. Bay, H.; Tuytelaars, T.; Van Gool, L. SURF: Speeded Up Robust Features. In *Computer Vision—ECCV 2006; Lecture Notes in Computer Science; Proceedings of the 9th European Conference on Computer Vision (ECCV 2006), Graz, Austria, 7–13 May 2006*; Leonardis, A., Bischof, H., Pinz, A., Eds.; Springer: Berlin/Heidelberg, Germany, 2006; Volume 3951. [[CrossRef](#)]
45. Dalal, N.; Triggs, B. Histograms of oriented gradients for human detection. In Proceedings of the Computer Vision and Pattern Recognition, San Diego, CA, USA, 20–25 June 2005; pp. 886–893.
46. Wu, J.; Rehg, J. CENTRIST: A visual descriptor for scene categorization. *IEEE Trans. Pattern Anal. Mach. Intell.* **2011**, *33*, 1489–1501.
47. Zou, C.; Lei, Z.; Lv, S. Remote Sensing Image Dam Detection Based on Dual Threshold Network. In Proceedings of the 2020 Chinese Control and Decision Conference (CCDC), Hefei, China, 23 August 2020.

48. Horhan, M.; Eidenberger, H. An Efficient DCT template-based Object Detection Method using Phase Correlation. In Proceedings of the 2016 50th Asilomar Conference on Signals, Systems and Computers, Pacific Grove, CA, USA, 6–9 November 2017.
49. Wu, Z.; Wan, Q.; Liang, J.; Zhou, Z. Line Detection in Remote Sensing Images Using Hough Transform Based on Granular Computing. *Geomat. Inf. Sci. Wuhan Univ.* **2007**, *32*, 860–863.
50. Zhang, L.; Zhang, L.; Tao, D.; Xin, H.; Bo, D. Hyperspectral Remote Sensing Image Subpixel Target Detection Based on Supervised Metric Learning. *IEEE Trans. Geosci. Remote Sens.* **2014**, *52*, 4955–4965. [[CrossRef](#)]
51. Hermosilla, T.; Ruiz, L.A.; Recio, J.A.; Estornell, J. Evaluation of Automatic Building Detection Approaches Combining High Resolution Images and LiDAR Data. *Remote Sens.* **2011**, *3*, 1188–1210. [[CrossRef](#)]
52. Li, X.; Xu, H.; An, S. Monitoring and assessment of intensive utilization of port area based on high spatial resolution remote sensing image with case study of five typical ports in the Bohai Sea. *J. Appl. Oceanogr.* **2019**, *38*, 126–134.
53. Ai, S.; Yan, J.; Li, D.; Xu, J.; Shen, J. An Algorithm for Detecting the Airport Runway in Remote Sensing Image. *Electron. Opt. Control* **2017**, *24*, 43–46.
54. Li, X.; Zhang, Z.; Lv, S.; Pan, M.; Yu, H. Road Extraction from High Spatial Resolution Remote Sensing Image Based on Multi-Task Key Point Constraints. *IEEE Access* **2021**, *9*, 95896–95910. [[CrossRef](#)]
55. Wei, S.; Chen, H.; Zhu, X.; Zhang, H. Ship Detection in Remote Sensing Image based on Faster R-CNN with Dilated Convolution. In Proceedings of the 2020 39th Chinese Control Conference (CCC), Shenyang, China, 27–29 July 2020.
56. Wang, X.; Luo, G.; Ke, Q.; Chen, A.; Tian, L. A Fast Target Locating Method for Remote Sensing Images Based on Line Features. *Int. J. Signal Process. Image Process. Pattern Recogn.* **2017**, *10*, 61–72. [[CrossRef](#)]
57. Zhang, Q.; Lin, Q.; Ming, G.; Li, J. Remote Sensing Image Analysis on Circulation Induced by the Breakwaters in the Huanghua Port. In Proceedings of the International Conference on Estuaries and Coasts, Hangzhou, China, 9–11 November 2003.
58. Song, J.; Hu, W. Experimental Results of Maritime Target Detection Based on SVM Classifier. In Proceedings of the 2020 IEEE 3rd International Conference on Information Communication and Signal Processing (ICICSP), Shanghai, China, 12–15 September 2020.
59. Huang, S.; Huang, W.; Zhang, T. A New SAR Image Segmentation Algorithm for the Detection of Target and Shadow Regions. *Sci. Rep.* **2016**, *6*, 38596. [[CrossRef](#)] [[PubMed](#)]
60. Chaudhuri, D.; Agrawal, A. Split-and-merge Procedure for Image Segmentation using Bimodality Detection Approach. *Def. Sci. J.* **2010**, *60*, 290–301. [[CrossRef](#)]
61. Sun, Y.J.; Lei, W.H.; Ren, X.D. Remote sensing image ship target detection method based on visual attention model. In *Proceedings of the Lidar Imaging Detection and Target Recognition 2017*; Lv, D., Lv, Y., Bao, W., Eds.; SPIE-Int. Soc. Optical Engineering: Bellingham, WA, USA, 2017; Volume 10605.
62. Wu, J.; Rehg, J.M. Beyond the Euclidean distance: Creating effective visual codebooks using the Histogram Intersection Kernel. In Proceedings of the 2009 IEEE 12th International Conference on Computer Vision (ICCV), Kyoto, Japan, 29 September–2 October 2009.
63. Perronnin, F. Universal and Adapted Vocabularies for Generic Visual Categorization. *IEEE Trans. Pattern Anal. Mach. Intell.* **2008**, *30*, 1243–1256. [[CrossRef](#)]
64. Su, Y.; Allan, M.; Jurie, F. Improving Image Classification Using Semantic Attributes. *Int. J. Comput. Vis.* **2012**, *100*, 59–77. [[CrossRef](#)]
65. Yang, J.; Kai, Y.; Gong, Y.; Huang, T. Linear spatial pyramid matching using sparse coding for image classification. In Proceedings of the 2009 IEEE Computer Society Conference on Computer Vision and Pattern Recognition (CVPR 2009), Miami, FL, USA, 20–25 June 2009.
66. Lee, H.; Battle, A.; Raina, R.; Ng, A.Y. Efficient sparse coding algorithms. In *Advances in Neural Information Processing Systems 19, Proceedings of the Twentieth Annual Conference on Neural Information Processing Systems, Vancouver, BC, Canada, 4–7 December 2006*; MIT Press: Cambridge, MA, USA, 2006.
67. Yu, K.; Zhang, T. Improved Local Coordinate Coding using Local Tangents. In Proceedings of the International Conference on International Conference on Machine Learning (ICML-10), Haifa, Israel, 21–24 June 2010.
68. Wang, J.; Yang, J.; Kai, Y.; Lv, F.; Huang, T.; Gong, Y. Locality-constrained Linear Coding for image classification. In Proceedings of the 23rd IEEE Conference on Computer Vision and Pattern Recognition, CVPR 2010, San Francisco, CA, USA, 13–18 June 2010.
69. Pham, T.T.; Maisonnasse, L.; Mulhem, P.; Gaussier, E. Visual Language Model for Scene Recognition. In Proceedings of the Singaporean-French Ipal Symposium 2009, Singapore, 18–20 February 2009.
70. Hofmann, T. Unsupervised Learning by Probabilistic Latent Semantic Analysis. *Mach. Learn.* **2001**, *42*, 177–196. [[CrossRef](#)]
71. Blei, D.M.; Ng, A.Y.; Jordan, M.I. Latent Dirichlet Allocation. *J. Mach. Learn. Res.* **2003**, *3*, 993–1022.
72. Wu, L.; Hu, Y.; Li, M.; Yu, N.; Hua, X. Scale-Invariant Visual Language Modeling for Object Categorization. *IEEE Trans. Multimed.* **2009**, *11*, 286–294. [[CrossRef](#)]
73. Jing, H.; Wei, H. Latent Dirichlet Allocation Based Image Retrieval. In *Information Retrieval*; Wen, J., Nie, J., Ruan, T., Liu, Y., Qian, T., Eds.; CCIR 2017, Lecture Notes in Computer Science; Springer: Cham, Switzerland, 2017; Volume 10390. [[CrossRef](#)]
74. Kato, H.; Harada, T. Visual Language Modeling on CNN Image Representations. *arXiv* **2015**, arXiv:1511.02872.
75. Zhao, H.; Wang, Q.; Wang, Q.; Wu, W.; Yuan, N. SAR image despeckling based on adaptive neighborhood window and rotationally invariant block matching. In Proceedings of the 2014 IEEE International Conference on Signal Processing, Communications and Computing (ICSPCC), Guilin, China, 5–8 August 2014.
76. Aytikin, Ö.; Koc, M.; Ulusoy, İ. Local Primitive Pattern for the Classification of SAR Images. *IEEE Trans. Geosci. Remote Sens.* **2013**, *51*, 2431–2441. [[CrossRef](#)]

77. Hudak, A.T.; Strand, E.K.; Vierling, L.A.; Byrne, J.C.; Eitel, J.; Martinuzzi, S.; Falkowski, M. Quantifying aboveground forest carbon pools and fluxes from repeat LiDAR surveys. *Remote Sens. Environ.* **2012**, *123*, 25–40. [[CrossRef](#)]
78. Li, S.; Zhang, B.; Li, A.; Jia, X.; Gao, L.; Peng, M. Hyperspectral Imagery Clustering with Neighborhood Constraints. *IEEE Geosci. Remote Sens. Lett.* **2013**, *10*, 588–592. [[CrossRef](#)]
79. Rahman, M.H.; Islam, H.; Neema, N. Compactness of Neighborhood Spatial Structure: A Case Study of Selected Neighborhoods of DNCC and DSCC Area. In Proceedings of the International Conference on Sustainability in Natural and Built Environment (iCSNBE 2019), Dhaka, Bangladesh, 19–22 January 2019.
80. Guan, X.; Huang, C.; Yang, J.; Li, A. Remote Sensing Image Classification with a Graph-Based Pre-Trained Neighborhood Spatial Relationship. *Sensors* **2021**, *21*, 5602. [[CrossRef](#)]
81. Sha, Z.; Bian, F. Object-Oriented Spatial Knowledge Representation and Its Application. *J. Remote Sens.* **2004**, *19*, 165–171.
82. Wei, C.; Zheng, Z.; Zhou, Q.; Huang, J.; Yuan, Y. Application of a parallel spectral-spatial convolution neural network in object-oriented remote sensing land use classification. *Remote Sens. Lett.* **2018**, *9*, 334–342.
83. Wang, Y.; Bao, W.; Yang, C.; Zhang, Y. A study on the automatic classification method on the basis of high resolution remote sensing image. In Proceedings of the 6th International Digital Earth Conference, Beijing, China, 9–12 September 2009.
84. Liu, X. Object Oriented Information Classification of Remote Sensing Image Based on Segmentation and Merging. *Appl. Mech. Mater.* **2014**, *568–570*, 734–739. [[CrossRef](#)]
85. Tan, Y.; Huai, J.; Tang, Z. An Object-Oriented Remote Sensing Image Segmentation Approach Based on Edge Detection. *Spectrosc. Spect. Anal.* **2010**, *30*, 1624–1627.
86. Tong, X.; Jin, B.; Ying, W. A new effective Hexagonal Discrete Global Grid System: Hexagonal quad balanced structure. In Proceedings of the 8th International Conference on Geoinformatics, Beijing, China, 18–20 June 2010.
87. Khromykh, V.; Khromykh, O. Analysis of Spatial Structure and Dynamics of Tom Valley Landscapes based on GIS, Digital Elevation Model and Remote Sensing. *Procedia Soc. Behav. Sci.* **2014**, *120*, 811–815. [[CrossRef](#)]
88. Ding, Y.; Pan, S.; Chong, Y. Robust Spatial–Spectral Block-Diagonal Structure Representation with Fuzzy Class Probability for Hyperspectral Image Classification. *IEEE Trans. Geosci. Remote Sens.* **2020**, *58*, 1747–1762. [[CrossRef](#)]
89. Gao, Y.; Zhang, Y.; Alsulaiman, H. Spatial structure system of land use along urban rail transit based on GIS spatial clustering. *Eur. J. Remote Sens.* **2021**, *54*, 438–445. [[CrossRef](#)]
90. Wurm, M.; Taubenbck, H.; Dech, S. Quantification of urban structure on building block level utilizing multisensoral remote sensing data. In Proceedings of the Earth Resources and Environmental Remote Sensing/GIS Applications 2010, Toulouse, France, 25 October 2010.
91. Chen, J.; Chen, S.; Chen, X.; Yang, Y.; Xing, L.; Fan, X.; Rao, Y. LSV-ANet: Deep Learning on Local Structure Visualization for Feature Matching. *IEEE Trans. Geosci. Remote Sens.* **2022**, *60*, 1–18. [[CrossRef](#)]
92. Du, Z.; Li, X.; Lu, X. Local structure learning in high resolution remote sensing image retrieval. *Neurocomputing* **2016**, *207*, 813–822. [[CrossRef](#)]
93. Lei, S.; Shi, Z.; Zou, Z. Super-Resolution for Remote Sensing Images via Local-Global Combined Network. *IEEE Geosci. Remote Sens. Lett.* **2017**, *14*, 1243–1247. [[CrossRef](#)]
94. Chen, J.; Fan, X.; Chen, S.; Yang, Y.; Bai, H. Robust Feature Matching via Hierarchical Local Structure Visualization. *IEEE Geosci. Remote Sens. Lett.* **2022**, *19*, 1–5. [[CrossRef](#)]
95. Bruzzone, L.; Prieto, D.F. Unsupervised Retraining of a Maximum Likelihood Classifier for the Analysis of Multitemporal Remote Sensing Images. *IEEE Trans. Geosci. Remote Sens.* **2001**, *39*, 456–460. [[CrossRef](#)]
96. Zeh, A.; Bezzateev, S. A New Bound on the Minimum Distance of Cyclic Codes Using Small-Minimum-Distance Cyclic Codes. *Design. Code. Cryptogr.* **2014**, *71*, 229–246. [[CrossRef](#)]
97. Yuan, Y.; Meng, Q. Polyp classification based on Bag of Features and saliency in wireless capsule endoscopy. In Proceedings of the 2014 IEEE International Conference on Robotics and Automation (ICRA), Hong Kong, China, 31 May–7 June 2014.
98. Guo, Y.; Ji, J.; Shi, D.; Ye, Q.; Xie, H. Multi-view feature learning for VHR remote sensing image classification. *Multimed. Tools Appl.* **2021**, *80*, 23009–23021. [[CrossRef](#)]
99. Hu, J.; Li, M.; Xia, G.; Zhang, L. Mining the spatial distribution of visual words for scene classification. In Proceedings of the 2016 IEEE International Geoscience and Remote Sensing Symposium (IGARSS), Beijing, China, 10–15 July 2016.
100. Chaib, S.; Liu, H.; Gu, Y.; Yao, H. Deep Feature Fusion for VHR Remote Sensing Scene Classification. *IEEE Trans. Geosci. Remote Sens.* **2017**, *55*, 4775–4784. [[CrossRef](#)]
101. Li, L.; Su, H.; Xing, E.; Li, F. Object bank: A high-level image representation for scene classification & semantic feature sparsification. In Proceedings of the 23rd International Conference on Neural Information Processing Systems, Red Hook, NY, USA, 6–9 December 2010.
102. Sadeghi, F.; Tappen, M.F. Latent Pyramidal Regions for Recognizing Scenes. In *Computer Vision—ECCV 2012, Proceedings of the 12th European Conference on Computer Vision (ECCV 2012), Florence, Italy, 7–13 October 2012*; Fitzgibbon, A., Lazebnik, S., Perona, P., Sato, Y., Schmid, C., Eds.; Springer: Berlin/Heidelberg, Germany, 2012.
103. Juneja, M.; Vedaldi, A.; Jawahar, C.; Zisserman, A. Blocks that shout: Distinctive parts for scene classification. In Proceedings of the Computer Vision and Pattern Recognition, Portland, OR, USA, 23–28 June 2013.
104. Wang, J.; Sun, X.; Nahavandi, S.; Kouzani, A.; Wu, Y.; She, M. Multichannel biomedical time series clustering via hierarchical probabilistic latent semantic analysis. *Comput. Meth. Prog. Biol.* **2014**, *117*, 238–246. [[CrossRef](#)] [[PubMed](#)]

105. Gong, C.; Li, Z.; Yao, X.; Guo, L.; Wei, Z. Remote Sensing Image Scene Classification Using Bag of Convolutional Features. *IEEE Geosci. Remote Sens. Lett.* **2017**, *14*, 1735–1739.
106. Hu, J.; Xia, G.-S.; Hu, F.; Zhang, L. A Comparative Study of Sampling Analysis in the Scene Classification of Optical High-Spatial Resolution Remote Sensing Imagery. *Remote Sens.* **2015**, *7*, 14988–15013. [\[CrossRef\]](#)
107. Yu, J.; Tao, D.; Rui, Y.; Cheng, J. Pairwise constraints based multiview features fusion for scene classification. *Pattern Recogn.* **2013**, *46*, 483–496. [\[CrossRef\]](#)
108. Wang, X.; Wang, B.; Bai, X.; Liu, W.; Tu, Z. Max-margin multiple-instance dictionary learning. In Proceedings of the 30th International Conference on International Conference on Machine Learning, Atlanta, GA, USA, 16–21 June 2013.
109. Shen, L.; Wang, S.; Sun, G.; Jiang, S.; Huang, Q. Multi-level discriminative dictionary learning towards hierarchical visual categorization. In Proceedings of the 2013 IEEE Conference on Computer Vision and Pattern Recognition, Portland, OR, USA, 23–28 June 2013.
110. Oliveira, G.; Nascimento, E.; Vieira, A.; Campos, M. Sparse spatial coding: A novel approach for efficient and accurate object recognition. In Proceedings of the 2012 IEEE International Conference on Robotics and Automation, Saint Paul, MN, USA, 14–18 May 2012.
111. Zhu, Q.; Zhong, Y.; Zhao, B.; Xia, G.; Zhang, L. Bag-of-Visual-Words Scene Classifier with Local and Global Features for High Spatial Resolution Remote Sensing Imagery. *IEEE Geosci. Remote Sens. Lett.* **2017**, *13*, 747–751. [\[CrossRef\]](#)
112. Hu, F.; Xia, G.-S.; Hu, J.; Zhong, Y.; Xu, K. Fast Binary Coding for the Scene Classification of High-Resolution Remote Sensing Imagery. *Remote Sens.* **2016**, *8*, 555. [\[CrossRef\]](#)
113. Kwitt, R.; Vasconcelos, N.; Rasiwasia, N. Scene recognition on the semantic manifold. In Proceedings of the 12th European Conference on Computer Vision, Florence, Italy, 7–13 October 2012.
114. Wang, Z.; Feng, J.; Yan, S.; Xi, H. Linear distance coding for image classification. *IEEE Trans. Image Process.* **2013**, *22*, 537–548. [\[CrossRef\]](#)
115. Xie, L.; Wang, J.; Guo, B.; Zhang, B.; Tian, Q. Orientational pyramid matching for recognizing indoor scenes. In Proceedings of the 2014 IEEE Conference on Computer Vision and Pattern Recognition, Columbus, OH, USA, 23–28 June 2014.
116. Singh, A.; Parmanand; Saurabh. Survey on pLSA based scene classification techniques. In Proceedings of the 2014 5th International Conference—Confluence the Next Generation Information Technology Summit (Confluence), Noida, India, 25–26 September 2014.
117. Veeranjaneyulu, N.; Raghunath, A.; Devi, B.J.; Mandhala, V.N. Scene classification using support vector machines with LDA. *J. Theor. Appl. Inf. Technol.* **2014**, *63*, 741–747.
118. Bosch, A.; Zisserman, A.; Muñoz, X. Scene classification via PLSA. In Proceedings of the 9th European Conference on Computer Vision, Graz, Austria, 7–13 May 2006.
119. Wu, J. A fast dual method for HIK SVM learning. In Proceedings of the 11th European Conference on Computer Vision, Heraklion, Crete, Greece, 5–11 September 2010.
120. Bosch, A.; Zisserman, A.; Muñoz, X. Scene classification using a hybrid generative/discriminative approach. *IEEE Trans. Pattern Anal. Mach. Intell.* **2008**, *30*, 712–727. [\[CrossRef\]](#)
121. Gu, Y.; Liu, H.; Wang, T.; Li, S.; Gao, G. Deep feature extraction and motion representation for satellite video scene classification. *Sci. China Inf. Sci.* **2020**, *63*, 140307. [\[CrossRef\]](#)
122. Tuia, D.; Marcos, D.; Schindler, K.; Saux, B.L. Deep Learning-based Semantic Segmentation in Remote Sensing. In *Deep Learning for the Earth Sciences: A Comprehensive Approach to Remote Sensing, Climate Science, and Geosciences*; Camps-Valls, G., Tuia, D., Zhu, X., Reichstein, M., Eds.; John Wiley & Sons: Hoboken, NJ, USA, 2021; Volume 5, pp. 46–66. [\[CrossRef\]](#)
123. Lin, D. MARTA GANs: Deep Unsupervised Representation Learning for Remote Sensing Images. *arXiv* **2016**, arXiv:1612.08879.
124. Qi, K.; Zhang, X.; Wu, B.; Wu, H. Sparse coding-based correlation model for land-use scene classification in high-resolution remote-sensing images. *J. Appl. Remote Sens.* **2016**, *10*, 042005.
125. Xie, J.; He, N.; Fang, L.; Plaza, A. Scale-Free Convolutional Neural Network for Remote Sensing Scene Classification. *IEEE Trans. Geosci. Remote Sens.* **2019**, *57*, 6916–6928. [\[CrossRef\]](#)
126. Du, P.; Tan, K.; Xing, X. A novel binary tree support vector machine for hyperspectral remote sensing image classification. *Opt. Commun.* **2012**, *285*, 3054–3060. [\[CrossRef\]](#)
127. Zhao, Z.; Luo, Z.; Li, J.; Chen, C.; Piao, Y. When Self-Supervised Learning Meets Scene Classification: Remote Sensing Scene Classification Based on a Multitask Learning Framework. *Remote Sens.* **2020**, *12*, 3276. [\[CrossRef\]](#)
128. Ma, A.; Wan, Y.; Zhong, Y.; Wang, J.; Zhang, L. SceneNet: Remote sensing scene classification deep learning network using multi-objective neural evolution architecture search. *ISPRS J. Photogramm. Remote Sens.* **2021**, *172*, 171–188. [\[CrossRef\]](#)
129. Risojevi, V.; Stojni, V. The Role of Pre-Training in High-Resolution Remote Sensing Scene Classification. *arXiv* **2021**, arXiv:2111.03690.
130. Boualleg, Y.; Farah, M.; Farah, I.R. Remote Sensing Scene Classification Using Convolutional Features and Deep Forest Classifier. *IEEE Geosci. Remote Sens. Lett.* **2019**, *16*, 1944–1948. [\[CrossRef\]](#)
131. Li, E.; Samat, A.; Du, P.; Liu, W.; Hu, J. Improved Bilinear CNN Model for Remote Sensing Scene Classification. *IEEE Geosci. Remote Sens. Lett.* **2022**, *19*, 1–5. [\[CrossRef\]](#)
132. Xu, K.; Huang, H.; Deng, P.; Shi, G. Two-stream Feature Aggregation Deep Neural Network for Scene Classification of Remote Sensing Images. *Inform. Sci.* **2020**, *539*, 250–268. [\[CrossRef\]](#)

133. Zou, Q.; Ni, L.; Zhang, T.; Wang, Q. Deep Learning Based Feature Selection for Remote Sensing Scene Classification. *IEEE Geosci. Remote Sens. Lett.* **2015**, *12*, 1–5. [\[CrossRef\]](#)
134. Liang, L.; Wang, G. Efficient recurrent attention network for remote sensing scene classification. *IET Image Process.* **2021**, *15*, 1712–1721. [\[CrossRef\]](#)
135. Cheng, G.; Zhou, P.; Han, J.; Han, J.; Guo, L.; Han, J. Auto-encoder-based shared mid-level visual dictionary learning for scene classification using very high resolution remote sensing images. *IET Comput. Vis.* **2015**, *9*, 639–647. [\[CrossRef\]](#)
136. Liang, J.; Deng, Y.; Zeng, D. A Deep Neural Network Combined CNN and GCN for Remote Sensing Scene Classification. *IEEE J. Sel. Top. Appl. Earth Obs. Remote Sens.* **2020**, *13*, 4325–4338. [\[CrossRef\]](#)
137. Duan, Y.; Tao, X.; Xu, M.; Han, C.; Lu, J. GAN-NL: Unsupervised Representation Learning for Remote Sensing Image Classification. In Proceedings of the 2018 IEEE Global Conference on Signal and Information Processing (GlobalSIP), Anaheim, CA, USA, 26–29 November 2018.
138. Yu, Y.; Li, X.; Liu, F. Attention GANs: Unsupervised Deep Feature Learning for Aerial Scene Classification. *IEEE Trans. Geosci. Remote Sens.* **2019**, *58*, 519–531. [\[CrossRef\]](#)
139. Zhu, Q.; Zhong, Y.; Zhang, L.; Li, D. Adaptive deep sparse semantic modeling framework for high spatial resolution image scene classification. *IEEE Trans. Geosci. Remote Sens.* **2018**, *56*, 6180–6195. [\[CrossRef\]](#)
140. Cheng, G.; Yang, C.; Yao, X.; Guo, L.; Han, J. When deep learning meets metric learning: Remote sensing image scene classification via learning discriminative CNNs. *IEEE Trans. Geosci. Remote Sens.* **2018**, *56*, 2811–2821. [\[CrossRef\]](#)
141. Zhang, W.; Tang, P.; Zhao, L. Remote Sensing Image Scene Classification Using CNN-CapsNet. *Remote Sens.* **2019**, *11*, 494. [\[CrossRef\]](#)
142. He, N.; Fang, L.; Li, S.; Plaza, J.; Plaza, A. Skip-connected covariance network for remote sensing scene classification. *IEEE T. Neur. Net. Lear.* **2020**, *31*, 1461–1474. [\[CrossRef\]](#)
143. Sumbul, G.; Charfuelan, M.; Demir, B.; Markl, V. BigEarthNet: A Large-Scale Benchmark Archive for Remote Sensing Image Understanding. *arXiv* **2019**, arXiv:1902.06148.
144. Qian, X.; Li, E.; Zhang, J.; Zhao, S.; Wu, Q.; Zhang, H.; Wang, W.; Wu, Y. Hardness recognition of robotic forearm based on semi-supervised generative adversarial networks. *Front. Neurobot.* **2019**, *13*, 73. [\[CrossRef\]](#) [\[PubMed\]](#)
145. Han, W.; Feng, R.; Wang, L.; Cheng, Y. A semi-supervised generative framework with deep learning features for high-resolution remote sensing image scene classification. *ISPRS J. Photogramm. Remote Sens.* **2018**, *145*, 23–43. [\[CrossRef\]](#)
146. Soto, P.J.; Bermudez, J.D.; Happ, P.N.; Feitosa, R. A comparative analysis of unsupervised and semi-supervised representation learning for remote sensing image categorization. *ISPRS Ann. Photogramm. Remote Sens. Spat. Inf. Sci.* **2019**, *IV-2/W7*, 167–173. [\[CrossRef\]](#)
147. Fan, J.; Tan, H.; Lu, S. Multipath sparse coding for scene classification in very high resolution satellite imagery. In Proceedings of the SPIE 9643, Image and Signal Processing for Remote Sensing XXI, Toulouse, France, 15 October 2015.
148. Othman, E.; Bazi, Y.; Melgani, F.; Alhichri, H.; Alajlan, N.; Zuair, M. Domain adaptation network for cross-scene classification. *IEEE Trans. Geosci. Remote Sens.* **2017**, *55*, 4441–4456. [\[CrossRef\]](#)
149. Gong, Z.; Zhong, P.; Yu, Y.; Hu, W. Diversity-promoting deep structural metric learning for remote sensing scene classification. *IEEE Trans. Geosci. Remote Sens.* **2018**, *56*, 371–390. [\[CrossRef\]](#)
150. Sermanet, P.; Eigen, D.; Zhang, X.; Mathieu, M.; Fergus, R.; LeCun, Y. OverFeat: Integrated Recognition, Localization and Detection using Convolutional Networks. *arXiv* **2014**, arXiv:1312.6229.
151. Donahue, J.; Jia, Y.; Vinyals, O.; Hoffman, J.; Zhang, N.; Tzeng, E.; Darrell, T. DeCAF: A Deep Convolutional Activation Feature for Generic Visual Recognition. *arXiv* **2013**, arXiv:1310.1531.
152. Jia, Y.; Shelhamer, E.; Donahue, J.; Karayev, S.; Long, J.; Girshick, R.; Guadarrama, S.; Darrell, T. Caffe: Convolutional Architecture for Fast Feature Embedding. In Proceedings of the 22nd ACM international conference on Multimedia, New York, NY, USA, 3–7 November 2014.
153. Chung, A.; Shafiee, M.; Wong, L. Random feature maps via a Layered Random Projection (LARP) framework for object classification. In Proceedings of the 2016 IEEE International Conference on Image Processing (ICIP), Phoenix, AZ, USA, 25–28 September 2016.
154. Luus, F.P.; Salmon, B.P.; Van Den Bergh, F.; Maharaj, B.T.J. Multiview deep learning for land-use classification. *IEEE Geosci. Remote Sens. Lett.* **2015**, *12*, 2448–2452. [\[CrossRef\]](#)
155. Hu, F.; Xia, G.-S.; Hu, J.; Zhang, L. Transferring Deep Convolutional Neural Networks for the Scene Classification of High-Resolution Remote Sensing Imagery. *Remote Sens.* **2015**, *7*, 14680–14707. [\[CrossRef\]](#)
156. Nogueira, K.; Penatti, O.; Santos, J. Towards better exploiting convolutional neural networks for remote sensing scene classification. *Pattern Recogn.* **2017**, *61*, 539–556. [\[CrossRef\]](#)
157. He, N.; Fang, L.; Li, S.; Plaza, A.; Plaza, J. Remote sensing scene classification using multilayer stacked covariance pooling. *IEEE Trans. Geosci. Remote Sens.* **2018**, *56*, 6899–6910. [\[CrossRef\]](#)
158. Penatti, O.; Nogueira, K.; Dos Santos, J.A. Do deep features generalize from everyday objects to remote sensing and aerial scenes domains? In Proceedings of the 2015 IEEE Conference on Computer Vision and Pattern Recognition Workshops (CVPRW), Boston, MA, USA, 7–12 June 2015.
159. Li, B.; Su, W.; Wu, H.; Li, R.; Zhang, W.; Qin, W.; Zhang, S. Aggregated Deep Fisher Feature for VHR Remote Sensing Scene Classification. *IEEE J. Sel. Top. Appl. Earth Obs. Remote Sens.* **2019**, *12*, 3508–3523. [\[CrossRef\]](#)

160. Scott, G.; Hagan, K.; Marcum, R.; Hurt, J.; Anderson, D.; Davis, C. Enhanced Fusion of Deep Neural Networks for Classification of Benchmark High-Resolution Image Data Sets. *IEEE Geosci. Remote Sens. Lett.* **2018**, *15*, 1451–1455. [[CrossRef](#)]
161. Yang, Y.; Newsam, S. Bag-of-visual-words and spatial extensions for land-use classification. In Proceedings of the 18th SIGSPATIAL International Conference on Advances in Geographic Information Systems (ACM 2010), San Jose, CA, USA, 3–5 November 2010; pp. 270–279.
162. Risojević, V.; Babić, Z. Aerial image classification using structural texture similarity. In Proceedings of the 2011 IEEE International Symposium on Signal Processing and Information Technology (ISSPIT), Bilbao, Spain, 14–17 December 2011.
163. Risojević, V.; Babić, Z. Orientation difference descriptor for aerial image classification. In Proceedings of the 2012 19th International Conference on Systems, Signals and Image Processing (IWSSIP), Vienna, Austria, 11–13 April 2012.
164. Chen, C.; Zhang, B.; Su, H.; Li, W.; Wang, L. Land-use scene classification using multi-scale completed local binary patterns. *Signal Image Video Processing* **2016**, *10*, 745–752. [[CrossRef](#)]
165. Yang, Y.; Newsam, S. Spatial pyramid co-occurrence for image classification. In Proceedings of the 2011 International Conference on Computer Vision, Barcelona, Spain, 6–13 November 2011.
166. Shao, W.; Yang, W.; Xia, G.; Liu, G. A hierarchical scheme of multiple feature fusion for high-resolution satellite scene categorization. In Proceedings of the 9th International Conference, ICVS 2013, Saint Petersburg, Russia, 16–18 July 2013.
167. Zhao, L.; Tang, P.; Huo, L. Land-use scene classification using a concentric circle-structured multiscale bag-of-visual-words model. *IEEE J. Sel. Top. Appl. Earth Obs. Remote Sens.* **2014**, *7*, 4620–4631. [[CrossRef](#)]
168. Zhao, L.; Tang, P.; Huo, L. A 2-D wavelet decomposition-based bag-of-visual-words model for land-use scene classification. *Int. J. Remote Sens.* **2014**, *35*, 2296–2310. [[CrossRef](#)]
169. Cheriyadat, A.M. Unsupervised feature learning for aerial scene classification. *IEEE Trans. Geosci. Remote Sens.* **2013**, *52*, 439–451. [[CrossRef](#)]
170. Cheng, G.; Han, J.; Zhou, P.; Guo, L. Multi-class geospatial object detection and geographic image classification based on collection of part detectors. *ISPRS J. Photogramm. Remote Sens.* **2014**, *98*, 119–132. [[CrossRef](#)]
171. Negrel, R.; Picard, D.; Gosselet, P. Evaluation of second-order visual features for land-use classification. In Proceedings of the 2014 12th International Workshop on Content-Based Multimedia Indexing (CBMI), Klagenfurt, Austria, 18–20 June 2014.
172. Zhang, F.; Du, B.; Zhang, L. Saliency-guided unsupervised feature learning for scene classification. *IEEE Trans. Geosci. Remote Sens.* **2014**, *53*, 2175–2184. [[CrossRef](#)]
173. Chen, S.; Tian, Y. Pyramid of spatial relations for scene-level land use classification. *IEEE Trans. Geosci. Remote Sens.* **2015**, *53*, 1947–1957. [[CrossRef](#)]
174. Hu, F.; Xia, G.; Wang, Z.; Huang, X.; Zhang, L.; Sun, H. Unsupervised feature learning via spectral clustering of multidimensional patches for remotely sensed scene classification. *IEEE J. Sel. Top. Appl. Earth Obs. Remote Sens.* **2015**, *8*, 2015–2030. [[CrossRef](#)]
175. Zhong, Y.; Zhu, Q.; Zhang, L. Scene classification based on the multifeature fusion probabilistic topic model for high spatial resolution remote sensing imagery. *IEEE Trans. Geosci. Remote Sens.* **2015**, *53*, 6207–6222. [[CrossRef](#)]
176. Castelluccio, M.; Poggi, G.; Sansone, C.; Verdoliva, L. Land use classification in remote sensing images by convolutional neural networks. *arXiv* **2015**, arXiv:1508.00092.
177. Luo, J.; Kitamura, G.; Arefan, D.; Doganay, E.; Panigrahy, A.; Wu, S. Knowledge-Guided Multiview Deep Curriculum Learning for Elbow Fracture Classification. In Proceedings of the 12th International Workshop, MLMI 2021, Held in Conjunction with MICCAI 2021, Strasbourg, France, 27 September 2021.
178. Zhang, F.; Du, B.; Zhang, L. Scene classification via a gradient boosting random convolutional network framework. *IEEE Trans. Geosci. Remote Sens.* **2016**, *54*, 1793–1802. [[CrossRef](#)]
179. Liu, Q.; Hang, R.; Song, H.; Zhu, H.; Plaza, J.; Plaza, A. Adaptive deep pyramid matching for remote sensing scene classification. *arXiv* **2016**, arXiv:1611.03589.
180. Han, X.; Zhong, Y.; Zhao, B.; Zhang, L. Scene classification based on a hierarchical convolutional sparse auto-encoder for high spatial resolution imagery. *Int. J. Remote Sens.* **2017**, *38*, 514–536. [[CrossRef](#)]
181. Lin, D.; Fu, K.; Wang, Y.; Xu, G.; Sun, X. MARTA GANs: Unsupervised representation learning for remote sensing image classification. *IEEE Geosci. Remote Sens. Lett.* **2017**, *14*, 2092–2096. [[CrossRef](#)]
182. Shawky, O.A.; Hagag, A.; El-Dahshan, E.S.A.; Ismail, M. A very high-resolution scene classification model using transfer deep CNNs based on saliency features. *Signal Image Video Processing* **2021**, *15*, 817–825. [[CrossRef](#)]
183. Bian, X.; Chen, C.; Tian, L.; Du, Q. Fusing local and global features for high-resolution scene classification. *IEEE J. Sel. Top. Appl. Earth Obs. Remote Sens.* **2017**, *10*, 2889–2901. [[CrossRef](#)]
184. Anwer, R.M.; Khan, F.S.; Van De Weijer, J.; Molinier, M.; Laaksonen, J. Binary patterns encoded convolutional neural networks for texture recognition and remote sensing scene classification. *ISPRS J. Photogramm. Remote Sens.* **2018**, *138*, 74–85. [[CrossRef](#)]
185. Qi, K.; Guan, Q.; Yang, C.; Peng, F.; Shen, S.; Wu, H. Concentric Circle Pooling in Deep Convolutional Networks for Remote Sensing Scene Classification. *Remote Sens.* **2018**, *10*, 934. [[CrossRef](#)]
186. Zeng, D.; Chen, S.; Chen, B.; Li, S. Improving Remote Sensing Scene Classification by Integrating Global-Context and Local-Object Features. *Remote Sens.* **2018**, *10*, 734. [[CrossRef](#)]
187. Wang, Q.; Liu, S.; Chanussot, J.; Li, X. Scene classification with recurrent attention of VHR remote sensing images. *IEEE Trans. Geosci. Remote Sens.* **2019**, *57*, 1155–1167. [[CrossRef](#)]



188. Wang, W.; Du, L.; Gao, Y.; Su, Y.; Wang, F.; Cheng, J. A Discriminative Learned CNN Embedding for Remote Sensing Image Scene Classification. *arXiv* **2019**, arXiv:1911.12517.
189. Yu, Y.; Liu, F. Dense Connectivity Based Two-Stream Deep Feature Fusion Framework for Aerial Scene Classification. *Remote Sens.* **2018**, *10*, 1158. [[CrossRef](#)]
190. Yu, Y.; Liu, F. A two-stream deep fusion framework for high-resolution aerial scene classification. *Comput. Intel. Neurosc.* **2018**, *2018*, 8639367. [[CrossRef](#)]
191. Ye, L.; Wang, L.; Sun, Y.; Zhao, L.; Wei, Y. Parallel multi-stage features fusion of deep convolutional neural networks for aerial scene classification. *Remote Sens. Lett.* **2018**, *9*, 294–303. [[CrossRef](#)]
192. Chen, J.; Wang, C.; Ma, Z.; Chen, J.; He, D.; Ackland, S. Remote Sensing Scene Classification Based on Convolutional Neural Networks Pre-Trained Using Attention-Guided Sparse Filters. *Remote Sens.* **2018**, *10*, 290. [[CrossRef](#)]
193. Akodad, S.; Vilfroy, S.; Bombrun, L.; Cavalcante, C.C.; Germain, C.; Berthoumieu, Y. An ensemble learning approach for the classification of remote sensing scenes based on covariance pooling of CNN features. In Proceedings of the 2019 27th European Signal Processing Conference (EUSIPCO), A Coruna, Spain, 2–6 September 2019.
194. Liu, Y.; Zhong, Y.; Qin, Q. Scene Classification Based on Multiscale Convolutional Neural Network. *IEEE Trans. Geosci. Remote Sens.* **2018**, *56*, 7109–7121.
195. Lu, X.; Ji, W.; Liu, W.; Zheng, X. Bidirectional adaptive feature fusion for remote sensing scene classification. *Neurocomputing* **2019**, *328*, 135–146. [[CrossRef](#)]
196. He, H.; Garcia, E. Learning from Imbalanced Data. *IEEE Trans. Knowl. Data Eng.* **2009**, *21*, 1263–1284. [[CrossRef](#)]
197. Johnson, J.M.; Khoshgoftaar, T.M. Survey on deep learning with class imbalance. *J. Big Data* **2019**, *6*, 27. [[CrossRef](#)]
198. Jaiswal, A.; Babu, A.R.; Zadeh, M.Z.; Banerjee, D.; Makedon, F. A Survey on Contrastive Self-Supervised Learning. *Technologies* **2021**, *9*, 2. [[CrossRef](#)]

Article

# Spatiotemporal Assessment of Air Quality and Heat Island Effect Due to Industrial Activities and Urbanization in Southern Riyadh, Saudi Arabia

Abeer Salman <sup>1,\*</sup>, Manahil Al-Tayib <sup>2</sup>, Sulafa Hag-Elsafi <sup>1</sup>, Faisal K. Zaidi <sup>3</sup> and Nada Al-Duwarij <sup>1</sup>

<sup>1</sup> Department of Geography, King Saud University, Riyadh 11564, Saudi Arabia; shagelsafi@ksu.edu.sa (S.H.-E.); nadahamadmohammad@gmail.com (N.A.-D.)

<sup>2</sup> Department of Quantitative Analysis, King Saud University, Riyadh 11564, Saudi Arabia; maltib@ksu.edu.sa

<sup>3</sup> Department of Geology and Geophysics, King Saud University, Riyadh 11564, Saudi Arabia; fzaidi@ksu.edu.sa

\* Correspondence: abalsalman@ksu.edu.sa

**Abstract:** The aim of this paper is to evaluate the air and thermal pollution in the southern suburbs of Riyadh, where people are suffering from poor air quality due to the rapid development of the industrial facilities in the area. The study involved the distribution of questionnaires to 405 residents living in that area in order to obtain their opinions about air pollution. In addition, land surface temperature and 12 components of air were measured at 18 points. In addition, the air quality data from 2016 to 2020 for Al Khaldya and Southern Ring Road air stations were assessed. Al Misfat (Oil Refinery) and the Second Industry City are significant contributors to air pollution and also result in the urban heat island effect from high temperature due to factories and industrial activities. However, all the measured components of air quality are lower than the standard limits except the element particulate matter (PM)<sub>10</sub>, which exceeds the standard limits in several parts of the study area and during several months of the year. This can surely have a negative impact on the health of residents. At the same time, this study found that the preventive measures taken to stop the spread of COVID-19 infections have led to a positive impact in the area in terms of improvement in air quality.

**Keywords:** air pollution; Riyadh; industrial city; land surface temperature; geostatistic

**Citation:** Salman, A.; Al-Tayib, M.; Hag-Elsafi, S.; Zaidi, F.K.; Al-Duwarij, N. Spatiotemporal Assessment of Air Quality and Heat Island Effect Due to Industrial Activities and Urbanization in Southern Riyadh, Saudi Arabia. *Appl. Sci.* **2021**, *11*, 2107. <https://doi.org/10.3390/app11052107>

Academic Editor: Tung-Ching Su

Received: 8 January 2021

Accepted: 19 February 2021

Published: 27 February 2021

**Publisher's Note:** MDPI stays neutral with regard to jurisdictional claims in published maps and institutional affiliations.



**Copyright:** © 2021 by the authors. Licensee MDPI, Basel, Switzerland. This article is an open access article distributed under the terms and conditions of the Creative Commons Attribution (CC BY) license (<https://creativecommons.org/licenses/by/4.0/>).

## 1. Introduction

Urbanization and industrialization are the main sources of air pollution in the world. Consequently, air pollution has become the main topic of many environmental studies [1–5]. The World Health Organization states that air pollution is a threat to human health and is responsible for millions of deaths annually [6–9]. Annually, about 21,000 Canadians die due to exposure to polluted air [10].

Several studies have shown a positive correlation between cancer and exposure to polluted air in different parts of the world [11,12] and in the Arabian Peninsula [13]. The industrial areas in the world are the main contributors to air pollution and are responsible for the deteriorating health of the population.

In Riyadh, the capital of Saudi Arabia, industrialization has increased dramatically during the past couple of decades in response to the increase in population and urban development. Establishment of two industrial cities has resulted in better employment opportunities and, consequently, a high population growth of about 4% in Riyadh [14]. The First Industrial City was established in 1973 and has an area of 0.5 km<sup>2</sup>. The Second Industrial City was established in 1976 and has an area of 19 km<sup>2</sup> [15].

Though the Second Industrial City and the Saudi Aramco Oil Refinery (Al-Misfat) were established in the south of Riyadh, far from the city, urban expansion and associated economical activities forced the people to live around the industrial cities. Accordingly,

overcrowded buildings, especially along roads; an increase in traffic and vehicular emissions; and frequent desert dust storms in the area were the principal sources that increased the level of environmental pollutants [16], leading to air pollution [17]. The cumulative effect of these factors resulted in deterioration of air quality indoors and outdoors at many sites in Riyadh [18].

During several visits to the study area in southern Riyadh, it was evident that the area is suffering from multiple aspects of pollution, reduction in visibility during the mornings, and dirty and eroded buildings. Accordingly, residents and workers complained of unhealthy air quality in the area.

Several efforts have been made to study the concentration of chemicals and particulate matter in the air in Saudi Arabi [19–21]; however, most studies were limited and not comprehensive due to insufficient data [18]. As a result, the Royal Commission for Riyadh City and the General Authority of Meteorology and Environment Protection are operating 32 air quality control stations in Riyadh, over the past few years, to monitor the air quality. Some of these monitoring stations are fixed, whereas others are mobile. In addition, the General Authority of Meteorology and Environment Protection launched a dashboard for Riyadh air quality [22] to visualize the air quality index (AQI).

Mapping techniques are useful to assist decision makers in quantifying and locating pollution sites, even with limited measurements. (Geographic information system) GIS and remote sensing are useful tools for spatial analysis and detection of thermal pollution. Geostatistics is a strong technique to assess the spatial analysis of the studied variables [23]. The kriging technique is widely used for investigating sources of pollution as it is a reliable technique with fewer errors, even with small samples [24–26]. In addition, remote sensing imageries, especially in the thermal bands, provide simpler and more accurate information about surface temperature and emissivity [27] to detect urban heat islands (UHIs) [28–30].

Accordingly, this study aims to shed light on the opinions of residents living in southern Riyadh, near the industrial city, regarding emissions of oxides and particulate matter from industrial areas and traffic congestion. Most studies when surveying about the quality of life in cities do not take into account people's opinions about air pollution aspects. The spatial and temporal changes in thermal and air pollution were evaluated from 2016 to 2020. Additionally, the impact of the lockdown on air quality during the coronavirus pandemic was also assessed.

## 2. Materials and Methods

### 2.1. Study Area

The study area is located in the southern suburbs of Riyadh. It lies between the coordinates 24.482–24.594 North and 46.759–46.946 East (Figure 1). It covers about 128.7 km<sup>2</sup> and includes the following seven districts: Ad-Difa, Al-Iskan, the second Industrial City, Al-Misfat, Al-Mansuriah, Ad-Dar Al-Baida, and Taybah.

The total number of inhabitants in the study area is 116,510 [31]. The Second Industrial City, including Al Iskan and Ad Dar Al Baida, has a higher population due to better infrastructure and amenities (Figure 2).

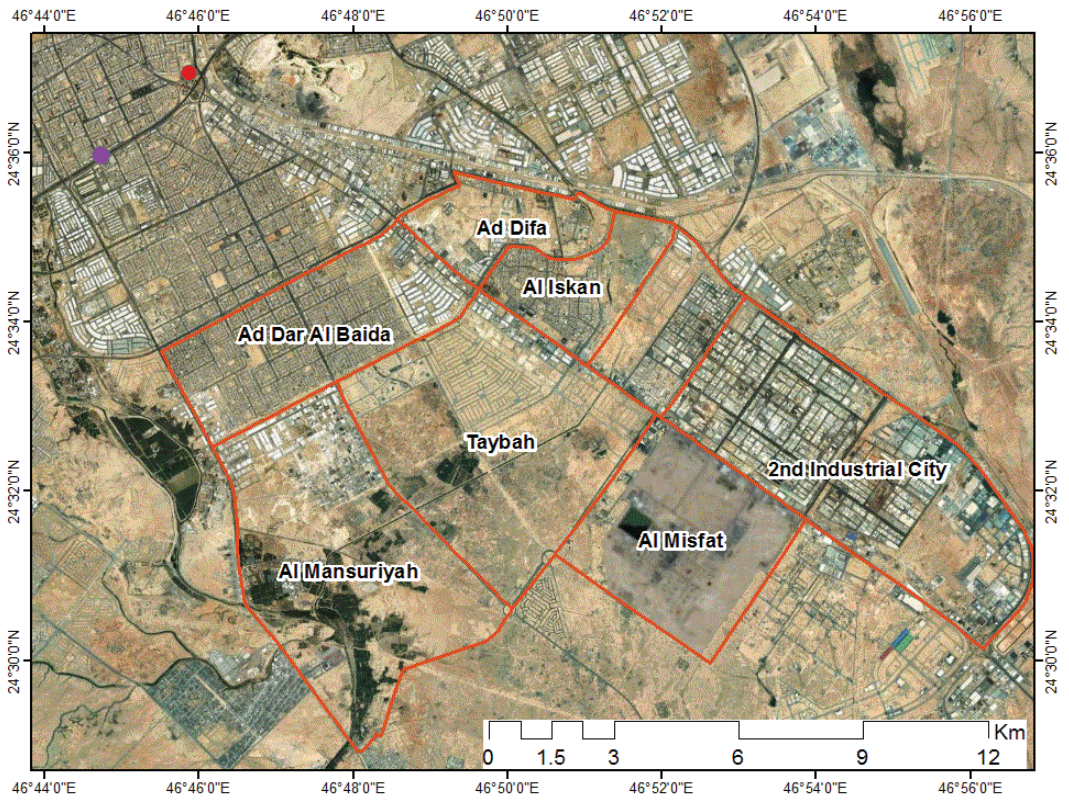


Figure 1. Study area location.

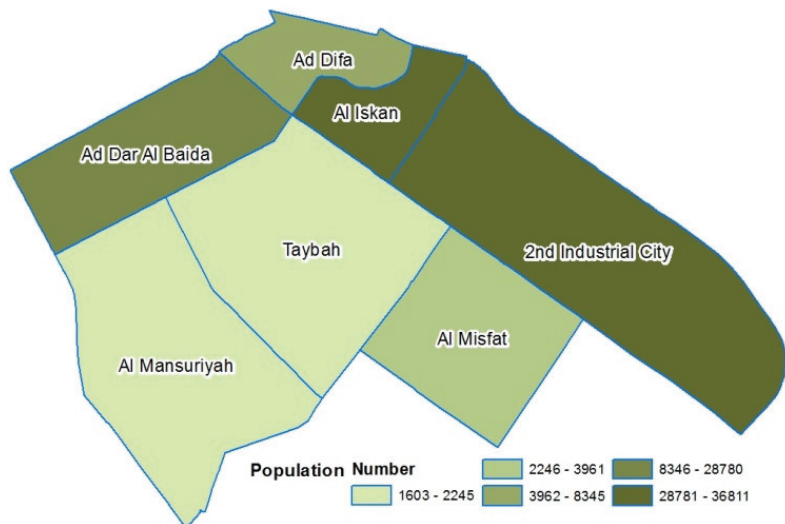


Figure 2. Population of the study area.

In the study area, two major industrial factories were established, namely the Second Industrial City and Al-Misfat (the Saudi Aramco Oil Refinery) (Figure 3). The Second

Industrial City was established in 1979 and has more than 823 factories with different activities [15]. The Al-Misfat refinery was established in 1974 and produces various kinds of petroleum derivatives. Moreover, there is heavy vehicular traffic throughout the day to support the industrial area.

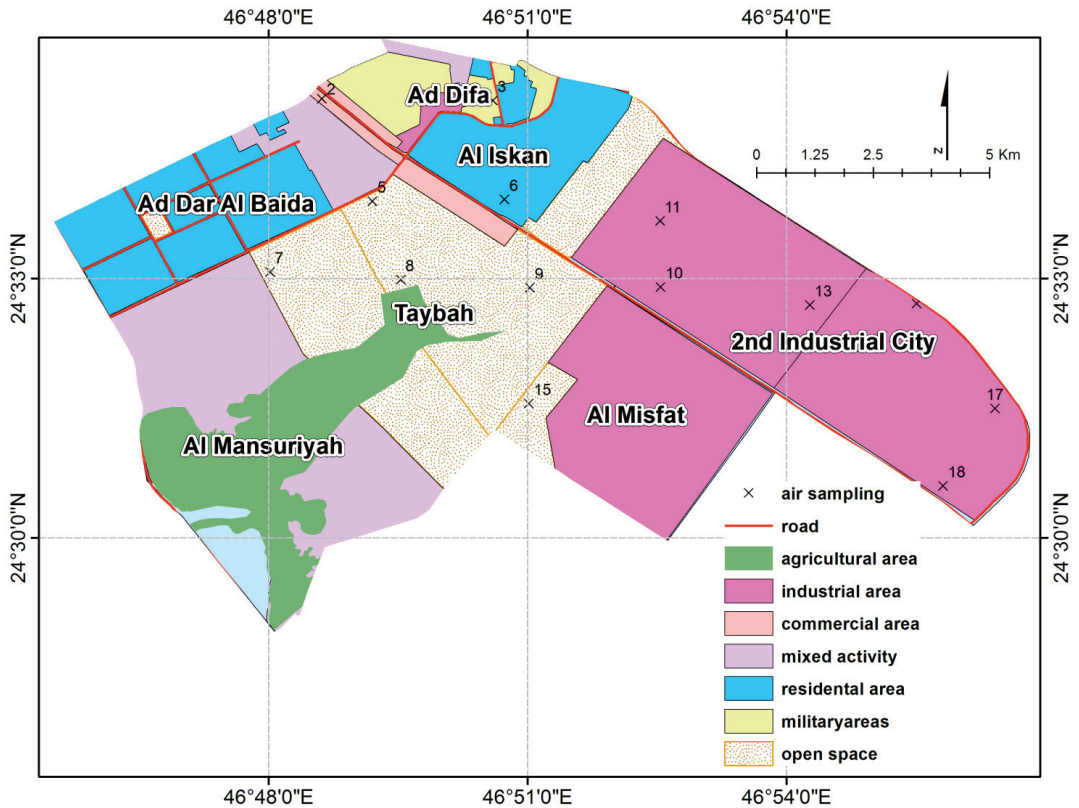


Figure 3. Land-use map of the study area and location of air sampling.

The western part of the study area is bounded by Wadi Hanifa, where the treated wastewater from Riyadh City is disposed. This water flows along the valley, with some agricultural activities in the Mansuriah and Taybah districts, which are less densely populated.

### 2.2. The Questionnaire

The study involved a survey about people’s opinions regarding air pollution. The survey was conducted through a questionnaire, which was prepared in accordance with relevant guidelines and regulations and was approved by the Geography Department at King Saud University. Random samples of the population were chosen from the seven suburbs, and the questionnaire was distributed to 405 persons. The sub-samples, determined by the study, were according to population, as shown in Table S1.

The questionnaire consists of three parts: inhabitants’ conditions, recognizing pollution, and pollution impact on the environment and health. The study applied chi-square and Cramer’s V tests to understand the relationship between districts and pollution aspects.

### 2.3. Spatial and Temporal Analysis

Thermal analysis was carried out using the Landsat 8 satellite sensor image, and the land surface temperature (LST) was calculated from band 10 and band 11 by using land

surface emissivity ( $\epsilon$ ). In addition, the normalized difference vegetation index (NDVI) was calculated using band 4 and band 5 to determine the proportion of vegetation ( $PV$  and  $\epsilon$ ) to estimate the LST [32–35], as shown in Figure 4. Three images from May 2014, 2017, and 2020, with a ground resolution of 30 m, were selected.

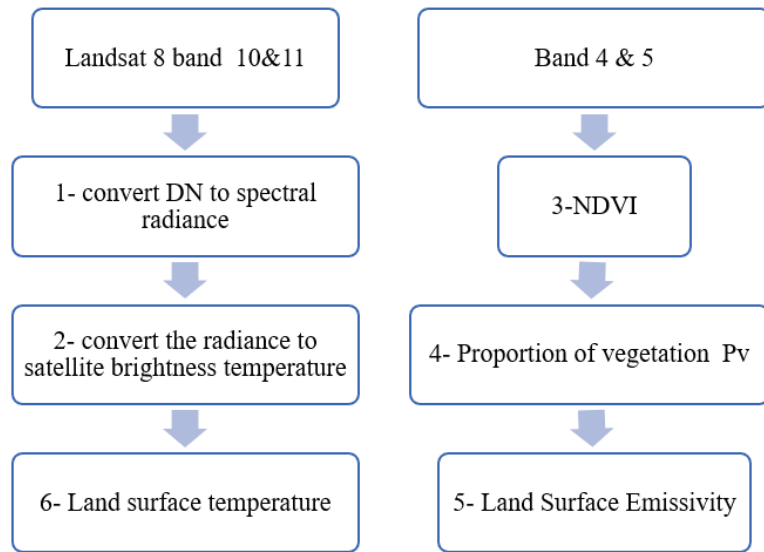


Figure 4. Flowchart to determine land surface temperature.

At the same time, the study involved the measurement of particulate matter (PM10, PM4, PM2.5, and PM1) and gases (CO, CO<sub>2</sub>, NO, NO<sub>2</sub>, SO<sub>2</sub>, O<sub>3</sub>, H<sub>2</sub>S, and Volatile organic compounds VOCs) using portable instruments at 18 points from 18 to 25 May 2014. The measuring was according to Presidency of Meteorology and Environment Protection standards (PME) in Riyadh and performed by Geotechnical and Environmental Company (GECO), as shown in Table S2. The distance between sample sites was 2–3 km, as shown in Figure 3.

The study used descriptive analysis for air sampling, to picture and summarize the data [36], and used correlation coefficients to assess the strength of linear relationship between variables. Principal component analysis (PCA) was carried out to transform the original set of variables into a smaller set of linear combinations [37].

Data analysis was carried out geostatistically, using ArcGIS 10.1, while ordinary kriging was done by creating a semivariogram. The study estimated the central tendency, dispersion, and shape to determine the type of distribution of numerical variables. A semivariogram was created by building the spatial variability structure of each attribute, as in shown in Equation (1).

$$\gamma(h) = \frac{1}{2N(h)} \sum_{i=1}^{N(h)} [(Z(x) - Z(x+h))]^2 \quad (1)$$

where  $\gamma(h)$  is the semi-variance,  $Z(x)$  is the value of initial potential at site  $x$ ,  $Z(x+h)$  is the value of potential at site  $(h)$  distance apart from  $(x)$ , and  $N$  is the number of sample pairs [38].

Ordinary kriging maps were established to predict values at a non-sampled point that assumes a constant unknown meaning, Equations (2a) and (2b):

$$Z(X_0) = \mu + \epsilon(X_0) \quad (2a)$$

$$Z(X_0) = \sum \lambda_i \gamma(x_i), \quad \sum \lambda_i = 1 \tag{2b}$$

where  $\mu$  is an unknown constant,  $\varepsilon(X_0)$  is the the error associated with an unknown location  $X_0$ ,  $Z(X_0)$  is the estimated value of  $Z$  at  $X_0$ , and  $\lambda_i$  is the the weight that gives the best-possible estimation from the surrounding points.

Finally, the trend of the monthly average of  $\text{NO}_2$  and  $\text{PM}_{10}$  concentrations was determined for the Southern Ring Road air station from January 2016 to September 2018 and the Al-Khaldiyah air station from September 2019 to May 2020. These two air stations were selected as they are the closest to the study area and have air quality conditions similar to those in the study area. Moreover, a continuous data set for the time period mentioned above was available from these two air-quality-monitoring stations.

### 3. Results

#### 3.1. The Questionnaire

Most respondents (nearly 64.85%) were in the age group of 20–40 years. Of these, 85.11% are employees (private sector or government), and their housing is near their workplace. Half of them are professionals and are living in the study area for more than 10 years.

Most of the respondents reported that the buildings they live in are dirty, the plants are dusty, and fine dusty clouds extending about 1–3 km or more are present around the residential buildings, as shown in Figure 5.

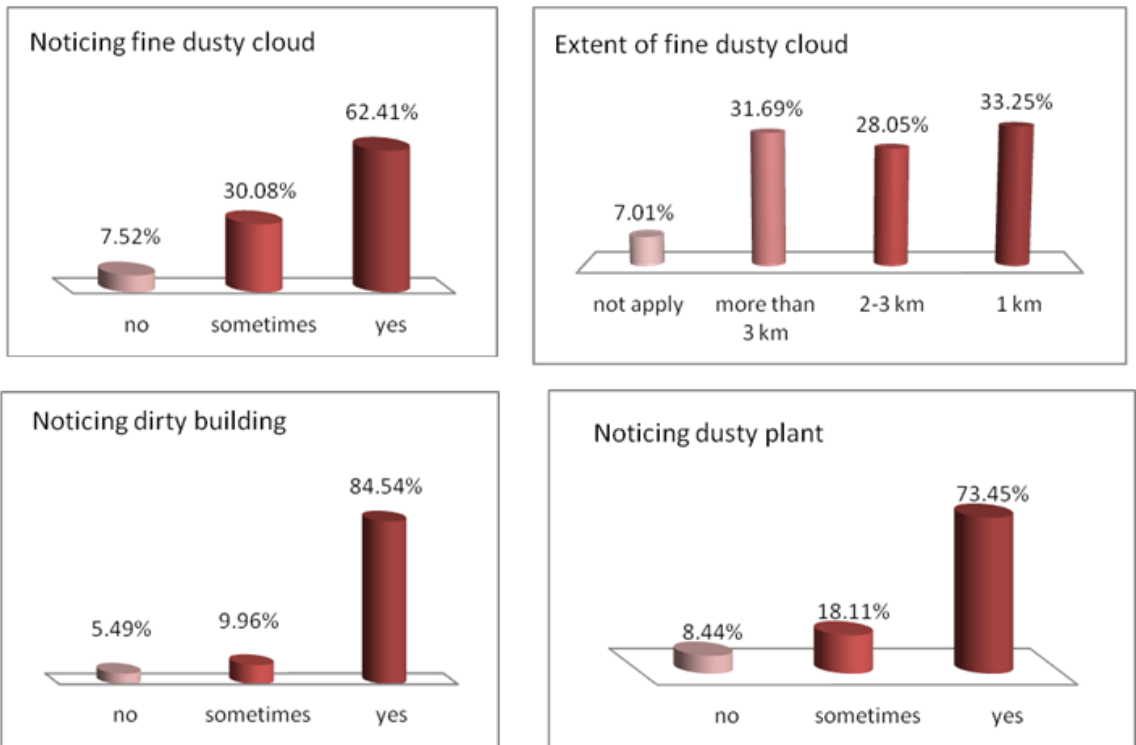
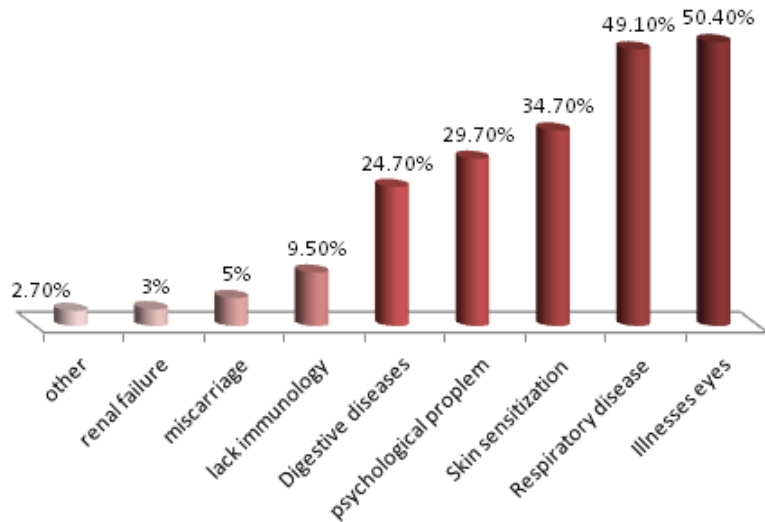


Figure 5. Noticing the pollution aspects in the study area.

They reported that most of the aspects related to air quality are similar in many residential districts of Riyadh; however, the problem of dirty buildings is specific to the study area, as shown in Table S3. Al-Iskan, Ad-Dar Al-Baida, and the Second Industrial

City are the most heavily polluted districts in the study area; and as a consequence, their residents suffer from many respiratory and eye diseases, as shown in Figure 6.



**Figure 6.** Diseases the population suffers from due to air pollution.

The survey results confirm the existence of problems related to air pollution in the study area. Field measurements and spatial analysis of gases and particulate matters, suspended in the air, are required to determine the extent and concentration of pollutants.

### 3.2. Thermal Analysis

The study widely used the NDVI as an indicator of the vegetation index and to calculate the LST. Generally, the study area shows a high variation in temperature. The highest temperature is observed in Al-Misfat, the factories, and the Second Industry City. The NDVI imageries from 2014 to 2020 (Figure 7) showed low values in most of the study area, except in the agricultural area in Taybah and Al-Mansuriah. The NDVI showed a gradual decrease in the study area, showing a steady increase in temperature. However, in May 2020, a lower temperature was recorded as much of the activities had stopped due to the lockdown to prevent the spread of COVID-19. This observation proves that human activities and reduced vegetation cover are major reasons for the development of heat islands in the region.



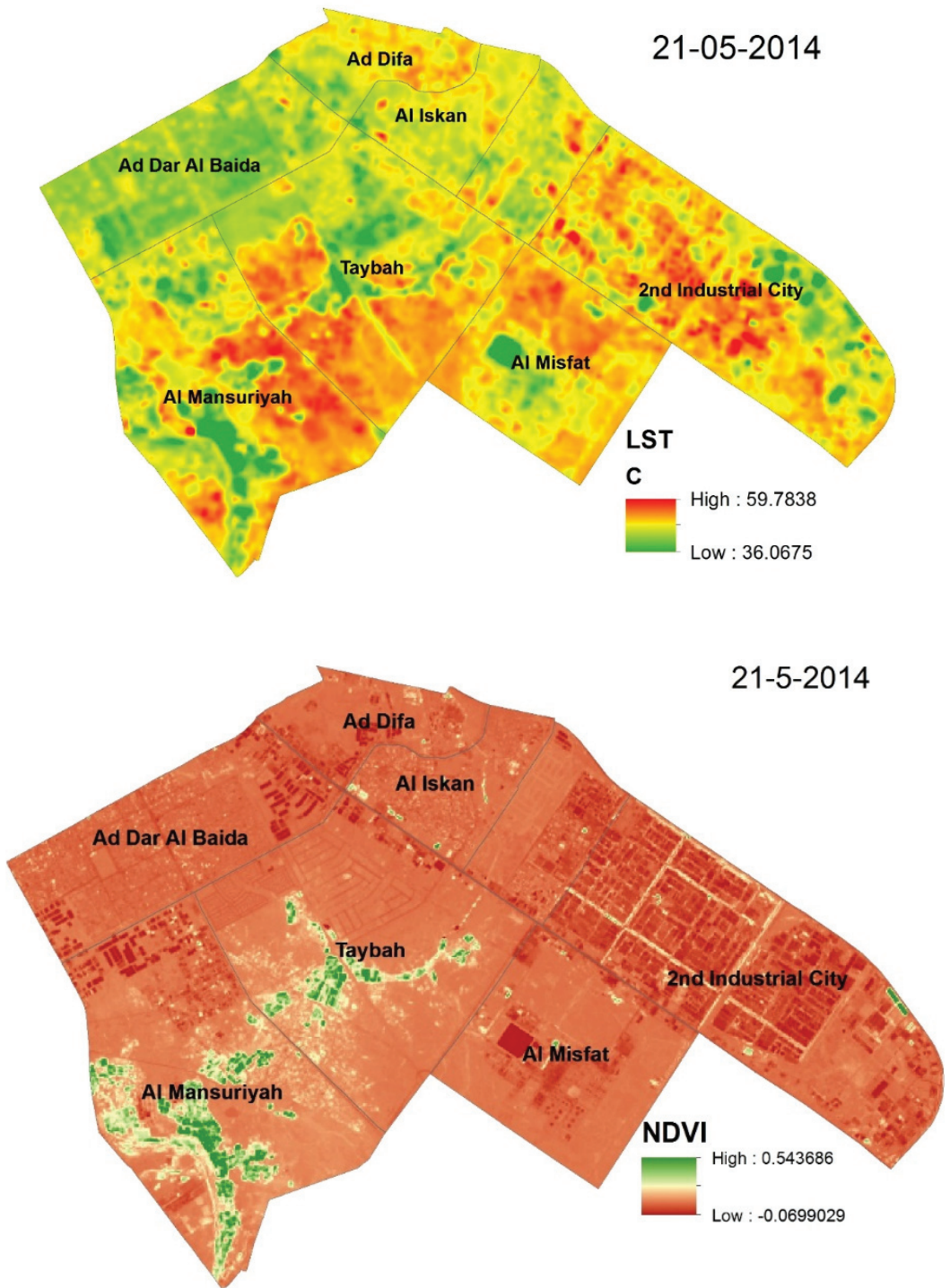


Figure 7. Cont.

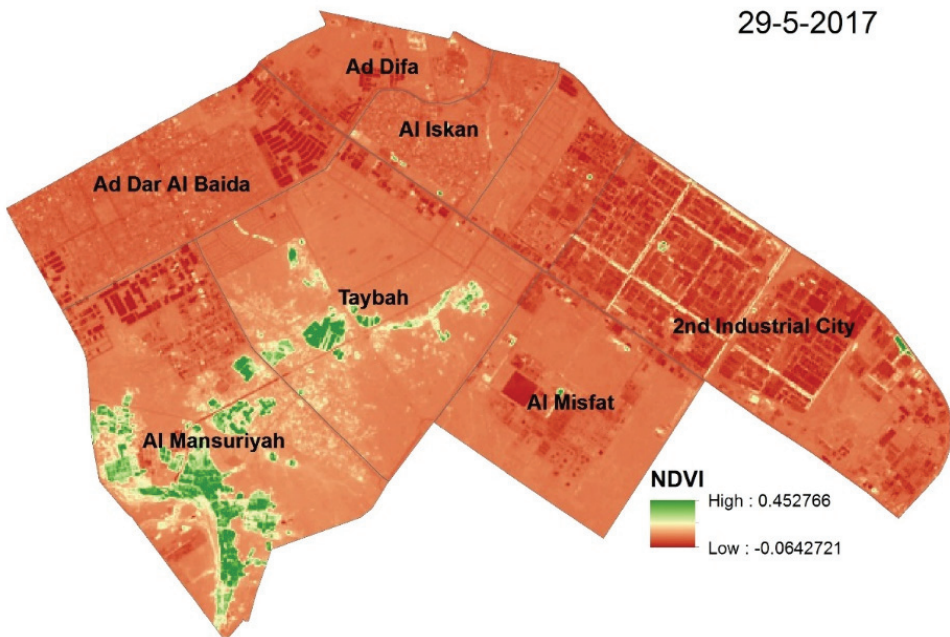
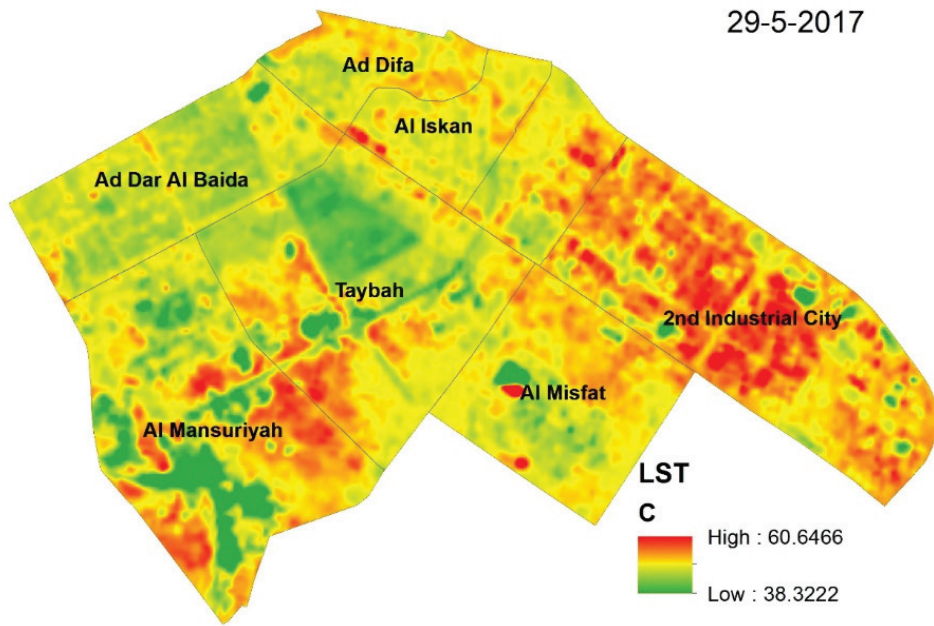


Figure 7. Cont.

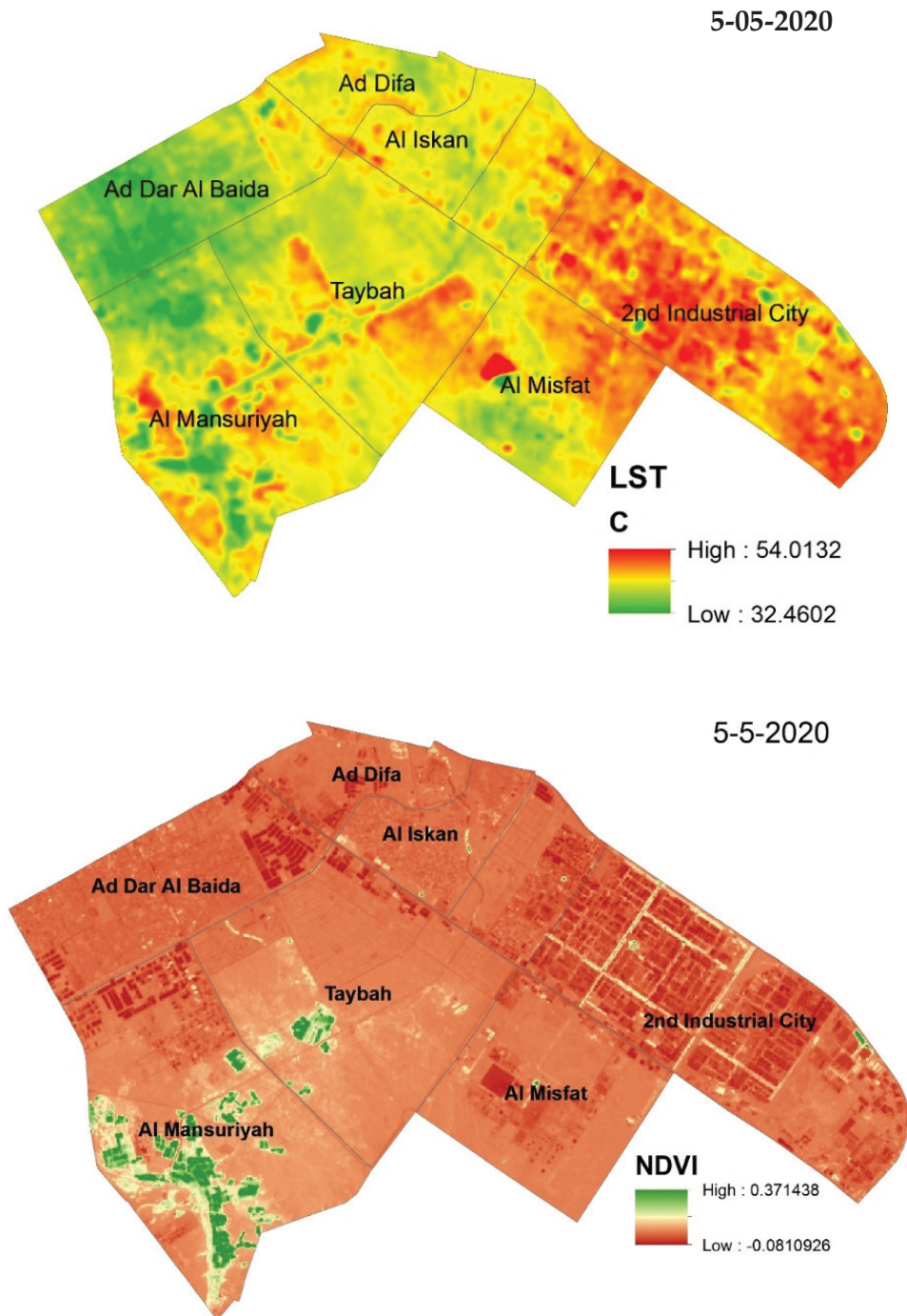


Figure 7. Land surface temperature and the normalized difference vegetation index (NDVI) (2014–2020).

### 3.3. Statistical and Geostatistical Analysis

The results of the descriptive statistics are given in (Table 1). The mean values of the particulate matter observed in the study area during most days of the year exceed the National Ambient Air Quality Standards (NAAQS).

**Table 1.** Descriptive statistics of air parameters.

	PM10 ug/m <sup>3</sup>	PM2.5 ug/m <sup>3</sup>	CO ppm	PM4 ug/m <sup>3</sup>	PM1 ug/m <sup>3</sup>	NO <sub>2</sub> ug/m <sup>3</sup>	SO <sub>2</sub> ug/m <sup>3</sup>	O <sub>3</sub> ppm	H <sub>2</sub> S ug/m <sup>3</sup>	VOC ug/m <sup>3</sup>	CO <sub>2</sub> ug/m <sup>3</sup>	NO ug/m <sup>3</sup>
Mean	214	119	5	133.6	58.4	35	288	0.014	0.25	0.07	23.3	1.5
Minimum	78	28	2	38	11	9	110	0.01	0.07	0	4.7	0.2
Maximum	307	187	10	245	136	64	510	0.02	0.95	0.23	65	3.9
Std. deviation	79	58	2.8	62.5	44.2	15.5	108	0.005	0.23	0.06	15.7	0.99
Skewness	−0.22	−0.28	0.36	0.2	0.52	0.54	0.45	0.24	1.9	1.1	1.4	0.99
Kurtosis	−0.7	−0.7	−0.3	−0.2	−0.1	−0.55	0.05	−0.2	0.7	1	1.9	0.74
NAAQS	150	35	35			100	1300	0.075				

PM, particulate matter; NAAQS, National Ambient Air Quality Standards.

The correlation coefficient shown in Table S4 shows strong-to-moderate correlation between particulates, CO<sub>2</sub>, CO, and NO<sub>2</sub> and indicates the same source of pollution.

Factor analysis (PC) helped in identifying four factors having eigen values of >1. The four factors explain 82.046% of the total variance, as shown in Table S5. PC1 accounts for 41.2% of the data variability and shows significant factor loadings of PM1, PM2.5, PM4, PM10, CO, and NO<sub>2</sub>, as shown in Table S6. These variables have strong-to-moderate correlation, as shown in Table S4. PC2 represents 14.5% of the total variability and has significant factor loadings of SO<sub>2</sub> and CO<sub>2</sub>. PC3 and PC4 represent 13.6% for O<sub>3</sub> and VOCs and 12.756% for H<sub>2</sub>S and NO, respectively.

Ordinary kriging maps were built, as shown in Figure 8, for the particulate matter and gases, except O<sub>3</sub> because there was no significant spatial variation, as seen in the semivariogram model shown in Table S7. The distribution of all variables was lognormal for different types of the chosen model, depending on the least mean square error.

High concentrations of pollutants and particulate matter are in Al-Misfat, the Second Industrial City, and along the highway.

The concentration of PM varies in the study area, depending on land use and working conditions. However, a high concentration of coarse particulate matter (PM10) covers large areas, and its mean (214 ug/m<sup>3</sup>) exceeds the standard limit (150 ug/m<sup>3</sup>). Fine particulates (smaller than 2.5) are more critical and may cause more respiratory problems. They are concentrated in specific areas around Al-Misfat and the Second Industrial City. These fine particulates, derived mostly from combustion, may remain suspended for weeks and drift for many kilometers [39]. Moreover, spatial distributions of particulates are similar to those of CO and NO<sub>2</sub> and consequently considered to be within PC1.

A high variation in the concentration of oxides, CO<sub>2</sub>, NO<sub>2</sub>, and SO<sub>2</sub>, is observed in the study area. The highest concentrations are around the Second Industrial City and Al-Misfat, where industries and automobile emissions are considered as the major sources of NO<sub>2</sub> [20]; however, emissions remained below standard at all places. VOC emission is concentrated in Al-Misfat and in the southeastern part of the Second Industrial City. The oil and natural gases sector is the main source of VOCs. H<sub>2</sub>S is concentrated in the urban area in the northern part of the study area and near Al-Misfat. The main sources of H<sub>2</sub>S are petroleum refineries, Al-Misfat, and the sewage system. Ad-Dar Al-Baida suffers from the leakage of an old sewage system, and the population suffers greatly from stagnant sewage pools and bad smells.

PM10 and NO<sub>2</sub> concentrations showed a continuous increase from 2016 to 2019. However, they clearly decreased during the spring of 2020 by 62% and 78%, respectively, due to the lockdown imposed during the coronavirus pandemic, as shown in Figure 9, wherever human activity decreased dramatically.

The southern part of the study area suffers from pollution, mainly particulate matter from factories and dust storms. In addition, vehicles are one of the main causes of air pollution and emissions of carbon from PM2.5 [21]. Ad-Dar Al-Baida, Taybah, and Al-Mansuriyah are the least affected due to their distance from the industrial area. Despite that, Ad-Dar Al-Baida residents complain of pollution, and remedial measures must be adopted to reduce the seriousness of the situation. More studies should be conducted in the study area to determine the general direction of the concentrations of oxides and to identify the chemical composition of the particulate matter.

Moreover, citizens may change their lifestyle to mitigate the sources of air pollution, such as transportation and energy consumption [40].

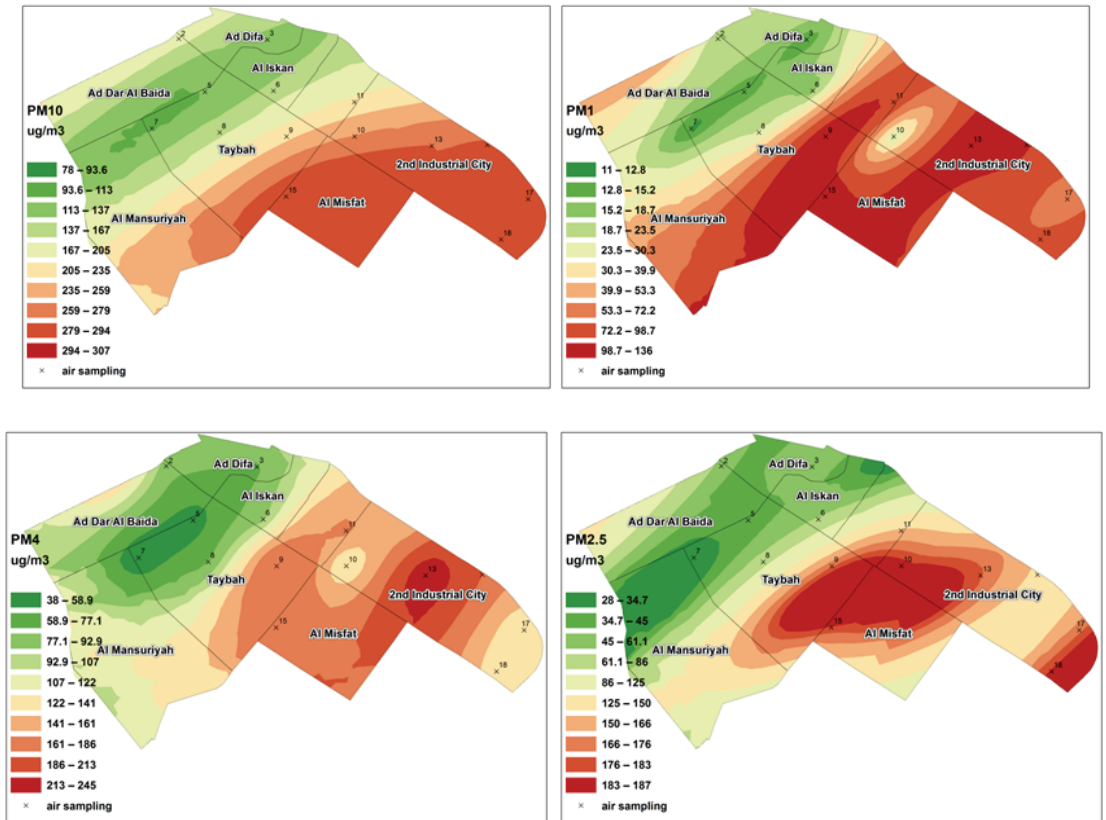


Figure 8. Cont.

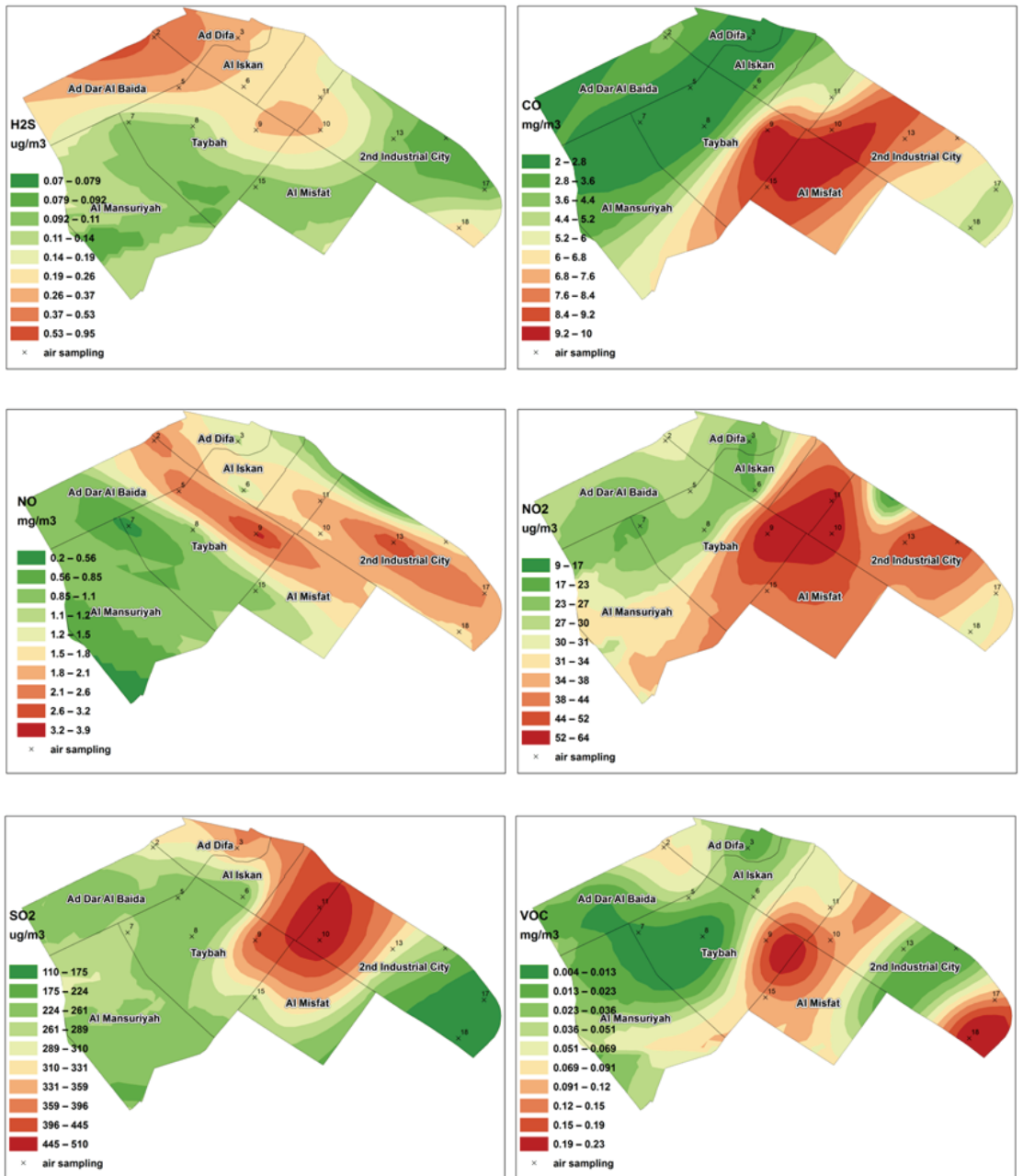


Figure 8. Ordinary kriging map of particulate matter and gases.

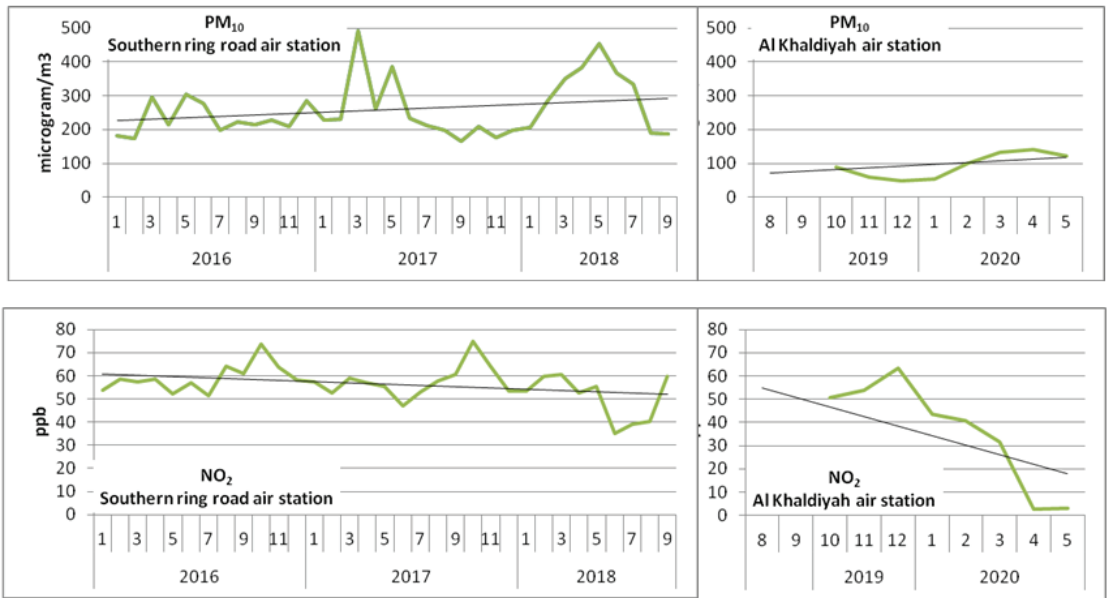


Figure 9. Trend in PM<sub>10</sub> and NO<sub>2</sub> during 2016–2020 on the Southern Ring Road and the Al Khaldiyyah air station.

#### 4. Conclusions

This study based on the questionnaire responses of residents living in southern Riyadh and air quality monitoring from 2016 to 2020 from a couple of air-monitoring stations close to the area of interest reveals that the adverse effects of poor air quality due to urbanization and industrialization are mostly felt by the residents of Al-Iskan, Ad-Dar Al-Baida, and the Second Industrial City. Respiratory problems and irritation in the eyes were reported by 49% and 50% of the residents, respectively, during the survey. A high concentration of PM<sub>10</sub> has been observed in many places in the study area, and it exceeds the permissible limits. Thermal analysis of the area showed the maximum temperature in the Second Industrial City and Al-Misfat, indicating the presence of the thermal island effect in these regions due to industrial activities. The anthropogenic influence on air quality was evident from the air quality data for 2020, which showed a marked decrease in parameters such as NO<sub>2</sub> due to the impacts of lockdown on various activities during the coronavirus pandemic. The land surface temperature image for May 2020 showed a temperature range between 54 °C and 32.4 °C, which is less than the temperature recorded during the same period in 2014 and 2017 and clearly shows the positive impact of minimal commercial/industrial activity during the lockdown period in 2020.

**Supplementary Materials:** The following are available online at <https://www.mdpi.com/2076-3417/11/5/2107/s1>, Table S1: Distribution of questionnaire in the study area; Table S2: Air sampling methods and instruments; Table S3: Relationship between districts and impact of pollution; Table S4: Correlation coefficients at 95% confidence level; Table S5: Eigen values of PC of the data sets; Table S6: Principal Component loadings of the data sets; Table S7: Semivariogram parameters.

**Author Contributions:** A.S. wrote the main manuscript and interpreted the data; M.A.-T. prepared questionnaires and analyzed the statistical data; S.H.-E. analyzed the Landsat images; F.K.Z. drafted and edited the work; N.A.-D. designed maps and prepared Figures 1–3. All authors have read and agreed to the published version of the manuscript.

**Funding:** This research was funded by the Deanship of Scientific Research at King Saud University through research group number RG-1438-023.

**Institutional Review Board Statement:** Not applicable.

**Informed Consent Statement:** Not applicable.

**Data Availability Statement:** Data sharing not applicable.

**Acknowledgments:** Sincere thanks to the Royal Commission for Riyadh City and the General Authority of Meteorology and Environment Protection for providing air quality data.

**Conflicts of Interest:** The authors declare no conflict of interest.

## References

- Al-Jelani, H. Air quality assessment at Al-Tan'eem area in the Holy Makkah City, Saudi Arabia. *Environ. Monit. Assess.* **2009**, *156*, 211–222. [CrossRef]
- Vicente, A.B.; Jordan, M.M.; Sanfeliu, T.; Sánchez, A.; Esteban, M.D. Air pollution prediction models of particles, As, Cd, Ni and Pb in a highly industrialized area in Castellón (NE, Spain). *Environ. Earth Sci.* **2012**, *66*, 879. [CrossRef]
- Pekey, B.; Özaskan, Ü. Spatial distribution of SO<sub>2</sub>, NO<sub>2</sub>, and O<sub>3</sub> Concentrations in an Industrial City of Turkey using a passive sampling method. *Clean Soil Air Water* **2013**, *41*, 423–428. [CrossRef]
- Al-Harbi, M. Assessment of Air Quality in two Different Urban Localities. *Int. J. Environ. Res.* **2014**, *8*, 15–26.
- Farahat, A. Air pollution in the Arabian Peninsula (Saudi Arabia, the United Arab Emirates, Kuwait, Qatar, Bahrain, and Oman): Causes, effects, and aerosol categorization. *Arab. J. Geosci.* **2016**, *9*, 1–17. [CrossRef]
- WHO. *Air Quality Guidelines: World Health Organization, Global Update WHO Regional Office for Europe 2006*; WHO: Copenhagen, Denmark, 2005.
- GHODR. *Urban Outdoor Air Pollution, Burden of Disease by Country, Global Health Observatory Data Repository*; World Health Organization: Geneva, Switzerland, 2008. Available online: <http://apps.who.int/gho/data/node.main.285> (accessed on 10 February 2021).
- IARC. *Outdoor Air Pollution as a Leading Environmental Cause of Cancer Deaths*; International Agency for Research on Cancer, World Health Organization: Lyon, France, 2013. Available online: [http://www.iarc.fr/en/media-centre/pr/2013/pdfs/pr221\\_E.pdf](http://www.iarc.fr/en/media-centre/pr/2013/pdfs/pr221_E.pdf) (accessed on 10 February 2021).
- Bourdrel, T.; Bind, M.A.; Béjot, Y.; Morel, O.; Argacha, J.F. Cardiovascular effects of air pollution. *Arch. Cardiovasc. Dis.* **2017**, *110*, 634–642. [CrossRef]
- Canadian Medical Association. No Breathing Room: National Illness Costs of Air Pollution. 2008. Available online: [http://www.healthyenvironmentforkids.ca/sites/healthyenvironmentforkids.ca/files/No\\_Breathing\\_Room.pdf](http://www.healthyenvironmentforkids.ca/sites/healthyenvironmentforkids.ca/files/No_Breathing_Room.pdf) (accessed on 10 February 2021).
- Nyberg, F.; Gustavsson, P.; Järup, L.; Bellander, T.; Berglind, N.; Jakobsson, R.; Pershagen, G. Urban air pollution and lung cancer in Stockholm. *Epidemiology* **2000**, *11*, 487–495. [CrossRef]
- Nafstad, P.; Haheim, L.L.; Oftedal, B.; Gram, F.; Holme, I.; Herrmann, I.; Leren, P. Lung cancer and air pollution: A 27 year follow up of 16 209 Norwegian men. *Thorax* **2003**, *58*, 1071–1076. [CrossRef]
- Al-Ahmadi, K.; Al-Zahrani, A. NO<sub>2</sub> and Cancer Incidence in Saudi Arabia. *Int. J. Environ. Res. Public Health* **2013**, *10*, 5844–5862. [CrossRef]
- ADA 2017, Regional Plan for the Region Riyadh, Al-Riyadh Development Authority. Available online: [http://www.ada.gov.sa/ADA\\_A/DocumentShow/?url=/res/ADA/Ar/Projects/regional\\_plan/index.html](http://www.ada.gov.sa/ADA_A/DocumentShow/?url=/res/ADA/Ar/Projects/regional_plan/index.html) (accessed on 10 February 2021).
- Modon. Industrial Cities Directory, Saudi Industrial Property Authority. 11\12\2016 9.12pm; 2017. Available online: <http://www.modon.gov.sa/EN/INDUSTRIALCITIES/INDUSTRIALCITIESDIRECTORY/INDUSTRIALCITIES/Pages/default.aspx> (accessed on 10 February 2021).
- Al-Jassir, M.; Shaker, A.; Khaliq, M. Deposition of Heavy Metals on Green Leafy Vegetables Sold on Roadsides of Riyadh City, Saudi Arabia. *Bull. Environ. Contam. Toxicol.* **2005**, *75*, 1020–1027. [CrossRef]
- Parrish, D.; Kuster, W.C.; Min, S.; Yokouchi, Y.; Kondo, Y.; Goldan, P.; De Gouw, J.; Koike, M.; Shirai, T. Comparison of air pollutant emissions among mega-cities. *Atmos. Environ.* **2009**, *43*, 6435–6441. [CrossRef]
- Al-Rehaili, A. Outdoor-indoor Air Quality in Riyadh: SO<sub>2</sub>, NH<sub>3</sub>, and HCHO. *Environ. Monit. Assess.* **2002**, *79*, 287. [CrossRef] [PubMed]
- Tawabini, B.; Lawal, T.; Shaibani, A.; Farahat, A. Morphological and Chemical Properties of Particulate Matter in the Dammam Metropolitan Region: Dhahran, Khobar, and Dammam, Saudi Arabia. *Adv. Meteorol.* **2017**, *2017*, 8512146. [CrossRef]
- Shareef, M.; Husain, T.; Alharbi, B. Analysis of Relationship between O<sub>3</sub>, NO, and NO<sub>2</sub> in Riyadh, Saudi Arabia. *Asian J. Atmos. Environ.* **2018**, *12*, 17–29. [CrossRef]
- Bian, Q.; Alharbi, B.; Shareef, M.; Husain, T.; Pasha, M.; Atwood, S.; Kreidenweis, S. Sources of PM<sub>2.5</sub> carbonaceous aerosol in Riyadh, Saudi Arabia. *Atmos. Chem. Phys.* **2018**, *18*, 3969–3985. [CrossRef]
- Air Quality Index. General Authority of Meteorology and Environment Protection. 2020. Available online: <https://www.pme.gov.sa/Ar/Environment/AirQuality/Pages/AQ-Dashboard.aspx> (accessed on 10 February 2021).
- Isaaks, E.H.; Srivastava, R.M. *An Introduction to Applied Geostatistic*; Oxford University Press: New York, NY, USA, 1989.



24. Carlon, C.; Critto, A.; Marcomini, A.; Nathanail, P. Risk based characterization of contaminated industrial site using multivariate and geostatistical tools. *Environ. Pollut.* **2001**, *111*, 417–427. [CrossRef]
25. Moral, F.; Ivarez, P.; Canito, J. Mapping and hazard assessment of atmospheric pollution in a medium sized urban area using the Rasch model and Geostatistic techniques. *Atmos. Environ.* **2006**, *40*, 1408–1418. [CrossRef]
26. Moradi Dashtpargerdi, M.; Sadatinejad, S.J.; Zare Bidaki, R.; Khorsandi, E. Evaluation of Air Pollution Trend Using GIS and RS Applications in South West of Iran. *J. Indian Soc. Remote Sens.* **2014**, *42*, 179. [CrossRef]
27. Roy, D.P.; Wulder, M.A.; Loveland, T.R.; Woodcock, C.E.; Allen, R.G.; Anderson, M.C.; Helder, D.; Irons, J.R.; Johnson, D.M.; Kennedy, R.; et al. Landsat-8: Science and product vision for terrestrial global change research. *Remote Sens. Environ.* **2014**, *145*, 154–172. [CrossRef]
28. Weng, Q.; Lu, D.; Schubring, J. Estimation of land surface temperature–vegetation abundance relationship for urban heat island studies. *Remote Sens. Environ.* **2004**, *89*, 467–483. [CrossRef]
29. Aniello, C.; Morgan, K.; Busbey, A.; Newland, L. Mapping micro-urban heat islands using LANDSAT TM and a GIS. *Comput. Geosci.* **1995**, *21*, 965–967, 969. [CrossRef]
30. Weng, Q.; Yang, S. Urban Air Pollution Patterns, Land Use, and Thermal Landscape: An Examination of the Linkage Using GIS. *Environ. Monit. Assess.* **2006**, *117*, 463. [CrossRef] [PubMed]
31. CDSI. Census of Population and Housing Report in Administrative Region. Central Department of Statistic and Information. Internal Report. 2004. Available online: <http://www.cdsi.gov.sa/english/> (accessed on 10 February 2021).
32. USGS. Landsat 8 Data Users Handbook—Section 5/Conversion of DN's to Physical Units. 2018. Available online: <https://landsat.usgs.gov/landsat-8-18-data-users-handbook-section-5> (accessed on 10 February 2021).
33. Syariza, M.A.; Jaelania, L.M.; Subehie, L.; Pamungkasb, A.; Koenhardonoc, E.S.; Sulisetyonod, A. Retrieval of sea surface temperature over Poteran island water of Indonesia with Landsat 8 TIRS image: A preliminary algorithm. In Proceedings of the International Archives of the Photogrammetry, Remote Sensing and Spatial Information Sciences 2015, Joint International Geoinformation Conference 2015, Kuala Lumpur, Malaysia, 28–30 October 2015; Volume XL-2/W4.
34. Anandababu, D.; Purushothaman, B.M.; Suresh, B.S. Estimation of Land Surface Temperature using LANDSAT 8 Data. *Int. J. Adv. Res. Ideas Innov. Technol.* **2018**, *4*, 177–186.
35. Solangi, G.; Siyal, A.; Siyal, P. Spatiotemporal Dynamics of Land Surface Temperature and Its Impact on the Vegetation. *Civ. Eng. J.* **2019**, *5*, 1753–1763. [CrossRef]
36. Brase, C.H. *Understanding Basic Statistics*; Brooks/Cole: Seattle, WA, USA, 2010; Volume 5.
37. Isa, D.E. Proceedings of the World Congress on Engineering. In *The Robust Principal Component*; WCE: London, UK, 2009; Volume I, p. 1.
38. Deutsch, C.V. *Geostatistical Reservoir Modeling*; Oxford UP: Oxford, UK, 2002.
39. Seaton, A.; MacNee, W.; Donaldson, K.; Godden, D. Particulate air pollution and acute health effects. *Lancet* **1995**, *345*, 176–178. [CrossRef]
40. Sofia, D.; Gioiella, F.; Lotrecchiano, N.; Giuliano, A. Mitigation strategies for reducing air pollution. *Environ. Sci. Pollut. Res.* **2020**, *27*, 19226–19235. [CrossRef] [PubMed]

MDPI  
St. Alban-Anlage 66  
4052 Basel  
Switzerland  
Tel. +41 61 683 77 34  
Fax +41 61 302 89 18  
[www.mdpi.com](http://www.mdpi.com)

*Applied Sciences* Editorial Office  
E-mail: [appls@mdpi.com](mailto:appls@mdpi.com)  
[www.mdpi.com/journal/appls](http://www.mdpi.com/journal/appls)







Academic Open  
Access Publishing

[www.mdpi.com](http://www.mdpi.com)

ISBN 978-3-0365-8279-5